Exploration of Sintering Behavior for Solid Solution Carbide Ceramics

A Dissertation Presented for the

Doctor of Philosophy

Degree

The University of Tennessee, Knoxville

Jonas Kessing

December 2024

© by Jonas Kessing, 2024
All Rights Reserved.

This work is dedicated to my wife, Dr. Julia Abraham, whose love and unwavering support has been my guiding light throughout this academic journey. I also dedicate this work to my daughter, June, my little sunshine; your innocence provides the purest inspiration, and your laughter lights up my world. Thank you both for being my constant sources of joy and motivation.

To my parents, your steadfast love, guidance, and sacrifices have been the foundation of my journey. This dissertation is a tribute to your boundless support and the countless ways you have shaped my path.

Acknowledgments

I would like to express my heartfelt gratitude to everyone who supported me throughout my PhD journey. First and foremost, I extend my deepest appreciation to my advisor, Dr. Steven Zinkle, whose guidance, insight, and support were invaluable to my research and personal growth. Your mentorship has profoundly shaped my academic career.

I am also grateful to my dissertation committee members, Dr. Khalid Hattar, Dr. Lawrence Heilbronn, and Dr. Katharine Page, for their constructive feedback and unwavering support, which have greatly enriched my work. My thanks extend to Dr. Justin Milner for his guidance and assistance throughout this process. This research was partially funded by the NASA Space Nuclear Propulsion project and NASA Glenn Research Center under grant number 80NSSC21K2011.

Special thanks go to Neal Evans and Michael Koehler for their exceptional training and support with the SEM and X-ray diffraction systems, respectively. I also wish to acknowledge Dr. Brian Jaques and Allyssa Bateman from the Advanced Materials Laboratory (AML) at Boise State University (BSU) for their expertise in LECO combustion analysis. My sincere thanks to Dr. David Sprouster at Stony Brook University for his high-resolution X-ray diffraction (XRD) and phase analysis work. I am especially grateful to Dr. Eddie Lopez Honorato from Oak Ridge National Laboratory (ORNL) for conducting Raman spectroscopy and analysis.

I would also like to extend my thanks to Dr. Brandon Shaver for his outstanding technical expertise and fabrication support, whose recommendations greatly contributed to the success of my research. My appreciation also goes to Alex Nadermann for his significant assistance throughout my PhD journey, including coursework, research collaboration, and valuable discussions—his contributions have been essential to my accomplishments. Additionally, I

am thankful for the support and insights provided by the other members of Dr. Zinkle's research group, which were vital to my success.

Finally, I owe a special thanks to my family, especially my wife, Dr. Julia Abraham, for their unconditional support and encouragement. Your belief in me kept me motivated through the highs and lows of this journey. Thank you all for being part of this experience.

Abstract

Solid solutions of niobium carbide (NbC), tantalum carbide (TaC), and zirconium carbide (ZrC), when mixed with uranium carbide (UC), emerge as promising fuel candidates for nuclear thermal propulsion (NTP) applications. Their appeal lies in high melting temperatures, stability in hot hydrogen, and low thermal neutron absorption cross-sections. Among these, the composition ($Zr_{0.8}$, $Nb_{0.1}$, $Ta_{0.1}$)C exhibits particularly favorable properties as a surrogate fuel for NTP.

This study focuses on optimizing spark plasma sintering (SPS) conditions for achieving over 95% relative density in ($Zr_{0.8}$, $Nb_{0.1}$, $Ta_{0.1}$)C. Various characterization techniques were employed, including grain size analysis, Archimedes' density measurements, scanning electron microscopy (SEM), X-ray diffraction (XRD), X-ray fluorescence (XRF), Raman spectroscopy, and Vickers hardness testing, to assess grain size, ideal density fraction, porosity, chemical composition, and hardness. Furthermore, the relationships among hardness, grain size, and density for samples consolidated under different sintering conditions were explored. Calculations of the activation energies for both sintering and grain growth were performed, identifying the underlying densification mechanisms through two distinct approaches.

Table of Contents

1 Introduction **1**

1.1 NTP Overview 3

1.2 NTP Specifications and Requirements 6

2 Literature Review **10**

2.1 History of NTP Fuel Testing 10

2.1.1 Rover & NERVA Programs 10

2.1.2 Soviet Twisted Ribbon 19

2.1.3 GE710 and ANL Programs 23

2.1.4 Space Nuclear Thermal Propulsion (SNTP) Project 26

2.1.5 Square Lattice Honeycomb Design 26

2.1.6 Summary of NTP Fuel Testing Results 29

2.2 NTP Fuel Materials 36

2.2.1 Hot Hydrogen Compatibility 36

2.2.2 High Melting Temperature Materials 39

2.2.3 Phase Stability of Solid Solution Refractory Carbide Fuels 43

2.2.4 Fuel Enrichment 53

2.3 Refractory Carbide Fabrication 57

2.3.1 Spark Plasma Sintering 57

2.3.2 SPS Densification and Grain Growth of Refractory Carbides 71

3 Methods **94**

3.1 Experimental Methods 94

3.1.1 Powder Characterization 94
3.1.2 Sample Preparation and Consolidation 95
3.1.3 Sample Characterization 97
3.2 Sintering Activation Energy Methods 100
3.2.1 Bernard-Granger and Guizard Method 100
3.2.2 Young-Cutler Method 103
3.3 Grain Growth Activation Energy 105

4 Results **106**
4.1 Powder Characterization 106
4.1.1 Particle Size Analysis 106
4.1.2 Quantification of Impurities 106
4.2 Phase 1 113
4.3 Phase 2 120
4.4 Phase 3 124
4.5 Sintering Activation Energy Results 142
4.5.1 Bernard-Granger and Guizard Method Results 142
4.5.2 Young-Cutler Method Results 149
4.6 Grain Growth Activation Energy 154

5 Discussion **157**
5.1 Powder Characterization 157
5.2 Relative Density, Hardness, and Grain Size 158
5.3 High Pressure Runs and Sintering Atmosphere 166
5.4 Sintering Activation Energy 169
5.5 Grain Growth Activation Energy 174

6 Conclusions **176**

Bibliography **179**

Vita **190**

List of Tables

1.1 Major Challenges for Developing NEP and NTP Systems 4

2.1 SNTP fuels summary 28
2.2 NTP Fuel Temperature Parameters 34
2.3 Summary of NTP Fuel Assessment 35

3.1 Graphite grade comparison of SPS tooling 96
3.2 Polishing Procedure 99
3.3 Values for Elastic Moduli and Poisson's Ratios 102

4.1 XRF Results 111
4.2 LECO Results 112
4.3 High resolution XRD results 114
4.4 Phase 1 Results 116
4.5 Phase 2 Results 123
4.6 Phase 3 Results 130

5.1 Calculated anion to cation ratio (C/M). 160
5.2 Impact of temperature, hold time, and applied pressure on RD, grain size, and Vickers hardness 164
5.3 Densification Activation Energy Comparison 172
5.4 Mono-Carbide Diffusion Values From Literature 173
5.5 Sintering Activation Energies for NbC, TaC, and ZrC 175

List of Figures

1.1 Chemistry, definition, and applications of UHTCs 2
1.2 DOE infographic on NTP 5
1.3 Comparison on various energy sources for rocket propulsion 7
1.4 NTP specific impulse vs. chamber temperature 8

2.1 Proof of principle being demonstrated with the 100 MW Kiwi-A 12
2.2 Summary of the testing program for the nuclear rocket reactors 14
2.3 Relative size of Los Alamos reactors 15
2.4 Chronology of major nuclear rocket reactor tests 17
2.5 Rover/NERVA fuel types 18
2.6 Cumulative testing time for all Rover reactor and engine system tests 20
2.7 Operating time versus coolant exit temperature for full-power reactor tests . 21
2.8 Photographs of a heating unit and twisted-rod two-blade HREs 22
2.9 Soviet twisted fuel element and fuel assembly 24
2.10 GE710 fuel element concept 25
2.11 Evolution of the Particle Bed Reactor – fuel particle to the reactor core . . . 27
2.12 SLHC fuel sub-assembly 30
2.13 An illustration of the induction furnace chamber 31
2.14 Representative x-ray diffraction profile for (U, Zr, Ta)C 32
2.15 Performance of tri-carbide nuclear fuels exposed to hot hydrogen 33
2.16 Conceptual Trade Off Between Performance and Efficiency 37
2.17 Hot hydrogen interaction process along a U-Zr-C material duct 38
2.18 Equilibrium partial pressures in hydrogen as a function of temperature . . . 40

2.19 Effects of surface cracks on corrosion 41
2.20 Comparison of different ultra-high temperature compounds 42
2.21 Spatial phase diagram for the Zr-Nb-C system 44
2.22 Liquidus surface for the Zr-Nb-C system 45
2.23 Isothermal sections of the surface of the $Zr_{1-x}Nb_xC_y$ exsolution region 46
2.24 Solidus surface of NbC-ZrC-UC system 47
2.25 Zr-C phase diagram 49
2.26 U-C phase diagram 50
2.27 The UC-$ZrC_{0.81}$ phase diagram 51
2.28 Isothermal ternary phase diagram for U-Zr-C 52
2.29 Uranium Enrichment Levels 54
2.30 Typical classification of sintering methods 58
2.31 Basic SPS System configuration 59
2.32 On-off DC pulsed current path 61
2.33 Pulsed current flow through powder particles 62
2.34 Effects of on-off DC pulse energizing 63
2.35 SPS insulator vs. conductor 64
2.36 The temperature difference between specimen and graphite die 65
2.37 Simulation vs. experiment: temperature evolution in SPS 66
2.38 Depictions of top and side pyrometer configurations 68
2.39 SPS temperature of top vs. side pyrometer 69
2.40 SPS double acting die 70
2.41 Map of ZrC relative densities 72
2.42 Hot pressing vs. control SPS of ZrC 73
2.43 ZrC SPS densification 74
2.44 TaC sintering routes 76
2.45 Effects of temperature on the density and grain size of TaC 77
2.46 Relative density and the average grain size of TaC 78
2.47 TaC densification routes 79
2.48 The effects of pressure and temperature on the densification of B_4C powders 81

2.49 Relative density and grain size of B_4C as a function of temperature 82
2.50 Densification and grain growth curves of TaC ceramics 83
2.51 Sintering mechanisms 84
2.52 SEM micrographs of TaC sample sintered at different temperatures 86
2.53 SEM micrographs of TaC sample sintered at 1800 °C for different holding times 87
2.54 SEM micrographs of TaC samples sintered at 1800 °C under different pressures 88
2.55 Densification of TaC samples sintered under different pressures 89
2.56 Densification curves of TaC samples during SPS at different temperatures . . 90
2.57 Apparent activation energy for densification of TaC powder 91
2.58 Relationship between $G_t^p - G_0^p$ and t for different grain size exponents 93

3.1 SPS Furnace at UTK 98

4.1 Powder morphology SEM micrographs 107
4.2 Particle size analysis results for NbC, TaC, and ZrC 108
4.3 Powder agglomeration SEM micrographs of NbC, TaC, and ZrC 109
4.4 Particle size analysis results including agglomerations 110
4.5 High resolution powder XRD spectra and phase identification 115
4.6 Secondary electron micrographs of ($Zr_{0.8}$, $Nb_{0.1}$, $Ta_{0.1}$)C consolidated in the SPS at various temperatures 117
4.7 Relative density, grain size, and Vickers hardness as a function of temperature for ($Zr_{0.8}$, $Nb_{0.1}$, $Ta_{0.1}$)C 118
4.8 Vickers hardness and grain size versus relative density for ($Zr_{0.8}$, $Nb_{0.1}$, $Ta_{0.1}$)C 119
4.9 A comparison of XRD spectra of ($Zr_{0.8}$, $Nb_{0.1}$, $Ta_{0.1}$)C consolidated in the SPS at various temperatures 121
4.10 Formation of single phase XRD spectra of ($Zr_{0.8}$, $Nb_{0.1}$, $Ta_{0.1}$)C consolidated at various temperatures 122
4.11 Secondary electron micrographs of ($Zr_{0.8}$, $Nb_{0.1}$, $Ta_{0.1}$)C consolidated in the SPS at various hold times 125
4.12 Relative density, grain size, and Vickers hardness versus hold time for ($Zr_{0.8}$, $Nb_{0.1}$, $Ta_{0.1}$)C 126

4.13 Vickers hardness and grain size versus relative density for ($Zr_{0.8}$, $Nb_{0.1}$, $Ta_{0.1}$)C consolidated in the SPS at various hold times 127
4.14 A comparison of XRD spectra of ($Zr_{0.8}$, $Nb_{0.1}$, $Ta_{0.1}$)C consolidated in the SPS at various hold times 128
4.15 Formation of single phase XRD spectra of ($Zr_{0.8}$, $Nb_{0.1}$, $Ta_{0.1}$)C consolidated at various hold times 129
4.16 Secondary electron micrographs of ($Zr_{0.8}$, $Nb_{0.1}$, $Ta_{0.1}$)C consolidated in the SPS in a vacuum at various applied pressures 132
4.17 Secondary electron micrographs of ($Zr_{0.8}$, $Nb_{0.1}$, $Ta_{0.1}$)C consolidated in the SPS in an argon purged environment at various applied pressures 133
4.18 Secondary electron micrographs of ($Zr_{0.8}$, $Nb_{0.1}$, $Ta_{0.1}$)C consolidated in the SPS in a vacuum or an argon purged environment at 30 MPa or 60 MPa . . 134
4.19 Relative density, grain size, and Vickers hardness vs pressure for ($Zr_{0.8}$, $Nb_{0.1}$, $Ta_{0.1}$)C sintered in vacuum 135
4.20 Relative density, grain size, and Vickers hardness vs pressure for ($Zr_{0.8}$, $Nb_{0.1}$, $Ta_{0.1}$)C sintered in argon 136
4.21 Vickers hardness and grain size vs relative density for ($Zr_{0.8}$, $Nb_{0.1}$, $Ta_{0.1}$)C sintered at various pressures 137
4.22 A comparison of XRD spectra of ($Zr_{0.8}$, $Nb_{0.1}$, $Ta_{0.1}$)C consolidated in the SPS in a vacuum at various pressures 138
4.23 XRD spectra of ($Zr_{0.8}$, $Nb_{0.1}$, $Ta_{0.1}$)C consolidated in a vacuum at various pressures 139
4.24 A comparison of XRD spectra of ($Zr_{0.8}$, $Nb_{0.1}$, $Ta_{0.1}$)C consolidated in the SPS in an argon purged environment at various pressures 140
4.25 XRD spectra of ($Zr_{0.8}$, $Nb_{0.1}$, $Ta_{0.1}$)C consolidated in an argon purged environment at various pressures 141
4.26 Raman spectra of ($Zr_{0.8}$, $Nb_{0.1}$, $Ta_{0.1}$)C 143
4.27 Micrograph of ($Zr_{0.8}$, $Nb_{0.1}$, $Ta_{0.1}$)C 144
4.28 Relative density as a function of temperature for ($Zr_{0.8}$, $Nb_{0.1}$, $Ta_{0.1}$)C 145
4.29 Densification rate as a function of temperature for ($Zr_{0.8}$, $Nb_{0.1}$, $Ta_{0.1}$)C . . . 146

4.30 Relative density as a function of time for ($Zr_{0.8}$, $Nb_{0.1}$, $Ta_{0.1}$)C 147
4.31 Relative density as a function of soak time for ($Zr_{0.8}$, $Nb_{0.1}$, $Ta_{0.1}$)C 148
4.32 Densification rate vs relative density for ($Zr_{0.8}$, $Nb_{0.1}$, $Ta_{0.1}$)C 150
4.33 Determination of stress exponent n for ($Zr_{0.8}$, $Nb_{0.1}$, $Ta_{0.1}$)C 151
4.34 Activation energy for sintering of ($Zr_{0.8}$, $Nb_{0.1}$, $Ta_{0.1}$)C 152
4.35 Activation energy for sintering of ($Zr_{0.8}$, $Nb_{0.1}$, $Ta_{0.1}$)C using the Young-Cutler method 153
4.36 Grain growth exponent of ($Zr_{0.8}$, $Nb_{0.1}$, $Ta_{0.1}$)C 155
4.37 Activation energy for grain growth of ($Zr_{0.8}$, $Nb_{0.1}$, $Ta_{0.1}$)C 156

5.1 Flow chart for calculating C/M ratio of ZrC 159
5.2 Vickers hardness and grain size vs relative density for all ($Zr_{0.8}$, $Nb_{0.1}$, $Ta_{0.1}$)C samples 162
5.3 Microstructural comparison of ($Zr_{0.8}$, $Nb_{0.1}$, $Ta_{0.1}$)C samples sintered at various temperatures, hold times, and pressures 165
5.4 Comparison of relative density versus lattice parameter for all ($Zr_{0.8}$, $Nb_{0.1}$, $Ta_{0.1}$)C samples 167

Chapter 1

Introduction

Ultra-high temperature ceramics (UHTC) are an advanced materials class for applications in extreme environments that exceed the capabilities of modern engineering ceramics. These UHTCs are commonly classified by either their melting temperature, end-use temperature, or chemical composition [1]. UHTCs are often described as materials with melting temperatures over 3000 °C (**Figure 1.1b**), although there is a high degree of uncertainty in the exact melting temperature of these high temperature compounds [1, 2, 3, 4, 5]. The end-use temperature is another method of defining UHTCs, where 2000 °C is generally used as the minimum operating temperature threshold [1, 2, 4]. Perhaps the most common categorization of UTHCs is by the chemical composition (**Figure 1.1a**); specifically, the majority of UHTCs are compounds containing borides, carbides, or nitrides of transition metals such as Zr, Hf, Ta, W, or Nb [1, 2, 3, 4, 5, 6, 7].

These compounds normally have high hardness, stiffness, and melting temperature and, when compared to oxide ceramics, have higher electrical and thermal conductivity [4], which are all desirable characteristics for withstanding extreme environments. The main applications for UHTCs are hypersonics (e.g. wing leading edges, nose cones, and propulsion system components) [1, 2, 3, 4, 6], space exploration (e.g. rocket propulsion, atmospheric reentry, nozzle components, and heat shields) [1, 4, 6], and nuclear energy (e.g. plasma facing components) [7, 8, 9], shown in **Figure 1.1c**, where the material performance is limited by extreme environmental temperature, chemical reactivity, mechanical stress, radiation, and

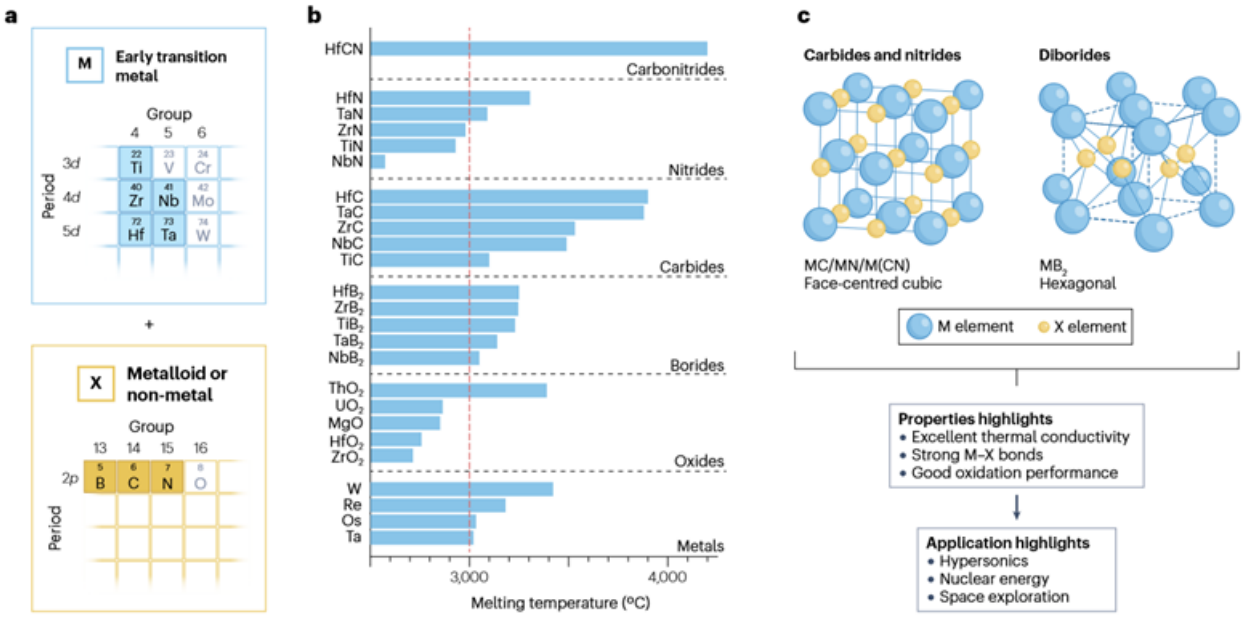


Figure 1.1: Chemistry, definition, and applications of UHTCs. a) Typical elements that are combined in UHTCs. b) UHTCs are typically defined as ceramic materials with melting points beyond 3,000 °C. c) Crystal structure, main properties and applications of UHTC carbides, nitrides and diborides in extreme environments [7].

wear [1]. The focus of this dissertation is the application of UHTC and uranium carbide (UC) compounds, or mixed carbide fuels, for space nuclear propulsion (SNP).

The two forms of SNP being considered by NASA to support a human exploration mission to Mars are nuclear electric propulsion (NEP) and nuclear thermal propulsion (NTP) [10]. NEP converts the thermal energy produced from an onboard nuclear reactor into electricity that can then be used to provide propulsion and power to the spacecraft. NTP uses thermal energy produced from an onboard nuclear reactor to heat a propellant, which expands out of a nozzle and provides thrust. **Table 1.1**, provided from a SNP technology committee report [10], summarizes the main challenges for developing NEP and NTP systems. The committee determined that the main challenge for NEP is the task of scaling up the power of each NEP subsystem to provide enough energy for a mission to Mars. For NTP, the main challenge determined was for reactor operation to reach temperatures up to 2700 K, to enable higher efficiencies, which is at the upper temperature limits of current known engineering materials. The use of NTP for a manned Mars mission was determined to be a lower risk than to use NEP due to the current status of technology development. Using UHTCs mixed with UC, in the form of mixed carbide fuels, is one of the leading fuel candidates for NTP applications, as UHTCs are currently some of the highest temperature compounds in existence.

1.1 NTP Overview

NTP is an alternative method of spacecraft propulsion to traditional chemical rockets. Liquid propellant is pumped into a nuclear reactor, heating and expanding the propellant, which is then expelled through a nozzle, providing thrust (**Figure 1.2**). The target operating temperature for an NTP reactor is around 2700 K, corresponding to a specific impulse (I_{sp}) of 900 seconds, which is limited by the core and structural materials [10, 11, 12, 13, 14]. By heating the propellant via a nuclear reactor instead of combustion, NTP rockets are predicted to reach a much higher specific impulse, a common measurement of rocket efficiency, than with chemical rockets. I_{sp} can be defined by **Equation 1.1** [15],

Table 1.1: Major Challenges for Developing NEP and NTP Systems [10]

Category	NTP	NEP
Reactor Core Fuel and Materials	• High reactor fuel operating temperature (more than 2700 K)	
System Operational Parameters	• Rapid system startup to full operating temperature (preferably in 1 min or less)	• Long system operational reliability (4 years for power generation, 1 to 2 years for thrust)
Scale		• Power conversion and thermal subsystem tests conducted to date have been at power levels orders of magnitude below that required for baseline mission • Limited full-scale, short duration electric propulsion subsystem testing at power levels an order of magnitude below that required for baseline mission
Ground-Based Testing	• Need to capture and process engine exhaust (resulting in high cost) • Facility preparation time (stresses baseline schedule) • Little integrated system testing experience; none of it recent • Last relevant-scale tests were nearly 50 years ago	• No fully integrated system testing experience
In-Space Propulsion Technology Needs	• Long-term storage of liquid hydrogen in space at 20 K with minimal loss	• Parallel development of chemical propulsion systems
System Complexity		• Highly complex: six NEP subsystems and a chemical propulsion system

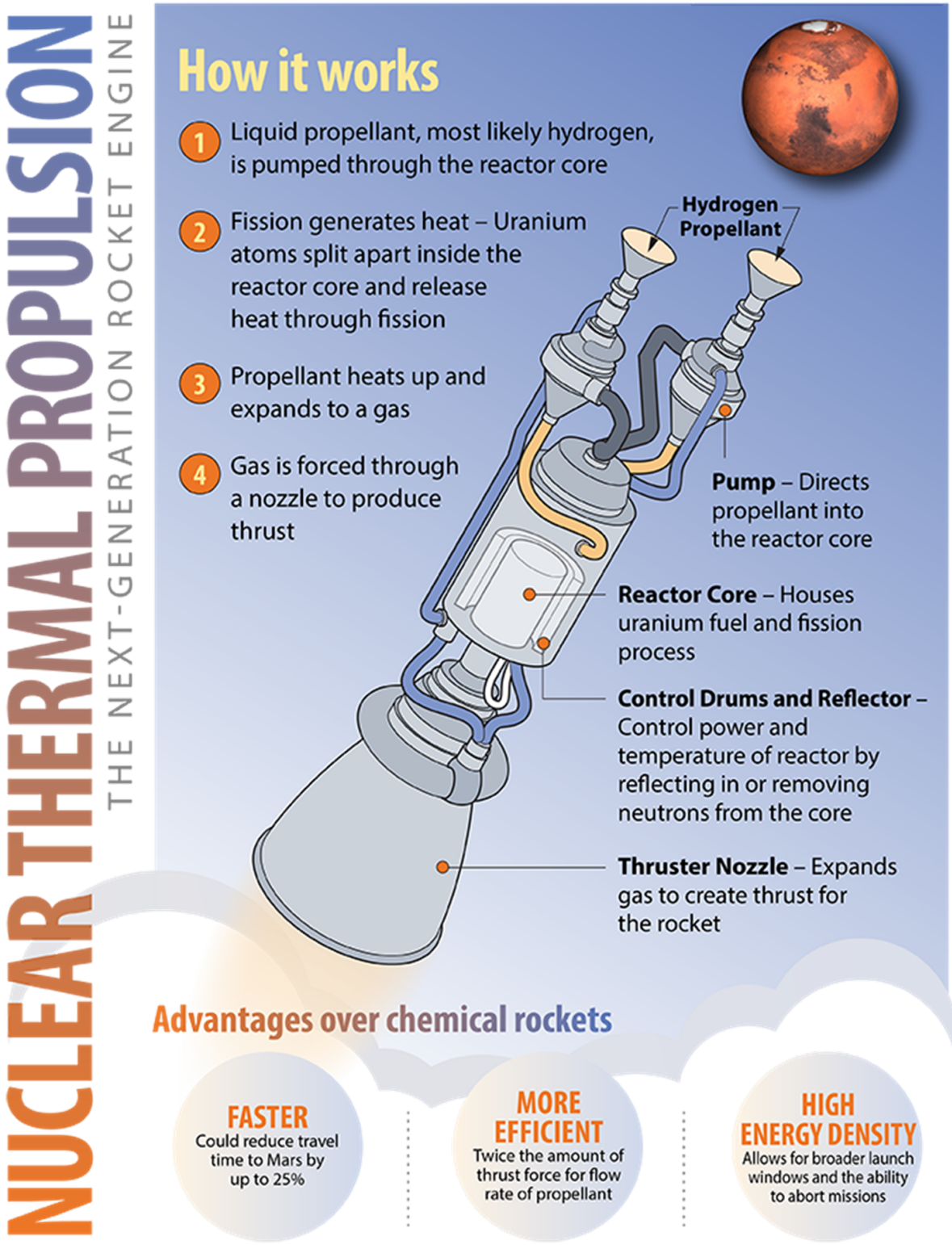


Figure 1.2: DOE infographic on NTP [16].

$$I_{sp} = \frac{F}{g_c \dot{m}} = \frac{1}{g_c} \sqrt{\frac{2\gamma}{\gamma - 1} \frac{R_u}{mw} T_c \left[1 - \frac{P_e}{P_c}\right]^{\frac{\gamma-1}{\gamma}}} \tag{1.1}$$

where F is the total engine thrust, g_c is a conversion factor, $\dot{m}$ is the propellant mass flow rate, γ is the specific heat ratio, R_u is the universal gas constant, mw is the propellant molecular weight, T_c is the temperature of propellant after leaving the nozzle, P_e is the pressure at the exit nozzle, and P_c is the pressure in the reactor chamber.

While the units for I_{sp} are seconds, it is comparable to the fuel efficiency of a car in miles per gallon and quantifies the length of time that one kilogram of propellant can produce one newton of thrust. A high I_{sp} is desirable and, when paired with high thrust capability, corresponds to shorter mission durations and higher cargo payloads. When compared to chemical rockets, solid core NTP engines have approximately twice the I_{sp}, as shown in **Figure 1.3**. However, there are many challenges facing the development of NTP rockets for interplanetary travel, including the restrictive requirements for fuel materials. The behavior of the fuel materials at operational conditions needs to be further analyzed to predict how routine operations will affect the structural integrity and performance of the NTP reactor.

1.2 NTP Specifications and Requirements

In order to achieve the desired fuel performance parameters required in an NTP environment, fuel material selection must be carefully considered. The I_{sp} of a NTP rocket is heavily dependent on the rocket's reactor chamber temperature, which is often limited by the melting temperature of the fuel and structural materials. Additionally, the corrosive environment in the NTP fuel elements from the hot flowing hydrogen propellant presents another difficult materials challenge. **Figure 1.4** shows several different NTP fuel material options and their corresponding I_{sp}; graphite composite fuels, ceramic metallic fuels (cermets), and carbide fuels are three potential fuel materials for NTP applications.

Due to high melting temperatures and desirable neutron economy, graphite composite fuels are presented as an intriguing option; however, graphite is incompatible with hot flowing hydrogen [11] and requires a protective coating which, if structurally compromised, would

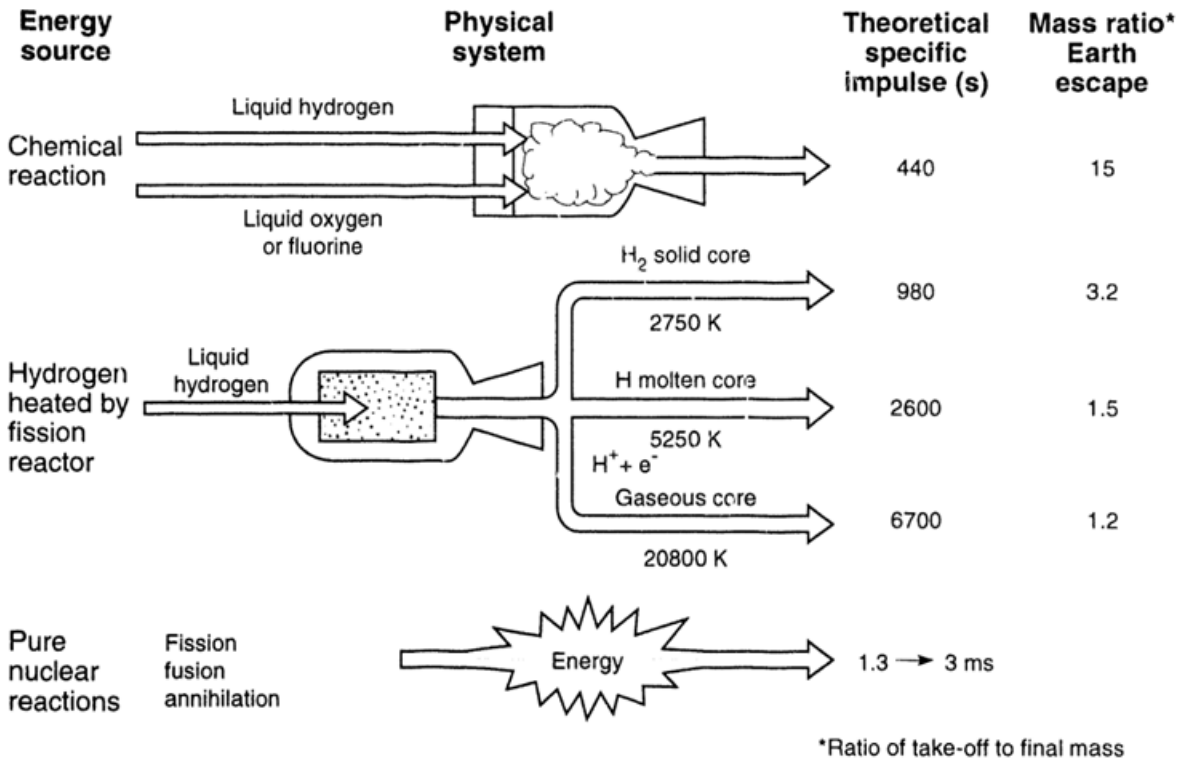


Figure 1.3: Comparison on various energy sources for rocket propulsion [20].

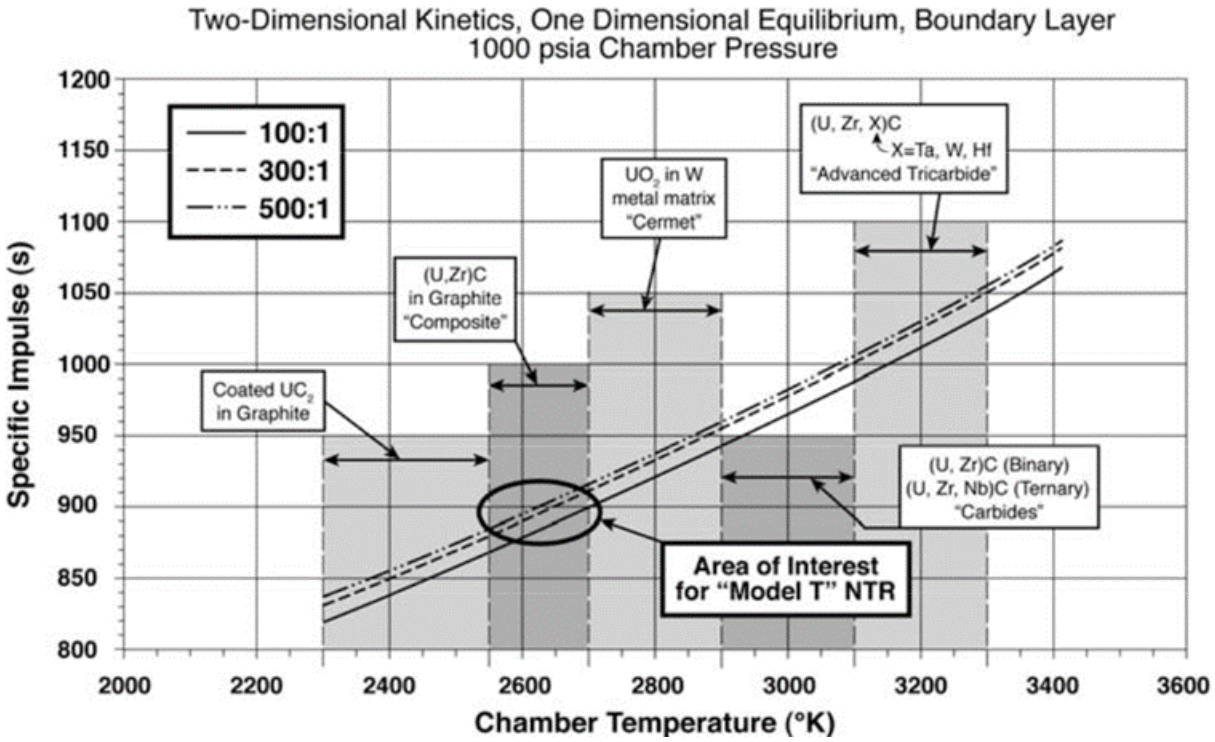


Figure 1.4: NTP specific impulse vs. chamber temperature for different fuels and nozzle area ratios [21].

lead to significant fuel corrosion. In the presence of hot flowing hydrogen, graphite composite materials undergo significant corrosion leading to a reduction in operational lifetime, overall engine performance, and the thrust to weight ratio of the rocket [17]. While a protective coating can inhibit hydrogen corrosion of graphite, cracking of the coating, caused by mechanisms such as mismatched coefficient of thermal expansion (CTE) or from the surface coating process, can increase corrosion and speed up mass loss rate [18]. This mass loss can negatively affect the structural integrity of the reactor as well as the neutronics of the core; losing graphite leads to a reduction in neutron moderation in the reactor, negatively impacting the flux profile and power [19].

Cermet fuels are made of ceramic fuel, normally either uranium nitride (UN) or uranium dioxide (UO_2), embedded in a refractory metal matrix of molybdenum (Mo) or tungsten (W)[22]. Benefits of cermet fuels over graphite composite fuels include higher strength, increased compatibility with hot hydrogen, and resistance to fission product release [23]. The refractory metal matrix is more resistant to hydrogen corrosion than graphite but has considerable drawbacks. W has a high melting point but a relatively high thermal neutron absorption cross section, which is not a desirable quality in an NTP fuel matrix material. The difference in the coefficient of thermal expansion between the fuel and the refractory matrix is enough to cause the fuel particles to separate from the matrix after numerous thermal cycles [22]. Despite having better neutron absorption characteristics, Mo has a much lower melting temperature than W, restricting the operating temperatures, and therefore the I_{sp}, of the NTP rocket.

Mixed carbide fuels, made from UC mixed with refractory metal carbides of zirconium and either niobium or tantalum, are promising NTP fuel candidates. By combining UC with refractory metal carbides, which have some of the highest melting temperatures of all known materials, the mixed carbide fuels hold the highest potential for withstanding the harsh conditions of NTP [22]. Despite lacking in technological development, these mixed carbide materials are a strong candidate for NTP fuels due to their high melting temperature, resistance to hydrogen corrosion, and I_{sp} potential [24].

Chapter 2

Literature Review

2.1 History of NTP Fuel Testing

Within a decade of first discovering nuclear fission, nuclear power was being discussed as a potential propulsion source for rockets:

> "The possibility of using a fission 'pile' to heat a working fluid to high temperatures for use as rocket propellant was discussed briefly as early as 1944 at both the Los Alamos Scientific Laboratory and the University of Chicago Metallurgical Laboratory" [25].

During the cold war, both the United States and the Soviet Union developed and tested nuclear rocket technology. NTP rocket fuel was assessed by these programs and creative solutions were implemented to address the significant challenges presented by the operating environment experienced by the fuel. The scope of these programs as well as a summary of the results are discussed in the subsequent sections.

2.1.1 Rover & NERVA Programs

In 1955, the Rover program was created to assess the viability of using nuclear rockets to power intercontinental ballistic missiles (ICBMs) [26]. The magnitude of the project was summed up by the chairman of the United States Atomic Energy Commission, Dr. Glenn T. Seaborg:

> "What we must do is build a flyable reactor, little larger than an office desk, that will produce the 1,500 megawatt power level of Hoover Dam and achieve this power in a matter of minutes from a cold start. During every minute of its operation, high-speed pumps must force nearly three tons of hydrogen, which has been stored in liquid form at 420 °F below zero, past the reactor's white-hot fuel elements, which reach a temperature of 4,000 °F. And this entire system must be capable of operating for hours and of being turned off and restarted with great reliability" [27].

Based out of Nevada, the Rover project enlisted the resources of both Los Alamos Scientific Laboratory (currently Los Alamos National Laboratory) and Lawrence Radiation Laboratory (currently Lawrence Livermore National Laboratory) to work on development and testing of a nuclear rocket. The first phase of testing was designed to demonstrate a baseline performance of nuclear rocket operations; astutely, the initial ground testing rockets were named after a flightless bird, the kiwi. The Kiwi reactors had two stages of prototypes; the lower power initial stage, the Kiwi-A series, with a designed power level of 100 megawatts of thermal power (MWt), and a higher power stage, the Kiwi-B series, which was 1,000 MWt. While some weaknesses were identified in the design of the reactor and the fuel, testing of Kiwi-A (**Figure 2.1**) was considered an overall success, demonstrating that "a high power reactor could operate stably and controllably at high temperatures for a period of time" [26].

The Kiwi-B rocket design incorporated some of the lessons learned from the Kiwi-A tests as well as testing not only the reactor performance, but also incorporating other auxiliary components and functionalities such as pumps, valves, test facilities, etc. to provide a more holistic understanding of the system. Many reactor and fuel design flaws were exposed throughout the testing process. Upon a successful reactor startup, the Kiwi-B4A test experienced a spectacular failure:

> "But paralleling the rapid increase in power was a rapid increase in the frequency of flashes of light from the nozzle; on reaching 500 MW, the flashes were so spectacular and so frequent that the test was terminated and shut down procedures began. Quick disassembly confirmed that the flashes of light were

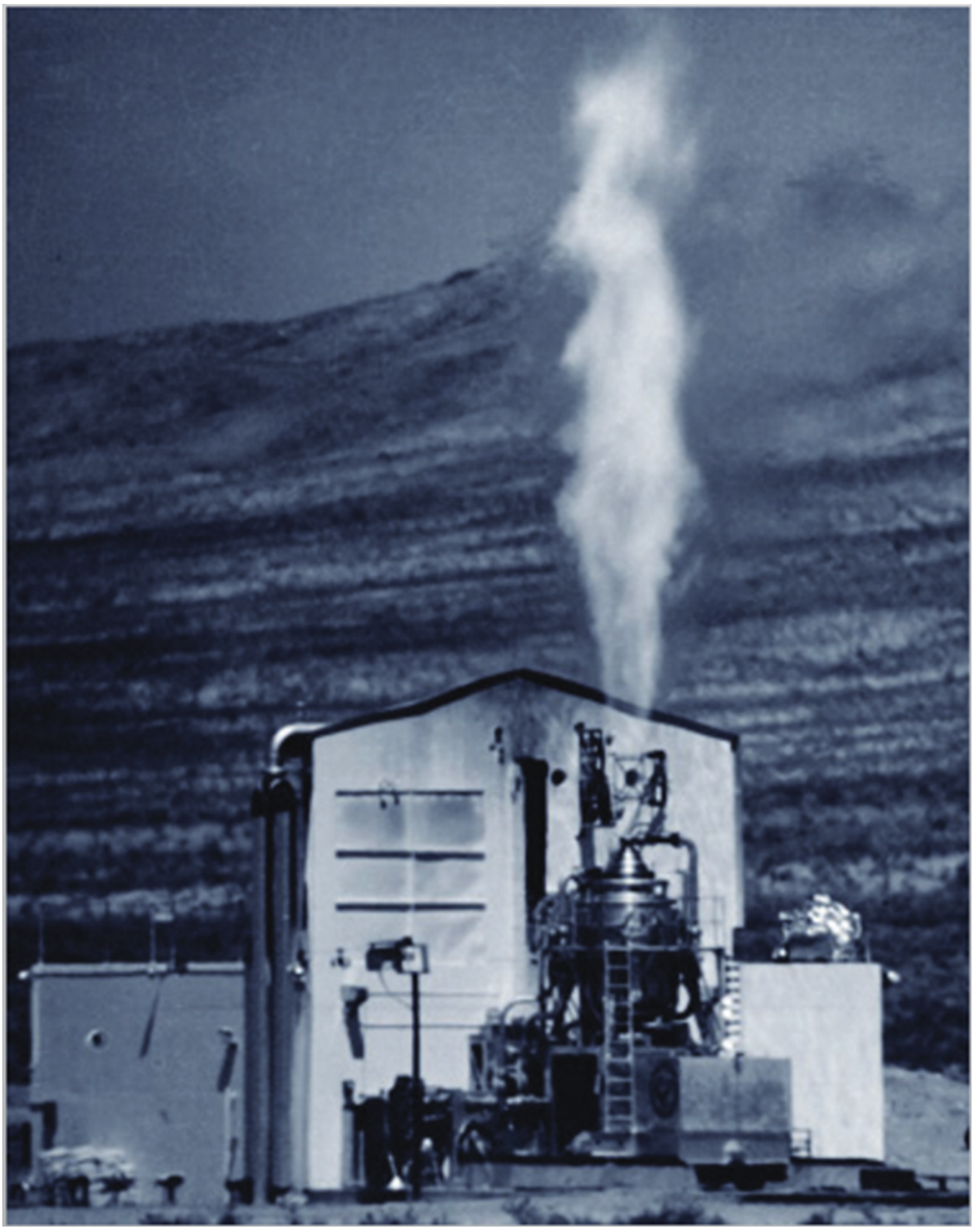


Figure 2.1: Proof of principle being demonstrated with the 100 MW Kiwi-A [28].

reactor parts being ejected from the nozzle; further disassembly and analysis revealed that over 90% of the reactor parts had been broken, mostly at the core's hot end" [26].

Incorporating design improvements from the earlier Kiwi-B rockets, the B4E rocket was the pinnacle of success for the Kiwi prototypes with two remarkable tests being completed; the first was a run at 90% power for 8 minutes, which was only cut short by the storage capacity of the hydrogen storage facility, while the second test operated at full power for 2.5 minutes with minimal signs of fuel degradation [26]. Concluding on a high note that far exceeded initial expectations, these Kiwi experiments provided crucial knowledge and acted as the building blocks for the next chapter of nuclear rocket testing: Nuclear Engine for Rocket Vehicle Application (NERVA).

The NERVA project had two different approaches to exploring NTP; the first approach involved scaling up to larger sized nuclear rocket engines with an emphasis on research, and the second approach was a technology demonstration of nuclear rocket engine integrated system testing. **Figure 2.2** shows the evolution of the Kiwi rockets into more advanced rockets in both the research phase and the technology demonstration phase.

The Phoebus designs were based on the knowledge gained from the Kiwi tests and aimed to increase specific impulse, core power density, and core power level [29]. As shown in **Figure 2.3**, Phoebus 1 had a very similar design and specifications as the Kiwi-B series of reactors. The Phoebus 2, however, was significantly larger than its predecessors; to this day it is the most powerful NTP reactor that has been built [29]. The completion of testing of the Phoebus 2 proved the feasibility of a high powered, high thrust NTP rocket.

The Peewee reactor was smaller than the Phoebus rockets and was designed primarily to test fuel elements. From the completed Peewee tests, zirconium carbide (ZrC) coated elements were shown to perform much better than niobium carbide (NbC) coated elements and the NbC-ZrC coated elements. The Nuclear Furnace (NF-1), an upgrade to the Peewee system, was designed to test full scale fuel elements and other core components without releasing radioactivity into the environment. The majority of the fuel tested was (UC-ZrC)C-carbon composite fuel, but a small cluster of (U, Zr)C fuel elements were also tested [29]. The results of the test suggested that the carbide fuel elements could withstand hours

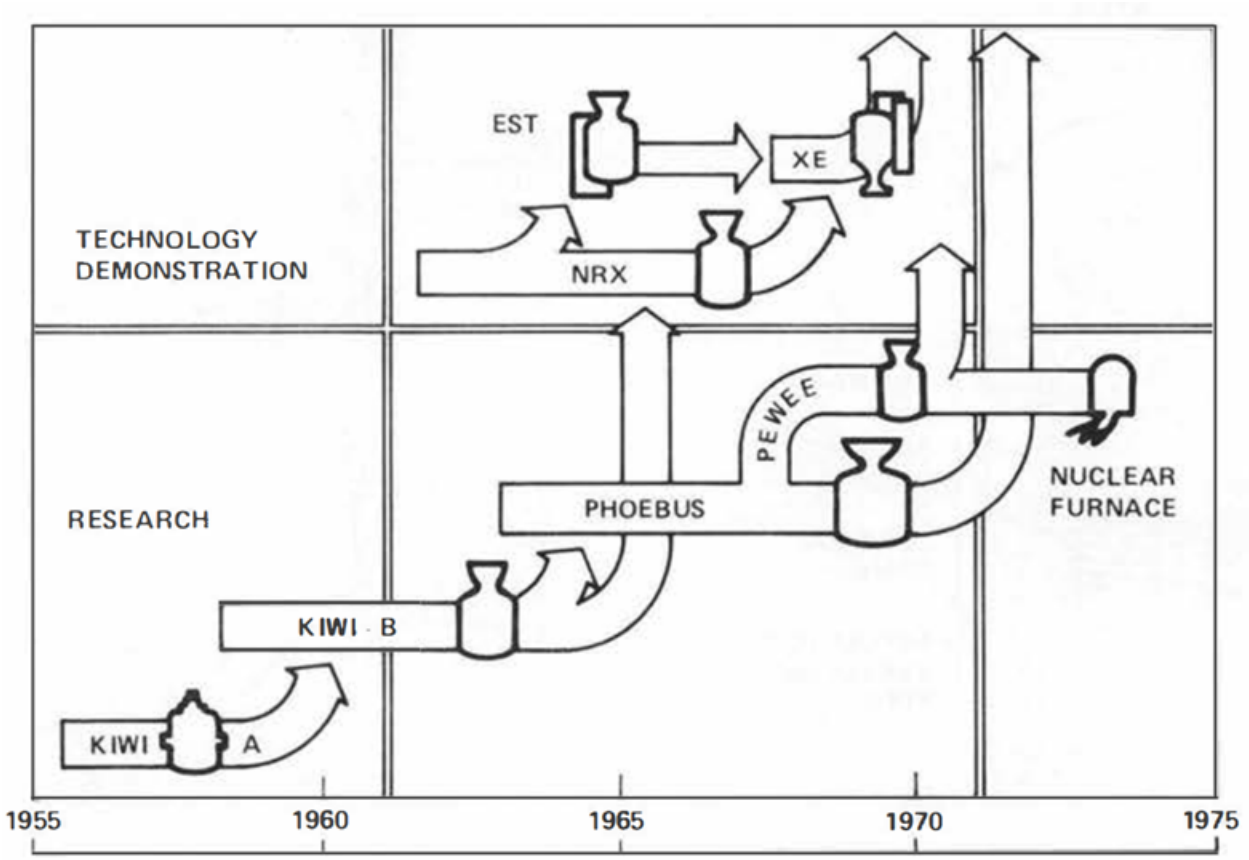


Figure 2.2: Summary of the testing program for the nuclear rocket reactors. The two top arrows point to that would have been the development of a flight engine had the program proceeded through a logical continuation [30].

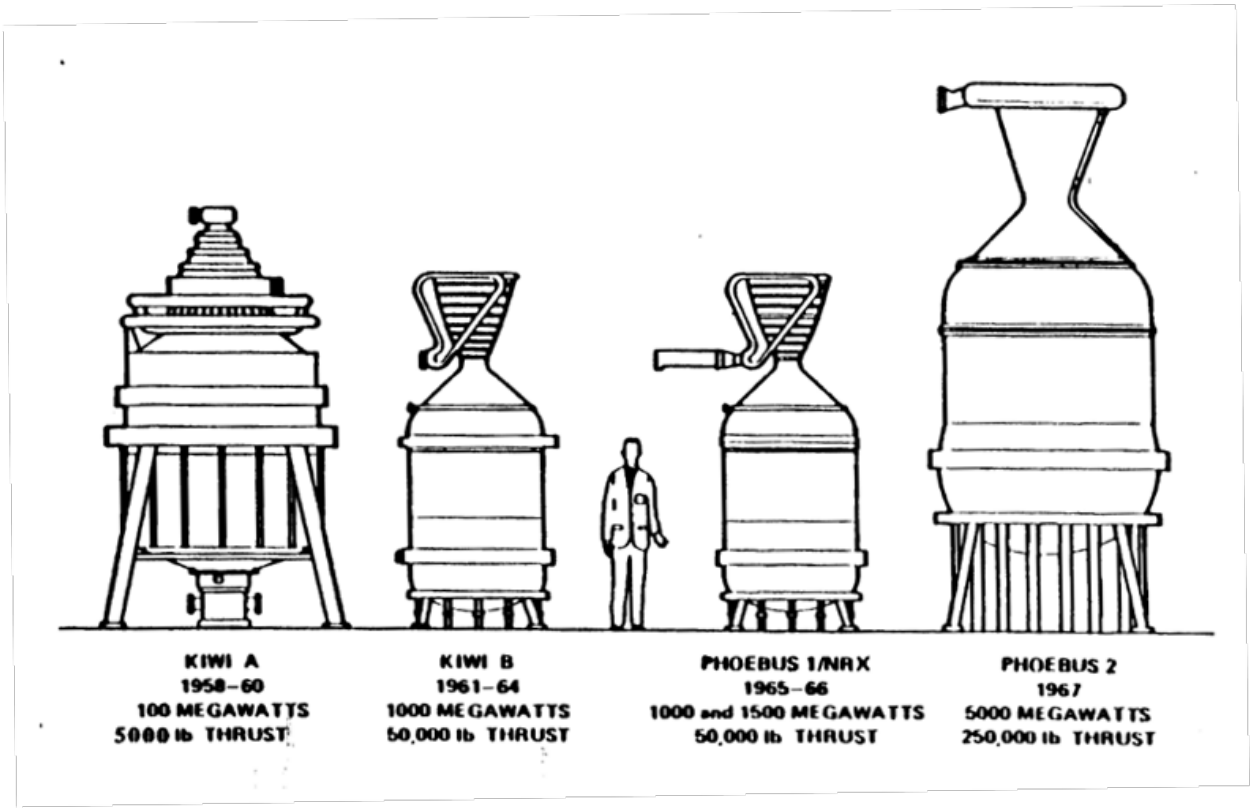


Figure 2.3: Relative size of Los Alamos reactors [29].

of operation at NTP temperatures. Despite four successful runs, the NF-1 was shut down in 1972 at the end of the NERVA project.

In parallel with the research reactors (**Figure 2.4**), the Nuclear Rocket Experimental (NRX) and XE Prime, the first downward firing NTP prototype, reactors were developed for nuclear rocket engine testing [29]. The NRX tests were designed to test the nuclear rocket engine and its supporting systems such as actuators for reactor control and startup, shielding for protection against radiation emitting from the reactor during operations, devices for control and steering of the nuclear engine, and hydrogen nozzles for thrust. The NRX reactors demonstrated that the nuclear rockets could handle repetitive startup and shutdown cycles at intermediate and full power levels and extended steady state operations at NTP temperatures and hydrogen flow rates.

After the NRX testing was completed, the XE Prime design was implemented and accounted for many of the findings and lessons learned from the NRX tests. The goal of the XE Prime tests was to prove that the engine design was technologically ready for spaceflight [31]. During testing, the downward firing rocket completed 24 startups, 15 of which were from unique control configurations or initial conditions. Examination of the fuel elements after operation showed reasonable mass loss and elevated corrosion towards the hot end of the propellant channels [29]. However, the primary goal of the XE Prime tests was not to develop the fuel assembly materials, and therefore used a previous generation fuel type. Marking an end to a generally successful testing campaign, the results of the XE Prime tests proved that a flight-capable NTP engine could be made with at least double the I_{sp} of a chemical rocket.

The evolution of the fuel materials for the Rover/NERVA project is shown in **Figure 2.5**. Initially, UC_2 particles were embedded in a graphite matrix, which was then coated with a thin NbC layer, to provide protection from the erosive flowing hot hydrogen. Fission gas buildup in the matrix led to significant structural failure of this fuel, causing fuel fragments to be ejected from the core during testing. To combat the fission gas buildup in the surrounding graphite, spherical UC_2 or UO_2 particles were coated in a pyrolytic graphite layer and embedded in a graphite matrix, which was then coated with a thin layer of either NbC or ZrC. The coated fuel particles contained the fission gas and prevented cracking of the

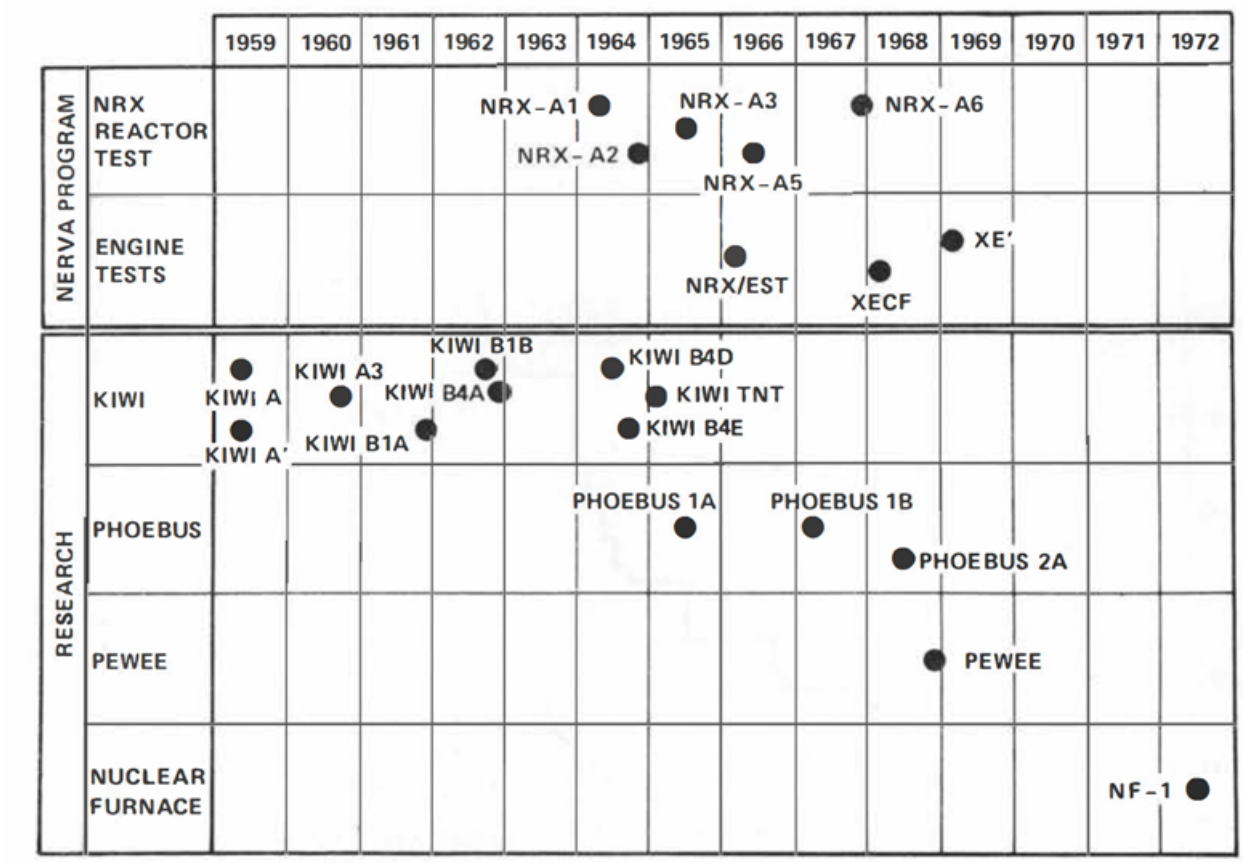


Figure 2.4: Chronology of major nuclear rocket reactor tests [30].

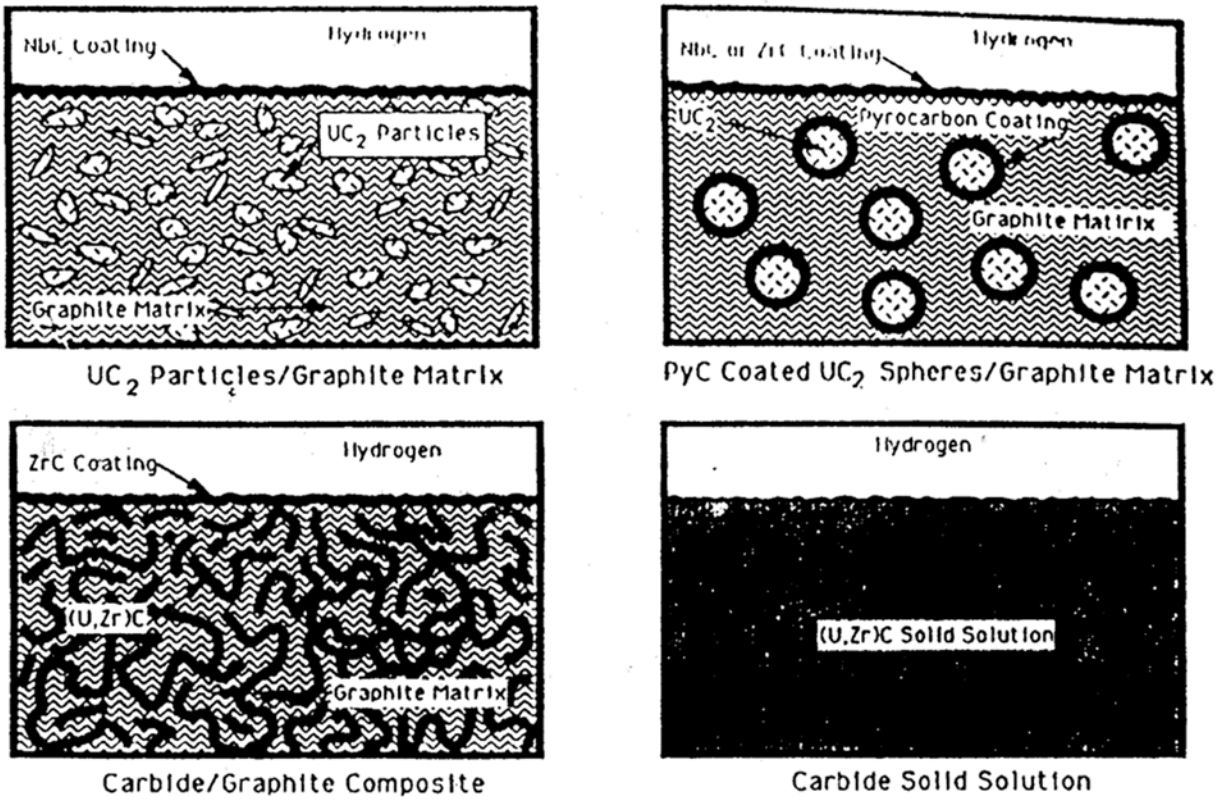


Figure 2.5: Rover/NERVA fuel types [22].

matrix material; however, the difference in thermal expansion of the NbC and graphite led to corrosion cracking of the fuel. An alternative fuel material was developed; (U, Zr)C dispersed in a graphite matrix, which was then coated with ZrC, to reduce the corrosion cracking of the fuel. The performance of this graphite composite fuel was limited by the extreme corrosion in a hot hydrogen environment and by the temperature constraints of the graphite matrix. These performance restrictions were reduced by developing a solid solution (U, Zr)C material, which could withstand much higher temperatures [22].

One of the main takeaways applicable to fuel materials from the Rover/NERVA project is the corrosion behavior of the carbide fuel when subjected to NTP temperatures and hydrogen flow rates. The corrosion was highest in the center region of the propellant channel. At the start of the channel, the temperature was low enough to limit thermal stresses which reduced cracking. At the end of the fuel elements, the temperature was the highest, but the power density was low, which also resulted in lower thermal stresses and reduced cracking. However, in the middle of the channel, temperatures were high and the power density was its highest and the mismatch in the coefficients of thermal expansion between the fuel, matrix, and coating led to significant cracking of the carbide coating, leading to elevated corrosion of the fuel [29].

Overall, the NEVRA tests culminated in 1020 minutes of operating time exceeding 1 MW and 376 minutes of operating time at high power, shown in **Figure 2.6** [30], at a total cost of $1.4 billion (1972 equivalent in dollars) [22]. Many tests were conducted at elevated temperatures pushing the material limits of the fuel materials (**Figure 2.7**), providing invaluable experimental data on the behavior of these components. An extensive amount of materials data is available from the testing completed during the Rover/NERVA project and is still relevant in NTP applications today.

2.1.2 Soviet Twisted Ribbon

Beginning in the late 1960s, for nearly 20 years, the Soviet Union developed NTP rockets. The materials used for their fuel primarily consisted of uranium carbide mixed with carbides of zirconium, niobium, and tantalum [22]. The fuel elements were constructed in a twisted ribbon shape, shown in **Figure 2.8**; however, little data is available regarding the fabrication

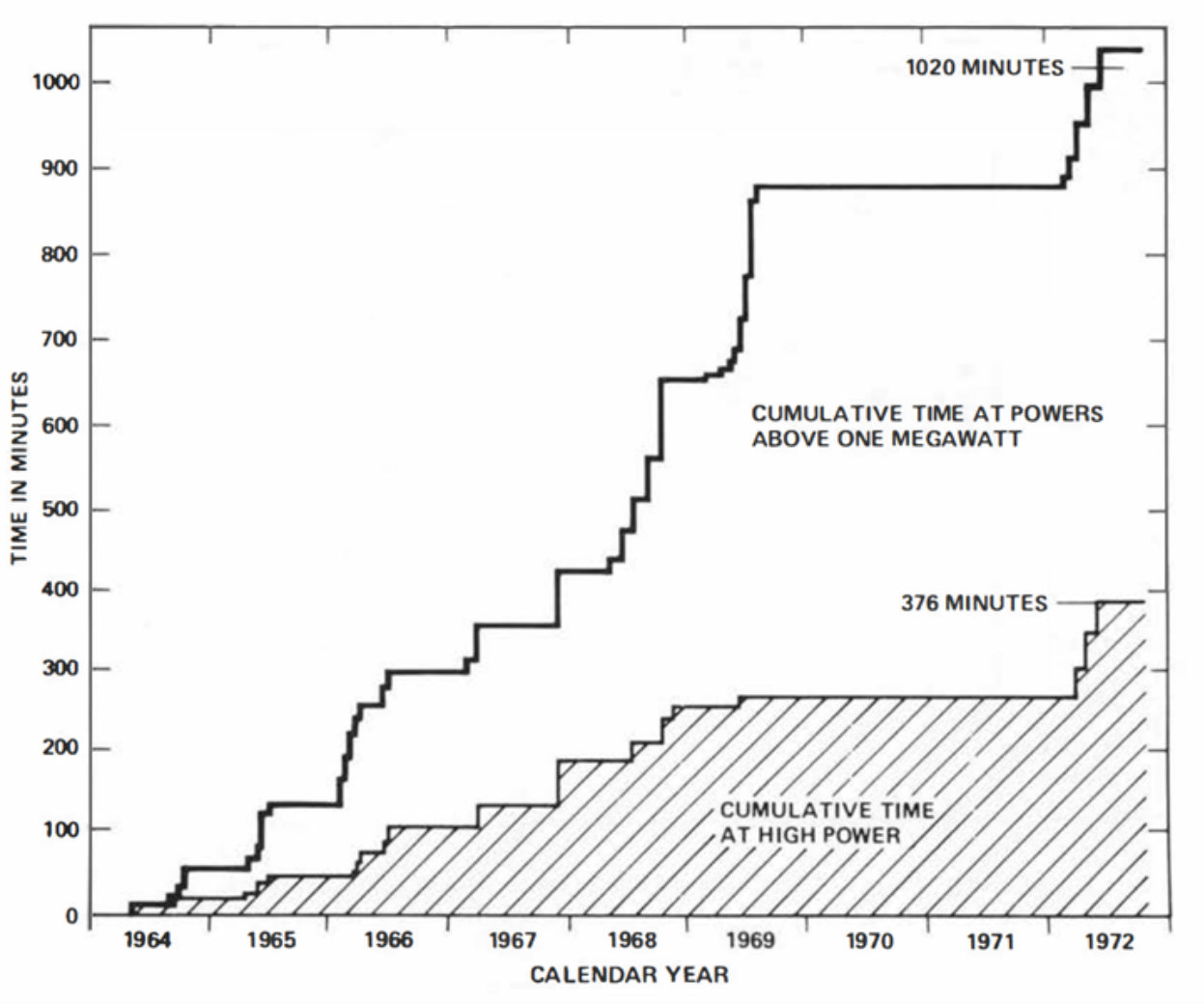


Figure 2.6: Cumulative testing time for all Rover reactor and engine system tests [30].

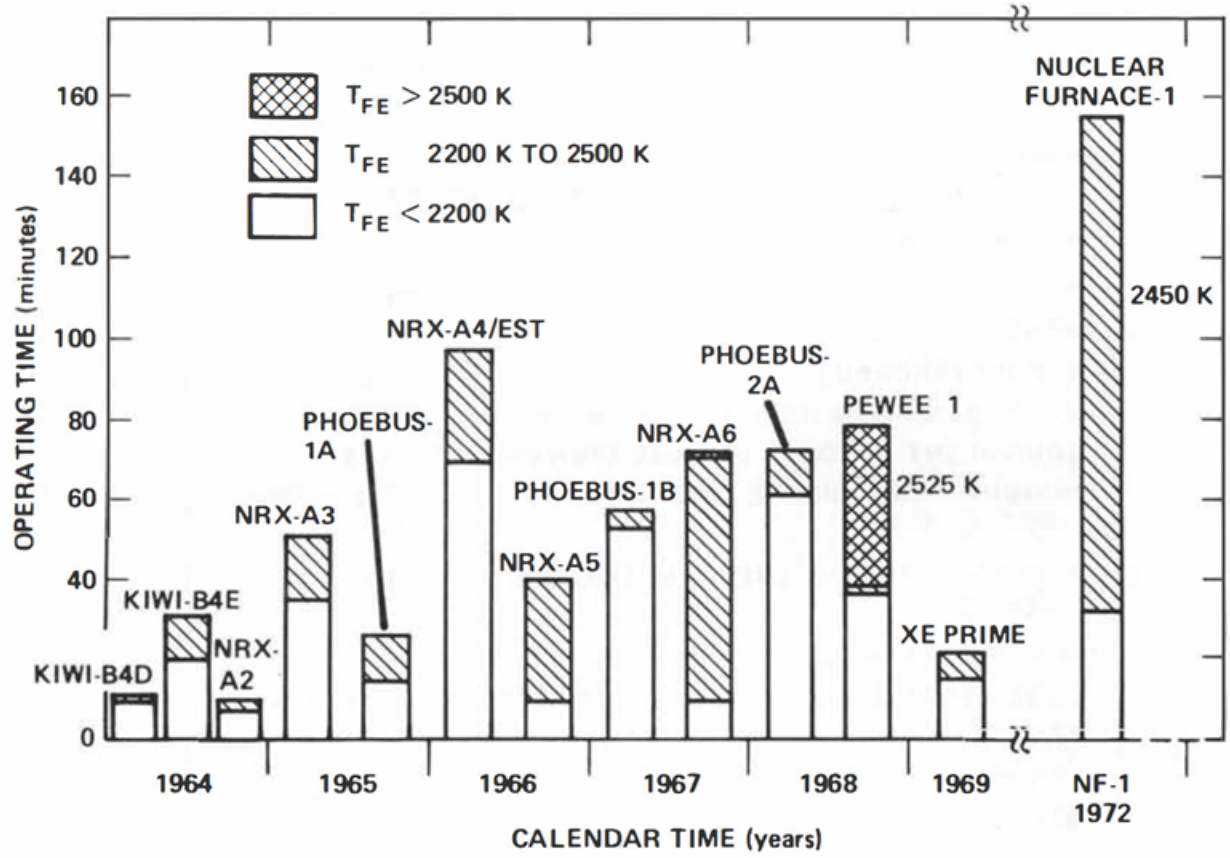


Figure 2.7: Operating time versus coolant exit temperature for the full-power reactor tests conducted after development of a successful design (Kiwi-B4D) [30].

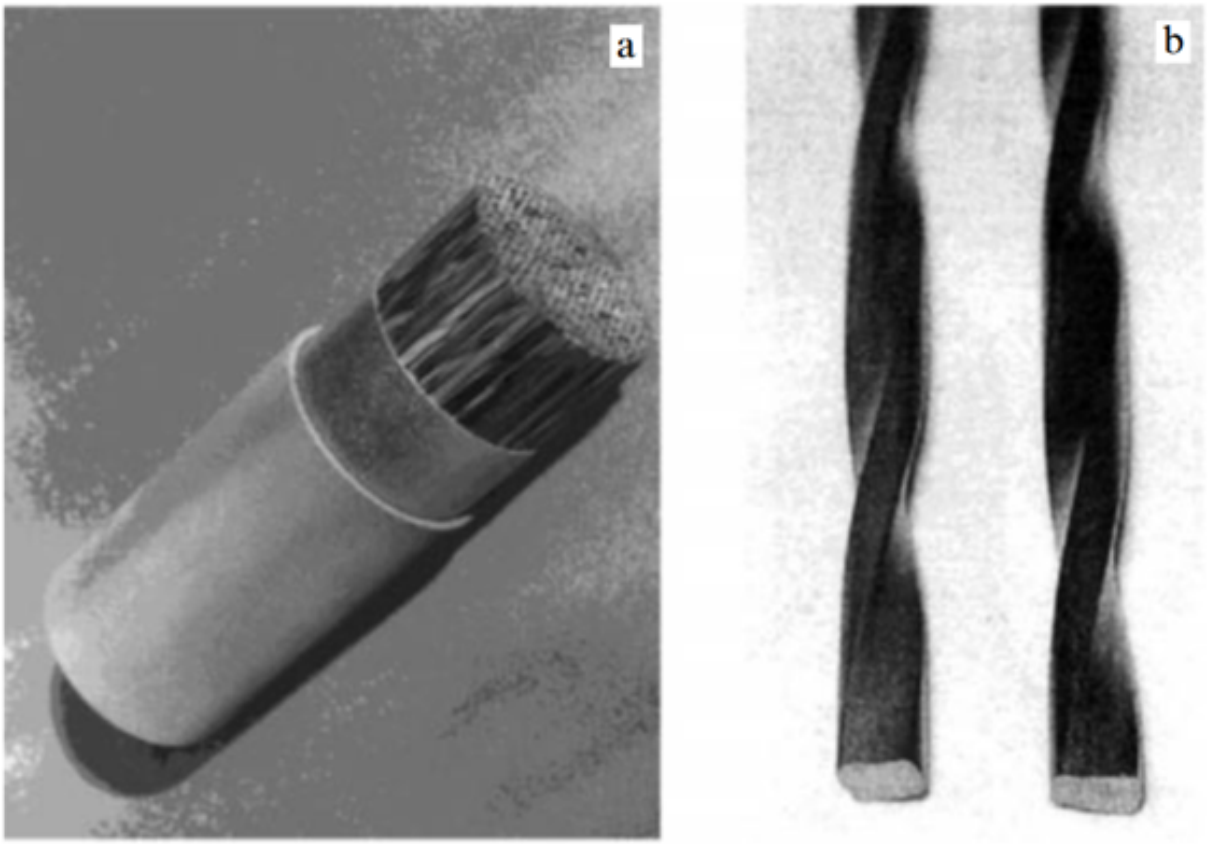


Figure 2.8: Photographs of a heating unit (a) and twisted-rod two-blade HREs 2.2 mm in diameter (b) [33].

process of the fuel. With the twisted ribbon geometry, the fuel elements were about 2.6 times higher in surface-to-volume ratio than the elements constructed during the NERVA testing [32], leading to elevated heat transfer properties between the fuel assembly and the propellant. The twisted fuel elements were bundled together (**Figure 2.8**) and 6-8 of the bundles were incorporated into each fuel assembly (**Figure 2.9**).

Over the course of the project, 1550 fuel assemblies were tested, including 7 full core tests and over 200 hours of hot hydrogen testing over 2800 K. During hydrogen testing, it was reported that a gas exit temperature of 3100 K was sustained for one hour and a gas exit temperature of 2000 K was demonstrated for 200 hours [22]. The results were very impressive when compared to the data obtained from the Rover/NERVA project; however, the lack of data, especially post irradiation, from the Soviet Union's NTP tests, leave many unanswered questions regarding the fabricability, functionality, and overall feasibility of the mixed carbide fuel. Overall, from the Soviet twisted ribbon data presented, mixed carbide fuels made from uranium, zirconium, niobium, and tantalum appear to be a promising candidate for NTP applications.

2.1.3 GE710 and ANL Programs

In the 1960s, two programs, GE710 by General Electric and ANL by Argonne National Lab were launched to develop NTP rockets. These programs both developed cermet fuel forms in an attempt to overcome the shortcomings of the graphite composite fuel used in the Rover/NERVA program. Composed of 60 wt% UO_2 and 40 wt% W, the cermet fuel was compatible with hot hydrogen and displays excellent strength and endurance in high temperature applications [34]. The cermet hexagonal shaped fuel elements of the GE710 engine (shown in **Figure 2.10**) were designed to be used in a fast neutron spectrum reactor. Extensive testing was performed on the cermet fuel materials, which demonstrated exceptional thermal and mechanical performance [35, 36, 37]. However, at high temperatures, UO_2 became unstable in the fuel matrix and there was a potential for the migration of free oxygen and uranium throughout the fuel, which would cause fission product release as well as compromise the structural reliability of the core [38].

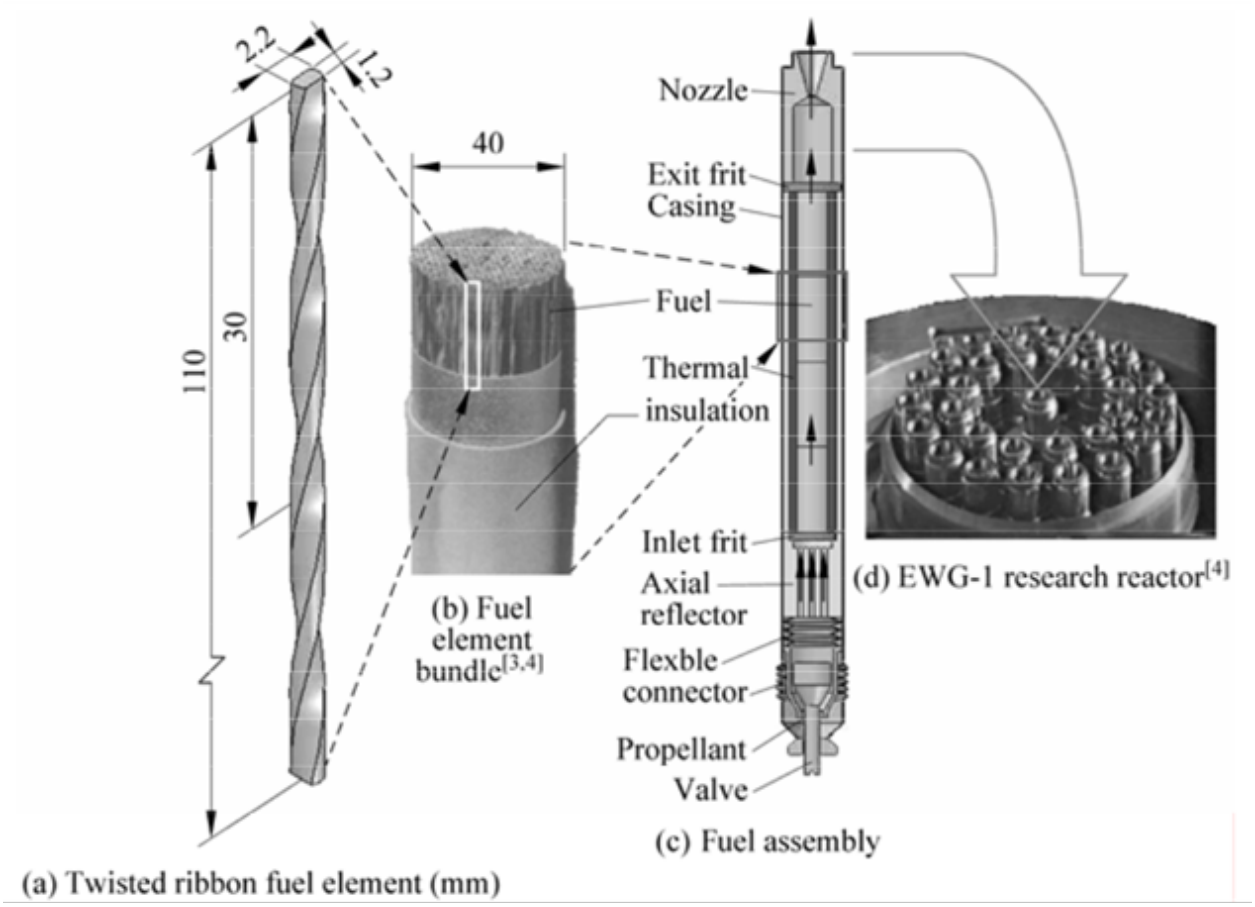


Figure 2.9: Soviet twisted fuel element and fuel assembly [32].

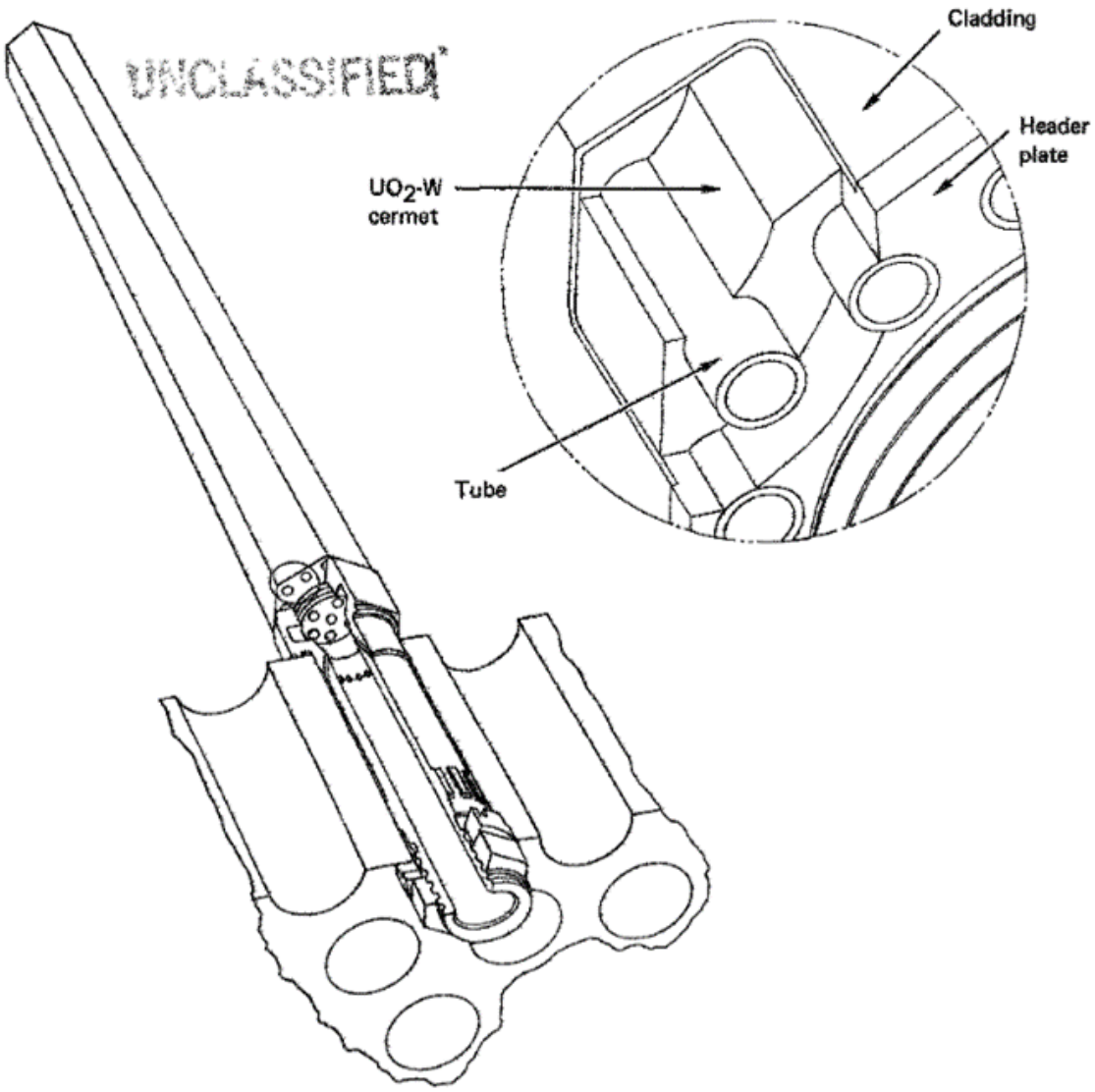


Figure 2.10: GE710 fuel element concept [40].

2.1.4 Space Nuclear Thermal Propulsion (SNTP) Project

The Space Nuclear Thermal Propulsion (SNTP) project was geared towards developing a particle bed reactor (PBR) capable of withstanding the high operating temperature environment of NTP. The project kicked off in 1987, funded by the Strategic Defense Initiative (more widely known as the "Star Wars" program), with a lofty goal of developing coated fuel particles, each around half of a millimeter in diameter, with a target hydrogen exhaust temperature of 3000 K [39]. A gelation process was used to produce the baseline UC_2 kernels which were then coated with two pyrocarbon layers, followed by a ZrC layer, using a chemical vapor deposition (CVD) process [22]. The baseline coated fuel particles, limited by a melting temperature of about 2500 K, were used to develop the manufacturing techniques involved in the fuel particle production before a more suitable fuel material was developed. The fuel particles were intended to be installed in between a cold frit and hot frit which was then embedded in a moderator block to construct a single prismatic fuel element, shown in **Figure 2.11**.

Several fuel materials were considered before a mixed-carbide fuel was selected (see **Table 2.1**) in part due to the limited data from the Rover/NERVA program, as well as the exceptional performance record from the Soviet nuclear rocket tests, especially the projected endurance and stability when exposed to hot hydrogen. In 1994, before any significant testing was performed on the mixed-carbide fuel, the program was cancelled after losing its funding; over the length of the program, an excess of 200,000 fuel particles were fabricated and tested in hot hydrogen and irradiation environments from 1800 K to over 3000 K [41].

2.1.5 Square Lattice Honeycomb Design

The Square Lattice Honeycomb (SLHC) fuel design was discussed in the early 2000s by Anghaie et al. [42] and allowed for the construction of fuel assemblies from simple-geometry wafers. Furthermore, the simplistic fuel shapes reduced the complexity of machining required, a necessity for hard to fabricate materials such as mixed carbide fuel. Tri-carbides of (U, Zr, Nb)C and (U, Zr, Ta)C were selected as the fuel materials based on the results of the Rover/NERVA and USSR NTP programs. When fitted together, the fuel wafers formed

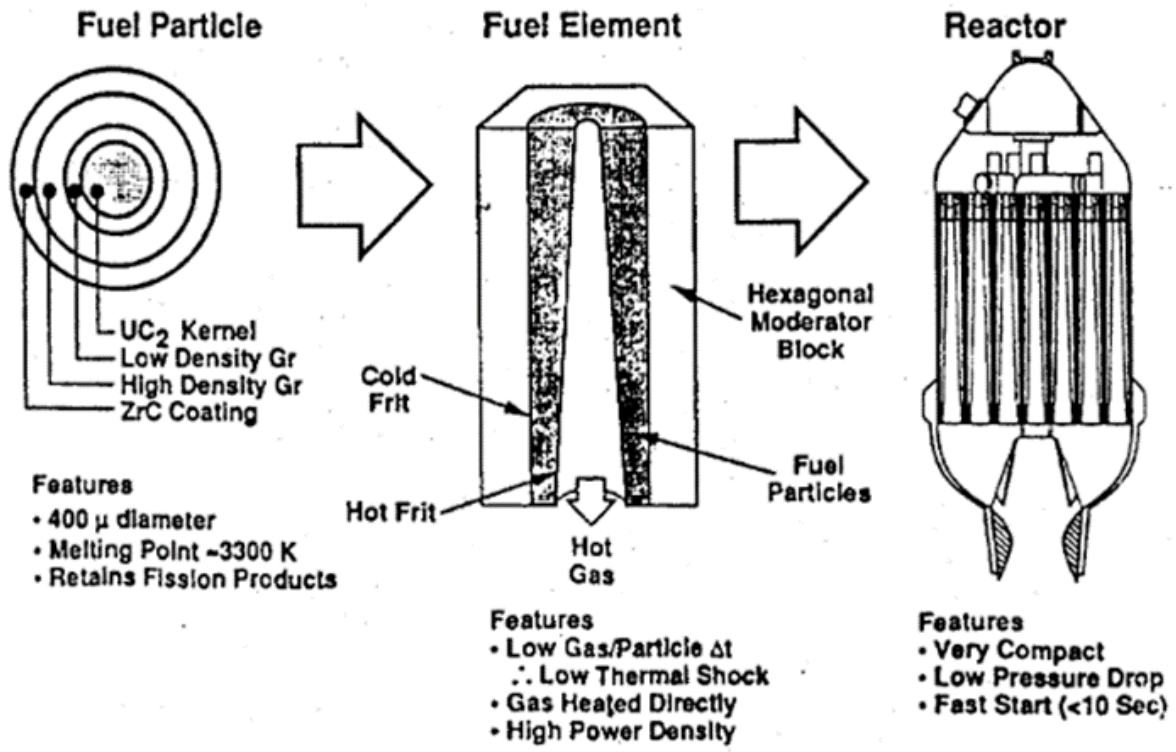


Figure 2.11: Evolution of the Particle Bed Reactor – fuel particle to the reactor core [22].

Table 2.1: SNTP fuels summary [22].

Particle Fuel Type	**Peak Temp. Potential**	**Comments**
Baseline	2400 - 2800 K	Adaptation of HTGR and NERVA/Rover technology.
UC_2 Kernel PyC Coating(s) ZrC Final Coating		
Advanced		
Infiltrated Kernel (IK) Porous graphite matrix Infiltration of coated UC_2	3500K	UC_2 expected to remain contained in molten state within matrix.
Mixed Carbide (U,Zr)C (U,Nb)C (U,Zr,Nb)C	3100 - 3400 K	Potential inferred from final phase of Rover/NERVA program and CIS experience.
Interstitial Dispersoid (ID) UC_2 fuel in graphite skeleton	3200 K	Synthetic percussion method was used to produce spherical graphite skeleton info which UC_2 is introduced using a solution chemistry process. The process is claimed to be optimizable to produce high performance fuel.

a disk with square propellant channels and the disks were stacked to form a fuel assembly (**Figure 2.12**).

An induction furnace, shown in **Figure 2.13**, was used to drive liquid-phase sintering on the tri-carbide fuel at temperatures up to 2800 K with an applied pressure of 3 MPa. Relative densities of over 93% were achieved using this sintering method and the tri-carbides were reported to form a single-phase solid solution, determined from X-ray diffraction (XRD) spectra (**Figure 2.14**). Hot hydrogen testing of the tri-carbide samples was performed at 2500 K, resulting in minimal mass losses after a duration of four hours (**Figure 2.15**), showing a significant improvement over the Rover/NERVA hot hydrogen results for carbide fuels [42]. Other than a brief evaluation across a few studies, this SLHC design was not further pursued.

2.1.6 Summary of NTP Fuel Testing Results

Experimental testing of NTP fuel candidates occurred primarily in the second half of the 20th century, with the majority of the testing occurring in the late 1960s and early 1970s. The most promising testing data for the leading fuel materials is presented in **Table 2.2**. The overall assessment of each fuel type is shown in **Table 2.3**. While the cermet materials that were tested are robust and have intrinsic safety to ensure subcriticality in the event of submersion in water [22], their operational performance is restricted by temperature limits. The composite fuel tested in the Rover/NERVA program underwent the most testing and development, including possessing the largest testing database of all potential fuel materials, and boasts the longest tested period (in the United States) in a hot hydrogen environment. However, the limited steady state irradiation exposure data and the extensive cracking that occurred during testing prove to be major hurdles for this fuel type. The mixed carbide fuels have the highest temperature potential of all the other fuel candidates and have promising experimental results, mainly from Soviet tests. However, the limited testing experience in the United States and the mechanical issues that arose from that testing, combined with the unverifiable results from the Soviet experiments, leaves mixed carbides with a lot of

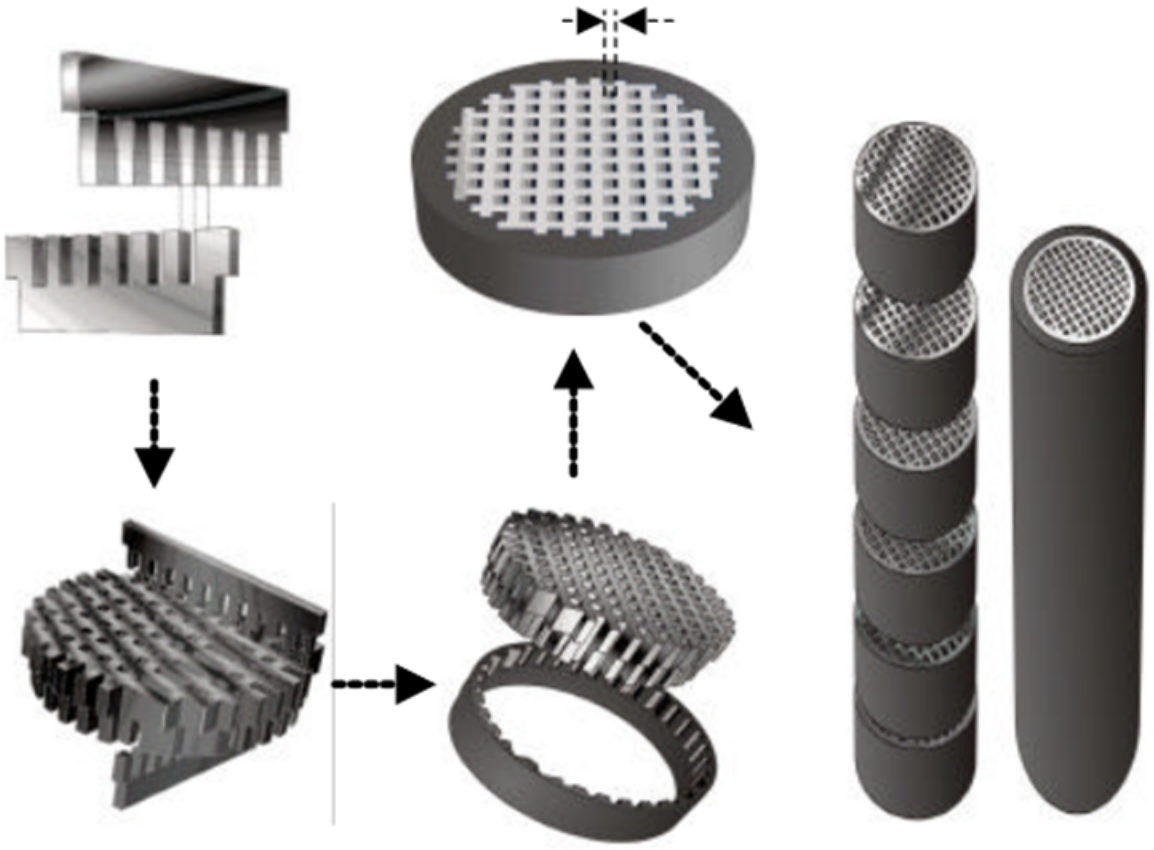


Figure 2.12: SLHC fuel sub-assembly [42].

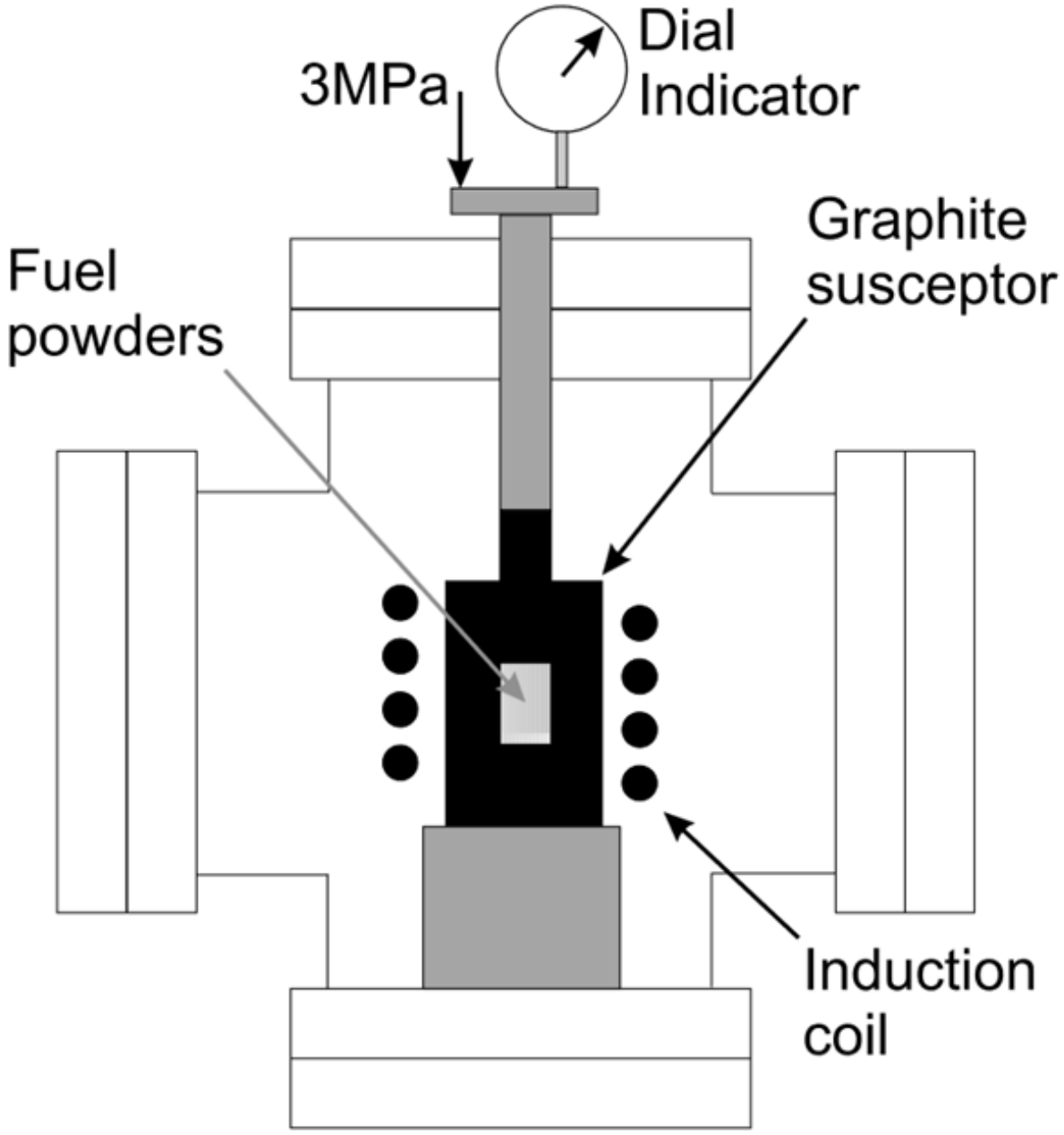


Figure 2.13: An illustration of the induction furnace chamber showing major components [43].

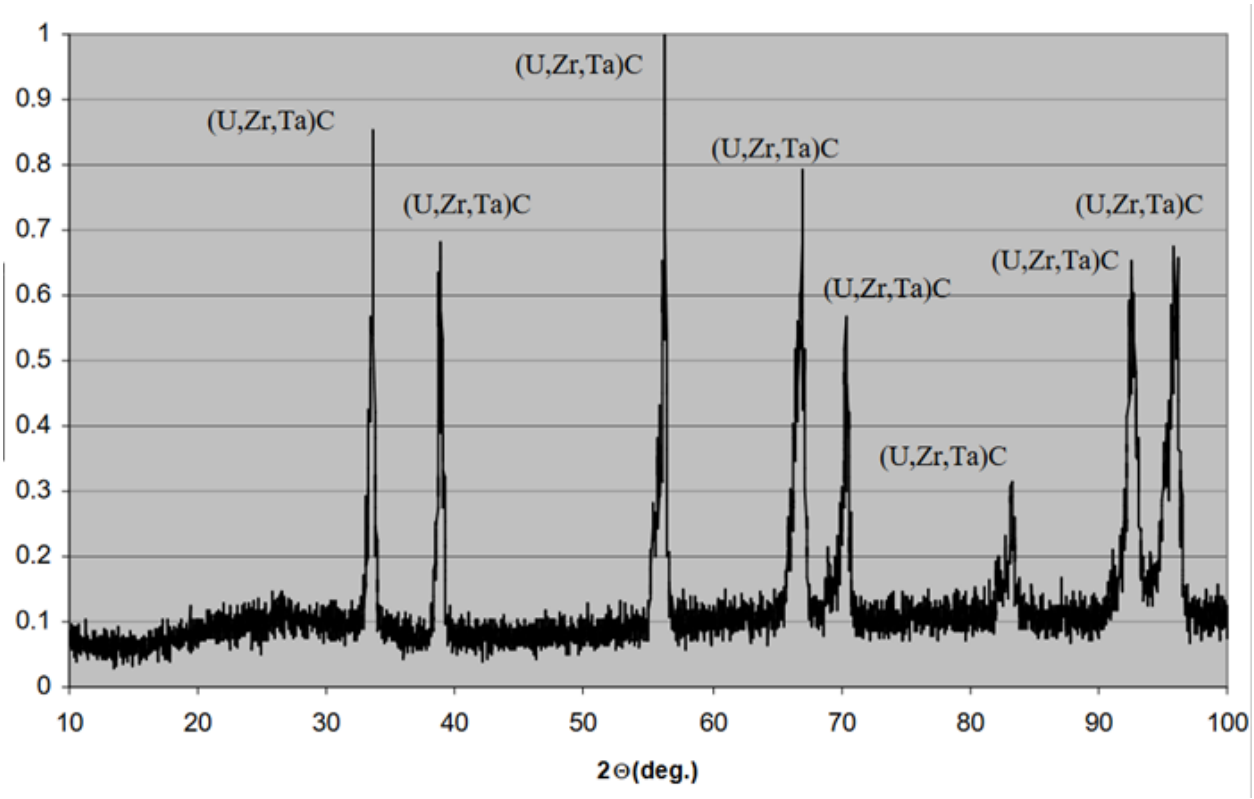


Figure 2.14: Representative x-ray diffraction profile for single phase solid solution (U, Zr, Ta)C [42].

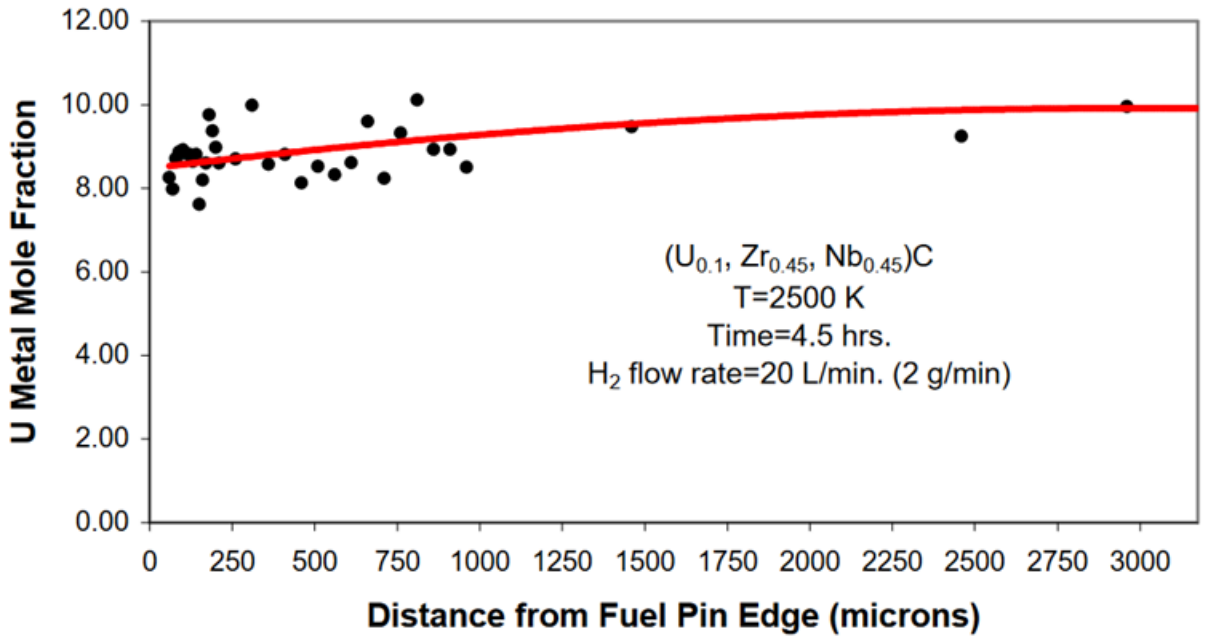


Figure 2.15: Performance of solid solution tri-carbide nuclear fuels exposed to hot hydrogen [42].

Table 2.2: NTP Fuel Temperature Parameters [22]

System	**Fuel Type**	**Coating /Clad**	**T(K)**	**Lifetime**	**# of Cycles**	**Year**
Rover/ Pewee 1	Pyrolitic C-UC_2 Particle Dispersion	ZrC	2600	40 min.	1	1968
Rover/ NF-1	(UC, ZrC)C Composite (U, Zr)C Solid Solution	ZrC	2450	109 min.	6	1972
Cermet	UO_2	W	2700	0.2 s	8	1967
Soviet	(U, Zr, Nb)C, C	?	3100	4000 s	?	1980s

Table 2.3: Summary of NTP Fuel Assessment [22]

Fuel Type	Positive Features	Negative Features
(U, Zr)C, C Composite Fuel		
Prismatic	• Most experience • Proven operating experience at 2550 K for 109 m in reactor	• Limited steady state irradiation experience • Thermal shock and cracking problems
Mixed Carbide Fuels	Highest temperature potential	
Prismatic	• In reactor experience	• Extensive cracking in tests • Limited experience • Fabrication process development needed
Particle Bed	• High T/W operation temperatures	• Limited experience • Fuel/FP loss anticipated • Mechanical issues
Twisted Ribbon	• Potential large database • Excellent high temperature performance reported	• Long effort at getting quantitative data not very successful • Uncertain mass losses
Cermet Fuels	• Robust fuel • Safety features	• Ultimate temperature potential is lower than mixed carbide

necessary research and development required before use as a fuel for NTP.

2.2 NTP Fuel Materials

The NTP fuel performance conditions were discussed by Matthews et al. [23], concluding that the most pivotal requirements, high operating temperature and functional longevity, had a negatively correlated relationship where, as the operating temperatures inside of the NTP fuel materials are increased, the expected lifetime of the core materials decreases. This relationship is illustrated in **Figure 2.16**, showing the different failure mechanisms that are prevalent at different time and temperature regimes. Burnup, or the depletion of the fissionable isotope from the fuel, is not usually a concern in NTP operations due to the short mission durations relative to the length of time required for burnup to cause a reduction in fuel performance. At moderate temperatures and times, swelling and fission gas release are the dominant fuel failure mechanisms, leading to fuel cracking or propellant channel restriction caused by bulk fuel expansion. At slightly higher temperatures, the diffusion and chemical compatibility between the fuel and the cladding or coating can cause chemical reactions or cladding failures that negatively affect the performance of the fuel. At temperatures just below the melting point, vaporization of the fuel materials leads to mass loss, which can have a detrimental effect on the functionality of the fuel including material properties and neutronics. The extreme upper bound and ultimate operating limit of fuel performance is the melting temperature of the core materials. When selecting fuel materials for NTP applications, a balance must be struck between melting temperature and expected operational lifetime.

2.2.1 Hot Hydrogen Compatibility

Figure 2.17 shows the interaction between the hot hydrogen and the carbide fuel channel. At temperatures under 1500 K (Region I), there is essentially no reaction between the hot, flowing hydrogen and the carbide fuel. However, when the temperature rises above 1500 K (Region II), the hydrogen strips away the carbon on the surface, creating hydrocarbons,

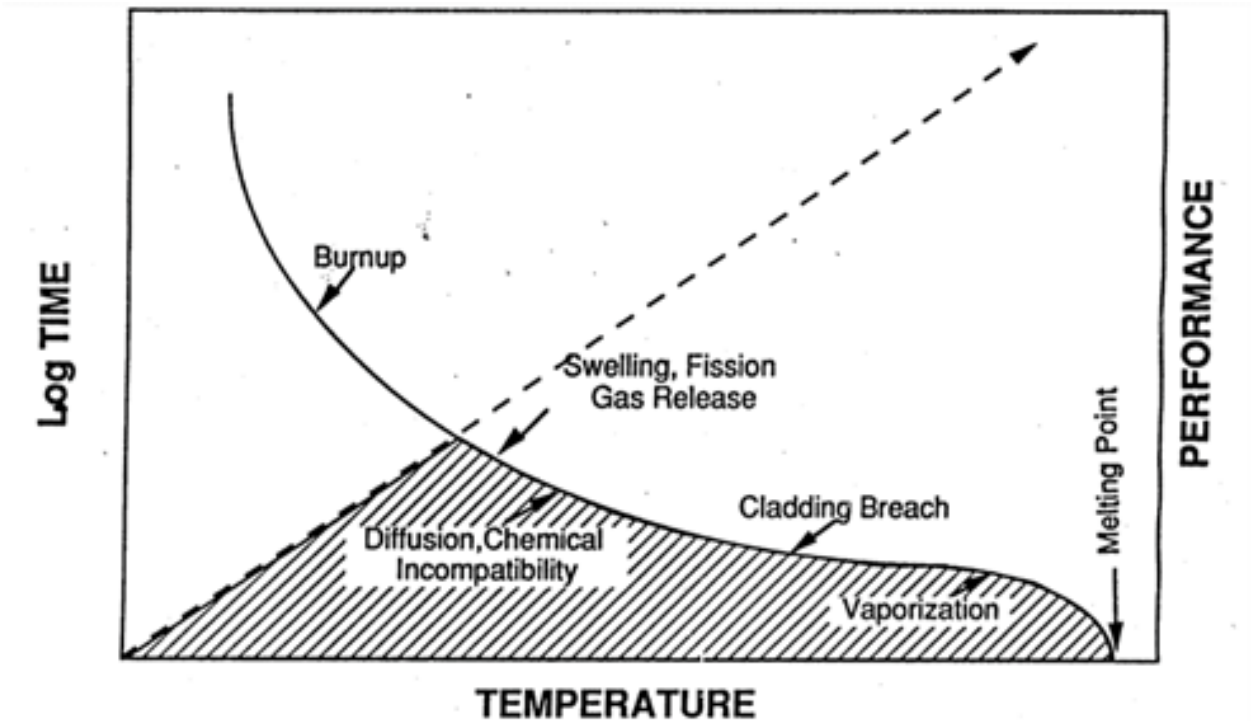


Figure 2.16: Conceptual Trade Off Between Performance and Efficiency [23].

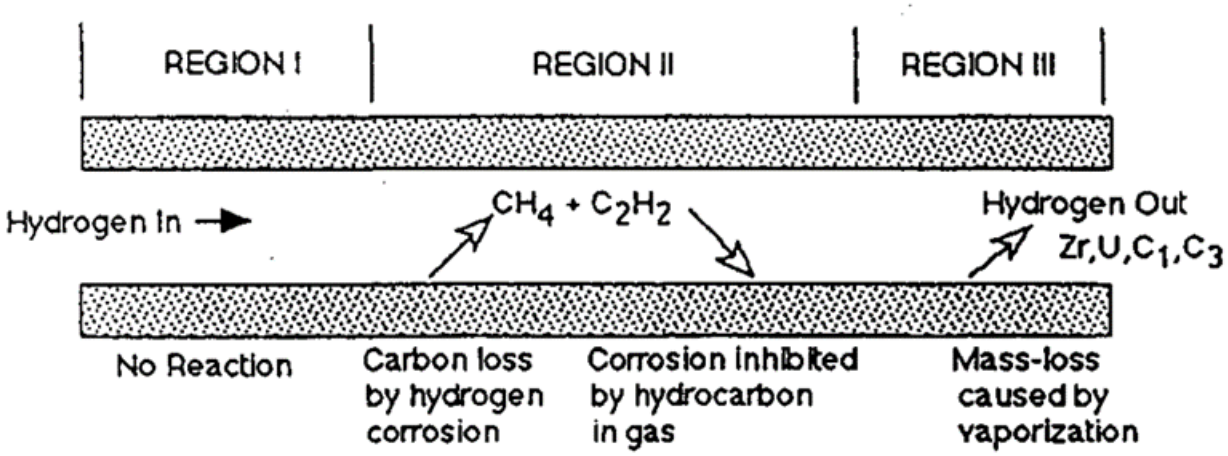


Figure 2.17: Hot hydrogen interaction process along a U-Zr-C material duct (not to scale) [18].

contributing to the mass loss of the fuel. At temperatures above 2900 K (Region III), the hydrogen begins stripping away all the components of the carbide fuel, leading to increased mass loss rates. The partial pressures of the products drive the hydrogen mass loss mechanism in the fuel element channels, shown in **Figure 2.18**. The presence of cracks on the fuel element channel surface also leads to an elevated mass loss rate, seen in **Figure 2.19**, due to the increased surface area. Resistance to the corrosive, hot hydrogen environment is an essential characteristic for NTP fuel materials. Stripping carbon, uranium, or other elements from the fuel can lead to undesirable consequences such as compromised mechanical properties, a lower to threshold to the melting point of the fuel, and a reduction in neutronics, potentially leading to irregular reactor performance. Due to the highly corrosive nature of a hot hydrogen environment, materials selected for NTP fuels need to be able to minimize the mass lost from the corrosive hydrogen environment. Unlike graphite composite fuel forms, tri-carbide fuels have demonstrated moderate stability in hot hydrogen [33]; however, extensive experimentation and modelling of mixed carbide fuel stability in a hot hydrogen environment is warranted.

2.2.2 High Melting Temperature Materials

The feasibility of various high melting temperature materials as candidates for NTP fuel (**Figure 2.20**) was discussed by Palomares et al. The review of these materials found that the melting temperature for silicides, sulphides, and phosphides are too low to be practicable for NTP fuel applications. Additionally, the neutron economy of borides and rhenium-containing intermetallides is undesirable for use with low enriched uranium (LEU) fuels, which eliminates these materials from the list of qualified fuel materials. Oxides are also not a promising option, as they are instable at high temperatures and expected to have a high rate of vaporization when exposed to the hot, flowing hydrogen found in the propellant channels of an NTP fuel element. Of the remaining high temperature compounds, carbides are the most desirable, due to their extremely high melting temperatures, predicted stability in hydrogen, and low thermal neutron absorption cross section (with the exception of hafnium carbide).

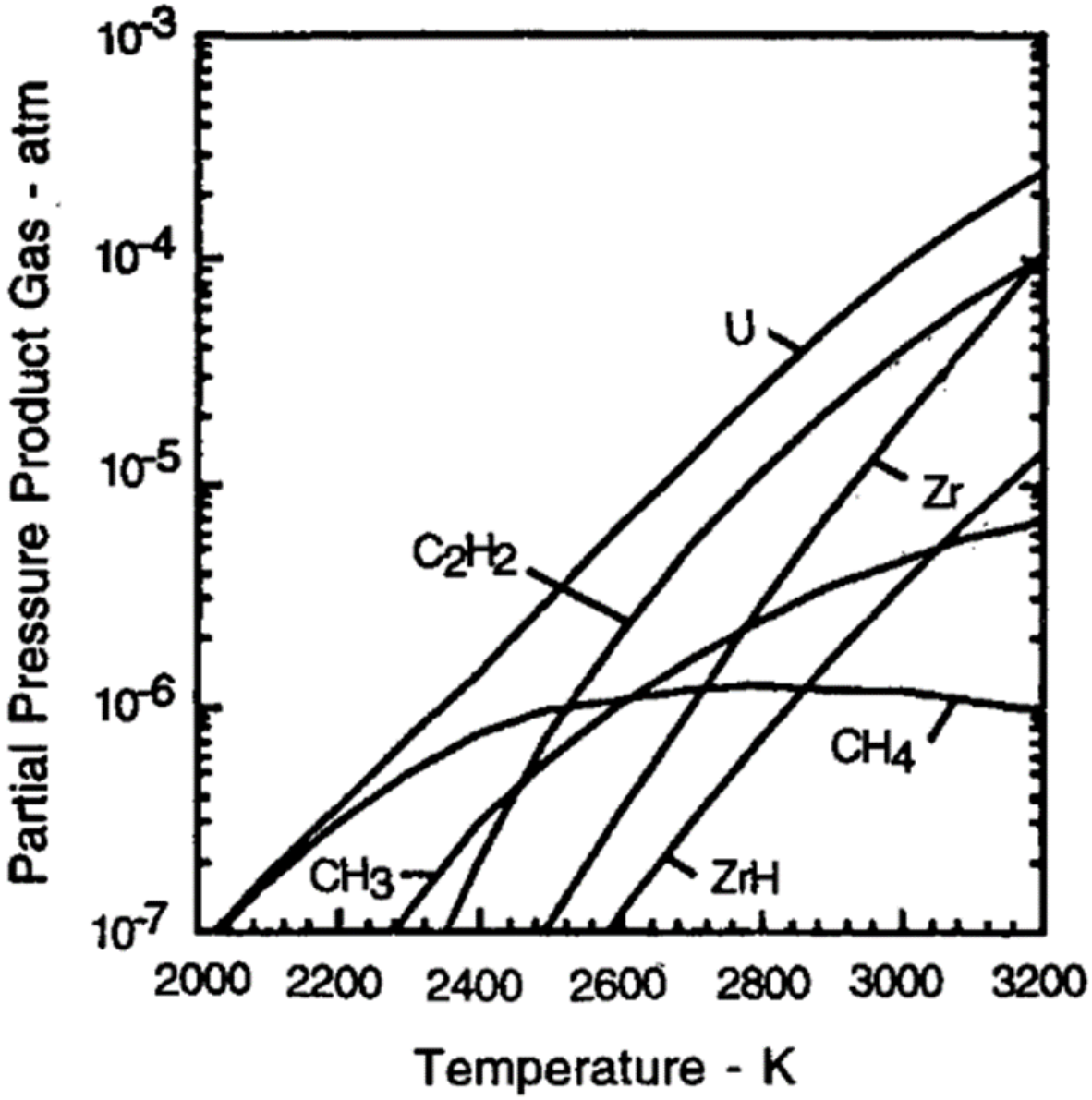


Figure 2.18: Equilibrium partial pressures of product constitutes above $U_{0.05}Zr_{0.95}C_{1.07}$ in 1 atm of hydrogen as a function of temperature [18].

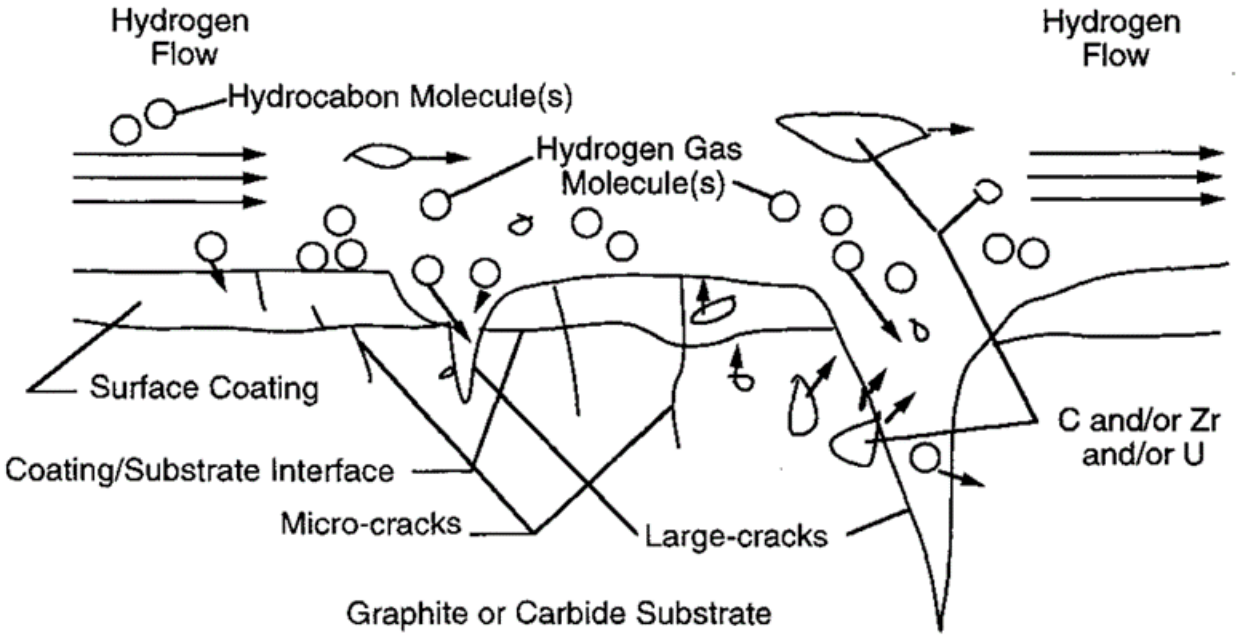
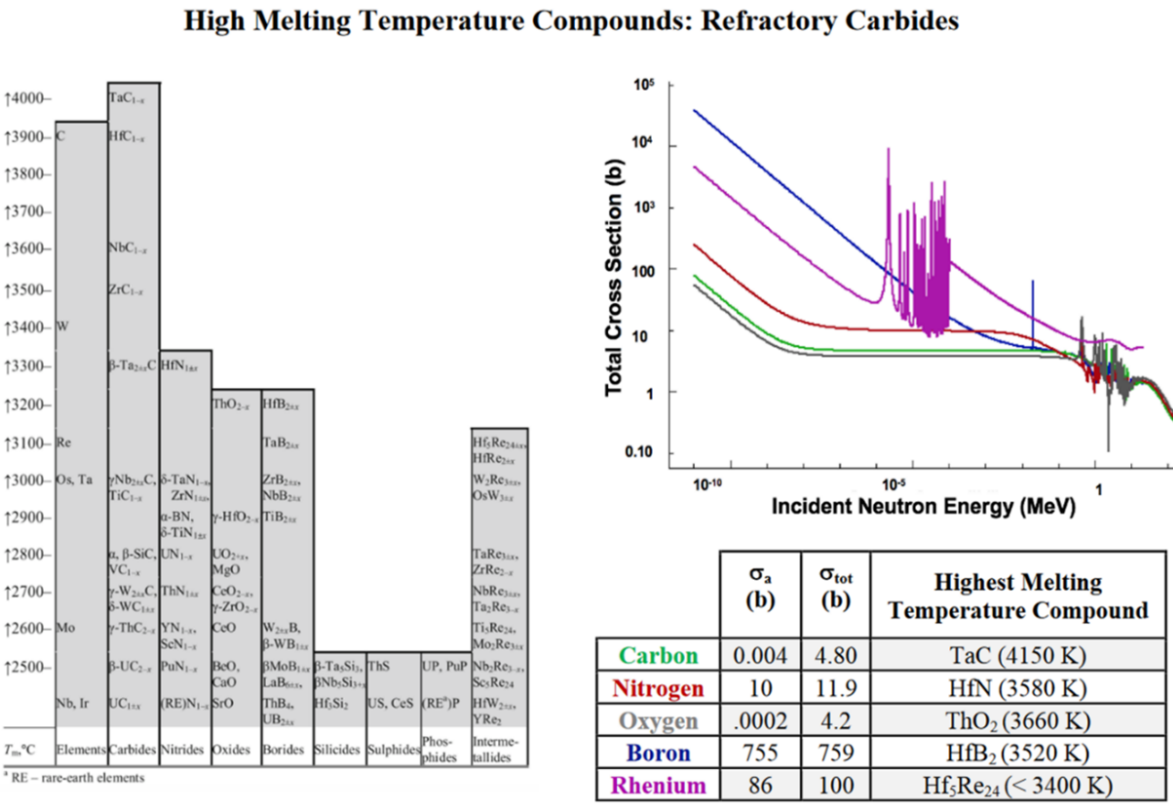


Figure 2.19: Effects of surface cracks on corrosion (not to scale) [18].



	σ_a (b)	σ_{tot} (b)	Highest Melting Temperature Compound
Carbon	0.004	4.80	TaC (4150 K)
Nitrogen	10	11.9	HfN (3580 K)
Oxygen	.0002	4.2	ThO_2 (3660 K)
Boron	755	759	HfB_2 (3520 K)
Rhenium	86	100	Hf_5Re_{24} (< 3400 K)

Figure 2.20: Comparison of different ultra-high temperature compounds [34].

2.2.3 Phase Stability of Solid Solution Refractory Carbide Fuels

A key characteristic for refractory carbide fuel materials is their ability to form a solid solution, in other words, maintaining a constant single phase crystal structure when combined. Mono-carbides NbC, ZrC, TaC, and UC all have a face centered cubic (FCC) crystal structure in the Fm-3m space group and, under the right conditions, potentially combine into an FCC structured solid solution. The compounds formed by mixing these carbides are defined as interstitial solid solutions, where the carbon atoms enter the interstitial voids in between the atoms in the crystal lattice of the transition metals [44]. These transition metal carbide solid solutions have many advantages including a higher melting temperature than their individual constituent metals [11]. Studies have been performed on various combinations of binary and ternary carbides containing NbC, ZrC, TaC, and/or UC to determine the conditions leading to continuous solid solution behavior of these compounds.

The phase equilibria in the Zr-Nb-C system were explored by Gusev and Rempel [45]. A subregular solutions model was used to calculate the Zr-Nb-C phase diagram, shown in **Figure 2.21**. There is a region in the simulated phase diagram at $Zr_{1-x}Nb_xC_y$ near stoichiometric carbon levels ($y \approx 1$) where an FCC structured solid solution is expected to form. **Figure 2.22** shows the Zr-Nb-C liquidus surface and **Figure 2.23** shows the exsolution surface of the $Zr_{1-x}Nb_xC_y$ and the region where the solid solution $Zr_{1-x}Nb_xC_y$ exists. Between the liquidus surface and the exsolution surface, from above about 1200 K to the melting temperature, a continuous region of single phase solid solution $Zr_{1-x}Nb_xC_y$ was shown to exist.

Although the solid solutions of binary mixtures of some refractory carbides with UC were reported to have extensive regions of continuous solubility, limited data exists on the ternary systems of similar constituents. The NbC-ZrC-UC ternary system was investigated by Tosdale and a solidus surface of the system was calculated and graphed [46]. The isothermal projections of the representative melting temperatures of various compositions or NbC-ZrC-UC are shown in **Figure 2.24**. In general, the melting temperature of this ternary system exceeds that of the individual mono-carbide components. This study shows

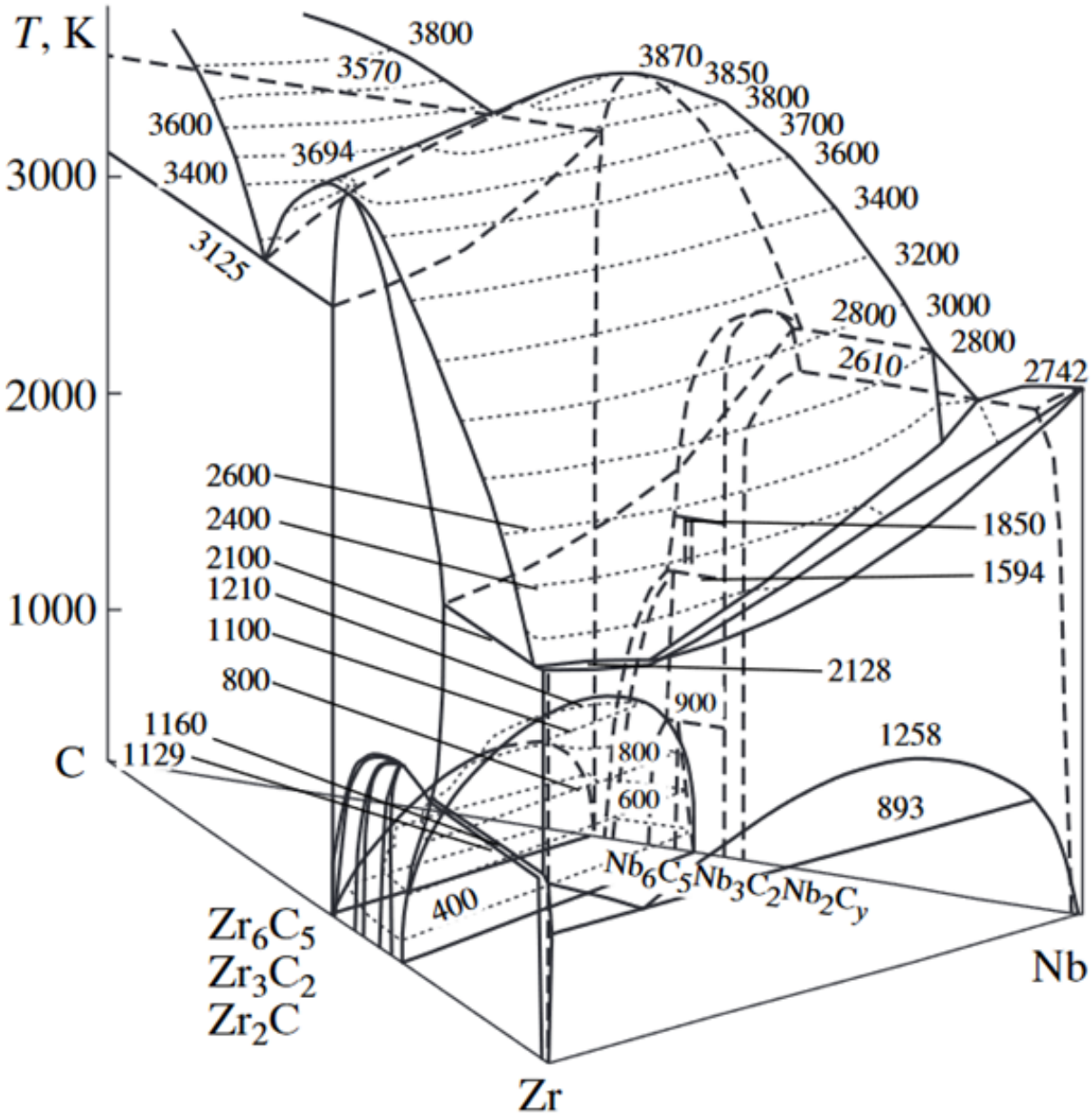


Figure 2.21: Spatial phase diagram for the Zr-Nb-C system for temperatures from 300 to 3900 K and isothermal sections of the liquidus surface and the surface of the subsolidus exsolution region [45].

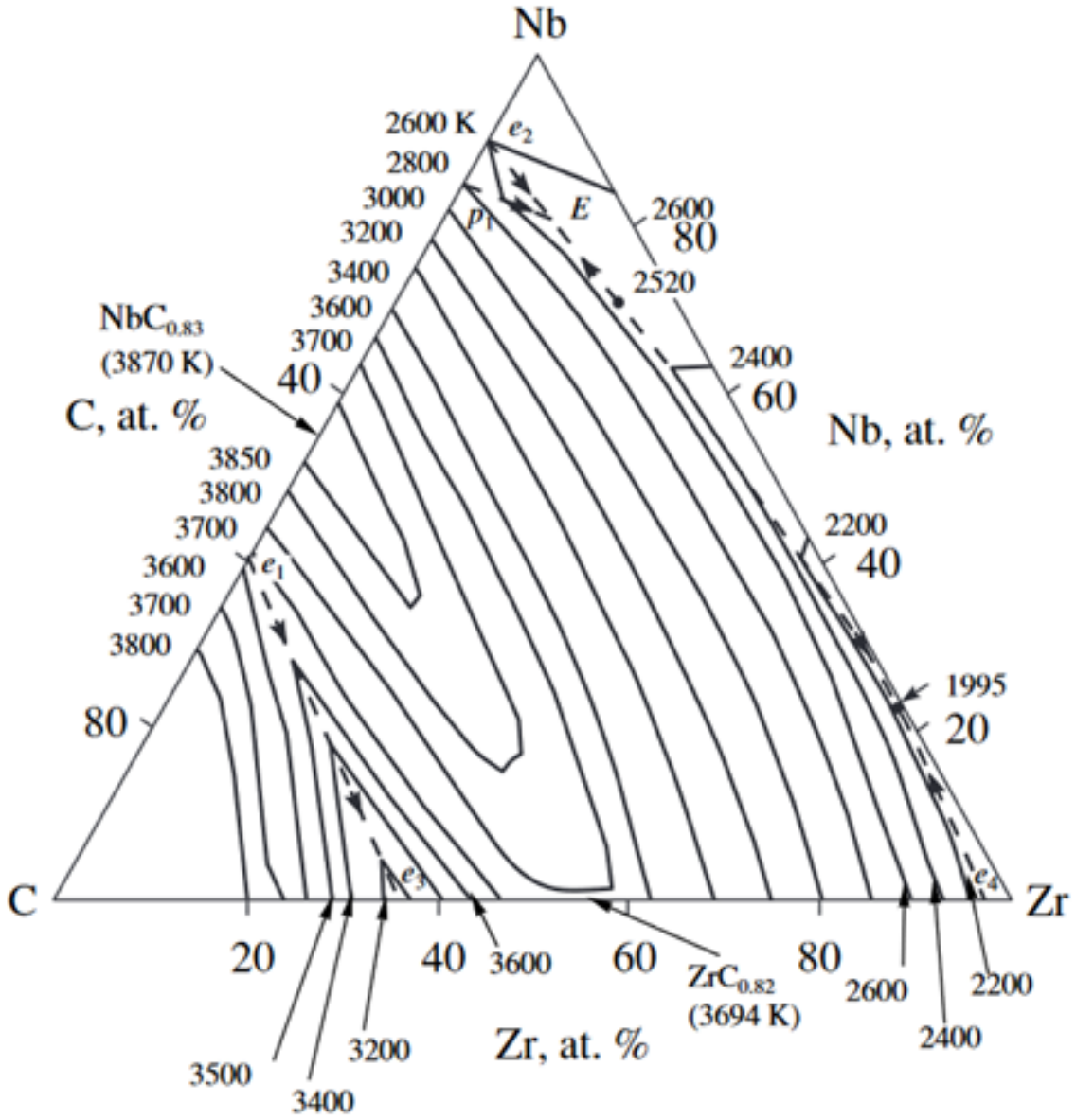


Figure 2.22: Liquidus surface for the Zr-Nb-C system [45].

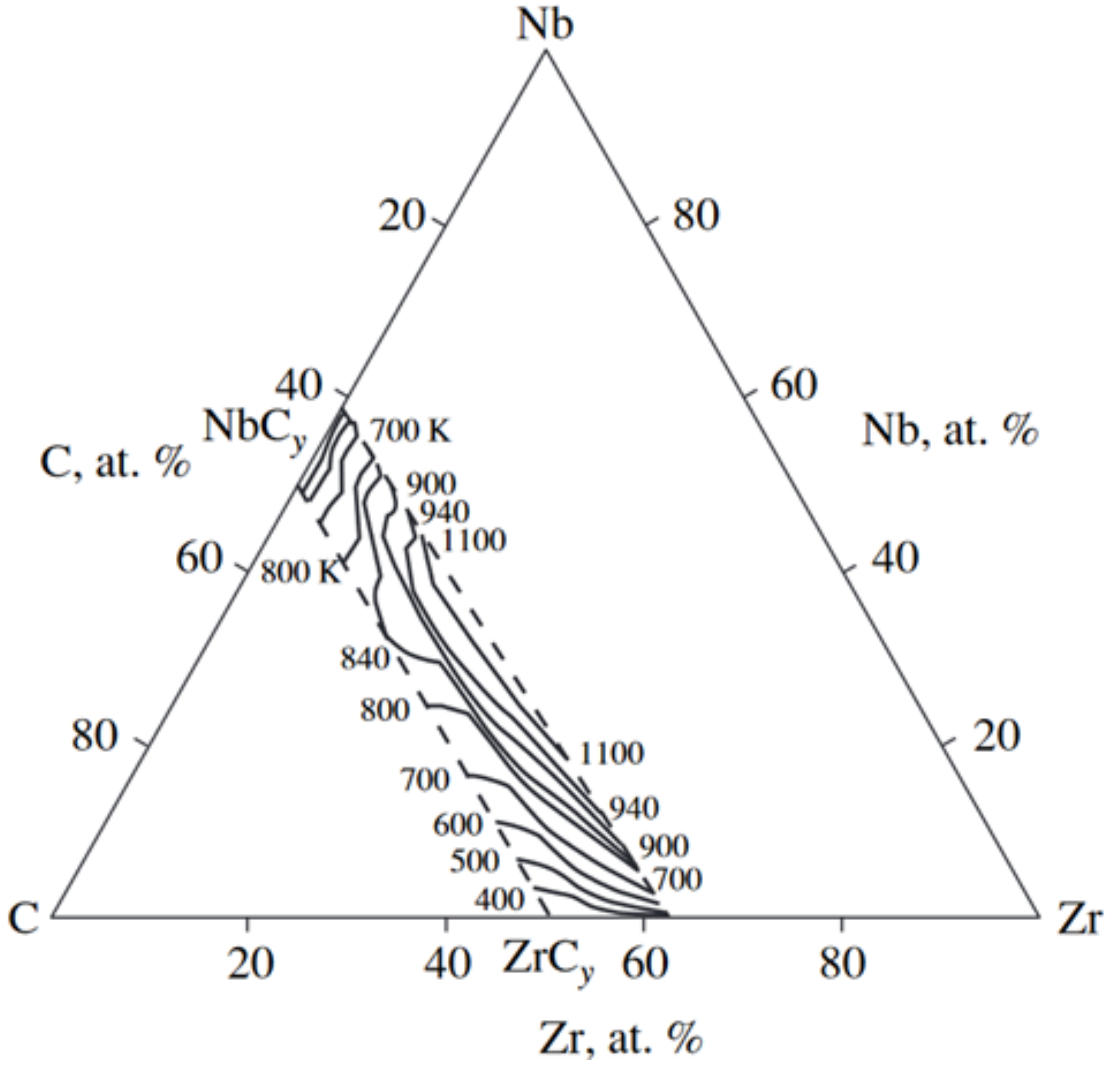


Figure 2.23: Positions of carbide solid solutions $Zr_{1-x}Nb_xC_y$ ($0 \leq x \leq 1$, $0.6 \leq y \leq 1.0$) with the B1 structure (NaCl structure) in the Zr-Nb-C system and isothermal sections of the surface of the $Zr_{1-x}Nb_xC_y$ exsolution region [45].

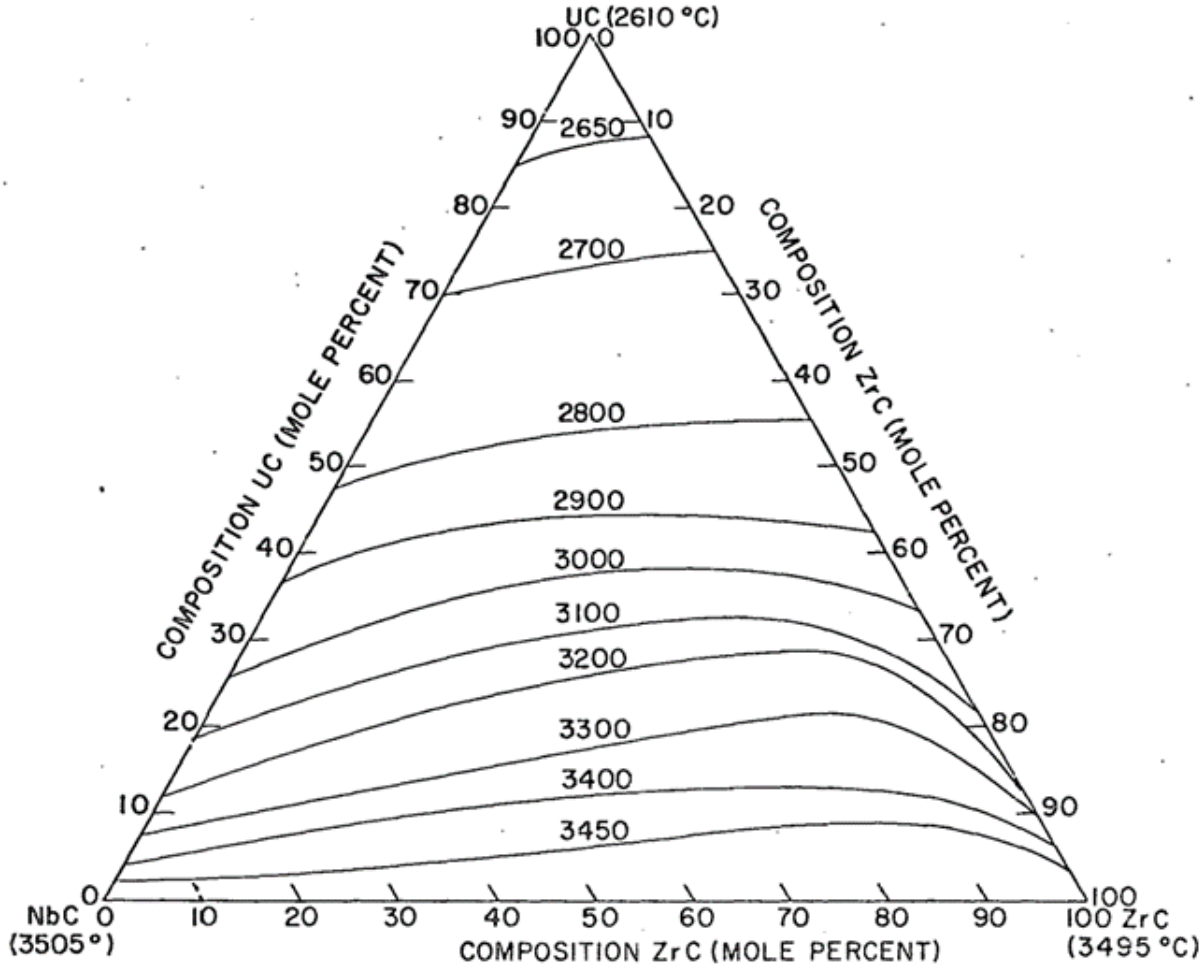


Figure 2.24: Solidus surface of NbC-ZrC-UC system [46].

that ternary carbide compounds have potentially advantageous properties over their mono- and bi-carbide components.

Isothermal phase diagrams of the U-Zr-C system were calculated over a range of temperatures based on a free-energy minimization method using thermodynamic and phase diagram data [47]. The Zr-C phase diagram is shown in **Figure 2.25**, comparing the calculated boundaries to the experimental phase boundary data. A single phase ZrC region appears in the slightly sub-stoichiometric region of the diagram. The phase diagram of UC, seen in **Figure 2.26**, shows a solid solution region at elevated temperatures and a wide range of stoichiometries. A continuous solid solution region of $(U_xZr_{1-x})C_y$ for the UC-$ZrC_{0.81}$ system is shown in **Figure 2.27**. Based on these phase diagrams, optimized ternary phase diagrams of the U-Zr-C system were generated for temperatures spanning from 2473 K to 3693 K. **Figure 2.28** shows the isothermal ternary U-Zr-C phase diagram at 2753 K, which is approximately the centerline temperature of an NTP reactor during operation. A continuous single phase solid solution region extends from UC to ZrC for a range of sub-stoichiometric concentrations [47]. As the temperature increases to 3693 K, the area of the U-Zr-C solid solution region decreases until the only non-liquid region that remains is $(U_xZr_{1-x})C_y$.

Continuous regions of single phase solid solutions have been shown to be present under certain conditions for compounds of refractory carbides mixed with UC. Additionally, experiential studies have used XRD spectra to show that different mixed carbide fuels exhibit complete single phase solubility [43, 46]. The phase equilibria of these compounds in solid solutions proves the feasibility of developing mixed refractory carbide materials for NTP reactors, which possess extremely desirable attributes for NTP applications due to their high melting temperatures [22]. However, further studies are required to provide experimental results to confirm the phase stability of these mixed carbide fuels. A methodical approach to defining the temperature and compositional bounds of these continuous solid solution regions is necessary to confirm the accuracy of these computationally generated phase diagrams. Once these temperature and compositional limitations of the solid solution carbide regions are better understood, engineering design specifications can more accurately be defined for NTP fuel applications.

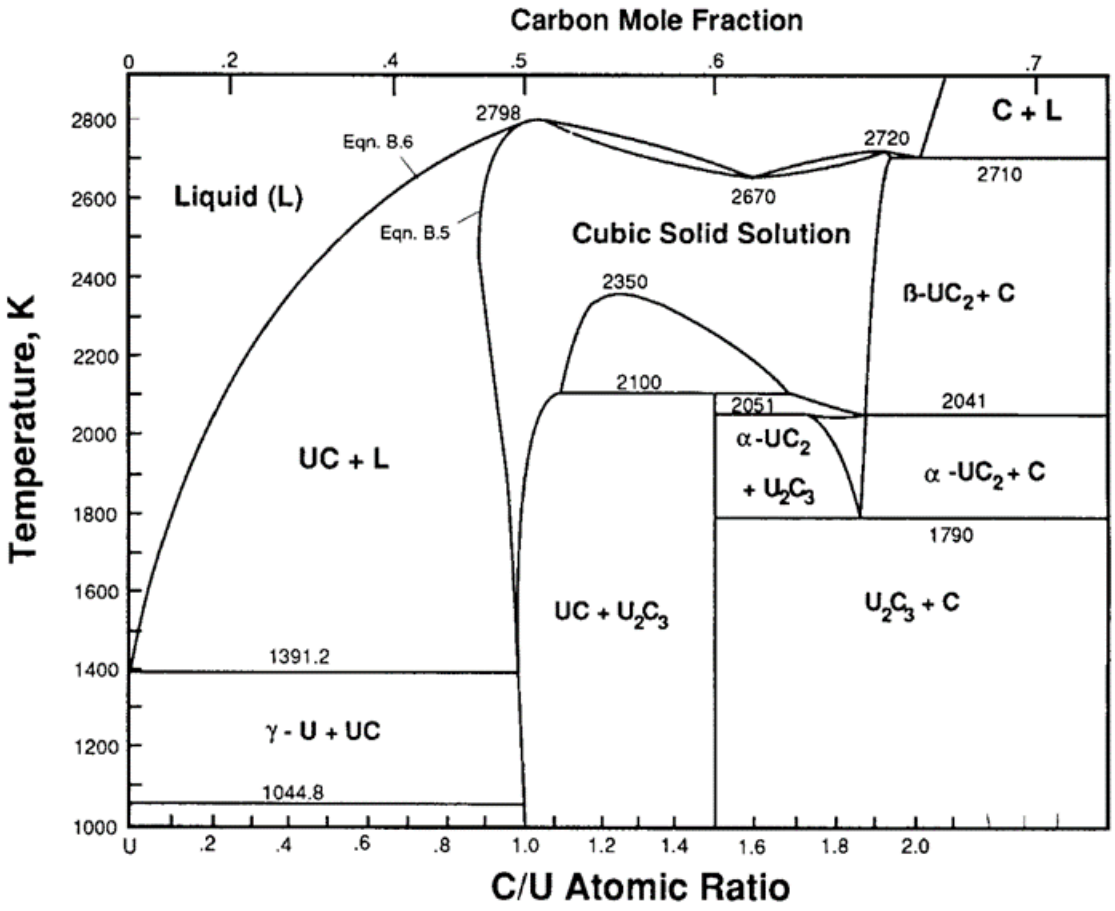


Figure 2.25: Zr-C phase diagram showing calculated phase boundaries and selected experimental data [47].

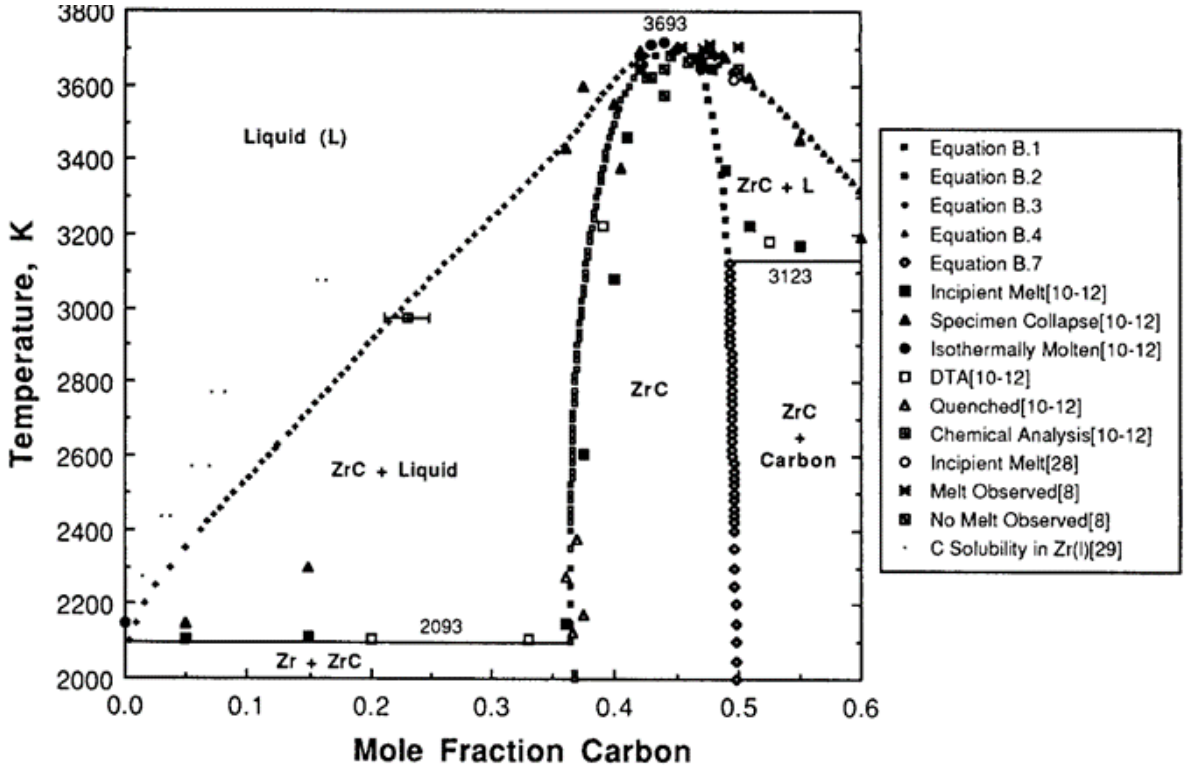


Figure 2.26: U-C phase diagram showing the calculated phase boundaries [47].

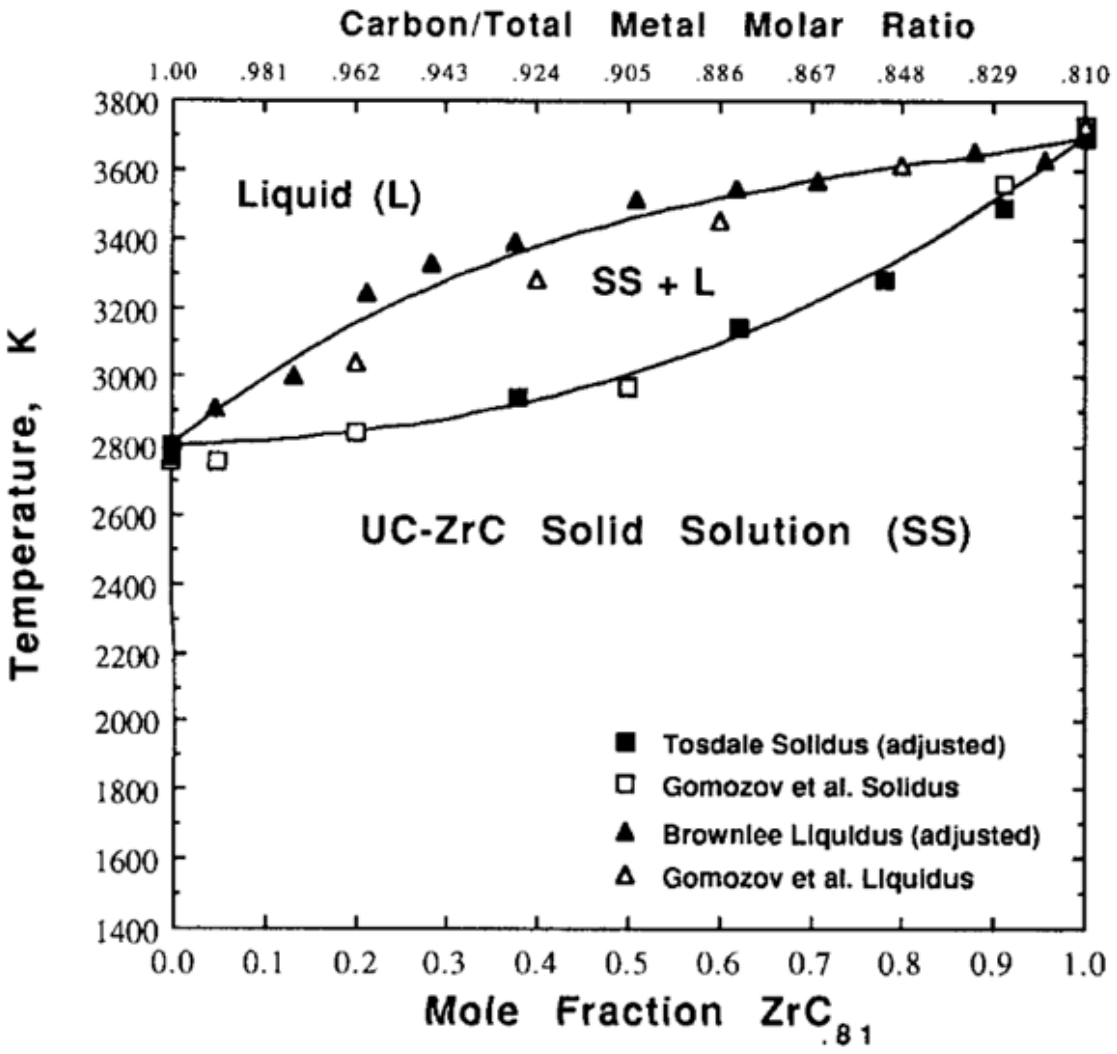


Figure 2.27: The UC-$ZrC_{0.81}$ phase diagram showing solidus and liquidus temperature data for the $(U_xZr_{1-x})C_y$ solid solution [47].

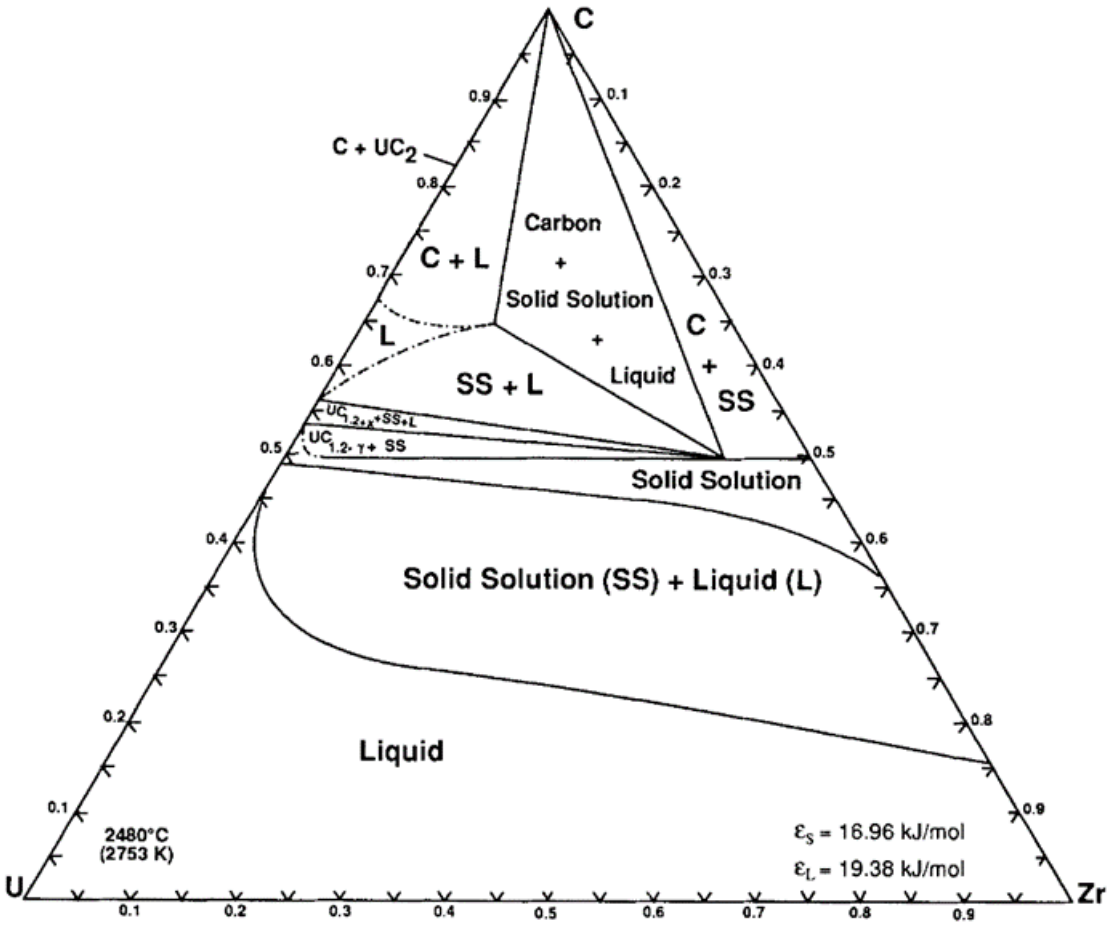


Figure 2.28: Isothermal ternary phase diagram for the system U-Zr-C at 2753 K [47].

2.2.4 Fuel Enrichment

Fissile isotope enrichment is another important attribute of NTP fuel. The level to which the nuclear fuel is enriched can drive many important factors of NTP design, production, and implementation such as the cost, weight, and size of the spacecraft as well as public perception, nuclear proliferation, and national security. Careful consideration must be taken when determining the enrichment of fuel for NTP reactors.

Enrichment is the process of enhancing the concentration of a specific isotope of an element. Uranium-235 (^{235}U) is the most commonly used fissile isotope in NTP reactor fuel materials. Natural uranium is mostly composed of ^{238}U, about 99.3% by weight (wt%), and only contains about 0.7 wt% ^{235}U. While ^{238}U is fertile, which means it can absorb a neutron and transmutate into a fissile isotope, it is not fissile, so it cannot undergo fission [48]. In order for uranium to produce a self-sustaining fission reaction, the concentration of ^{235}U must be increased, which can be accomplished by separating it from the more abundant isotope, ^{238}U, found in natural uranium. This process of isotope separation is called enrichment. Uranium enriched up to 20 wt% ^{235}U is commonly called low enriched uranium (LEU); furthermore, any enrichment higher than 20 wt% ^{235}U is considered high enriched uranium (HEU) [48]. The "waste" of the enrichment process, or the excess ^{238}U that is removed, is referred to as depleted uranium (DU), which has a lower percentage of ^{235}U (<0.7 wt%) than naturally occurring uranium.

Although uranium is generally considered "weapons grade" when enrichment levels surpass around 90 wt% ^{235}U [48, 49], all HEU material is theoretically enriched enough to be used in a nuclear weapon, and therefore its use necessitates many restrictions and regulations. While traditionally LEU used in fuel for commercial reactors was enriched to about 5 wt% ^{235}U [49], a more specific class of LEU has emerged. High Assay Low Enriched Uranium (HALEU), with enrichment between 5 wt% and 20 wt% ^{235}U (although the most common target enrichment level for HALEU is ∼19.75 wt% ^{235}U), has become the latest standard of fuel for advanced reactors (**Figure 2.29**) including NTP reactors, due to having a higher energy density than traditional 5 wt% ^{235}U LEU and fewer restrictions and regulations than HEU.

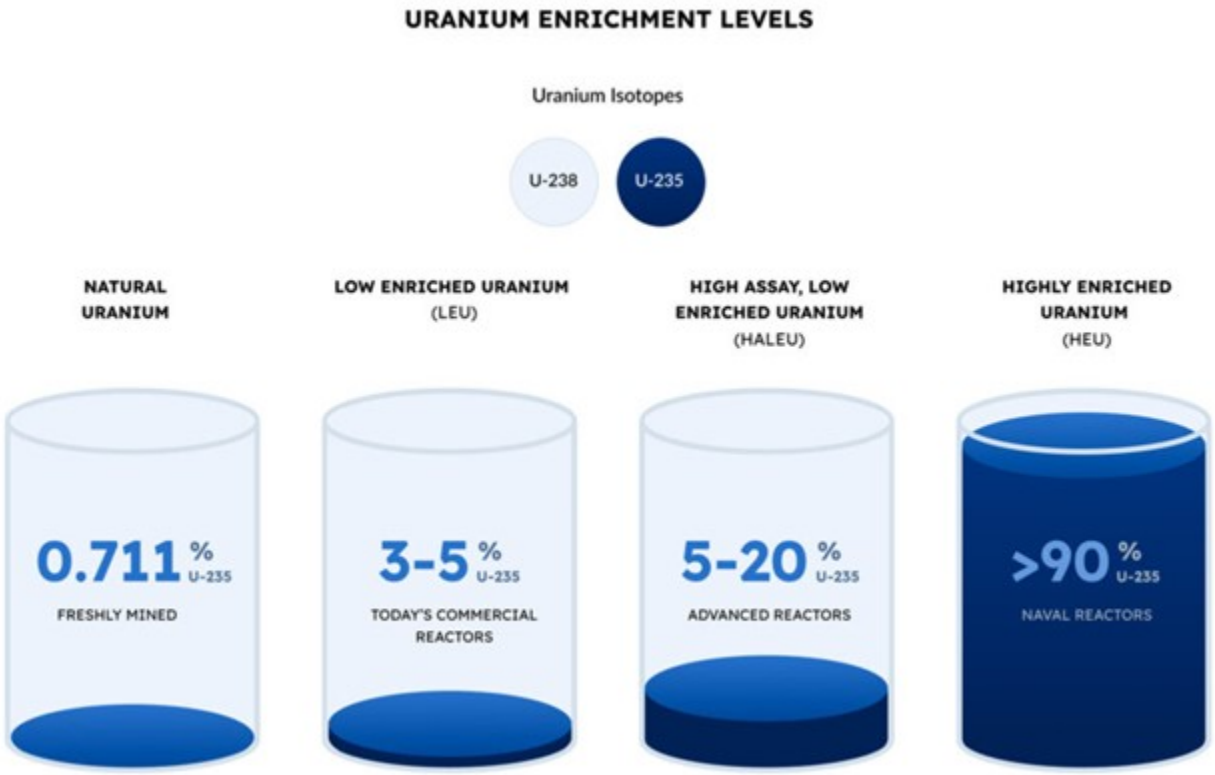


Figure 2.29: Uranium Enrichment Levels [52].

As far as its application in NTP fuels is concerned, LEU fuel has many advantages over HEU fuel. Firstly, LEU is much cheaper and more easily enriched than HEU. As the enrichment level goes up, the production costs increase exponentially [49], in addition to the numerous costs inherently associated with HEU (e.g. handling, storage, transportation, design, testing, and security) [34, 50, 51]. Additionally, use of LEU fuel leads to a much lower proliferation risk [50]. If an NTP reactor with HEU fuel were to land in a nefarious country seeking nuclear weapons materials due to an accident or aborted launch, then nuclear proliferation would most likely become a major problem. Lastly, due to national security concerns, any handling of HEU must involve the oversight of a government agency, severely restricting the technological development of the HEU NTP reactor.

With several distinctive advantages over HEU, LEU (including HALEU) presents itself as a viable option for NTP fuel, as long as it can be implemented without having too much of a negative impact on the performance of the reactor. Several studies have investigated the feasibility of using LEU as a fuel for NTP; furthermore, it has been shown that LEU fueled NTP engines of thrusts varying from 7.5 klbf to greater than 35 klbf are nearly equivalent to similar HEU fueled NTP designs [51, 53, 54, 55]. Above engine thrusts of about 16 klbf, the design of the NTP reactor is limited by thermodynamic requirements rather than neutronics [54]. By using the highest enrichment levels possible while maintaining the LEU classification (i.e. HALEU enriched to 19.75 wt% ^{235}U), the benefits of LEU can be maximized while avoiding the regulations and restrictions of using HEU. Therefore, in almost all modern NTP designs, the fuel is designated as HALEU, due to the significant advantages that LEU holds over the more historic HEU fueled designs.

When considering NTP fuel materials, an important reactor classification needs to be defined; specifically, the decision to use a fast spectrum or a thermal spectrum nuclear reactor (thermal neutron spectrum, not to be confused with the "thermal" classification used in the name nuclear "thermal" propulsion). Whether a reactor operates in the fast or the thermal spectrum is determined by the energy of the neutrons absorbed in the reactor fuel, which results in fission. Fast spectrum reactors are designed to use high energy neutrons produced from fission to continue the chain reaction. Thermal spectrum reactors are designed to use thermal neutrons, or lower energy neutrons. To create a thermal neutron spectrum, the high

energy "fast neutrons" produced from fission undergo moderation, or the process of slowing down the neutrons by energy transfer, until the neutrons are at a low enough energy to be absorbed in the thermal spectrum of the fuel. For thermal spectrum reactors, additional materials are needed to provide moderation in the core.

Fast spectrum reactors do provide several advantages over thermal spectrum reactors including improved fission product retention, longer operating life (taking into account reactor restarts and temperature cycling), and an intrinsic neutronic spectral shift, which acts as a safety feature to prevent the reactor from going critical in the event of being submerged in water (such as during a launch or reentry accident) [56]. Additionally, when compared to thermal spectrum reactors, fast spectrum reactors can be designed to be much smaller in size, but not necessarily with an improved thrust-to-weight ratio. The main disadvantage of fast spectrum reactors is the necessity for higher fissile mass in the core when compared to thermal spectrum reactors. Increasing fuel loading is one method to raise the fissile mass in the core, leading to a lower thrust-to-weight ratio, which is undesirable. Another technique to raise fissile mass in the core is fissile isotope enrichment, which introduces a number of barriers and challenges, as discussed previously, which often outweigh the benefits of using a fast spectrum reactor. Due to this disadvantage, the majority of the NTP reactor designed that have been tested and assessed, are thermal neutron spectrum reactors.

In the past several decades, there has been a paradigm shift amongst the NTP development community to use LEU fuels, specifically HALEU, instead of HEU, mainly due to the previously discussed benefits of LEU NTP fuel. Cermet fuel materials were mainly used in fast spectrum reactor designs with HEU fuel. The high thermal neutron cross section of absorption of W commonly used as the matrix material in cermet fuels prohibits the use of LEU in cermet fuels, unless the expensive process of enriching ^{184}W, which has a much lower thermal neutron cross section, in natural W is performed. This W enrichment process is costly and not very refined, which introduces its own host of problems. On the other hand, the wide range of stoichiometries that produce a solid solution tri-carbide fuel allows for a much larger uranium fuel loading tolerance, which helps contribute to making mixed carbide fuels an excellent candidate for NTP applications.

2.3 Refractory Carbide Fabrication

When considering tri-carbides as a candidate for NTP fuel, fabricability was brought up as one of the major technical issues that needed to be addressed [22]. Production of ceramics, such as tri-carbides, is normally performed via sintering, which is the process of consolidating powders into a solid mass using elevated temperature and oftentimes pressure [57]. There are many different sintering methods, as outlined in **Figure 2.30**, each one having its own strengths and weaknesses. Of the possible sintering methods, Spark Plasma Sintering (SPS) provides unique capabilities, allowing for the consolidation of high melting temperature compounds at lower temperatures than some of the other more traditional sintering techniques.

2.3.1 Spark Plasma Sintering

Spark plasma sintering is a method of powder consolidation implementing a uniaxial pressure and pulsed DC current, while containing the sample in a controlled atmosphere environment. Furthermore, SPS allows for sintering at a lower temperature with an increased heating rate, enabling a shorter sintering time and a reduced rate of grain growth when compared to other sintering methods. For fabricating samples via SPS, a hollow cylindrical die, typically graphite, is lined with a thin foil, also normally graphite, and loaded with powder. Cylindrical punches are inserted into the top and bottom of the hollow die to contain the powder. The hollow die is then wrapped in a carbon felt insulation layer and inserted into the chamber of the SPS furnace. A typical SPS configuration is shown in **Figure 2.31**. The die is oriented such that the punches are in contact with the upper and lower electrodes, using cylindrical graphite spacers as necessary. A uniaxial pressure is applied along the vertical axis through the electrodes and graphite spacers, compacting the powder contained within the hollow die. A small hole in the insulation allows for an external pyrometer to measure the wall temperature of the die. The SPS chamber may be evacuated or filled with gas and the electrodes are normally water-cooled. A pulsed DC current is applied to the die and powder through the electrodes, providing the energy for sintering. The exact sintering mechanisms are still being studied, but one theory postulates that the pulsing DC current

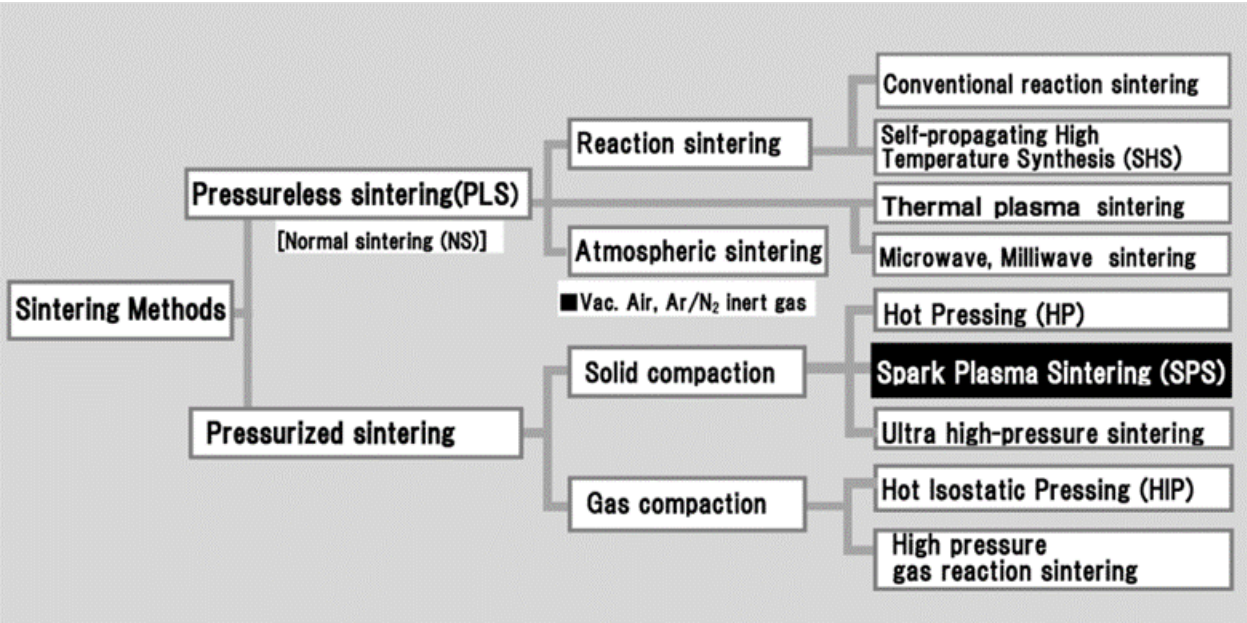


Figure 2.30: Typical classification of sintering methods [58].

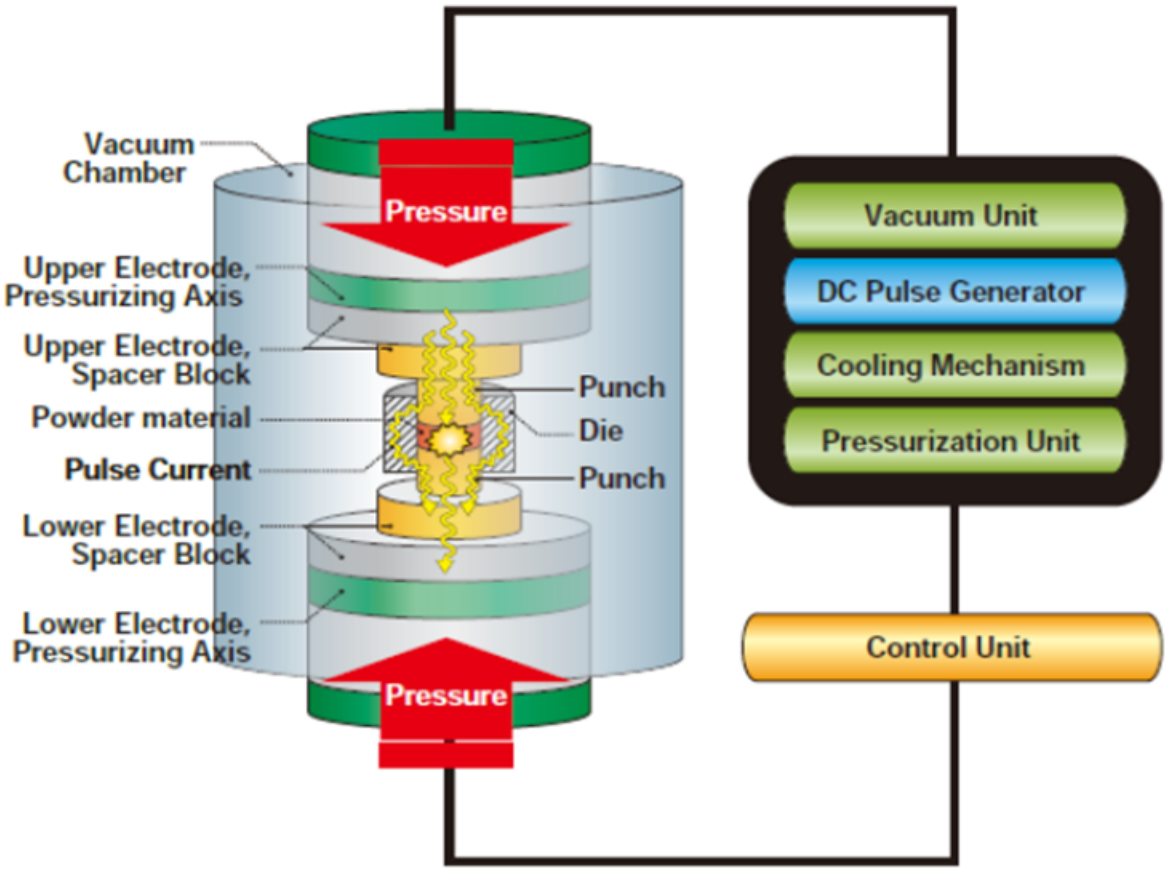


Figure 2.31: Basic SPS System configuration [58].

generates several effects: a spark plasma, a spark impact pressure, Joule heating, and an electric field diffusion effect [58].

Figure 2.32 shows the potential paths of the pulsed DC current; the current flows through either the powder (1), the graphite die (2), or the foil lining the die (3). The current flow through the powder is dependent on a number of properties including powder morphology, powder conductivity, particle size, applied pressure, and current pulse intervals to name a few. The current flow through the powder is dependent on a number of properties including powder morphology, powder conductivity, particle size, applied pressure, and current pulse intervals to name a few. The pulsed DC current flow through conductive powder particles results in Joule heating and sparking, as shown in **Figure 2.33**. The effects of pulsed DC current change based on the magnitude of the pulsed voltage are shown in **Figure 2.34**, including the generation of spark plasma and impact pressure as well as Joule heating, allowing for short duration consolidation of hard to sinter materials at a relatively low temperature [58].

The behavior of current flow and the corresponding temperature in a sample during SPS consolidation is not uniform. **Figure 2.35** shows finite element models of the temperature, current density, and dissipated energy gradients in insulative and conductive materials [59]. There are significant differences in each of these profiles, influenced by the conductivity of the sample. These distributions should be accounted for when planning and conducting experiments, since the differences in the gradients may have a significant impact on the densification of the material. Specifically, since the temperature during the SPS process is typically measured via a pyrometer aimed at the wall of the hollow graphite die, the internal sample temperature may be significantly different than the measured temperature. Experiments have shown [58, 60] that the difference between the internal sample temperature and graphite die wall may vary based on material and temperature and must be considered (**Figure 2.36** and **Figure 2.37**).

Different methods of measuring the sample temperature have been investigated. Kelly and Graeve [61] conducted an experiment to compare the temperature during an SPS run using a pyrometer focused on the interior of a modified punch with the normal temperature reading from a pyrometer focused on the outer wall of the hollow cylindrical die (**Figure**

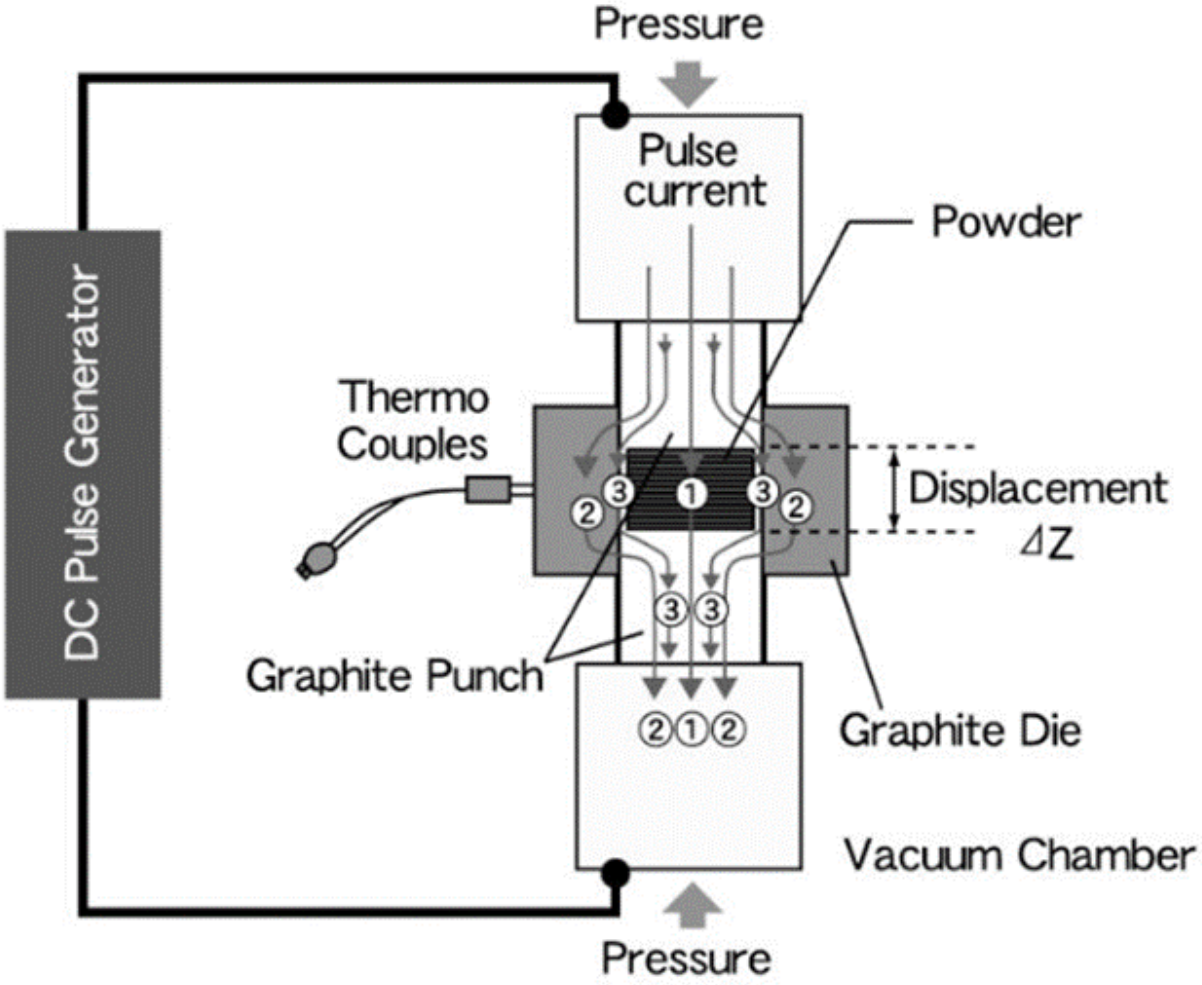


Figure 2.32: On-off DC pulsed current path [56].

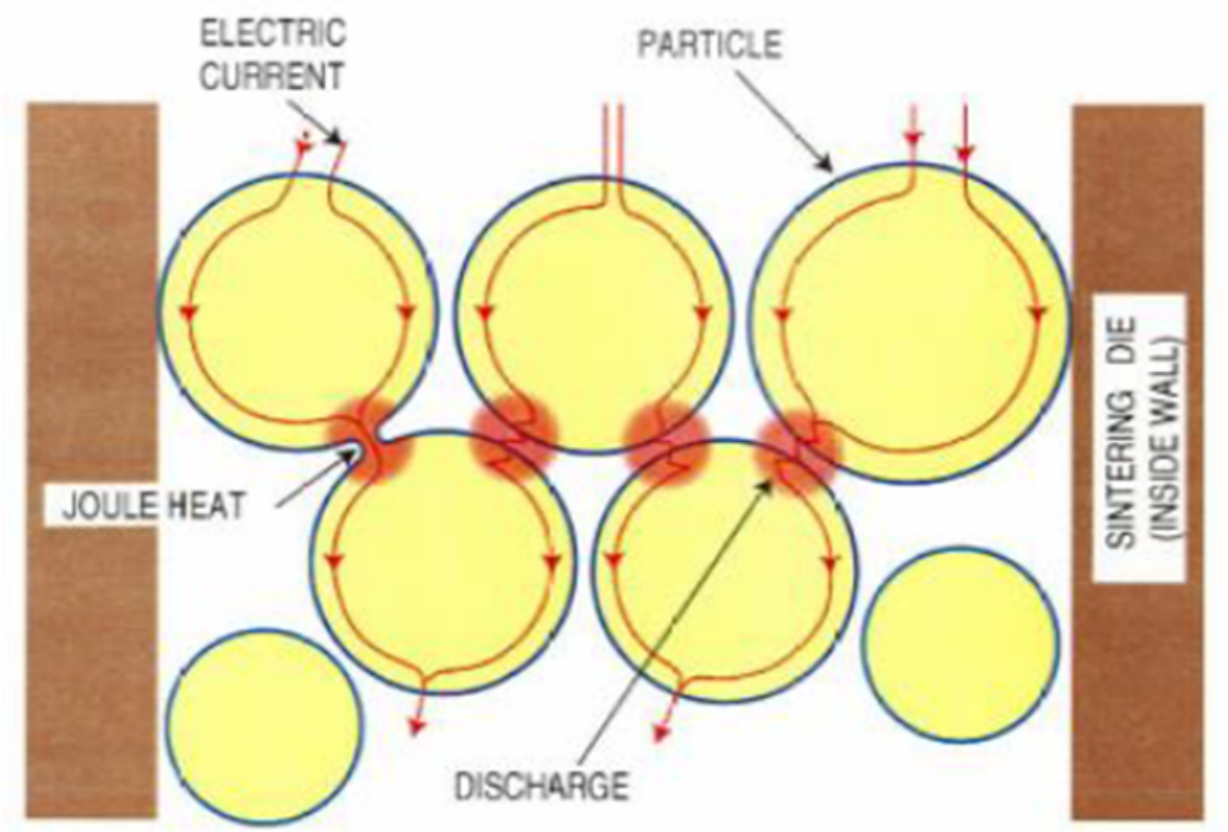


Figure 2.33: Pulsed current flow through powder particles [58].

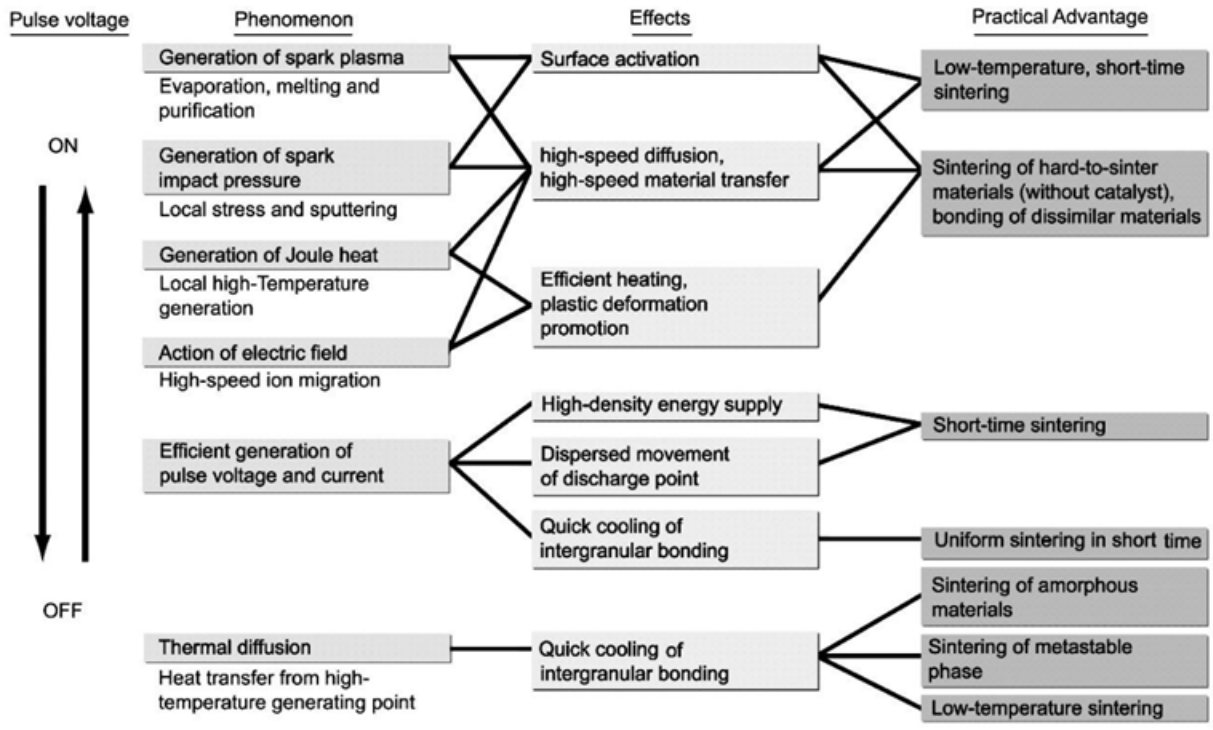


Figure 2.34: Effects of on-off DC pulse energizing [58].

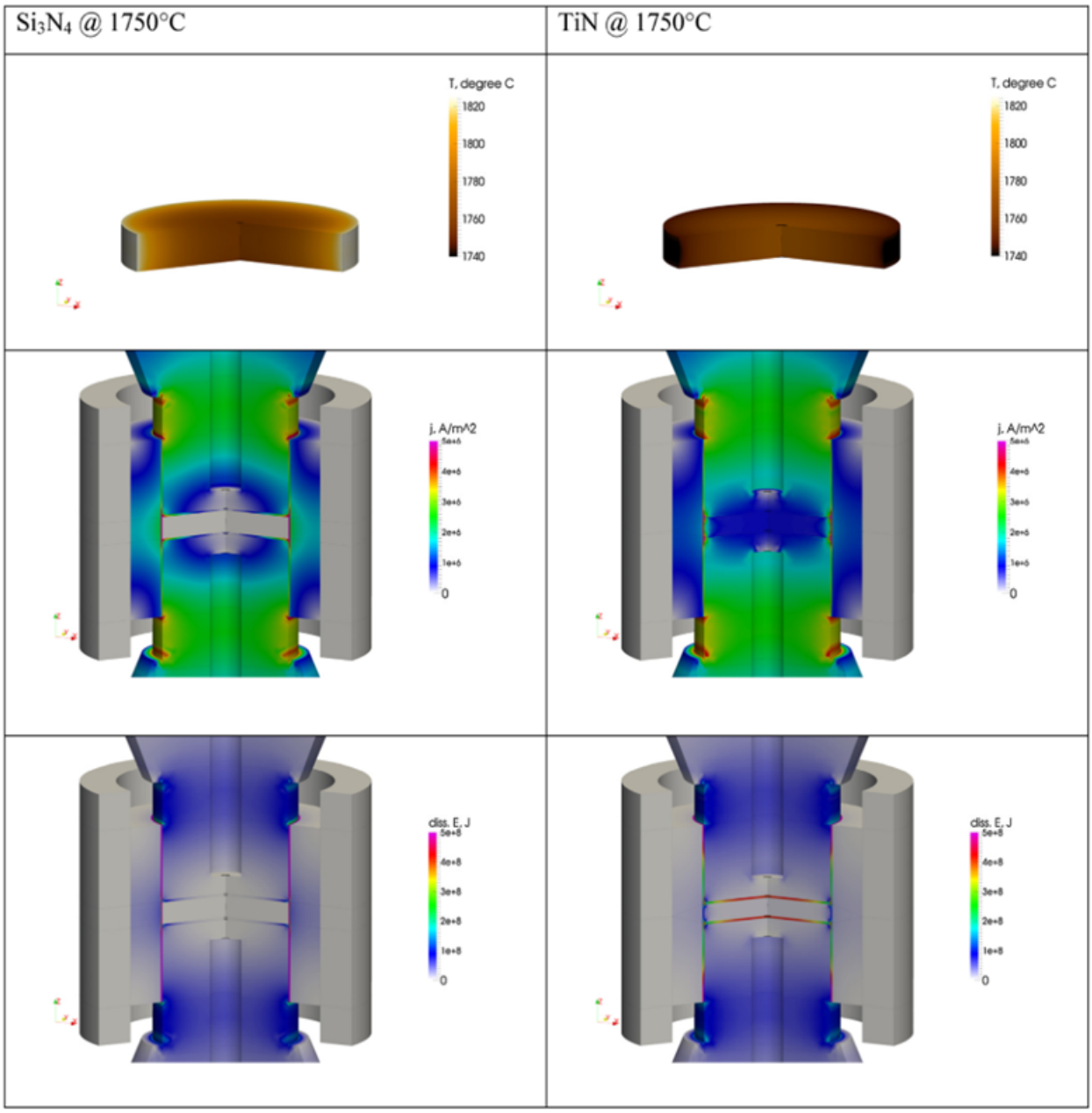


Figure 2.35: Temperature, current density, and dissipated energy distributions for an electrically insulating material (Si_3N_4) and an electrical conductor (TiN) after 5 min at 1750 °C (inner tool diameter: 40 mm) [59].

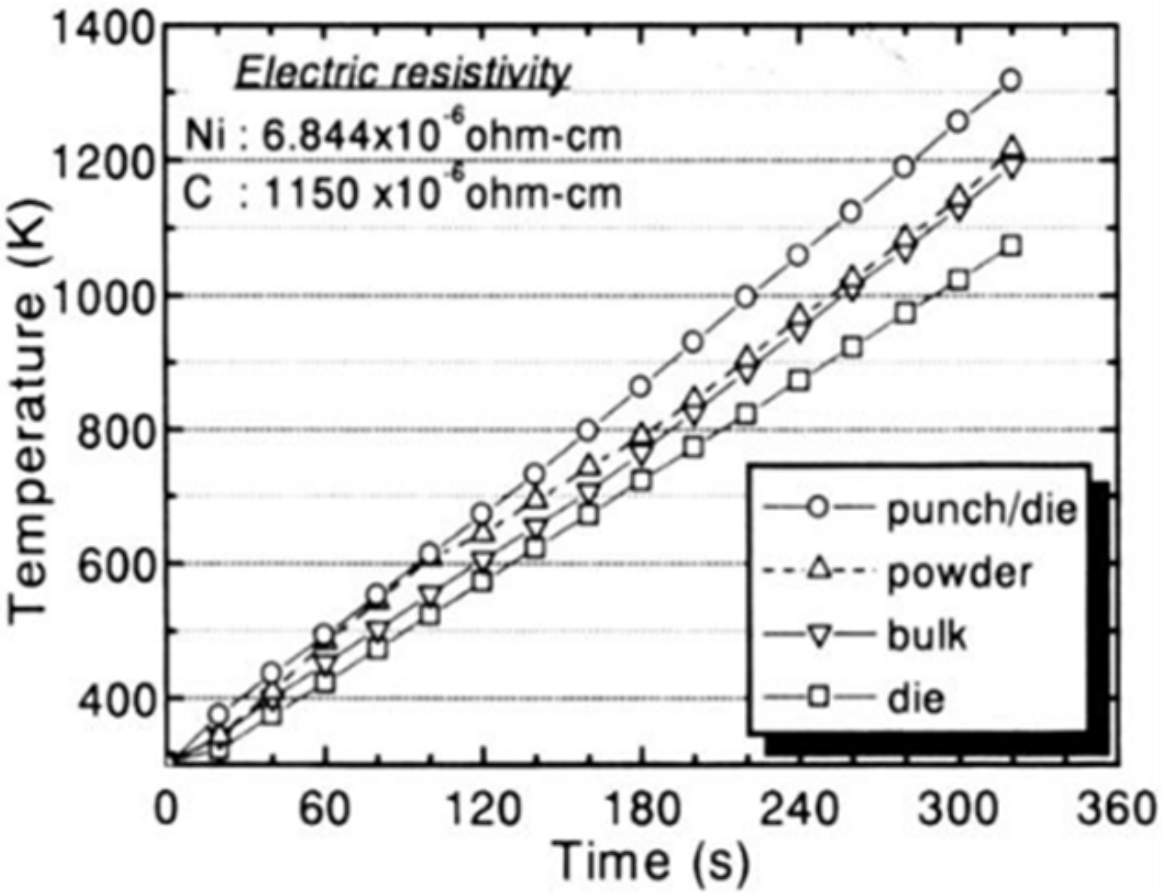


Figure 2.36: The temperature difference between specimen and graphite die [58].

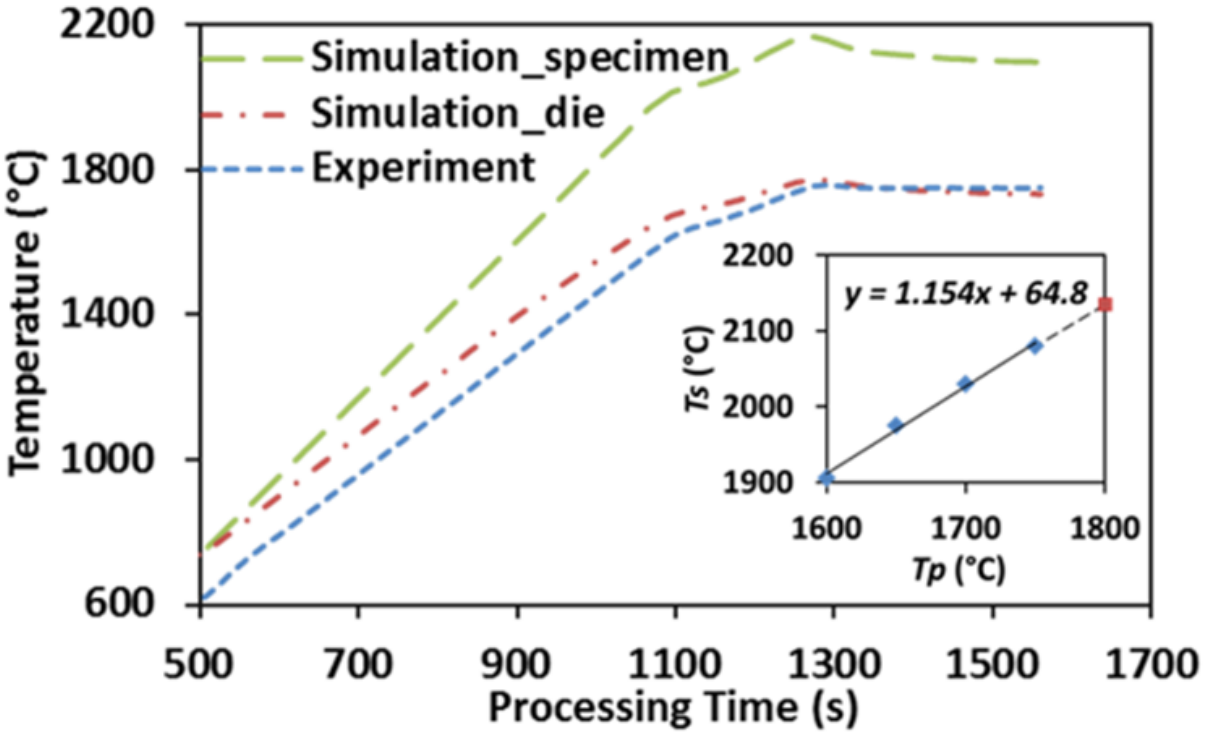


Figure 2.37: Simulation vs. experiment: temperature evolution in SPS of ArC (up to 1750 °C) [60].

2.38). Calibration curves were generated (**Figure 2.39**) to normalize the top pyrometer readings with the side pyrometer readings, allowing for a more accurate quantification of the bulk sample temperature. However, the calibration curves are unique to the powder material, powder quantity, die size, heating rate, applied pressure, sintering temperature, and other SPS variables.

The influence of current, pressure, and heating rate during the SPS process was investigated by Munir et al. [62]. Several mass transport mechanisms are enhanced by the current, including electromigration, point defect generation, and enhanced defect mobility. The current has other impacts including field effects on grain growth, increased solubility in liquid metals, decreased incubation time for the nucleation of new phases, improved neck formation, and increased diffusion coefficients [62]. Ultra-high pressure tooling has been designed for use in an SPS furnace, as shown in **Figure 2.40**. Pressures as high as 1 GPa may be used allowing for high relative dense samples sintered at low temperatures with minimal grain growth. Other effects of pressure during the SPS process include an increase in chemical potential, influencing the diffusion-related mass transport, improved densification, and lower temperature difference between the hollow die and sample. While SPS heating rates lead to a reduction in time that the sample soaks at lower temperatures, experiments conducted investigating the effects of heating rates during SPS processing have resulted in inconsistent outcomes [62].

SPS is a novel sintering method that provides many advantages over more traditional sintering processes such as lower sintering temperatures, higher heating rates, shorter sintering times, and lower grain growth rates [63]. However, there are many shortcomings of the SPS process including a lack of understanding of the sintering mechanisms and the uncertainty of the temperature in the center of the sample due to the temperature being measured only on the outside of the die. Additionally, an SPS furnace is a very complex system with many variables that affect sintering behavior; when performing experiments, one must ensure to record as much of these variables as possible, since the omission of this data could lead to confounding and under reported results. Another major disadvantage of SPS is the difficulty to upsize to a production scale. While SPS is ideal for lab scale applications, creating more advanced geometry samples that are more practical for production are at

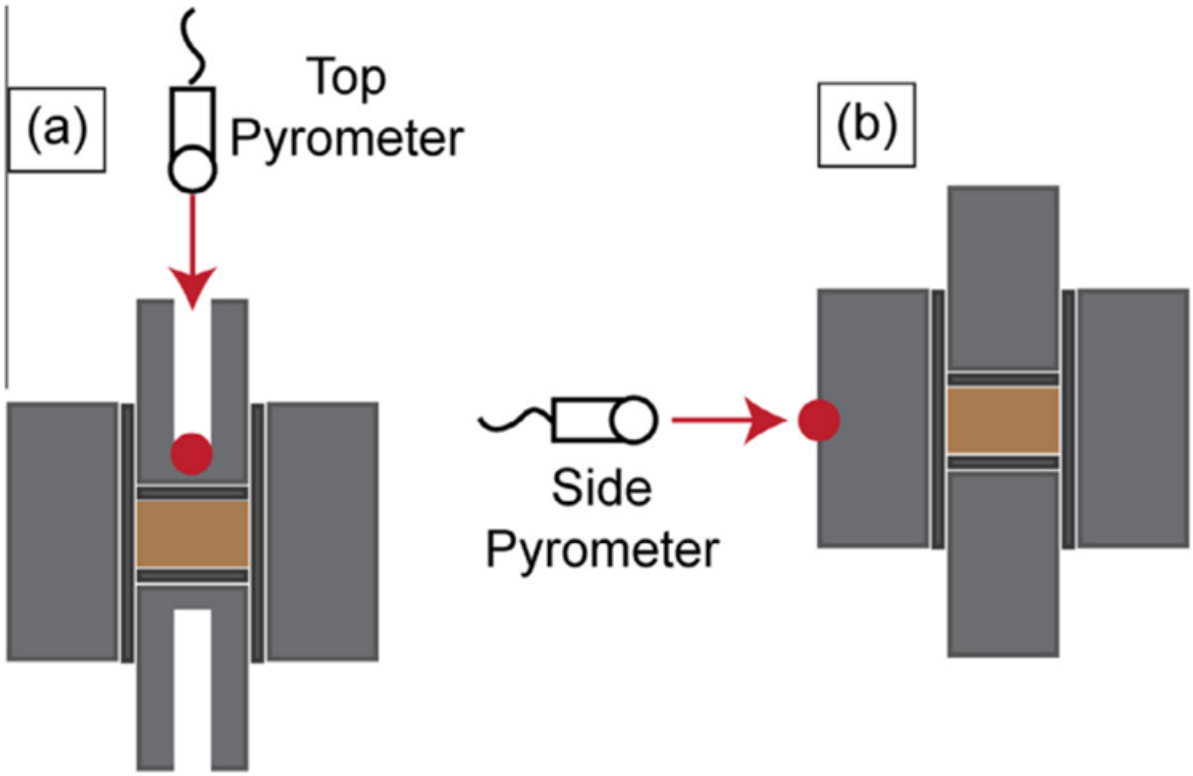


Figure 2.38: Depictions of top and side pyrometer configurations [61].

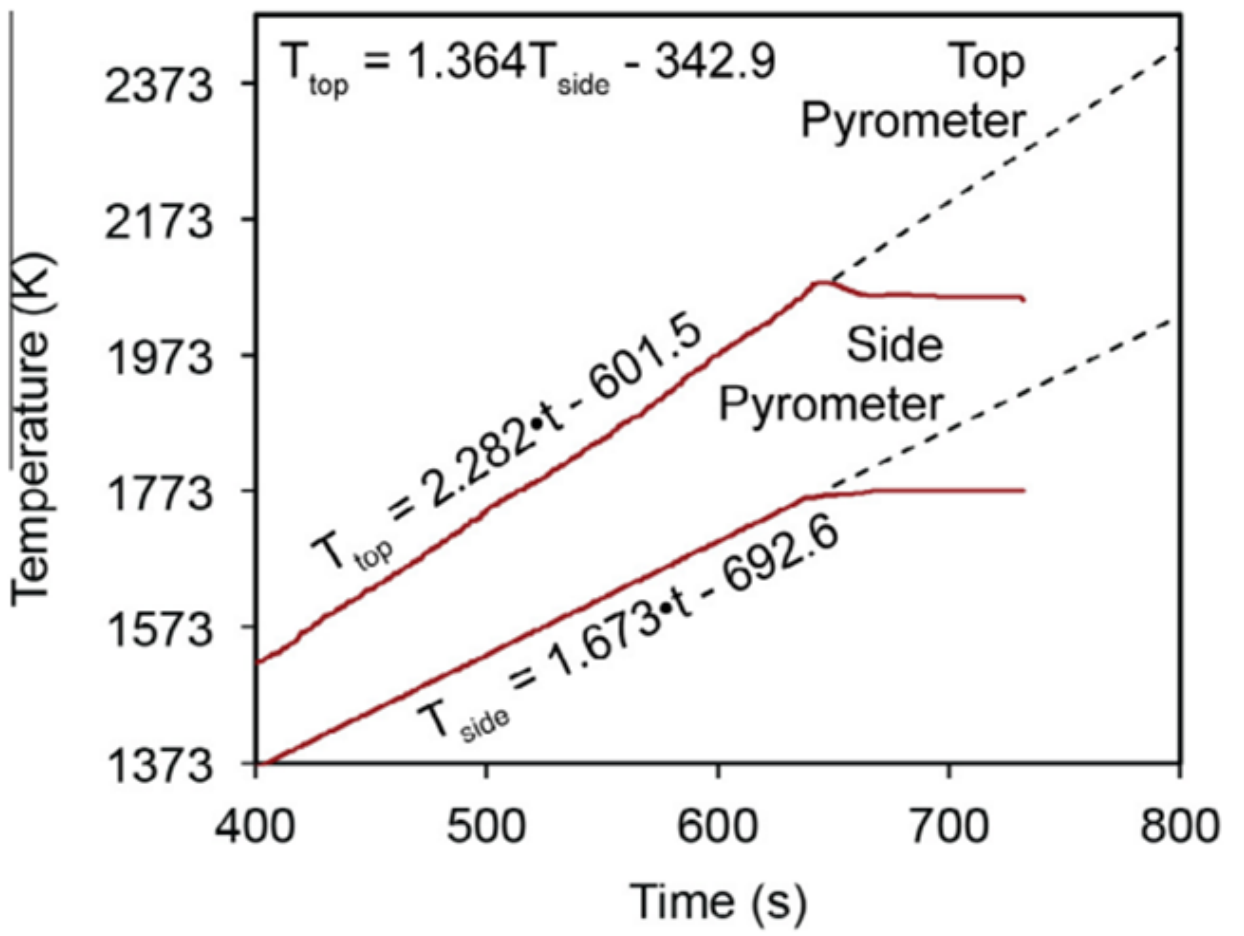


Figure 2.39: Calibration curves used to normalize the side pyrometer temperature reading (T_{side}) to the top pyrometer reading (T_{top}) for the side pyrometer configuration [61].

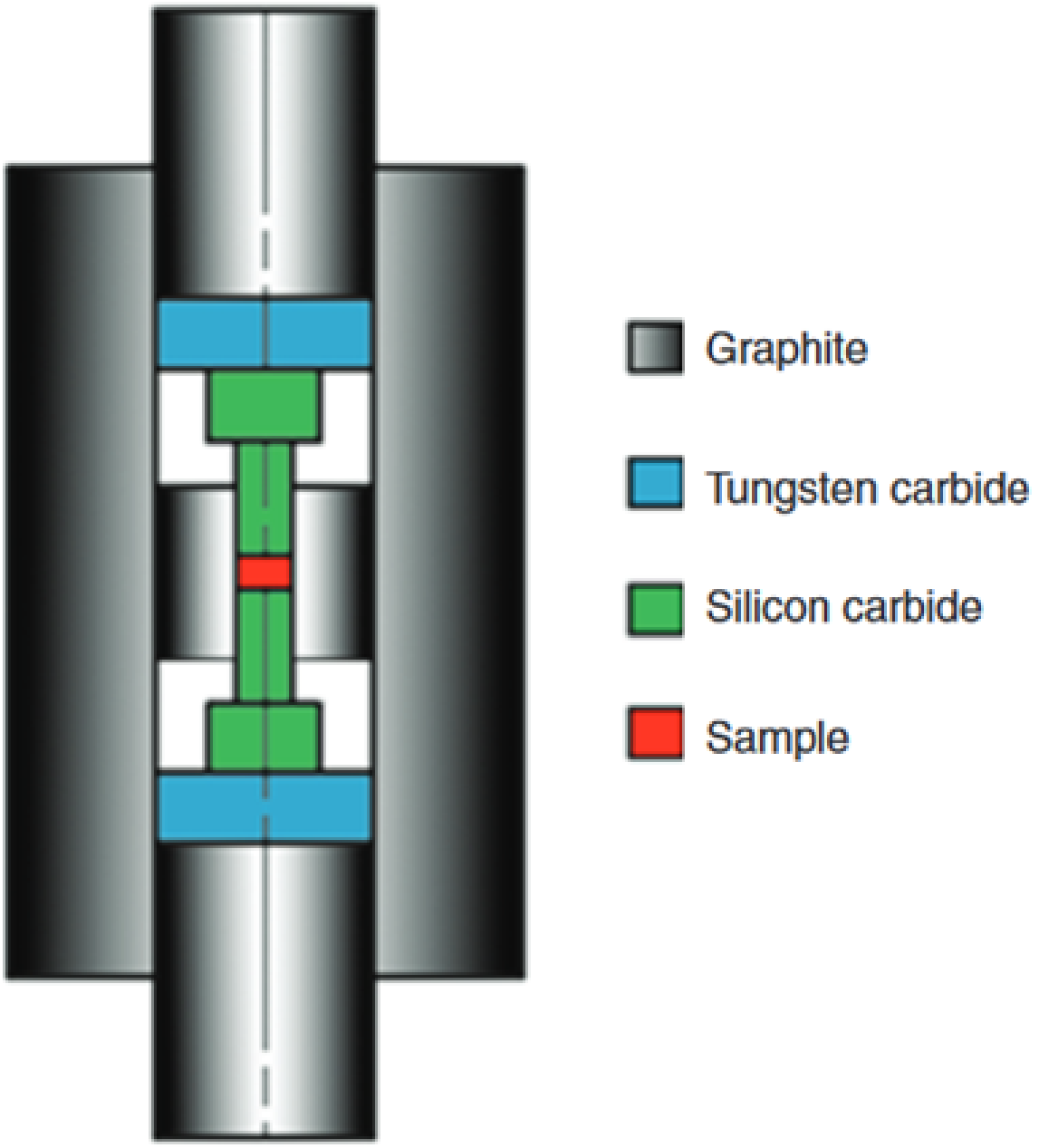


Figure 2.40: Schematic of a double acting die that allows the use of much higher pressures [62].

best tricky, if not impossible (the complex current and temperature profiles through these advanced geometry samples also introduce additional hurdles). As the SPS sample size increases, additional complications are introduced; the temperature gradient between the measured die wall and the center of the sintered sample is likely to increase with larger diameter dies. Larger SPS samples also require extended cooldown periods on the order of additional hours to days, depending on the size, material, and sintering environment, which may lead to extended production timelines, and may outweigh many of the advantages of SPS. However, despite these numerous disadvantages of SPS, it is still a desirable sintering method, especially for difficult to sinter materials, such as UHTCs, used for NTP fuel applications.

2.3.2 SPS Densification and Grain Growth of Refractory Carbides

Wei et al. compared the sintering behavior of ZrC at various temperatures, pressures, and hold times as well as the densification when using hot press (HP) sintering versus SPS, as shown by the circle and triangle markers in **Figure 2.41**, respectively [60]. Although a much lower temperature was used for the SPS comparison sample, the relative density (RD) after sintering was much higher than for the HP sample. The SPS consolidation of ZrC powders was found to be significantly more efficient than the HP sintering method.

Densification kinetics of SPS vs HP of ZrC samples were also studied (**Figure 2.42**). The activation energy of ZrC was found to be lower for samples consolidated with SPS when compared to HP using similar processing parameters. The lower activation energy was attributed to the improvement of particle neck growth due to the pulsed electrical current, which accelerated the activation of plastic flow.

The relationship between grain growth and relative density compared to various hold times at 1700 °C is shown in **Figure 2.43**. It appears that the samples were in the final stage of densification during the hold times since, even at the lowest hold time, the relative density is ∼92%. Therefore, while the change in relative density was small as the hold time was increased, the grain size steadily increased. The internal temperature of the sample was estimated to be ∼2030 °C by using the relationship between grain size and the transition from open to closed porosity. By iteratively solving this relationship by best fit, the dominating

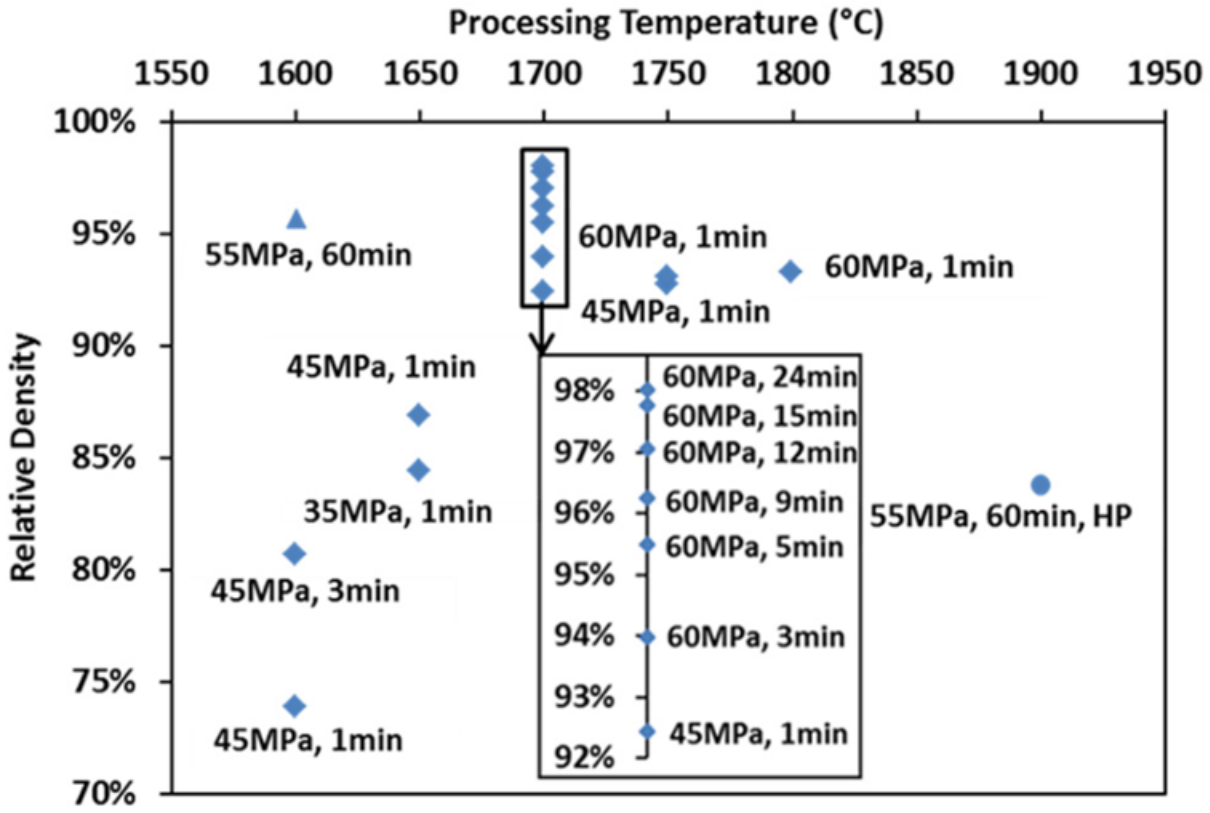


Figure 2.41: Map of relative densities for specimens prepared under various processing conditions [60].

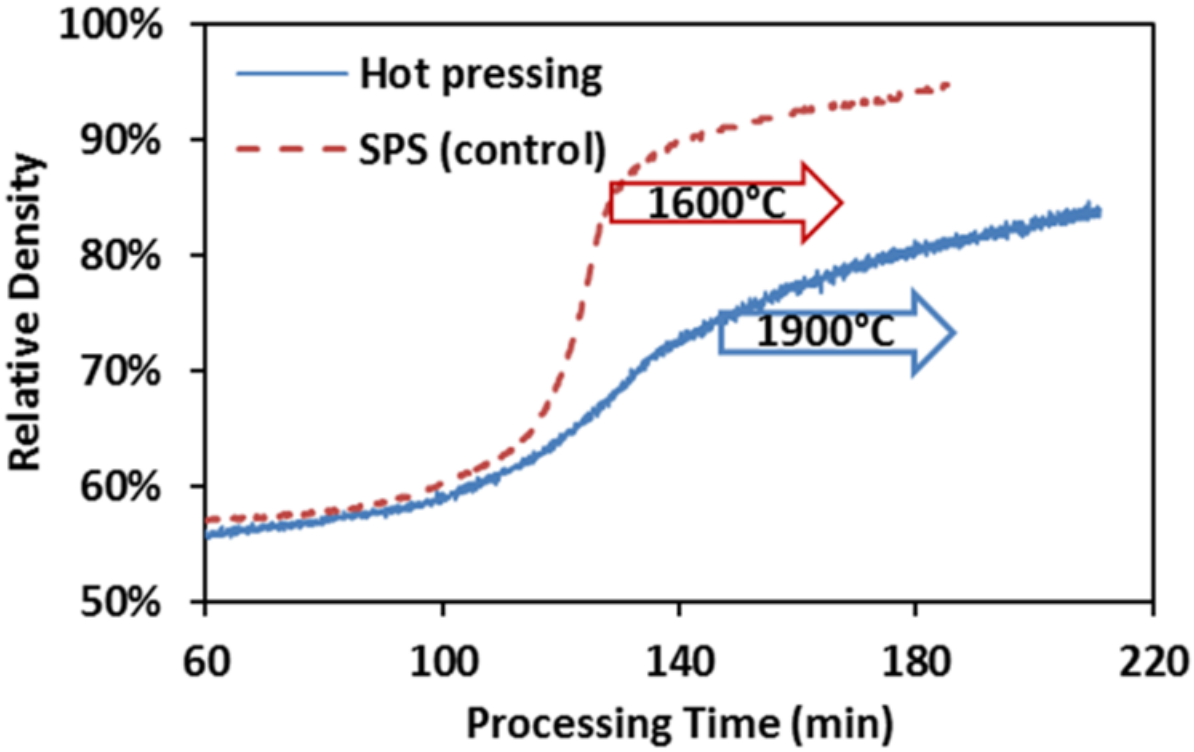


Figure 2.42: Hot pressing vs. control SPS of ZrC: Comparison of densification kinetics, under 55 MPa and 60 min holding [60].

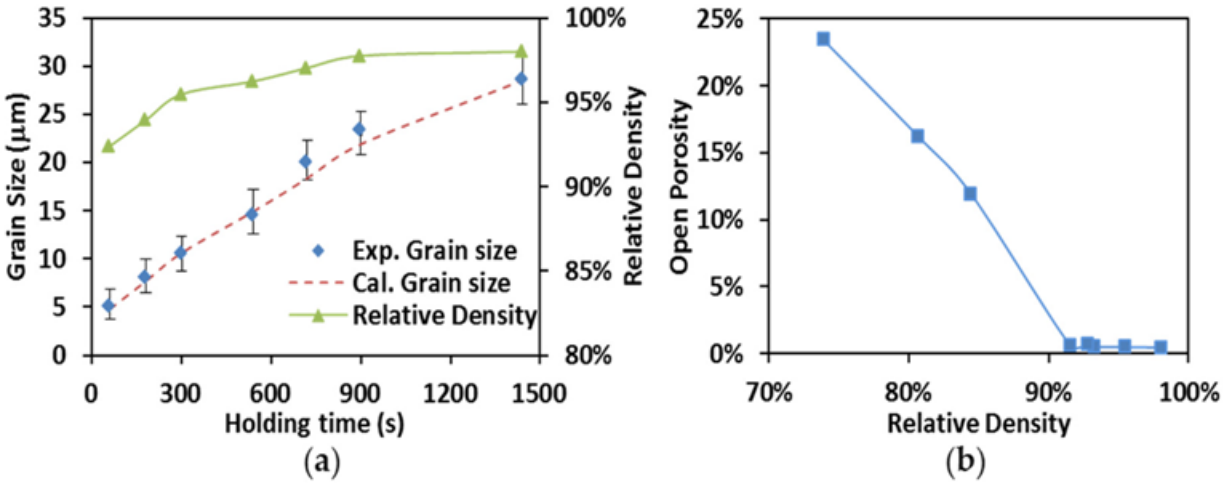


Figure 2.43: (a) Grain size and relative density vs. holding time (SPS at 1700 °C); (b) open porosity vs. relative density [60].

grain growth mechanism was found to be grain boundary diffusion and the activation energy was calculated to be 290 kJ/mol.

Gu et al. studied the densification and grain growth of an ultra-high temperature ceramic, tantalum carbide (TaC) [64]. The effect of temperature on grain growth and densification mechanism was compared and divided into three regimes (**Figure 2.44**). Route I encompasses high temperature (greater than 2000 °C) and low pressure (less than 100 MPa) sintering, which results in high relative densities, mainly by lattice diffusion, and severe grain growth. At lower temperatures (less than 2000 °C) and very high pressures (greater than 1 GPa), plastic deformation and dislocation creep lead to moderately high relative densities with little to no grain growth and is described as Route II in **Figure 2.44**. The last region, Route III, occurs at low temperatures (less than 2000 °C) and high pressures (from 100 MPa to 1 GPa), which shows grain boundary sliding and diffusion as the primary driving mechanisms for densification, leading to high relative densities with restricted grain growth.

The critical temperature for grain growth (T_g), shown in **Figure 2.44** and **Figure 2.45**, is the temperature at which the grain growth is observed to increase rapidly. This is an attribute seen during the densification of most ceramics where the grain growth is restricted at the early stages of sintering and accelerates after a certain threshold temperature, T_g. A modification in the sintering methods and conditions may lead to a different T_g within the same material system (e.g. the T_g for a hot pressed sample may be much higher than the T_g of a sample consolidated using SPS). Gu et al. found that by selecting a sintering temperature just above T_g, the grain growth of the sample would be minimized while higher densification would occur by increasing the pressure as needed.

Samples sintered at a constant temperature slightly greater than T_g while stepping up the pressure leads to increasingly higher relative density with restricted grain growth (**Figure 2.46**). **Figure 2.47** shows a comparison of the densification of samples sintered via Routes I, II, and III including the sintering temperature, initial powder size, and final grain size. For this study, sintering using high pressure and lower temperature (Route III) led to a high relative density with minimal grain growth.

An SPS densification study was conducted by Ji et al. to investigate the sintering behavior of boron carbide (B_4C) at various temperatures, pressures and hold times. **Figure 2.48a**

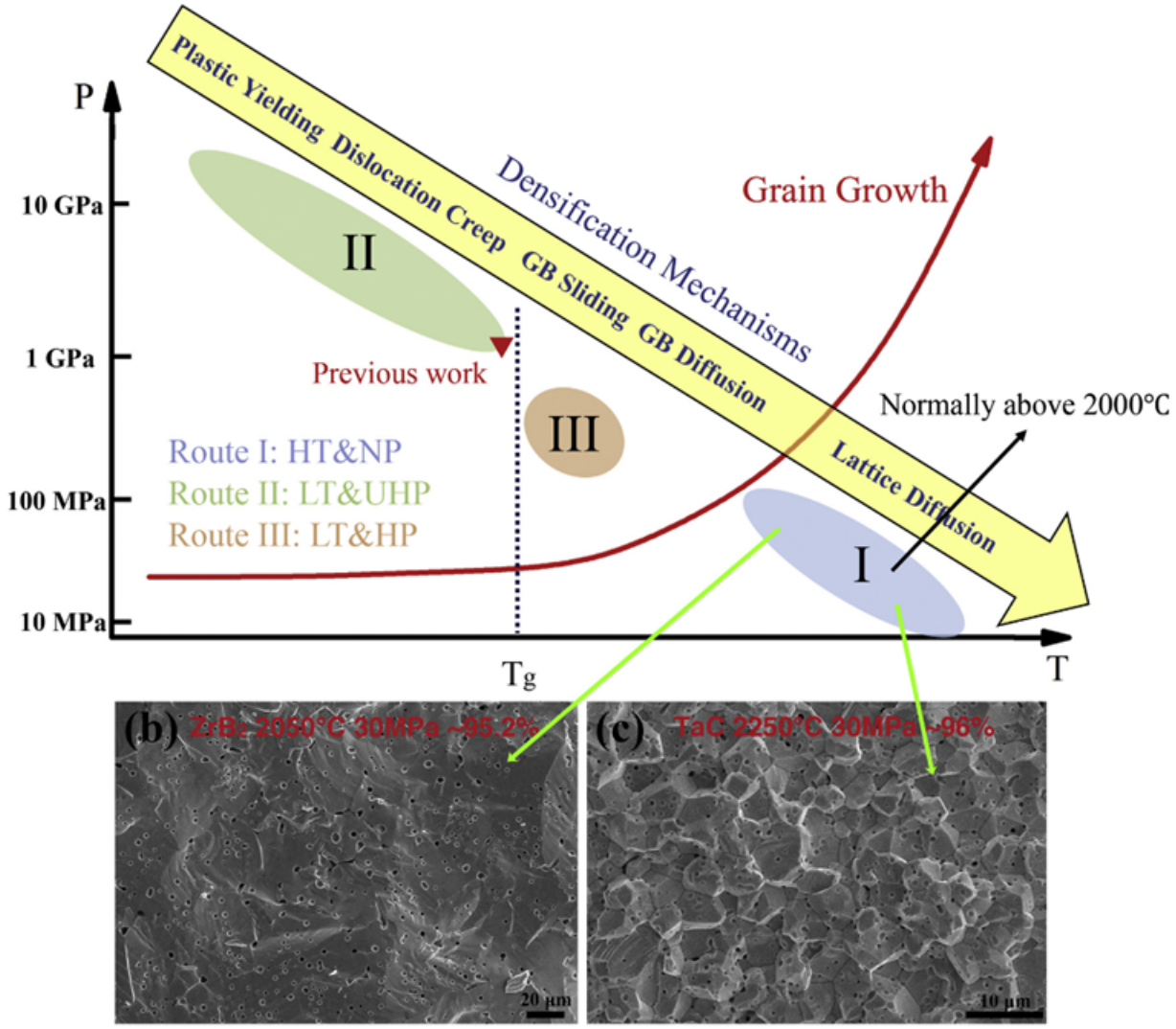


Figure 2.44: (a) Different sintering routes and corresponding densification mechanisms. Route I: high temperature (HT) & normal pressure (NP), Route II: low temperature (LT) & ultra-high pressure (UHP), Route III: low temperature (LT) & high pressure (HP). (b) Morphology of ZrB_2 ceramics and (c) TaC ceramics sintered by Route I, both showing large amounts of pores trapped within grains [64].

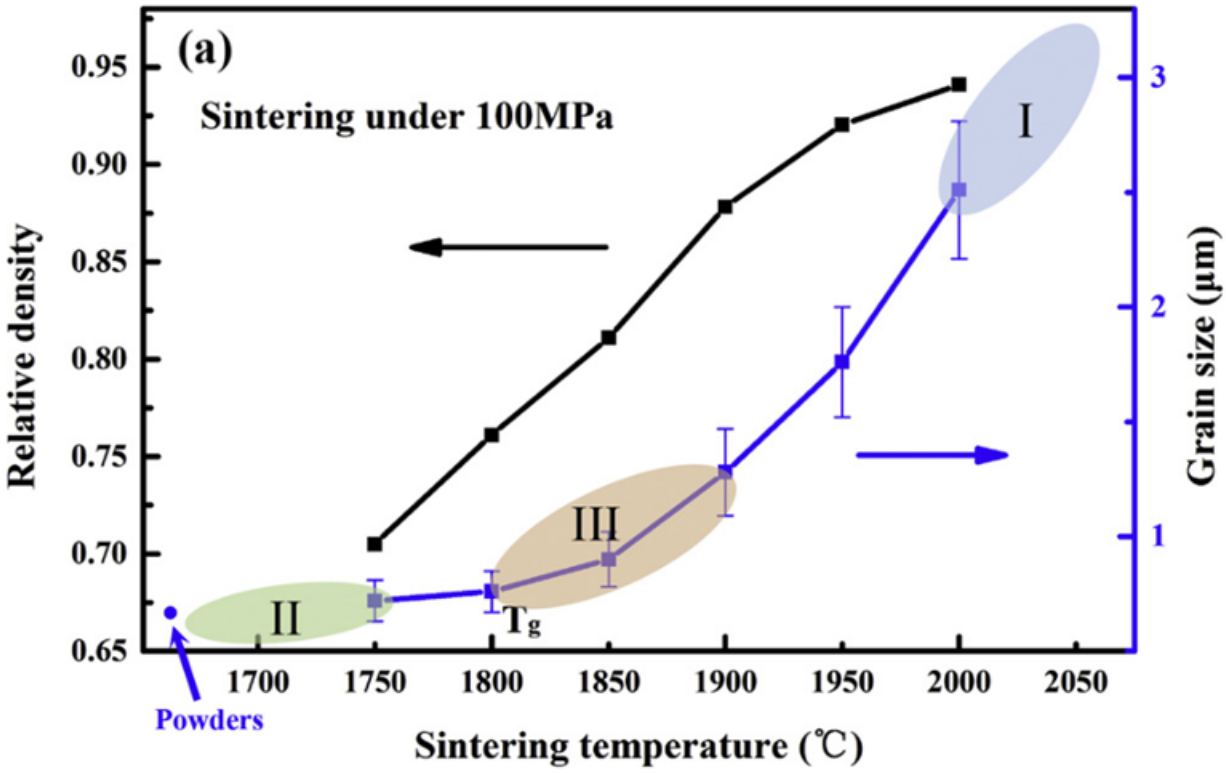


Figure 2.45: Effects of temperature on the relative density and the average grain size of TaC ceramics sintered under 100 MPa for 5 min [64].

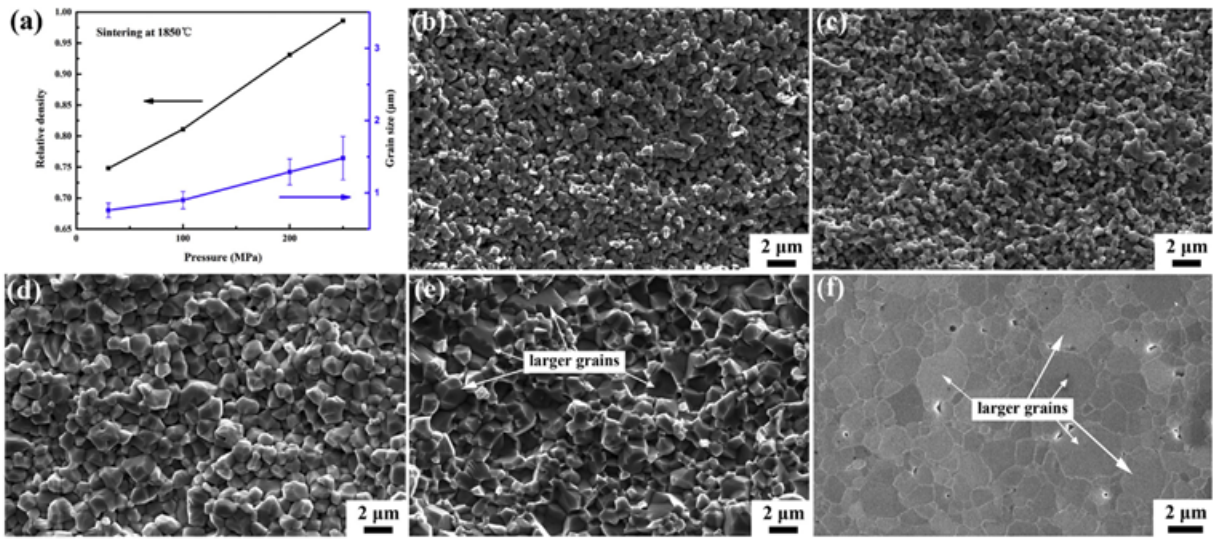


Figure 2.46: (a) Effects of pressure on the relative density and the average grain size of TaC ceramics sintered at 1850 °C for 5 min. Representative SEM micrographs of specimens prepared under (b) 30 MPa (c) 100 MPa (d) 200 MPa and (e) 250 MPa, (f) The polished surface of the specimen prepared at 250 MPa after thermal etch [64].

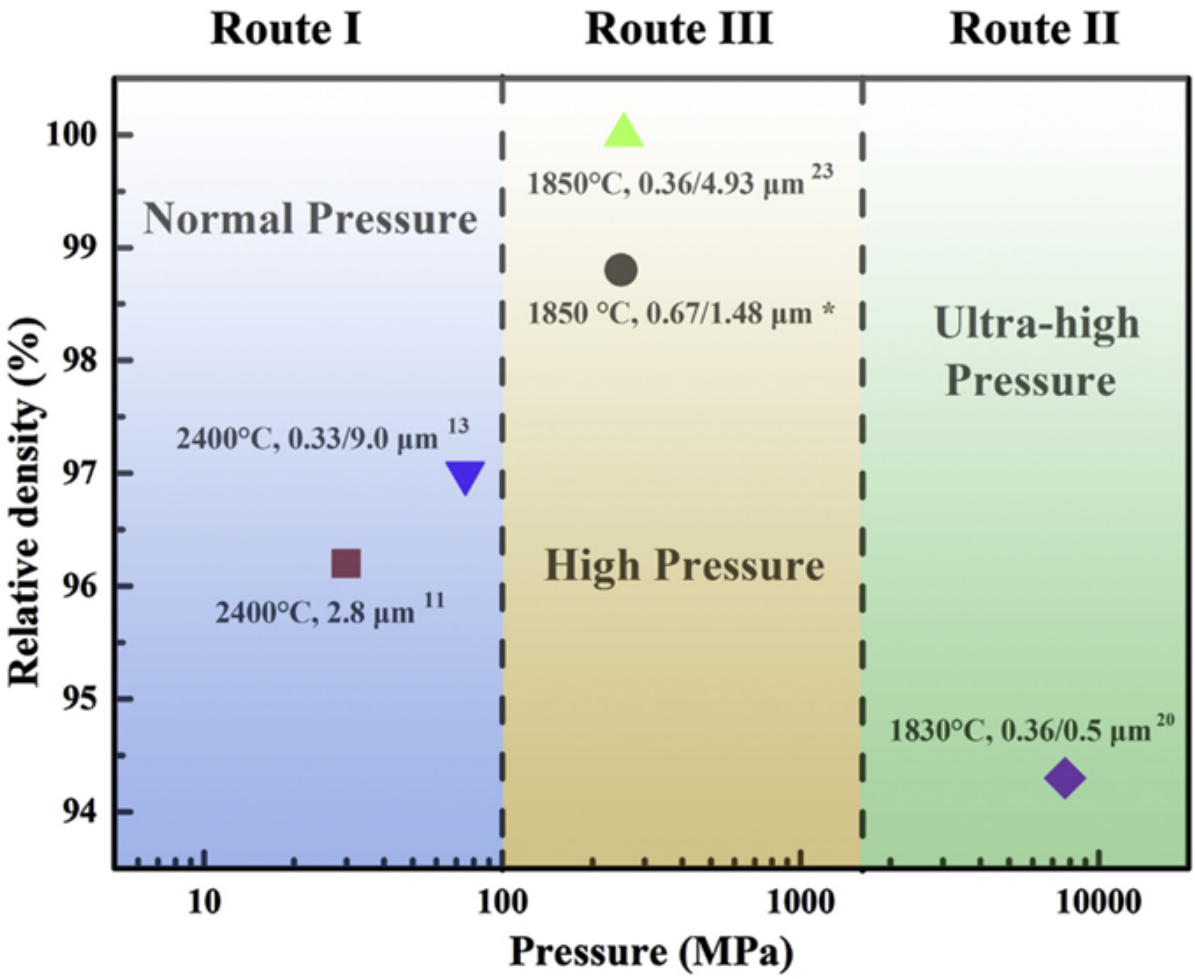


Figure 2.47: An overview of the relative density and the average grain size of TaC ceramics prepared with application of different mechanical pressures. [64].

shows that increasing pressure, up to a certain level, dramatically increased the relative density. After about 50 MPa, an increase of pressure did not lead to a significant increase in the relative density of B_4C at 1700 °C with a 5 minute hold time. The rate of change of the displacement (**Figures 2.48b and c**) show that there was an appreciable change in densification between 30 MPa and 50 MPa at 1700 °C and a similar change in densification between 1700 °C and 1800 °C at 80 MPa. **Figure 2.49** shows that, at a fixed pressure and hold time, there was a certain temperature (T_d) after which there was a significant increase in the densification rate. Additionally, there was a critical temperature (T_g) at which the grain growth began to rapidly increase. In most cases, T_d is less than T_g, which leaves a region below T_g where a high relative density can be achieved with minimal grain growth, labeled in **Figure 2.49** as "M".

In a similar approach, Zheng et al. studied the densification and grain growth of TaC ceramics consolidated using high pressure SPS. TaC powder was sintered at temperatures ranging from 1500 °C to 2000 °C at 50 MPa and 200 MPa for a constant hold time of 5 minutes. The relative density was compared to the grain size of the samples sintered at different temperatures and pressures, shown in **Figure 2.50**. TaC samples sintered at 200 MPa reached higher relative densities at much lower temperatures than the samples sintered at 50 MPa. At elevated temperatures, the grain growth increased sharply; however, by reaching nearly full density at lower temperatures, the high pressure samples minimized the grain growth. While sintering at higher pressures, plastic deformation becomes the leading densification mechanism.

Figure 2.51a shows the effect of plastic deformation on powder compact densification. The relationships of contact area diameter with compact force and relative density are shown in **Figure 2.51b and c**, respectively. At a higher pressure and lower temperature, the diameter of the TaC sample was larger with an equivalent contact force, leading to a higher relative density than the lower pressure, higher temperature sample. Plastic deformation under higher sintering pressures was shown to lead to more fully dense samples with limited grain growth.

An analogous approach was taken by Liu et al. investigating the sintering and densification mechanisms of TaC prepared via SPS using a multi-phased method. At first, the

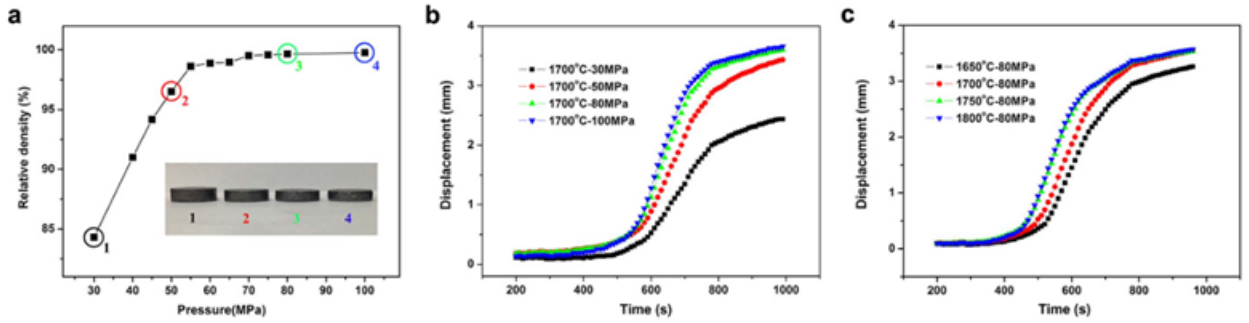


Figure 2.48: The effects of pressure and temperature on the densification of B_4C powders. (a) The relative density as a function of pressure at 1,700 °C soaking for 5 min. (b) The sintering curves with different pressures at 1,700 °C. (c) The sintering curves with different temperatures under 80 MPa [65].

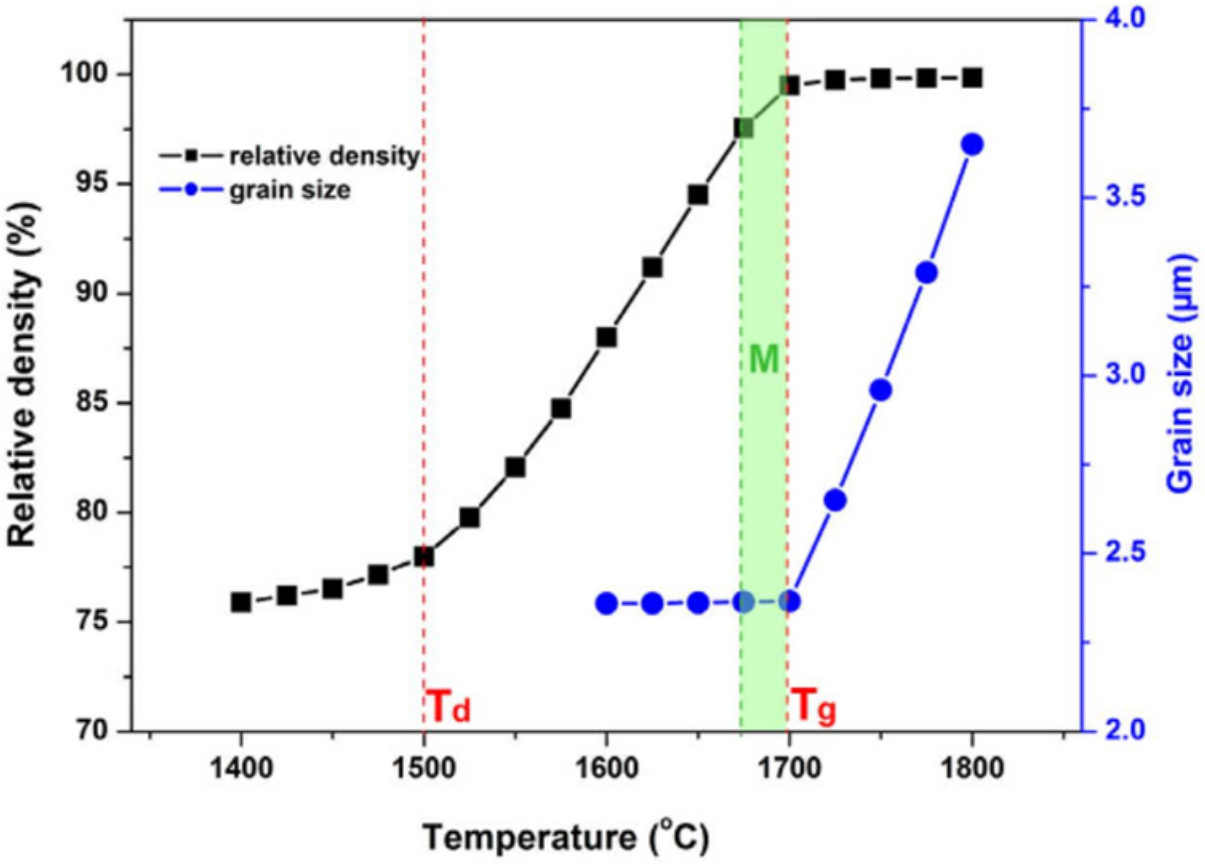


Figure 2.49: Relative density and grain size of B_4C as a function of temperature, sintered under 80 MPa, with soaking for 5 min [65].

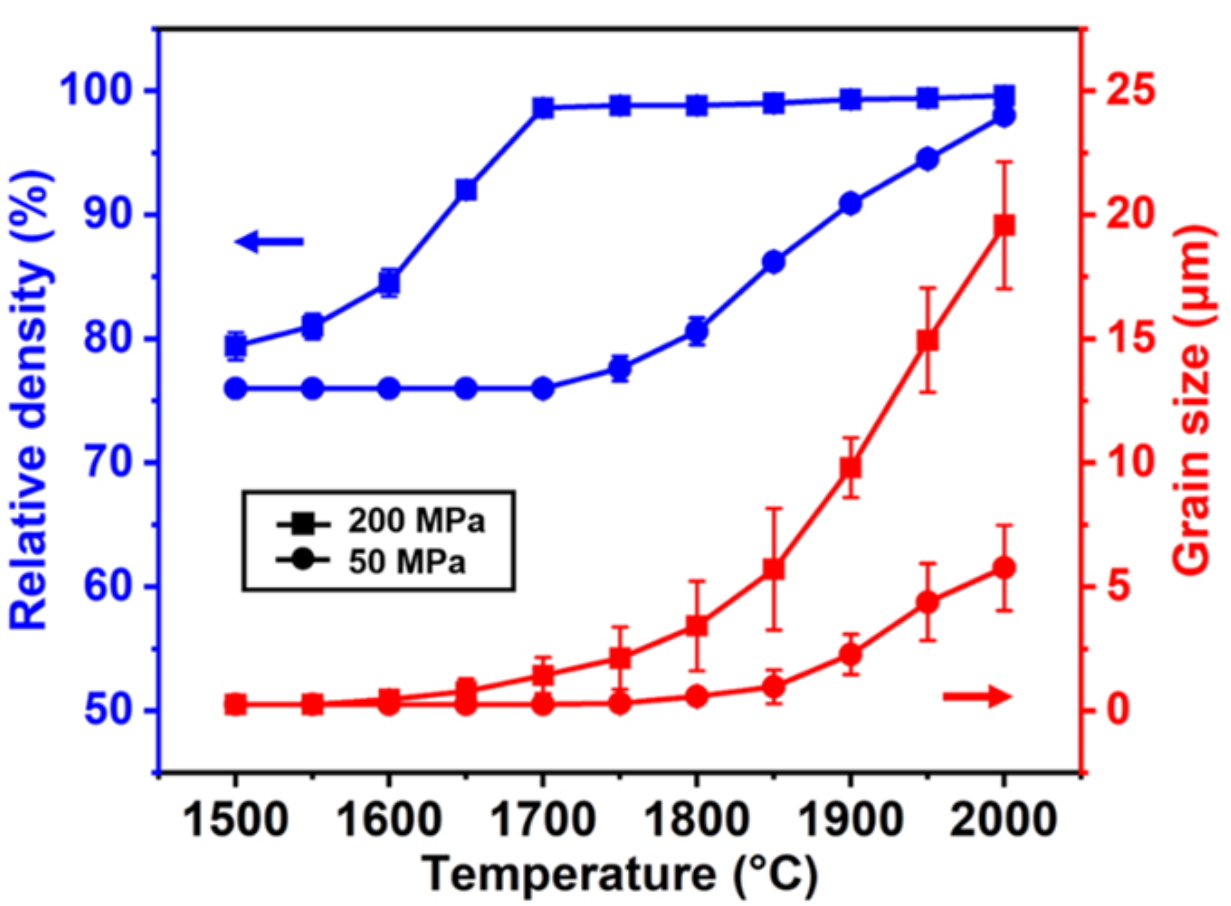


Figure 2.50: Densification and grain growth curves of TaC ceramics under different sintering conditions [66].

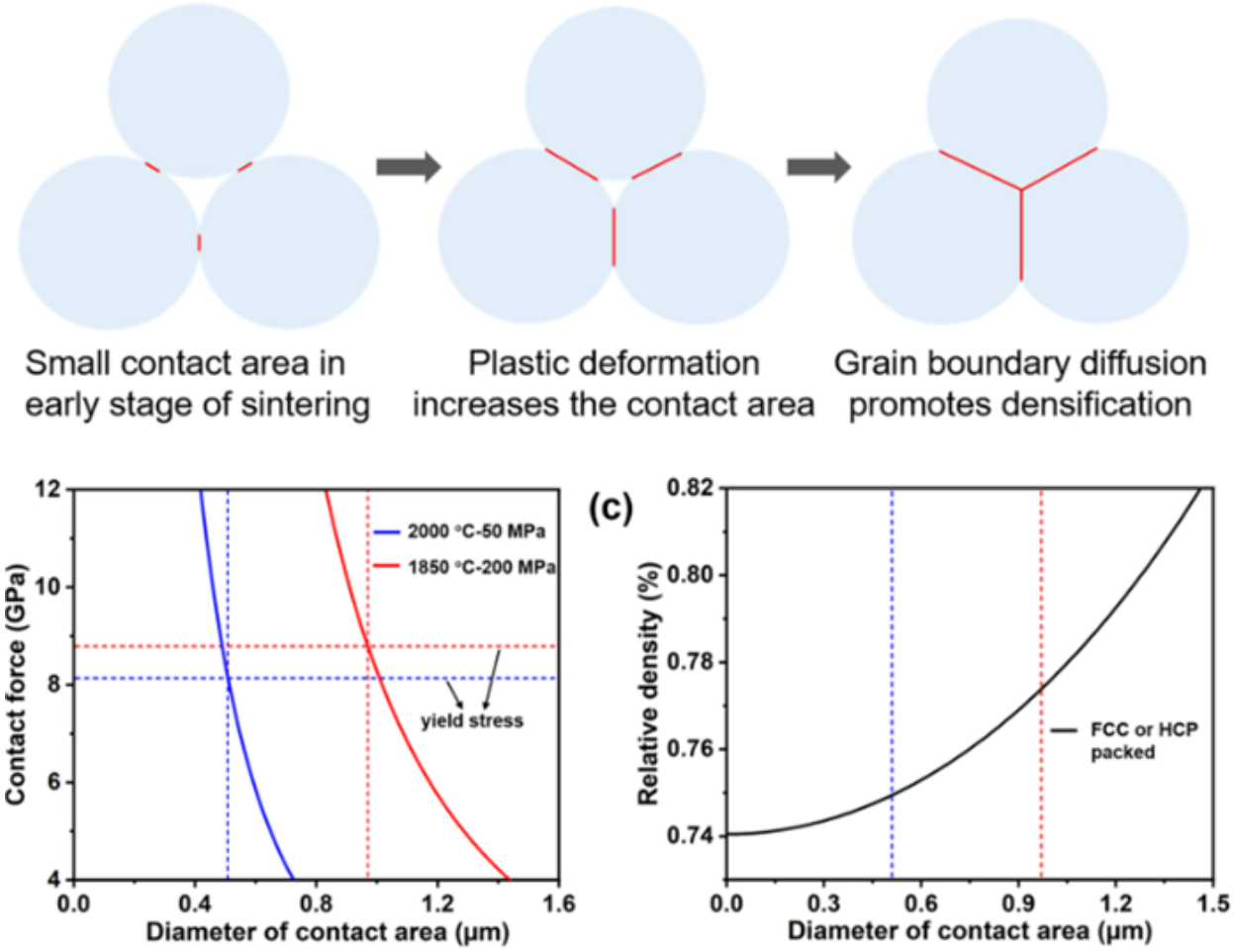


Figure 2.51: (a) Sintering diagram with plastic deformation as the dominant densification mechanism in high-pressure sintering; (b) Relationship between the contact force and the correspondingdiameter of contact area; (c) Relationship between the relative density and the diameter of contact area (Blue represents 2000 °C-50 MPa sintered sample; Red represents 1850 °C-200 MPa sintered sample) [66].

pressure and hold times were held constant at 80 MPa and 5 minutes respectively, while the sintering temperature of the sample was increased. As the sintering temperature increased, the powders changed from a spherical shape to a polyhedral shape (**Figure 2.52a-d**) and relative density increased from under 73% at 1600 °C to almost 98% at 1900 °C. The relative density was compared to the grain size in **Figure 2.52e** and at 1800 °C, the sample reached near full density before rapid grain growth had occurred.

The next phase of the study used a constant pressure and temperature of 80 MPa and 1800 °C while varying the hold times. **Figure 2.53a-e** shows the decreasing porosity as the hold time was increased. The comparison of hold time versus relative density (**Figure 2.53g**) shows that after a hold time of 10 minutes, the sample was near fully dense with relatively minimal grain growth.

The last phase of this study changed the applied sintering pressure and used the constant sintering temperature (1800 °C) and hold time (10 minutes) that was determined to lead to high relatively dense samples with minimal grain growth. **Figure 2.54** shows that the increasing pressure led to higher relative densities and grain sizes.

In order to clarify the densification of the TaC samples under increasing pressures, the relative density and densification rates were compared to the temperature during sintering, as seen in **Figure 2.55a and b**, respectively. During the initial sintering (stage I), the relative density of the samples at different pressures were approximately constant. After a certain temperature, the densification increased rapidly (stage II) while temperature increased. During the constant temperature hold (stage III), the lower pressure samples reached a maximum densification rate at an increasingly longer hold time.

The hold times were compared to relative density at various temperatures (**Figure 2.56a**). Increasing temperature resulted in a higher relative density, independent of hold time. The comparison of relative density and grain size of samples sintered at various temperatures is shown in **Figure 2.56b**. Regardless of sintering temperature, the grain size was constant until a relative density of about 90% was reached. As the sintering temperature increased, the hold time at which rapid grain growth occurred decreased. The densification activation energy was calculated to be approximately 252.94 kJ/mol using **Equation 2.1** and a linear fit to the data in **Figure 2.57**.

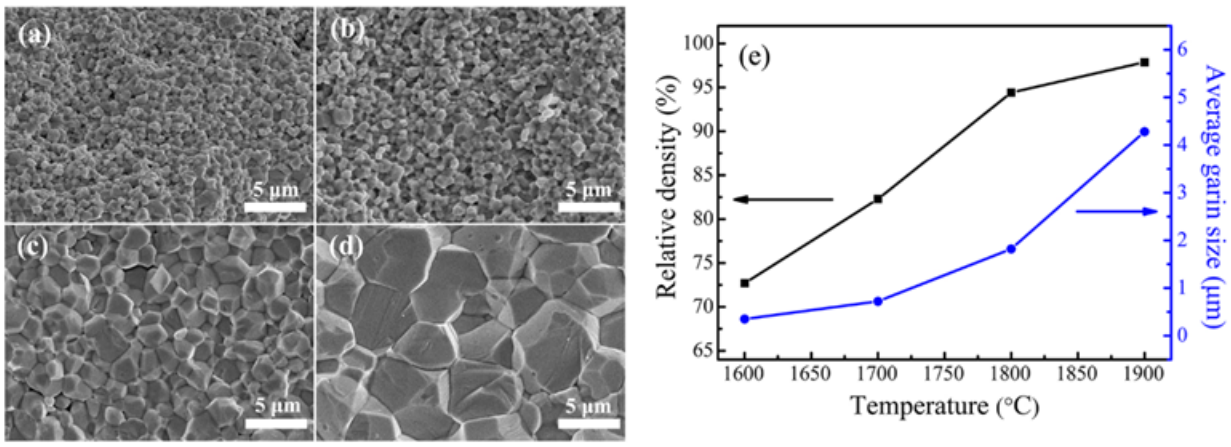


Figure 2.52: SEM micrographs of TaC sample sintered at different temperatures under 80 MPa for 5 min (a-d): (a) 1600 °C, (b) 1700 °C, (c) 1800 °C, (d) 1900 °C; evolution of the relative density and average grain size as a function of temperature (e) [67].

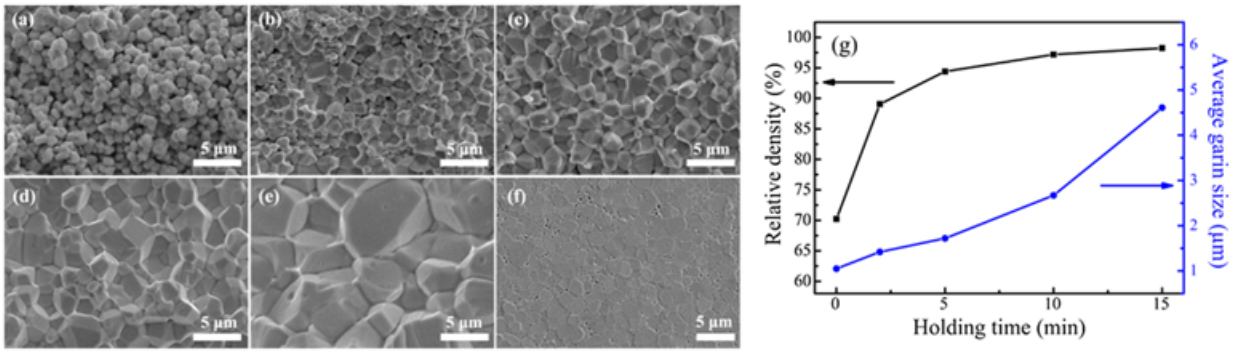


Figure 2.53: SEM micrographs of TaC sample sintered at 1800 °C for different holding times (a-d): (a) 0min, (b) 2 min, (c) 5 min, (d) 10 min, (e) 15 min; the polished surface of the specimen prepared at 1800 °C for 10 min after thermal etch (f); effects of holding time on the relative density and average grain size of TaC ceramics sintered at 1800 °C (g) [67].

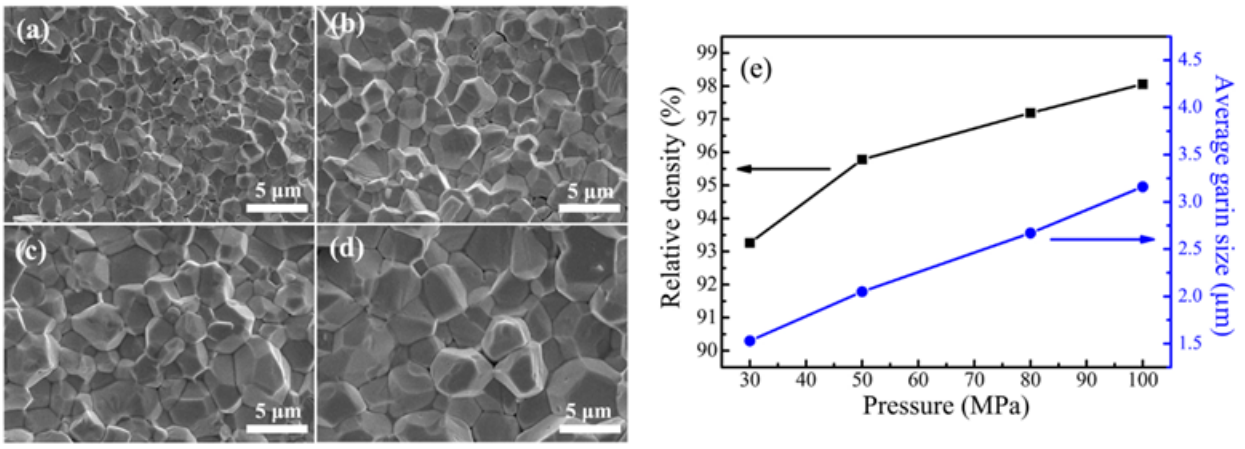


Figure 2.54: SEM micrographs of TaC samples sintered at 1800 °C under different pressures (a-d): (a) 30 MPa, (b) 50 MPa, (c) 80 MPa, (d) 100 MPa; relative density and average grain size of TaC samples sintered at 1800 °C as a function of pressure (e) [67].

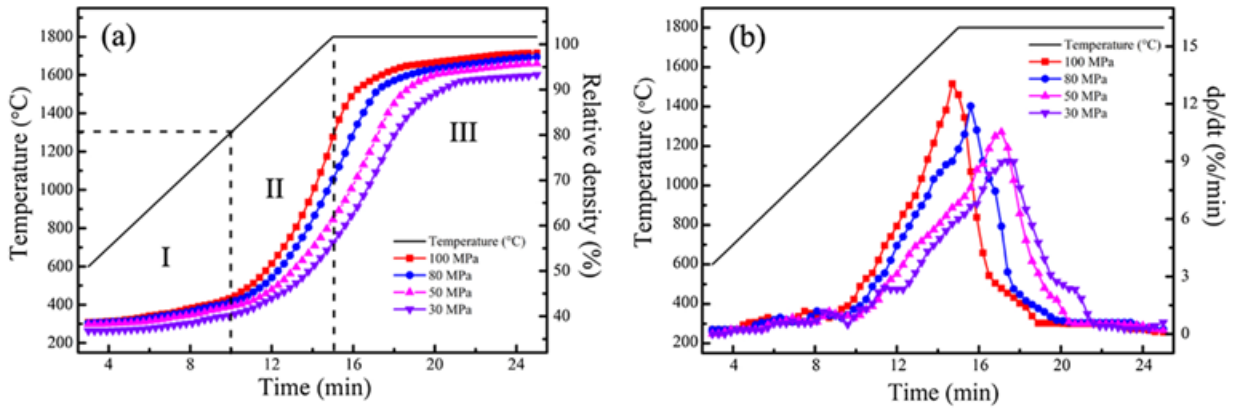


Figure 2.55: Densification curves (a) and the corresponding densification rate curves (b) of TaC samples sintered at 1800 °C for 10 min under different pressures [67].

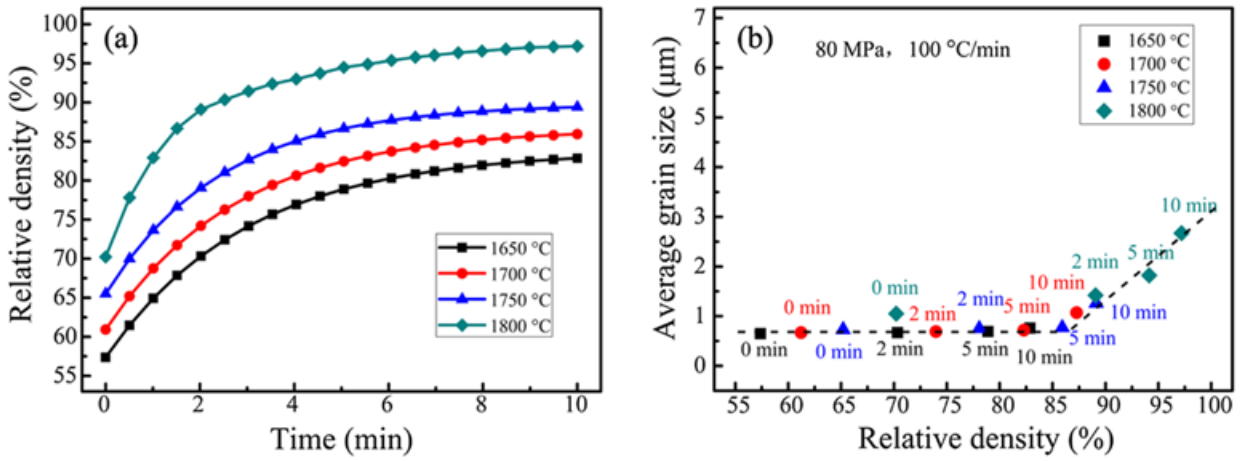


Figure 2.56: Densification curves of TaC samples during SPS at different temperatures for a holding time of 10 min (a); the average grain size/relative density trajectory (b) [67].

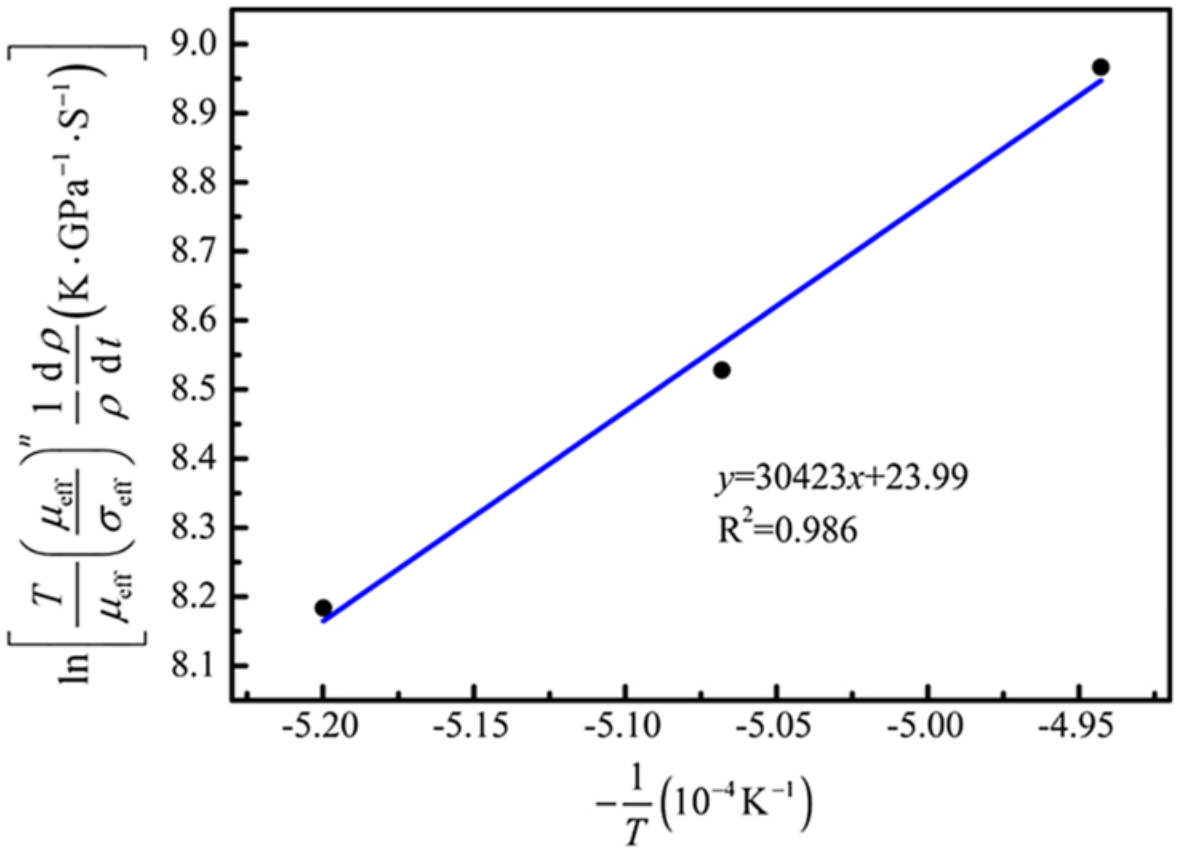


Figure 2.57: Apparent activation energy for densification of TaC powder [67].

$$\ln\left[\frac{T}{\mu_{eff}}\left(\frac{\mu_{eff}}{\sigma_{eff}}\right)^{n}\frac{1}{\rho}\frac{d\rho}{dt}\right] = -\frac{Q_d}{RT} + K \tag{2.1}$$

Equation 2.2 was used to define the grain growth where t is the time, G_{t} and G_0 are the grain sizes at times t and $t = 0$, respectively, p is the grain growth exponent (with possible values of 2, 3, and 4), and K is a variable that can be assumed constant at constant temperatures. **Figure 2.58** shows the relationship between $G_t^p - G_0^p$ and time, where the slope of the linear fitted line is the densification activation energy. The higher linear regression coefficients for the grain growth exponents of 2 and 3 suggest that the grain growth mechanisms were grain boundary diffusion and lattice diffusion (for p = 2 and p = 3, respectively).

$$G_t^p - G_0^p = Kt \tag{2.2}$$

By taking a rigorous, multi-phased approach, Lui et al. were able to determine the SPS conditions (hold time, pressure, and temperature) leading to sintering and densification of TaC with minimal grain growth as well as calculating the densification activation energy and determining the primary grain growth mechanisms.

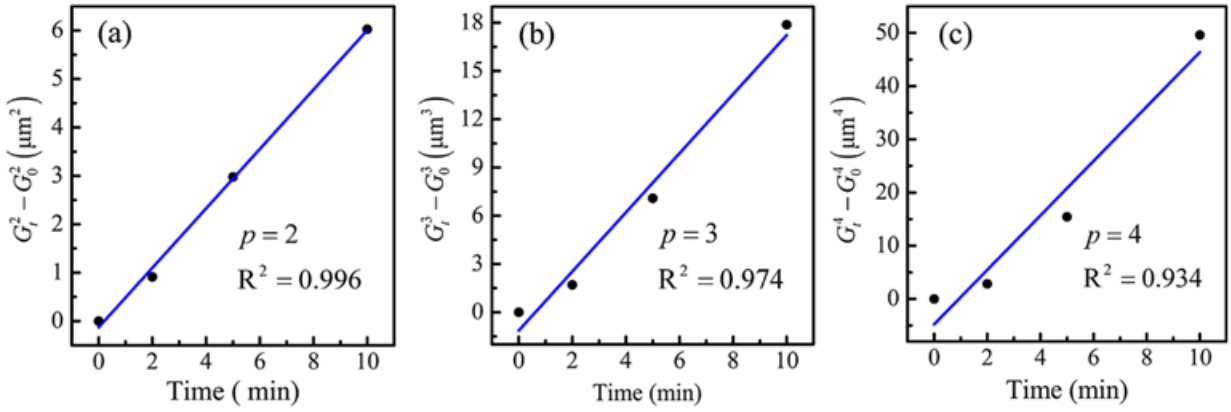


Figure 2.58: Relationship between $G_t^p - G_0^p$ and t for different grain size exponents: (a) p = 2, (b) p = 3, (c) p = 4 [67].

Chapter 3

Methods

3.1 Experimental Methods

3.1.1 Powder Characterization

NbC, TaC, and ZrC powders were sourced from Stanford Advanced Materials (SAM) which reported, for all three powders, an average particle diameter of about 1 μm and a purity of 99.5%. The Malvern Mastersizer 3000 Laser Diffraction Particle Size Analyzer, located in the Laboratory of Environmental Archaeology at the University of Tennessee, Knoxville (UTK), was used to quantify the particle size distribution of the NbC, TaC, and ZrC powders. Scanning Electron Microscopy (SEM) micrographs of each powder were acquired using a Zeiss Auriga SEM with the Everhardt-Thornley secondary electron detector and the in-lens electron detector, which was performed at the Institute for Advanced Materials and Manufacturing (IAMM) at UTK. All powder SEM micrographs captured were secondary electron images or in-lens electron images taken at 2 kV with a 30 μm aperture at a working distance of 2 mm. Additionally, X-ray fluorescence (XRF) spectrometry was performed at IAMM utilizing a Malvern PANalytical Epsilon 1 XRF spectrometer setup using a silver (Ag) radiation source and was used to characterize the powders. High resolution XRD was performed by Dr. David Sprouster at the X-ray Powder Diffraction (XPD) Beamline at the National Synchrotron Light Source-II using a monochromatic X-ray energy of 74 keV and data reduction was performed using PyFai software. LECO combustion analysis was

performed at the Advanced Materials Laboratory (AML) located at Boise State University (BSU) and at the NASA Glenn Research Center (GRC). Due to equipment failures, the LECO carbon analysis was performed at BSU and the LECO oxygen and nitrogen analyses were performed at NASA GRC.

3.1.2 Sample Preparation and Consolidation

A mixture of 80 atomic percent (at%) ZrC, 10 at% NbC, and 10 at% TaC was used to make the tri-carbide samples. The mono-carbide powders were weighed and mixed in a solution of isopropyl alcohol, with a 1:1 ratio of grams of powder to milliliters of isopropyl alcohol. Due to its tendency to form large agglomerations, the TaC powder was first mixed using a mortar and pestle before being added to the powder mixture. The slurry was then blended in a FlackTek Inc. SpeedMixer, model DAC 1100.1 FVZ-HV for 2.5 minutes alternating between speeds of 1600 and 800 RPM for 30 seconds each. The mixture was then placed in a drying oven at 100 °C overnight to evaporate the isopropyl alcohol and any entrained water vapor.

For each sample, 5 grams of powder mixture was loaded into a graphite die, with an inner diameter of 13.5 mm, that was lined with grafoil. The standard graphite dies and punches were made from ET-10 grade graphite sourced from IBIDEN. In some cases, such as high pressure sintering runs, alternative die and punches, made from isotropic graphite grade G540, were used. The properties of these two grades of graphite are listed in **Table 3.1**. The standard graphite tooling, constructed of grade ET-10 graphite from IBIDEN, was designed for SPS runs up to 50 MPa at 2000 °C. The high pressure graphite tooling, made of G540 grade graphite from CalNano, was designed for SPS runs up to 100 MPa at 2000 °C. Note that the G540 grade graphite, that constructs the high pressure die and punches, has a slightly higher electrical resistance and a lower thermal conductivity.

The graphite punches were inserted into each end of the graphite die and the assembly was loaded into the SPS chamber. All powders were consolidated in a LABOX-675-FC, NJS Co. Ltd SPS machine in pulsed electric current sintering mode using the default 40:7 on:off DC pulse (**Figure 3.1**). All samples were heated at a rate of 100 °C/min. A vacuum of 5 Pa was established at the beginning of the run and a uniaxial pressure was applied ranging

Table 3.1: Graphite grade comparison of SPS tooling

Description	**Grade of Graphite**	**Vendor**	**Max Press. at 2000 °C (MPa)**	**El. Resist. ($\mu\Omega$m)**	**Thermal Cond. (W/mK)**
Standard	ET-10	IBIDEN	50	14.0	104.4
High Pressure	G540	CalNano	100	15.0	93

from 10 MPa to 90 MPa. In general, for samples sintered at or above 60 MPa, the SPS chamber was often filled with an argon purge gas, instead of being held at a vacuum, to reduce the chemical erosion on the graphite die. Unless otherwise noted, standard graphite dies and punches were used in a vacuum during sintering. The samples were sintered at temperatures ranging from 1800 °C to 2100 °C and soaking times ranging from 1 to 20 minutes. The temperature was measured via pyrometer directed at a recessed area on the surface of the graphite die. The SPS automatically recorded the time, temperature, pressure, displacement, displacement rate, voltage, and current during sintering operations.

3.1.3 Sample Characterization

The height and diameter of each sample were measured using calipers; readings were taken at five locations on the sample and averaged for both the height and diameter measurements. The final sintered height of each sample was typically around 5 mm. Densities were determined using the Archimedes technique in room temperature water; the dry mass, soaked mass, and submerged mass were measured and used in the density calculation. The soaked mass was obtained by soaking the sintered samples in a beaker of distilled water and sonicating for at least three minutes. After the beaker was removed from the sonicator, the excess moisture was then removed from the sample using a damp cloth. The submerged mass was measured using an Archimedes density kit, which measures the mass of the sample when fully under water.

The samples were mounted in epoxy and polished before XRD and SEM were performed. The general polishing procedure is listed in **Table 3.2**. An automatic polisher, the Pace Technologies FEMTO-1500, was used to polish samples down to 1 μm. To produce grain boundary resolution for secondary electron imaging, a Buehler LTD Vibromet Polisher was used with a 0.05 μm colloidal silica solution.

XRD was performed at IAMM utilizing a Malvern PANalytical Empyrean diffractometer setup with a PIXcel3D area detector using a Cu-Kα radiation source and was used to characterize consolidated samples. SEM of sintered samples was performed at IAMM using a Zeiss Auriga SEM with the Everhardt-Thornley secondary electron detector and the in-lens electron detector. All micrographs captured were secondary electron images or in-lens



Figure 3.1: SPS Furnace at UTK.

Table 3.2: Polishing Procedure

Step	Description
1	Polish for 15 min. with 250 μm Pace Tech. metal bonded diamond grinding disk
2	Polish for 15 min. with 30 μm Pace Tech. diamond grinding disk
3	Polish for 15 min. with 15 μm Pace Tech. metal bonded diamond grinding disk
4	Polish for 60-75 min. at 5 μm on a Struers MD-Piano 4000
5	Sonicate for 5 min. to remove any debris
6	Polish for 5 min. in 3 μm diamond solution on a TRICOTE polishing pad
7	Sonicate for 5 min. to remove any debris
8	Polish for 15 min. in 1 μm diamond solution on a TRICOTE polishing pad
9	Sonicate for 5 min. to remove any debris
10	Wipe with a wet cotton ball under running water
11	Polish for 4-5 hours vibratory polish in 0.05 μm colloidal silica solution
12	Sonicate for 10 min. to remove any debris
13	Wipe with a wet cotton ball under running water

electron images taken at 2 kV with a 30 μm aperture at a working distance of 2 mm. The SEM micrographs were used to determine grain sizes using the ASTM E112-13 Heyn Lineal Intercept Procedure. Energy dispersive X-ray spectroscopy (EDS) was performed at IAMM using a Helios 5 dual beam FIB/SEM and EDAX software. A Wilson® Hardness TUKON™ 1102 tester with a load of 0.5 kilogram (kg) was used to measure the Vicker's hardness of the samples. Raman spectroscopy was performed at Oak Ridge National Laboratory (ORNL) by Dr. Eddie Lopez Honorato.

3.2 Sintering Activation Energy Methods

3.2.1 Bernard-Granger and Guizard Method

A method of determining the sintering activation energy and driving mechanism for sintering, based on creep rate and first introduced by Bernard-Granger and Guizard, is shown below. The equation for creep rate [68], and the baseline equation for this method of calculating sintering activation energy, is:

$$\dot{\varepsilon} = \frac{d\varepsilon}{dt} = A\frac{D\mu b}{kT}\left(\frac{b}{G}\right)^m\left(\frac{\sigma}{\mu}\right)^n \tag{3.1}$$

Where $\dot{\varepsilon}$ is the creep rate, t is the time, A is a constant, D is the diffusion coefficient, μ is the shear modulus, b is the Burgers vector, k is Boltzmann's constant, T is the absolute temperature, G is the grain size, m is the grain size exponent, σ is the macroscopic applied stress, and n is the stress exponent.

The high temperature creep rate can be used to describe the matter transport occurring during SPS densification [67, 68, 69, 70]. Creep rate can be defined as the linear strain rate [57] which, for SPS consolidation, is equivalent to the densification rate due to the nature of the uniaxial displacement during densification. Therefore, using the Bernard-Granger model [68], the relationship describing the densification rate during SPS is the following:

$$\frac{1}{\rho}\frac{d\rho}{dt} = B\frac{D\mu_{eff}b}{kT}\left(\frac{b}{G}\right)^m\left(\frac{\sigma_{eff}}{\mu_{eff}}\right)^n \tag{3.2}$$

Where ρ is the instantaneous relative density, B is a constant, μ_{eff} is the instantaneous effective shear modulus of the powder bed, and σ_{eff} is the instantaneous effective stress acting on the powder bed.

Given the displacement data recorded during SPS consolidation, the relationship between instantaneous sample height and density can be described by the following equation [68]:

$$\rho = \left(\frac{L_f}{L}\right)\rho_f \tag{3.3}$$

where L_f is the final height, L is the instantaneous height, and ρ_f is the final relative density.

Continuing to follow the Bernard-Granger model [68], the instantaneous effective stress acting on the powder bed can be described by:

$$\sigma_{eff} = \frac{(1-\rho_0)}{\rho^2(\rho-\rho_0)}\sigma_{mac} \tag{3.4}$$

Where ρ_0 is the green density and σ_{mac} is the macroscopic compaction pressure applied to the powder bed. For the calculation of sintering activation energy in this study, the macroscopic compaction pressure, or the applied SPS pressure during sintering, was 30 MPa.

The instantaneous effective shear modulus of the powder bed is:

$$\mu_{eff} = \frac{E_{th}}{2(1+\nu_{eff})}\frac{\rho-\rho_0}{1-\rho_0} \tag{3.5}$$

Where E_{th} is the Young's modulus of the theoretically dense material and ν_{eff} is the effective Poisson's ratio. Values of E_{th} and ν_{eff} for NbC, TaC, and ZrC were taken to be 488 GPa, 537 GPa, and 397 GPa, respectively, and 0.22, 0.24, and 0.2, respectively [71, 72] and are shown in **Table 3.3**.

The diffusion coefficient is given by the following:

$$D = D_0 \exp\left(-\frac{Q_d}{RT}\right) \tag{3.6}$$

Table 3.3: Values for Elastic Moduli and Poisson's Ratios

Material	E_{th} **(GPa)**	ν	**Additional Reference Values [73]**
NbC	488[a]	0.22[a]	C/Nb=0.96-0.99, E=370-518 GPa and ν=0.21-0.24
TaC	537[a]	0.24[a]	C/Ta=0.96-0.99, E=515-567 GPa and ν=0.21-0.26
ZrC	397[b]	0.20[b]	C/Zr=0.78-0.98, E=300-452 GPa and ν=0.16-0.25
(ZrNbTa)C	474[c]	0.22[c]	N/A

[a] *[71] Properties were corrected to relative density*

[b] *[72] Determined using impulse excitation*

[c] *Calculated using rule of mixtures with the values for NbC, TaC, ZrC in the table*

Where D_0 is a constant pre-exponential factor, Q_d is the apparent activation energy of the controlling mechanism of densification, and R is the universal gas constant. **Equations 3.4, 3.5, and 3.6** can then be used to transform **Equation 3.2** into:

$$\frac{1}{\mu_{eff}}\frac{1}{\rho}\frac{d\rho}{dt} = K\frac{\exp\left(-\frac{Q_d}{RT}\right)}{T}\left(\frac{b}{G}\right)^m\left(\frac{\sigma_{eff}}{\mu_{eff}}\right)^n \tag{3.7}$$

Where $K = B\frac{D_0 b}{k}$ is a constant.

By analyzing samples with constant grain size and taking the natural log of both sides after rearranging, the Bernard-Granger model [68] results in:

$$\ln\left(\frac{1}{\mu_{eff}}\frac{1}{\rho}\frac{d\rho}{dt}\right) = n\ln\left(\frac{\sigma_{eff}}{\mu_{eff}}\right) + K_0 \tag{3.8}$$

Where K_0 is a constant for a fixed soak temperature. The slope of the line that results from graphing **Equation 3.8** corresponds to the value of n.

By determining the relative density of each sample at a fixed densification rate, values of σ_{eff} and μ_{eff} can be determined. Then **Equation 3.7** can be rearranged to:

$$\ln\left[\frac{T}{\mu_{eff}}\left(\frac{\mu_{eff}}{\sigma_{eff}}\right)^n\frac{1}{\rho}\frac{d\rho}{dt}\right] = -\frac{Q_d}{RT} + K_1 \tag{3.9}$$

Where K_1 is a constant. The slope of the straight line drawn using the **Equation 3.9** corresponds to $-\frac{Q_d}{R}$, which can be solved to determine the value of the activation energy of the predominant densification mechanism.

3.2.2 Young-Cutler Method

An alternative method for calculating the sintering activation energy was proposed by Young and Cutler in 1970 [74]. This model focuses on the densification occurring during the heat up phase of sintering at a constant rate of heating (CRH). Refined from Frenkel's model for sintering [75] and a derivation by Johnson [76], this method uses an equation with volumetric and grain boundary diffusion components, shown below:

$$\left(\frac{\Delta L}{L_0}\right)^{2.06}\left(\frac{d\left(\frac{\Delta L}{L_0}\right)}{dt}\right)=\frac{2.63\gamma\Omega D_V\left(\frac{\Delta L}{L_0}\right)^{1.03}}{kTa^3}+\frac{0.7\gamma\Omega bD_B}{kTa^4} \tag{3.10}$$

where ΔL is the change in length, L_0 is the initial length, γ is the surface energy, Ω is the vacancy volume, bD_B is the grain boundary diffusion coefficient (equal to $bD_{0B}\exp\left(-\frac{Q}{RT}\right)$), D_V is the volume diffusion coefficient (equal to $D_{0V}\exp\left(-\frac{Q}{RT}\right)$), t is the time, T is the absolute temperature, k is the Boltzmann constant, and a is the radius of the particles. This method assumes that the powder particles are spherical.

To simplify, **Equation 3.10** was separated out into volumetric and grain boundary diffusion dominate forms and set $T = ct$:

$$T\left(\frac{\Delta L}{L_0}\right)^{1.03}\left(\frac{d\left(\frac{\Delta L}{L_0}\right)}{dT}\right)=\frac{2.63\gamma\Omega D_V}{ka^3c}\ (volumetric) \tag{3.11}$$

$$T\left(\frac{\Delta L}{L_0}\right)^{2.06}\left(\frac{d\left(\frac{\Delta L}{L_0}\right)}{dT}\right)=\frac{0.7\gamma\Omega bD_B}{ka^4c}\ (grain\ boundary) \tag{3.12}$$

Through integration and then subsequent differentiation, with the assumption $Q/T^2 >> 1/T$, **Equations 3.11 and 3.12** transform into:

$$\frac{d\left(\frac{\Delta L}{L_0}\right)}{dT}\cong\left(\frac{5.34\gamma\Omega D_{0V}RT}{ka^3cQ}\right)^{\frac{1}{2}}\left(\frac{Q}{2RT^2}\right)\exp\left(-\frac{Q}{2RT}\right) \tag{3.13}$$

$$\frac{d\left(\frac{\Delta L}{L_0}\right)}{dT}\cong\left(\frac{2.14\gamma\Omega D_{0B}RT}{ka^4cQ}\right)^{\frac{1}{3}}\left(\frac{Q}{3RT^2}\right)\exp\left(-\frac{Q}{3RT}\right) \tag{3.14}$$

Equations 3.13 and 3.14, presented by Young and Cutler [74], can be condensed into the following equation:

$$T^m\left(\frac{d\left(\frac{\Delta L}{L_0}\right)}{dT}\right)\cong A^n\exp\left(-\frac{nQ}{RT}\right) \tag{3.15}$$

Where A is a constant encompassing all physical properties, m is a constant (3/2 for volumetric diffusion and 5/3 for grain boundary diffusion), and n is the activation energy

coefficient (1/2 for volumetric diffusion and 1/3 for grain boundary diffusion). By calculating the slope of the relationship below, equal to $-\frac{nQ}{mR}$, the activation energy can be determined:

$$\ln\left(T\frac{d\left(\frac{\Delta L}{L_0}\right)}{dT}\right) \cong \frac{n}{m}\ln(A) - \frac{nQ}{mRT} \tag{3.16}$$

3.3 Grain Growth Activation Energy

The grain growth activation energy can be determined by using the grain growth equation, shown below:

$$D_t^m - D_0^m = K_0 t \times \exp\left(-\frac{Q}{RT}\right) \tag{3.17}$$

Where t is the time, D_t is the grain size at time t, D_0 is the initial grain size, m is the grain growth exponent, K_0 is a constant, Q is the grain growth activation energy, R is the universal gas constant, and T is the temperature.

For a constant temperature, **Equation 3.17** can be simplified to the following:

$$D_t^m - D_0^m = K_1 t \tag{3.18}$$

Where the constant $K_1 = K_0 \exp\left(-\frac{Q}{RT}\right)$. Referencing **Equation 3.18**, $D_t^m - D_0^m$ can be graphed versus time at various values of m. The value of m with the highest coefficient of determination, r^2, corresponds to the primary grain growth mechanism.

For a constant hold time, **Equation 3.17** can be transformed into the following:

$$\ln(D_t^m - D_0^m) = \ln(K_0 t) - \frac{Q}{RT} \tag{3.19}$$

Where the slope of the graph of $\ln(D_t^m - D_0^m)$ versus $\frac{1}{T}$ is equal to $-\frac{Q}{R}$. Solving for Q results in the activation energy for a specific grain growth mechanism, determined by the value of m.

Chapter 4

Results

4.1 Powder Characterization

4.1.1 Particle Size Analysis

Powder SEM was performed on the NbC, TaC, and ZrC powders. **Figures 4.1a-c** show the morphology of the NbC, TaC, and ZrC powders, respectively. **Figure 4.2** shows the particle size distribution for the NbC, TaC, and ZrC with an average diameter of 1.45 μm, 1.60 μm, and 1.35 μm, respectively. **Figures 4.3a-c** are zoomed out views of the NbC, TaC, and ZrC powders showing the presence of agglomerations in the NbC and TaC powders. These agglomerations were measured and quantified in the particle size analyzer and shown in **Figure 4.4**.

4.1.2 Quantification of Impurities

The results of the XRF spectrometry are shown in **Table 4.1**. The metallic purity of the NbC, TaC, and ZrC powders was measured to be 99.7 wt% Nb, 99.1 wt% Ta, and 97.6 wt% Zr, respectively. For ZrC, the most significant impurity was hafnium, at 2.32 wt%. The ZrC powder was about 99.9% pure when accounting for 2.32% hafnium (Hf), which is naturally found with Zr (about 3% Hf on average), virtually identical to Zr chemically, and very difficult to separate from Zr [77]. LECO combustion analysis results for NbC, TaC, and ZrC powders are shown in **Table 4.2**. The NbC and ZrC powders contained greater than

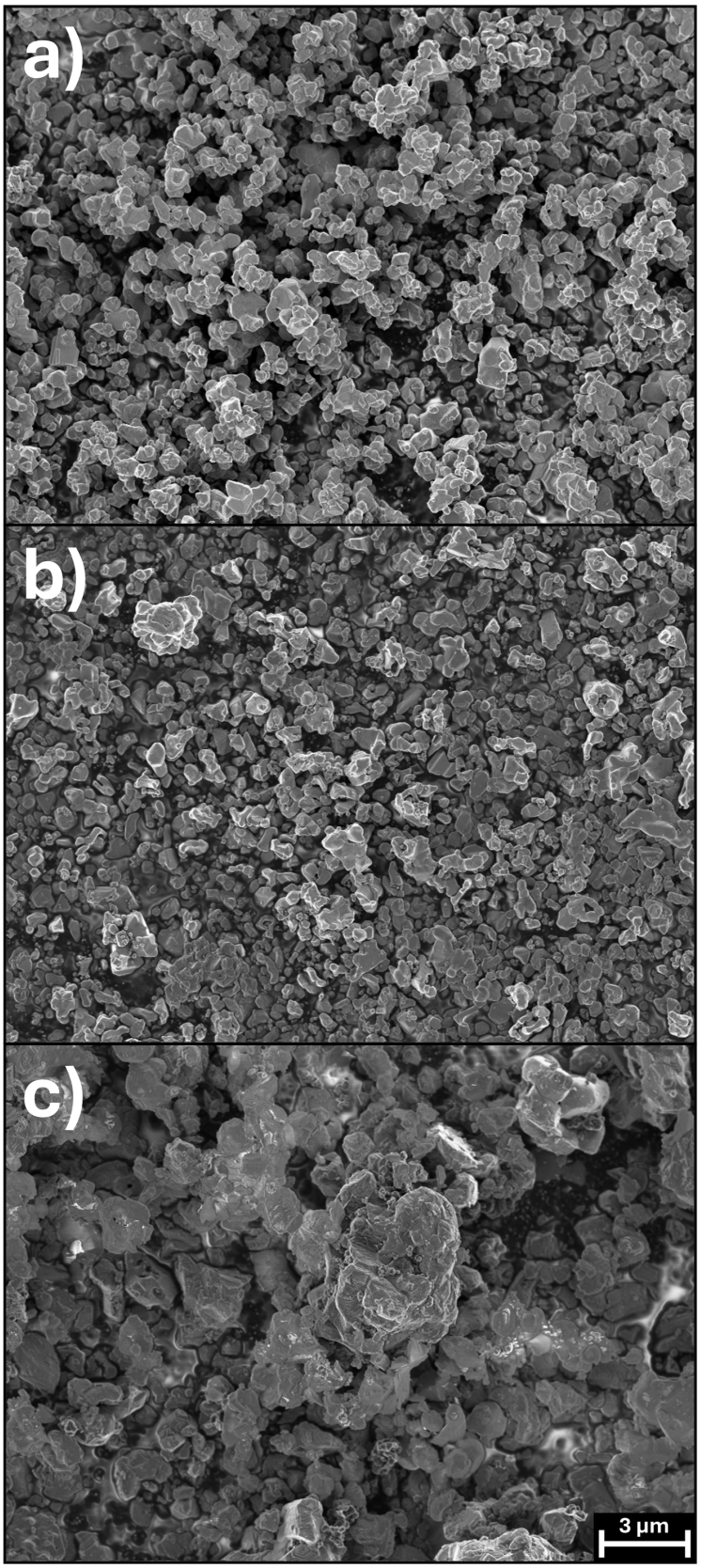


Figure 4.1: Powder morphology SEM micrographs of a) NbC, b) TaC, and c) ZrC powders.

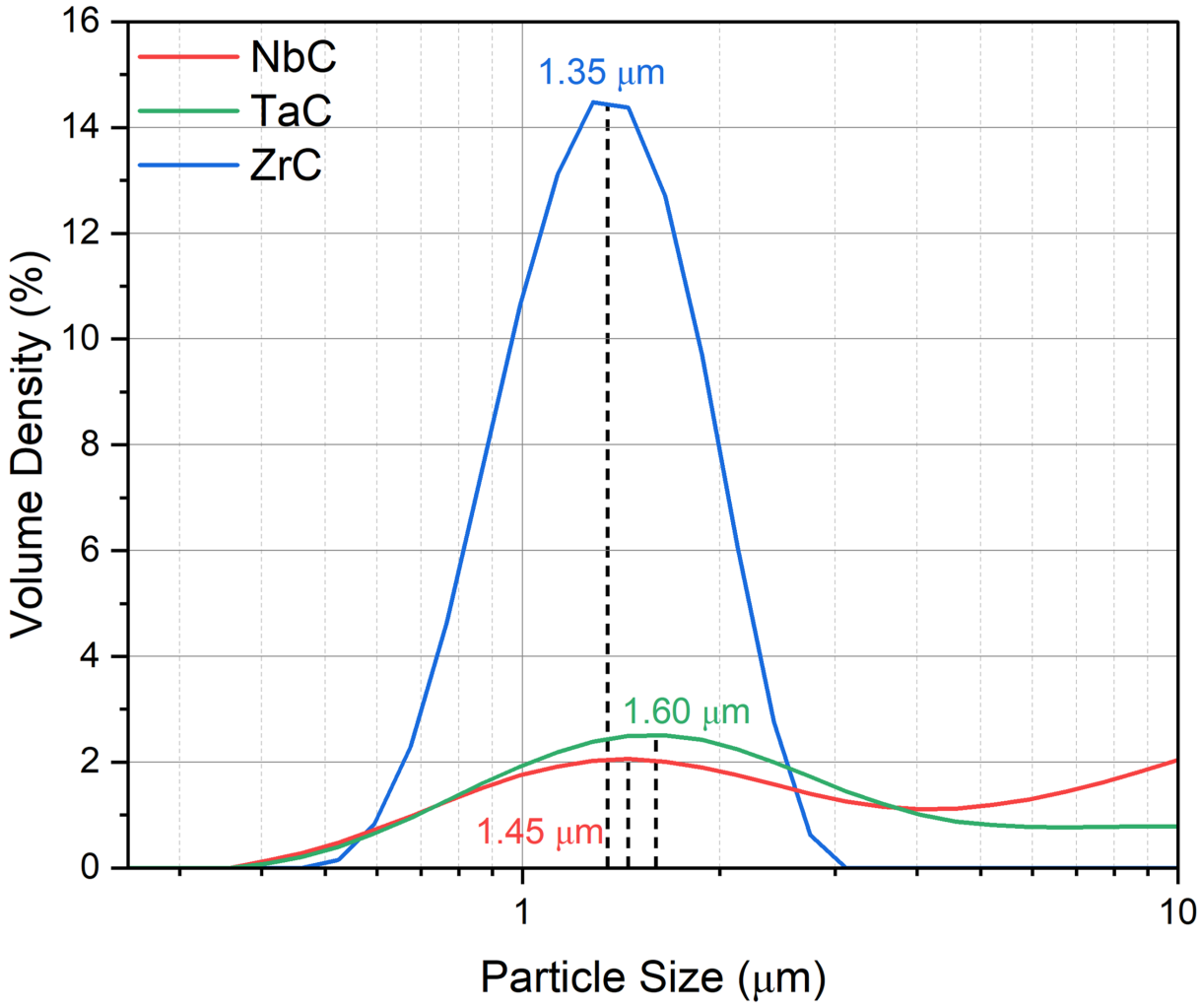


Figure 4.2: Particle size analysis results for NbC, TaC, and ZrC.

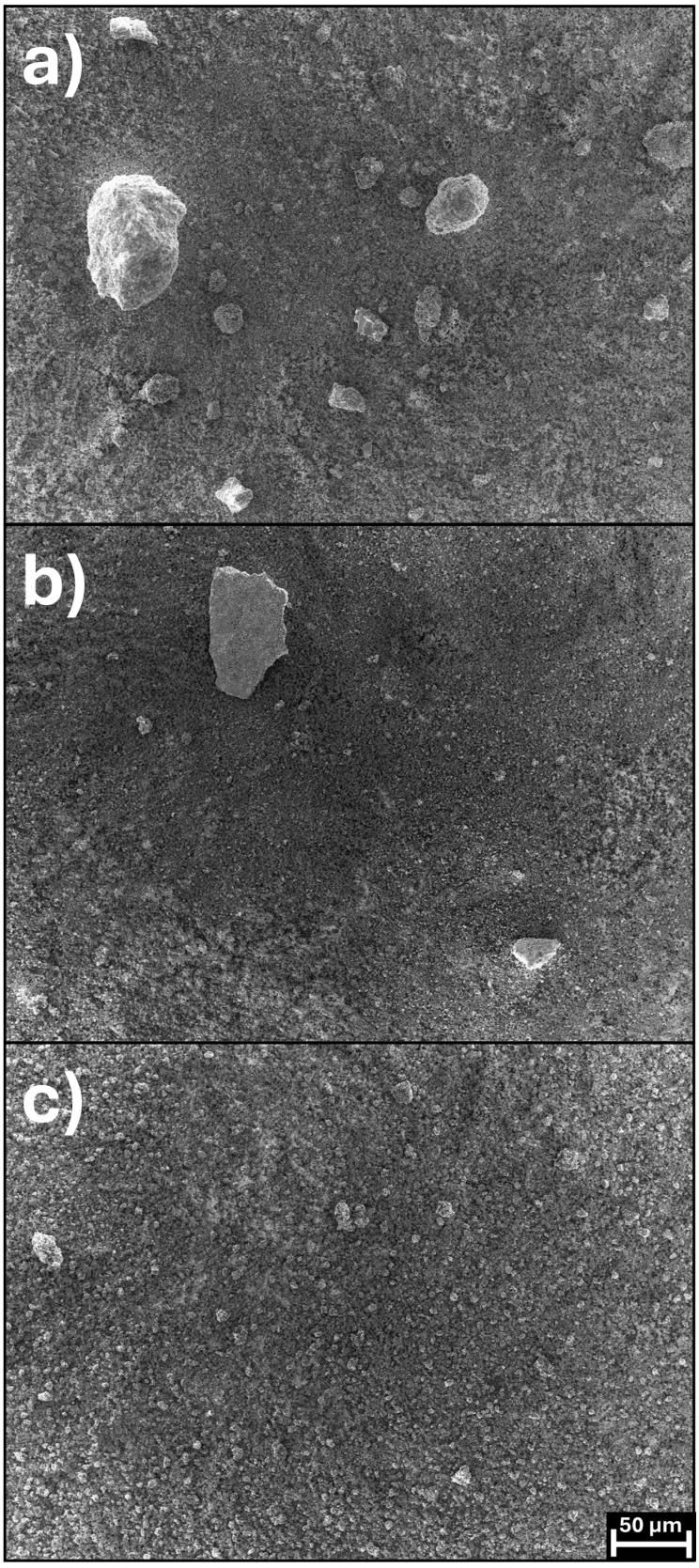


Figure 4.3: Powder agglomeration SEM micrographs of a) NbC, b) TaC, and c) ZrC powders.

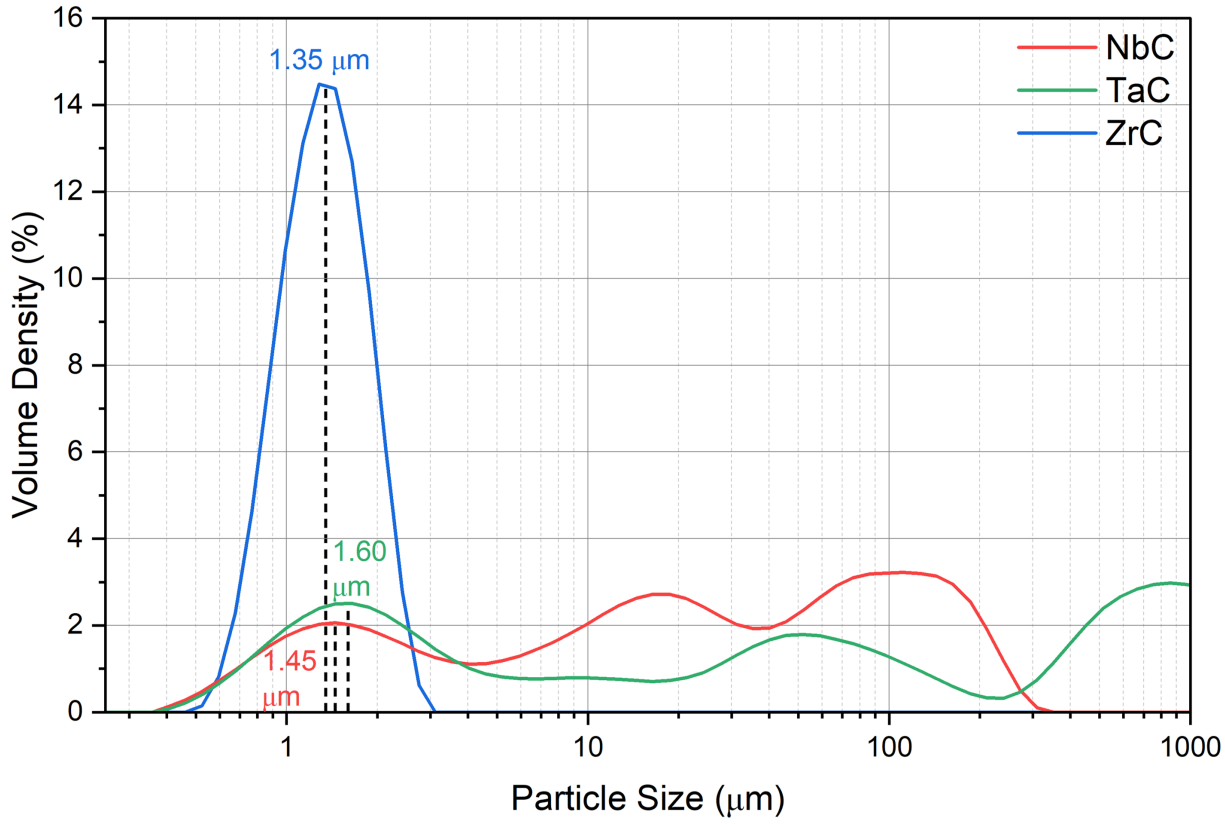


Figure 4.4: Particle size analysis results (including agglomerations) for NbC, TaC, and ZrC.

Table 4.1: XRF Results

Powder	Element (wt% or ppm)										
	Zr	**Nb**	**Ta**	**Ti**	**Mo**	**Hf**	**W**	**V**	**Cr**	**Fe**	**Ni**
NbC	0.114 %	99.7 %	0.054 %	19.1 ppm	-	186 ppm	-	59.8 ppm	215 ppm	411 ppm	78.5 ppm
TaC	35.7 ppm	0.099 %	99.1 %	77.1 ppm	369 ppm	0.324 %	0.389 %	18.3 ppm	283 ppm	80.0 ppm	142 ppm
ZrC	97.6 %	146 ppm	45.7 ppm	45.2 ppm	-	2.32 %	115 ppm	108 ppm	223 ppm	327 ppm	42.8 ppm

Table 4.2: LECO Results

Powder	**Element (wt%)**		
	C	**N**	**O**
NbC	11.8	0.012	1.39
TaC	6.43	0.003	0.119
ZrC	12.6	0.43	1.83

1 wt% oxygen. The TaC powder did not contain a significant amount of oxygen (about 0.1 wt%). All three powders contained an insignificant amount of nitrogen (less than 0.5 wt%).

The impurities in each powder, measured using high resolution XRD, are listed in **Table 4.3** with the associated fractional two theta angle and phase fraction. **Figures 4.5a-c** show the high resolution XRD and phase identification for NbC, TaC, and ZrC, respectively. Note that the y-axes are logarithmic scales. The NbC powder had small amounts (less than 1 wt%) of niobium oxide and zirconium oxide. The TaC powder had trace amounts (less than or equal to 0.1 wt%) of hafnium oxide. The ZrC had small amounts (about 0.3 wt%) of niobium oxide and zirconium oxides.

4.2 Phase 1

For the first phase of this project, ($Zr_{0.8}$, $Nb_{0.1}$, $Ta_{0.1}$)C samples were sintered at increasing temperatures from 1800 °C to 2100 °C. The relative densities, grain sizes, and Vickers hardness values are shown in **Table 4.4**. **Figure 4.6** shows secondary electron micrographs illustrating the grain growth and microstructural evolution of the ($Zr_{0.8}$, $Nb_{0.1}$, $Ta_{0.1}$)C samples. Significant densification occurred between 1800 °C and 1950 °C and visible grain coarsening started at 2000 °C and continued through 2100 °C. The relationships between relative density, grain growth, and Vickers hardness compared to temperature are shown in **Figure 4.7**. Rapid densification occurred up until about 2000 °C, which corresponds to around 95% relative density, after which the densification slowed and continued to increase until 2100 °C, where the sample approached full densification.

The grain size stayed relatively stable at around 1.4 μm from 1800 °C to 1950 °C and minimal grain growth occurred between 1950 °C and 2000 °C. Rapid grain growth occurred after 2000 °C and increased with increasing temperature up to 2100 °C. The temperature that best captures the stagnation of densification and acceleration of grain growth is 2000 °C, marked as T_g in **Figure 4.7**, where the relative density surpassed 95% and began to approach full density but before the onset of increased grain growth. The increase in Vickers hardness value is nearly identical to the densification with respect to temperature, shown in

Table 4.3: High resolution XRD results

Powder	**Impurity**	**Approximate Angle (2θ)**	**Quantity (wt%)**
NbC	Nb_2O_5	2.4, 3.0, 4.8	0.5
	$Nb_{12}O_{29}$	2.5, 2.6, 2.8, 4.6, 5.0	0.9
	ZrO_2 (T^1)	3.2, 3.4	<0.1
TaC	HfO_2	3.2, 5.0	0.1
	Hf_6O	5.2	<0.1
ZrC	NbO_2	2.8	0.3
	ZrO_2 (T^1)	3.4, 3.8, 5.3	0.3
	ZrO_2 (MC^2)	3.0, 3.8, 4.3	0.3

[1] *T: tetragonal*
[2] *MC: monoclinic*

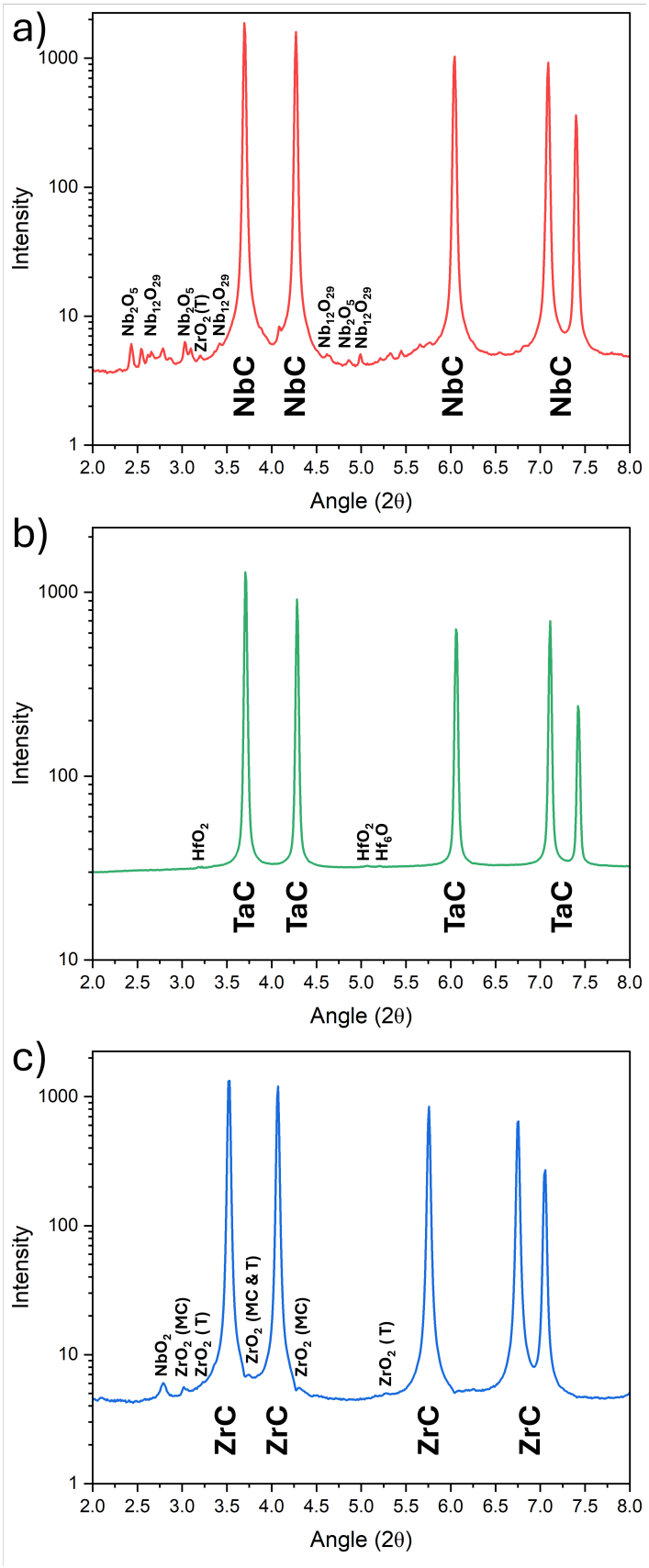


Figure 4.5: High resolution powder XRD spectra and phase identification of a) NbC, b) TaC, and c) ZrC.

Table 4.4: Phase 1 Results

Temperature (°C)	**Relative Density (%)**	**Grain Size (μm)**	**Vickers Hardness (GPa)**	**(ZrNbTa)C Lattice Parameter (Å)**
1800	76.9 ± 2.8	1.4 ± 0.2	4.9 ± 0.2	-
1850	82.1 ± 3.7	1.4 ± 0.1	8.0 ± 0.3	-
1900	87.0 ± 1.0	1.3 ± 0.2	11.0 ± 0.3	4.675
1950	90.8 ± 0.5	1.4 ± 0.1	15.0 ± 0.4	4.658
2000	96.2 ± 0.5	1.9 ± 0.1	16.9 ± 0.5	4.653
2050	97.4 ± 0.2	3.3 ± 0.1	19.1 ± 0.3	4.645
2100	99.3 ± 0.2	6.1 ± 0.2	18.9 ± 0.2	4.644

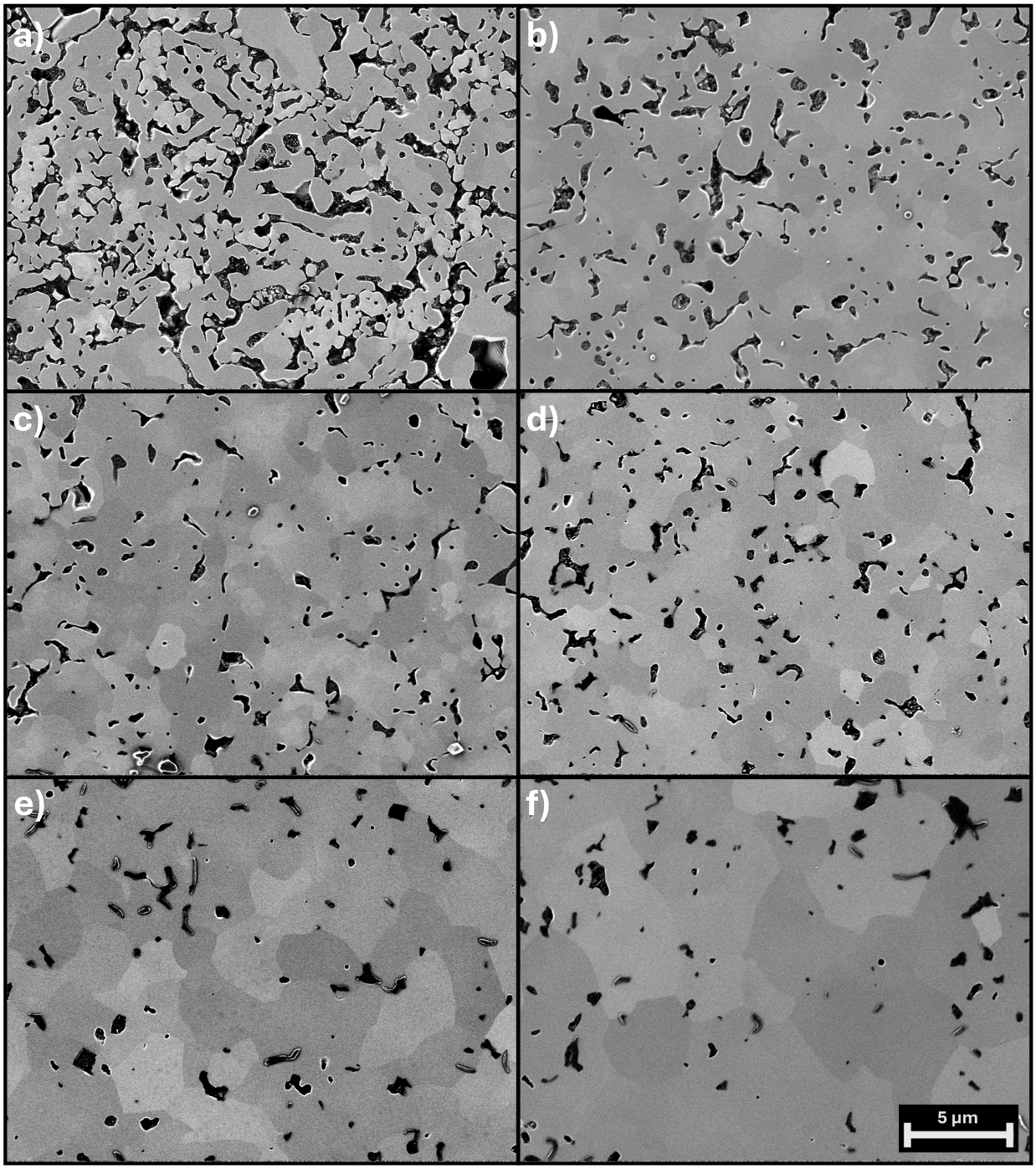


Figure 4.6: Secondary electron micrographs of ($Zr_{0.8}$, $Nb_{0.1}$, $Ta_{0.1}$)C consolidated in the SPS with an applied load of 30 MPa and 5 minute hold time at a) 1800 °C, b) 1900 °C, c) 1950 °C, d) 2000 °C, e) 2050 °C, and f) 2100 °C.

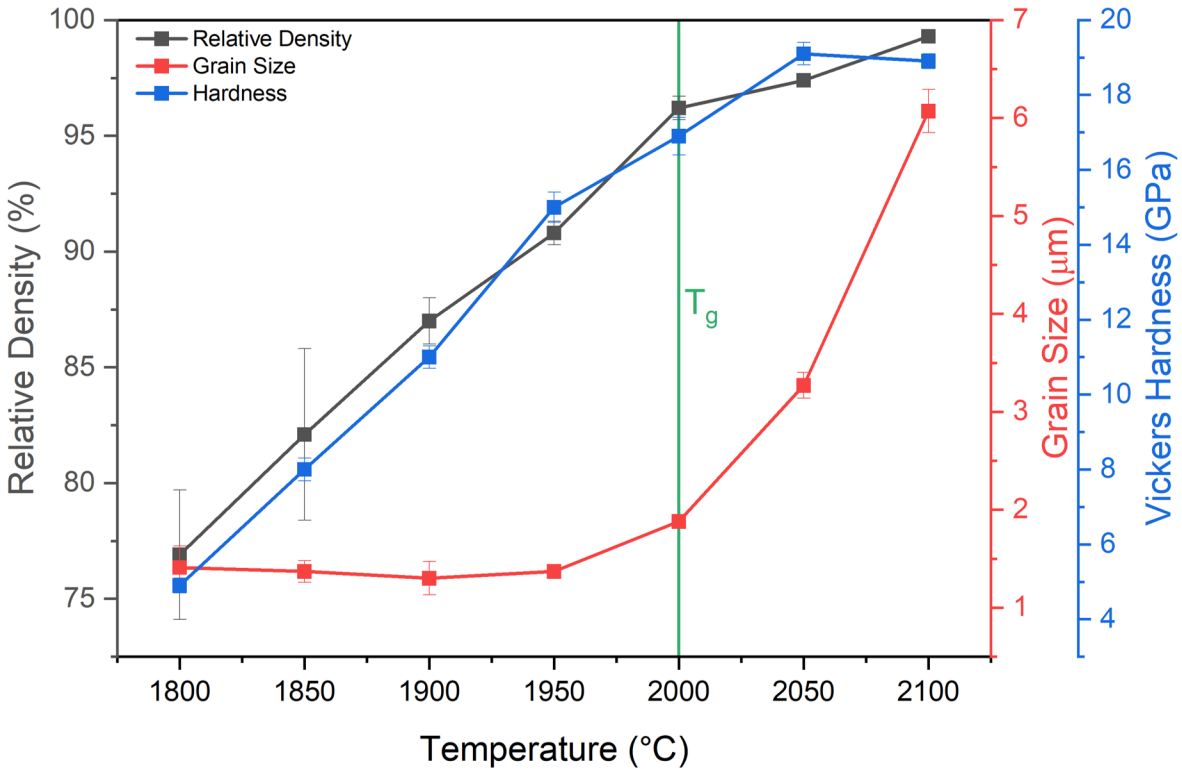


Figure 4.7: Relative density, grain size, and Vickers hardness as a function of temperature for ($Zr_{0.8}$, $Nb_{0.1}$, $Ta_{0.1}$)C consolidated in the SPS with an applied load of 30 MPa and 5 minute hold time.

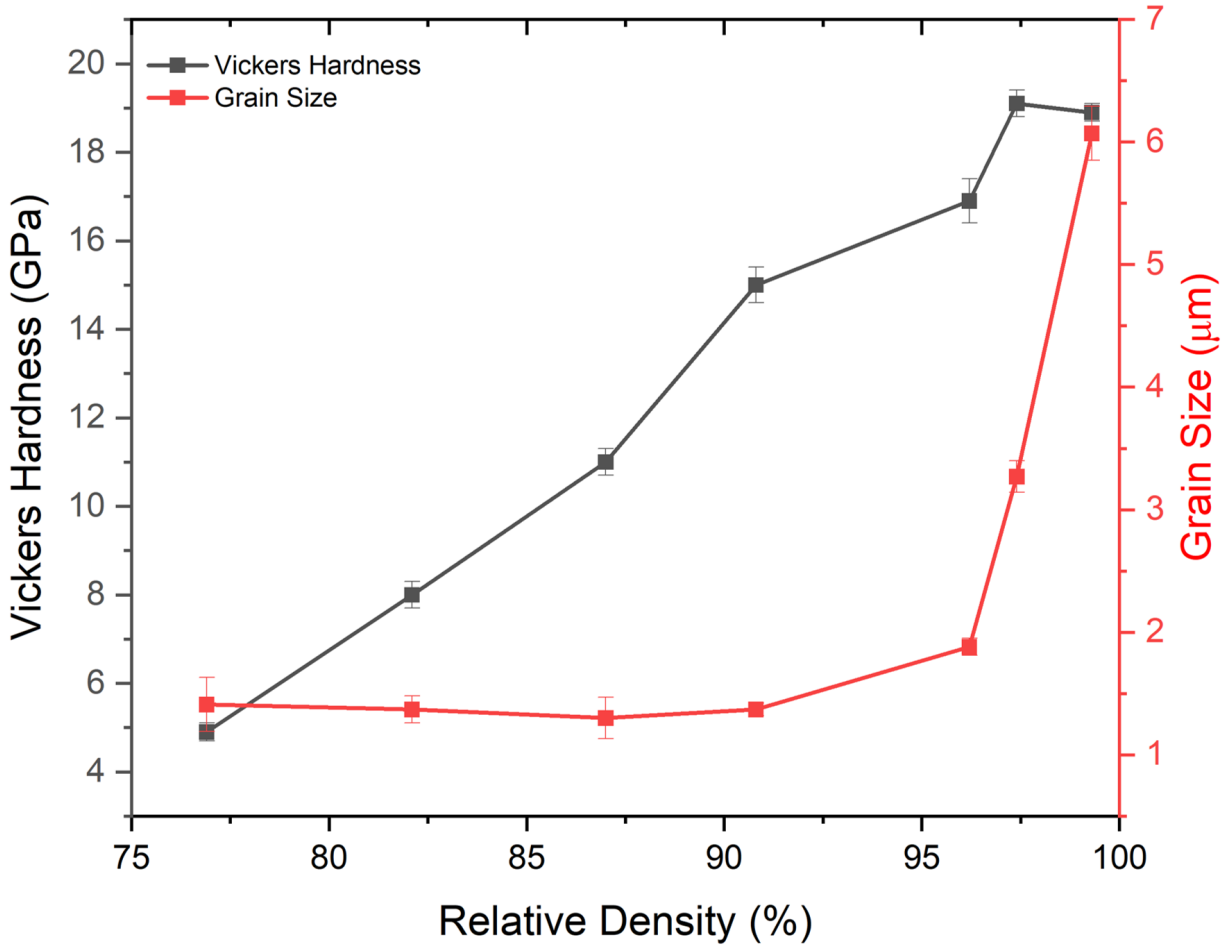


Figure 4.8: Vickers hardness and grain size as a function of relative density for ($Zr_{0.8}$, $Nb_{0.1}$, $Ta_{0.1}$)C consolidated in the SPS with an applied load of 30 MPa and 5 minute hold time.

Figure 4.7. **Figure 4.8** shows the Vickers hardness and grain size as a function of relative density.

The XRD spectra of ($Zr_{0.8}$, $Nb_{0.1}$, $Ta_{0.1}$)C consolidated in the SPS with an applied load of 30 MPa and for a hold time of 5 minutes at sintering temperatures of 1800 °C to 2100 °C are shown in **Figure 4.9**. The same spectra are overlayed in **Figure 4.10**, showing the transformation of a multiphase material at 1800 °C (shown in yellow) to a single phased material at 2100 °C (shown in purple). The development of the ($Zr_{0.8}$, $Nb_{0.1}$, $Ta_{0.1}$)C phase appears to begin at around 1900 °C. The individual phases of NbC, TaC, and ZrC can be seen in the sample consolidated at 1800 °C with an additional unidentified intermediate phase. At 2100 °C, there is only one prominent phase remaining, indicating that the sample is a single phase solid solution. The lattice parameters for the ($Zr_{0.8}$, $Nb_{0.1}$, $Ta_{0.1}$)C phase are recorded in **Table 4.4**. Since the development of the ($Zr_{0.8}$, $Nb_{0.1}$, $Ta_{0.1}$)C phase did not begin until the sample sintered at 1900 °C, lattice parameters for the lower temperature samples were not representative of the ($Zr_{0.8}$, $Nb_{0.1}$, $Ta_{0.1}$)C phase, and therefore not recorded in **Table 4.4**.

4.3 Phase 2

In the second phase of this project, ($Zr_{0.8}$, $Nb_{0.1}$, $Ta_{0.1}$)C samples were sintered at increasing hold times of 1, 5, 10, and 20 minutes. The relative densities, grain sizes, and Vickers hardness values are shown in **Table 4.5**. **Figure 4.11** shows secondary electron micrographs illustrating the grain growth and microstructural evolution of the ($Zr_{0.8}$, $Nb_{0.1}$, $Ta_{0.1}$)C samples. Significant densification occurred between hold times of 1 and 5 minutes and visible grain coarsening started at a hold time of 5 minutes and continued through a hold time of 20 minutes. The relationships between relative density, grain growth, and Vickers hardness compared to hold time are shown in **Figure 4.12**. Rapid densification occurred up until a hold time of 10 minutes, which corresponds to over 98% relative density, after which the density remained approximately constant when the sample approached full density.

The grain size increased slightly from 1.4 μm to 1.9 μm for a 1 minute and 5 minute hold time, respectively. Rapid grain growth occurred after a hold time of 5 minutes and increased

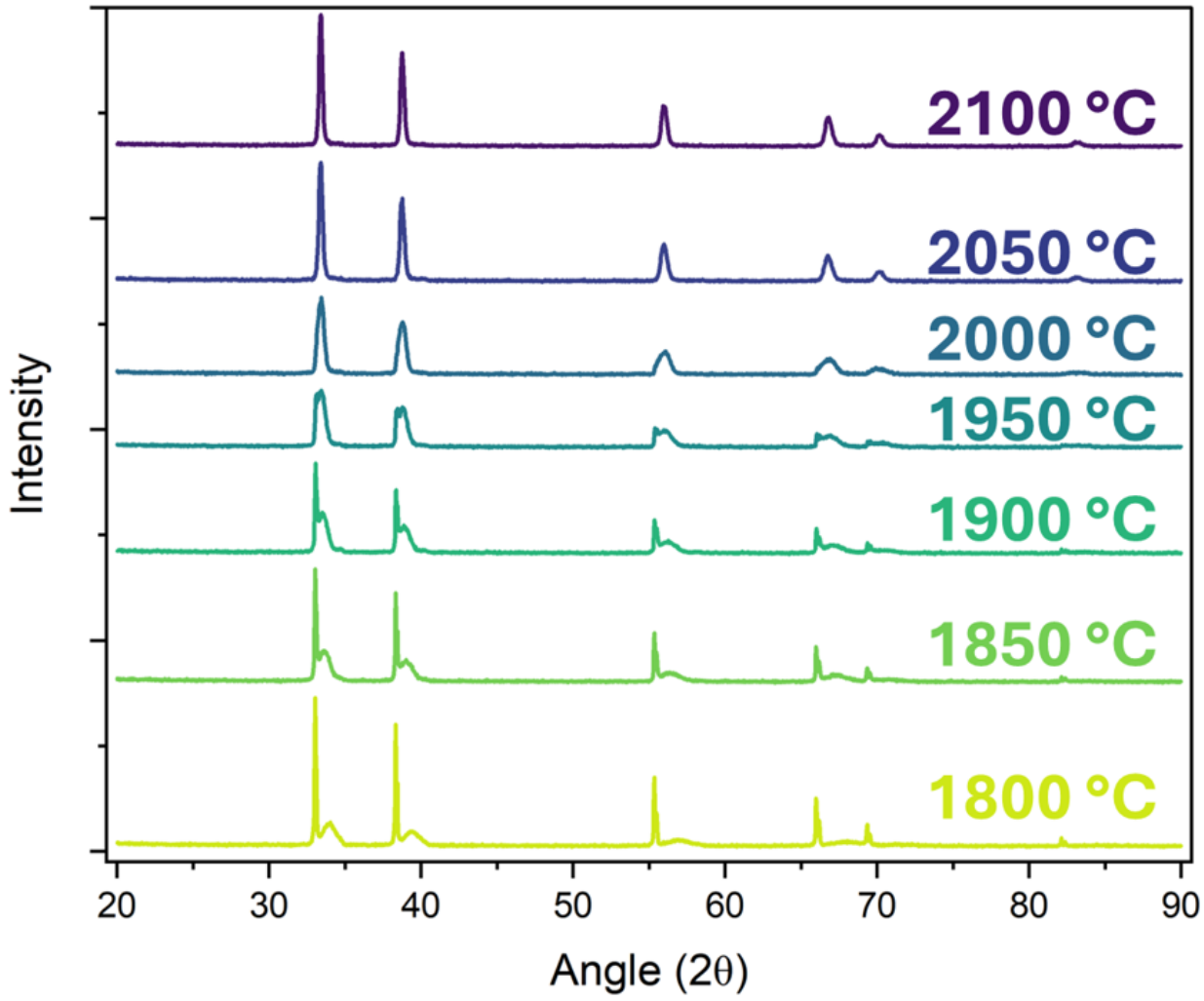


Figure 4.9: A comparison of XRD spectra of ($Zr_{0.8}$, $Nb_{0.1}$, $Ta_{0.1}$)C consolidated in the SPS with an applied load of 30 MPa and 5 minute hold time at temperatures ranging from 1800 °C to 2100 °C

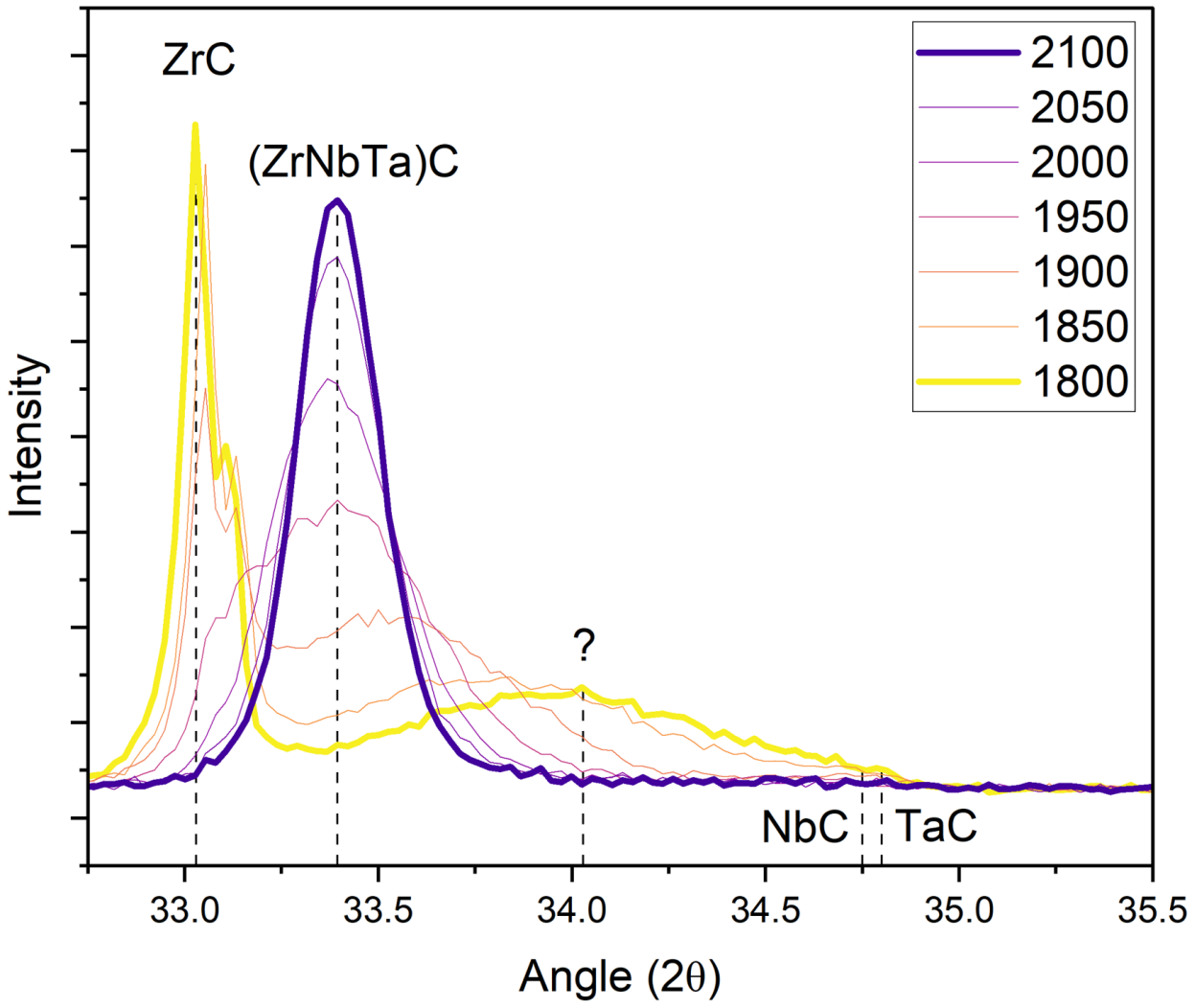


Figure 4.10: A comparison of XRD spectra of ($Zr_{0.8}$, $Nb_{0.1}$, $Ta_{0.1}$)C consolidated in the SPS at various temperatures showing the formation of a single phase solid solution.

Table 4.5: Phase 2 Results

Hold Time (min)	**Relative Density (%)**	**Grain Size (μm)**	**Vickers Hardness (GPa)**	**(ZrNbTa)C Lattice Parameter (Å)**
1	89.6 ± 0.2	1.4 ± 0.1	11.9 ± 0.3	4.663
5	96.2 ± 0.5	1.9 ± 0.1	16.9 ± 0.5	4.653
10	98.4 ± 0.1	4.4 ± 0.1	17.9 ± 0.3	4.644
20	98.5 ± 0.1	5.7 ± 0.2	18.3 ± 0.3	4.644

with increasing hold times up to 20 minutes. The hold time that best captures the stagnation of densification and acceleration of grain growth is 5 minutes, marked with a vertical line in **Figure 4.12**, where the relative density surpassed 96% and began to approach full density but before the onset of increased grain growth. As seen in Phase 1, the increase in the Vickers hardness value was nearly identical to the densification (**Figure 4.12**), but with respect to the hold time instead of temperature. **Figure 4.13** shows the Vickers hardness and grain size as a function of relative density.

The XRD spectra of ($Zr_{0.8}$, $Nb_{0.1}$, $Ta_{0.1}$)C consolidated in the SPS with an applied load of 30 MPa and at a temperature of 2000 °C for hold times ranging from 1 minute to 20 minutes are shown in **Figure 4.14**. The same spectra are overlayed in **Figure 4.15**, showing the transformation of a multiphase material at a hold time of 1 minute (shown in yellow) to a single phased material at a hold time of 20 minutes (shown in purple). The individual phases of NbC, TaC, and ZrC can be seen in the sample consolidated for a hold time of 1 minute. For a hold time of 20 minutes, there is only one prominent phase remaining, indicating that the sample is a single phase solid solution. The lattice parameters for the ($Zr_{0.8}$, $Nb_{0.1}$, $Ta_{0.1}$)C phase are recorded in **Table 4.5**.

4.4 Phase 3

In the third and final phase of this project, ($Zr_{0.8}$, $Nb_{0.1}$, $Ta_{0.1}$)C samples were initially planned to be sintered in a vacuum at increasing pressures of 10, 30, 60, and 90 MPa. When sintering the first sample at 60 MPa in a vacuum, significant chemical erosion occurred on the graphite die and punches. In order to reduce the wear on the graphite tooling, an argon purged atmosphere was used during the sintering process instead of a vacuum. As seen in **Table 4.6**, an argon purged environment was used for runs at 15, 30, 60, and 90 MPa (with a hold time of 5 minutes at 2000 °C) in conjunction with a high pressure die. Also, sintering runs were performed in vacuum at 10 and 30 MPa with a standard graphite die, as well as at 60 MPa with a high pressure die.

The relative densities, grain sizes, and Vickers hardness values of the samples sintered in both a vacuum and in an argon purged environment at various pressures are shown in

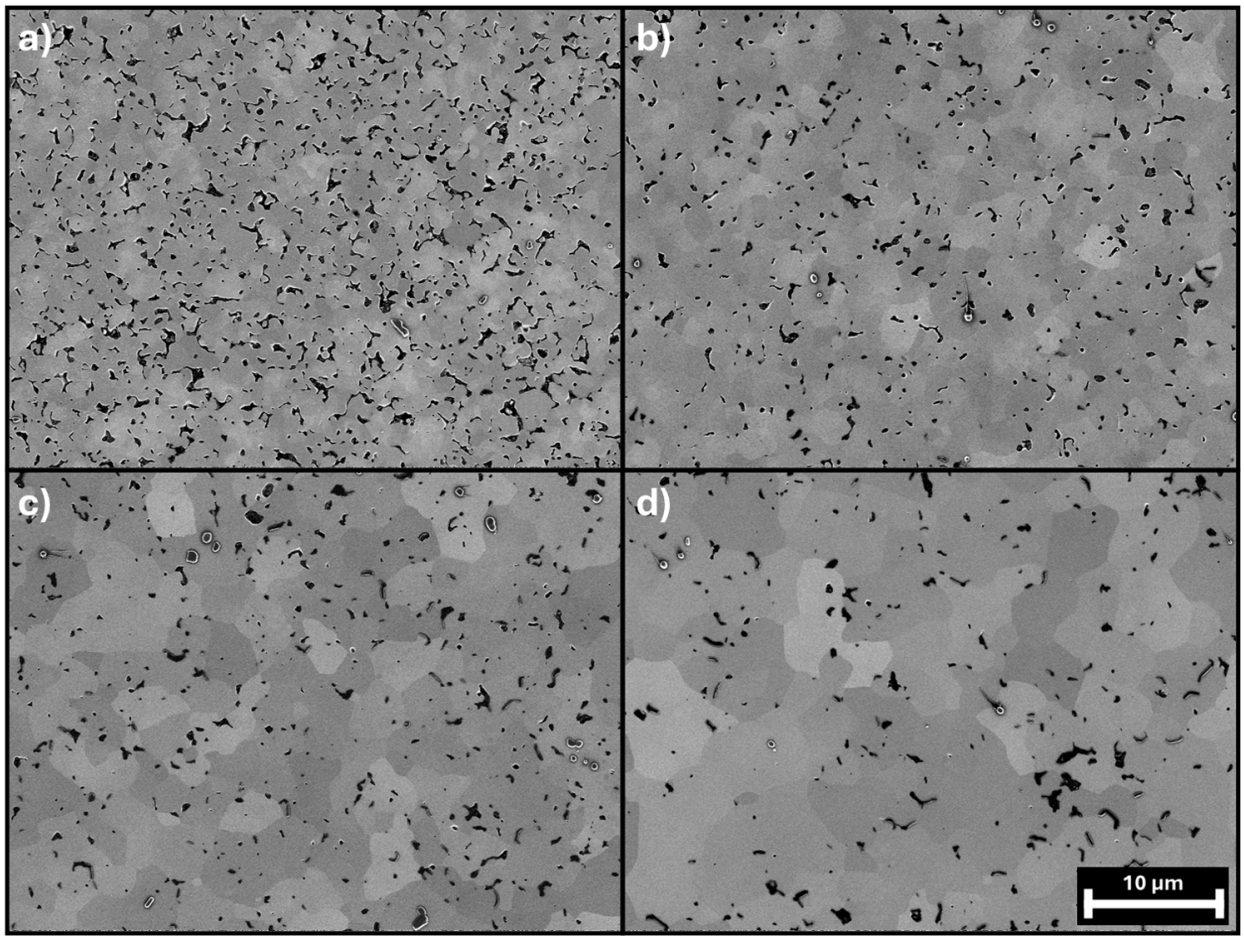


Figure 4.11: Secondary electron micrographs of ($Zr_{0.8}$, $Nb_{0.1}$, $Ta_{0.1}$)C consolidated in the SPS with an applied load of 30 MPa at 2000 °C for hold times of a) 1 min, b) 5 min, c) 10 min, d) 20 min.

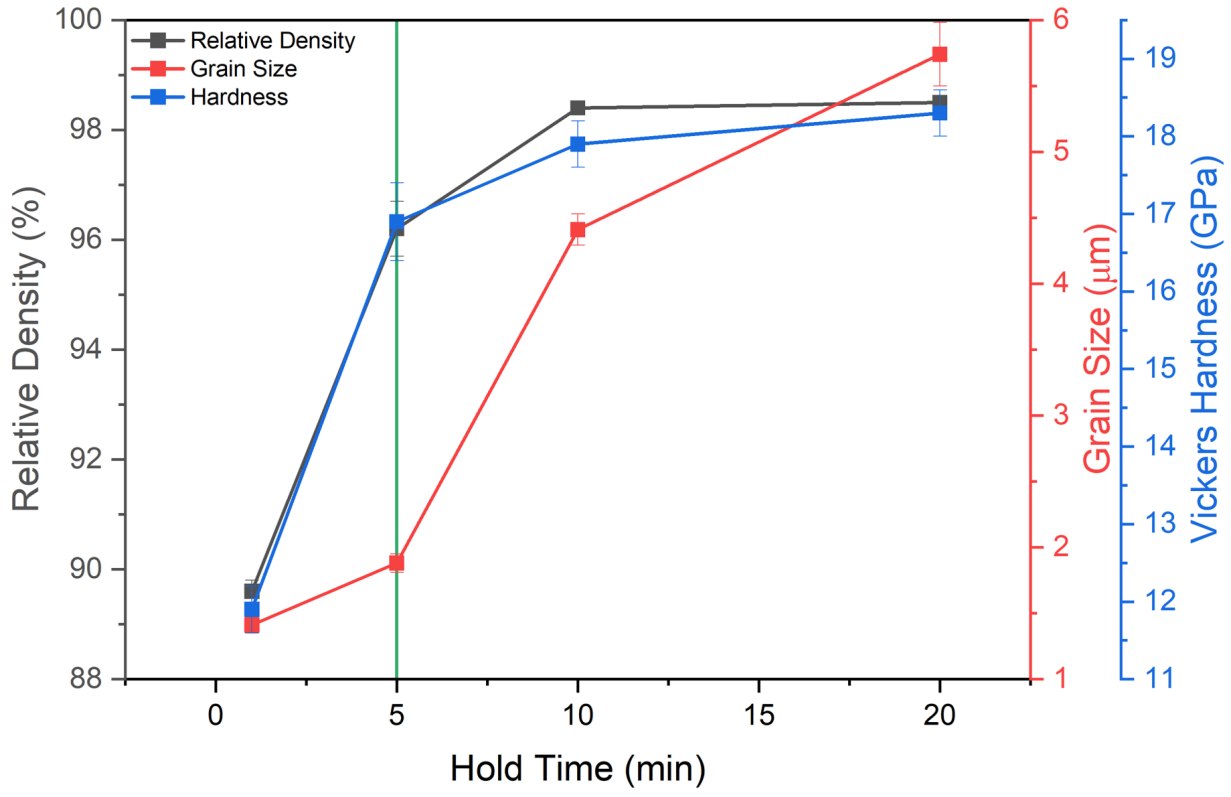


Figure 4.12: Relative density, grain size, and Vickers hardness as a function of hold time for ($Zr_{0.8}$, $Nb_{0.1}$, $Ta_{0.1}$)C consolidated in the SPS with an applied load of 30 MPa at 2000 °C.

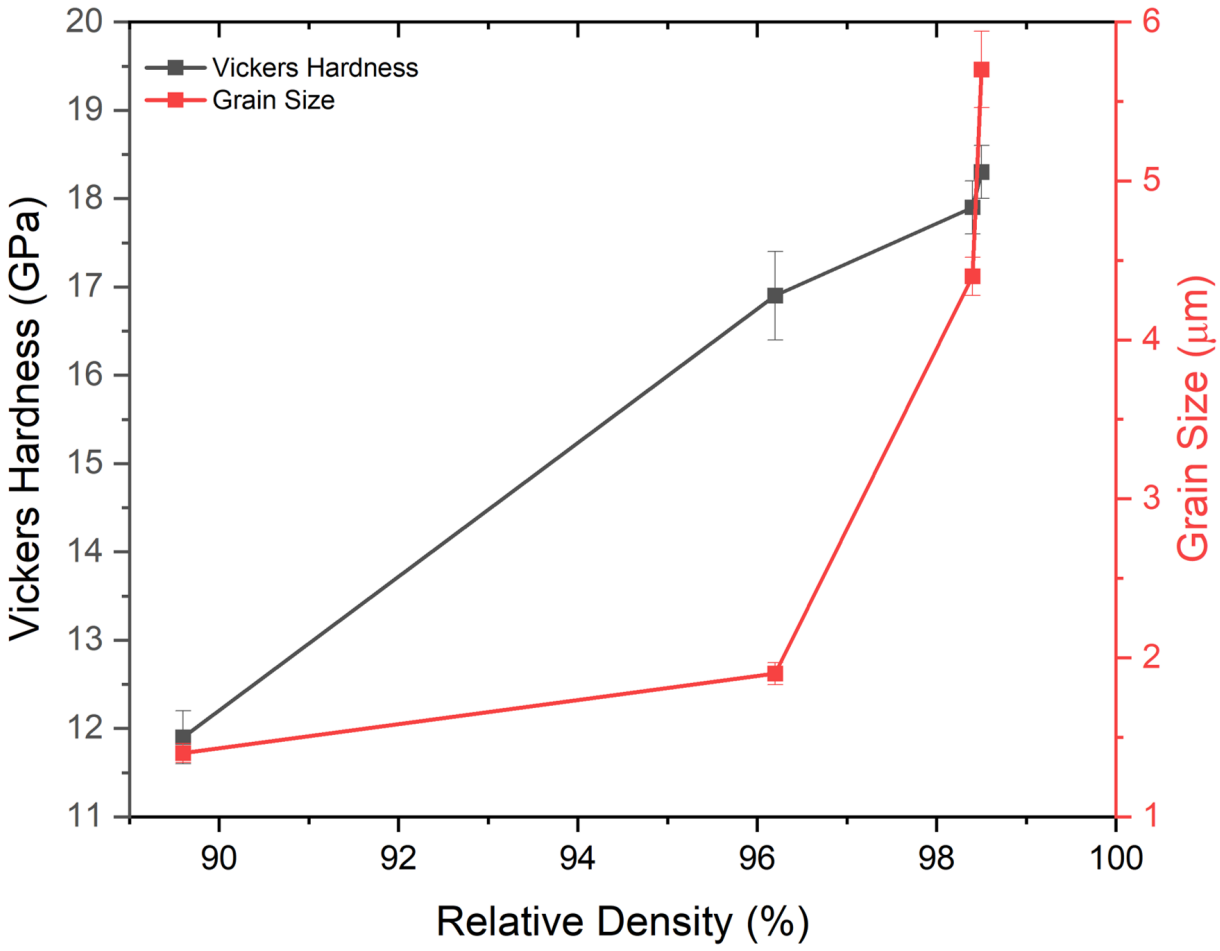


Figure 4.13: Vickers hardness and grain size as a function of relative density for ($Zr_{0.8}$, $Nb_{0.1}$, $Ta_{0.1}$)C consolidated in the SPS with an applied load of 30 MPa at 2000 °C for various hold times.

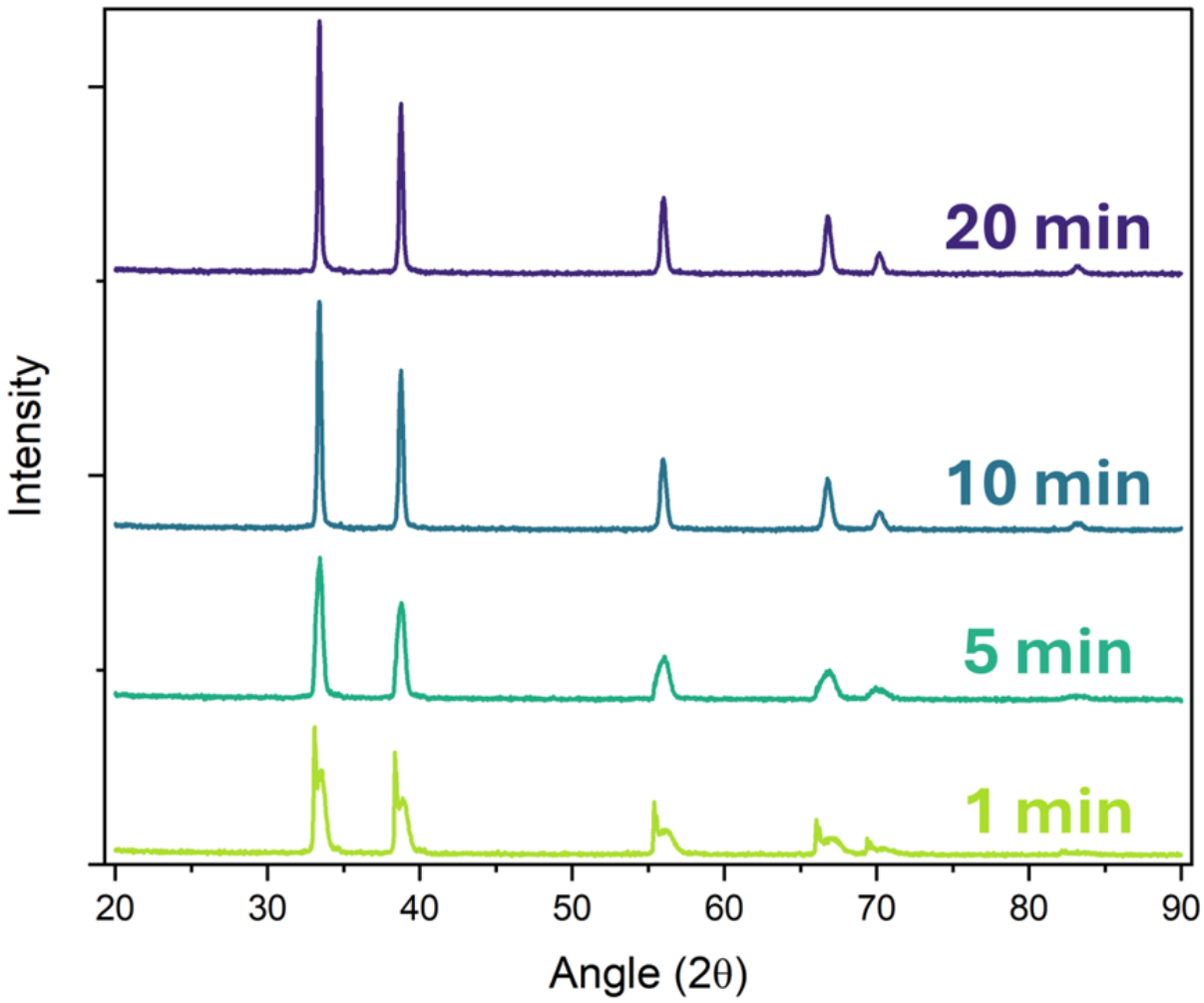


Figure 4.14: A comparison of XRD spectra of ($Zr_{0.8}$, $Nb_{0.1}$, $Ta_{0.1}$)C consolidated in the SPS with an applied load of 30 MPa at 2000 °C for hold times ranging from 1 to 20 minutes.

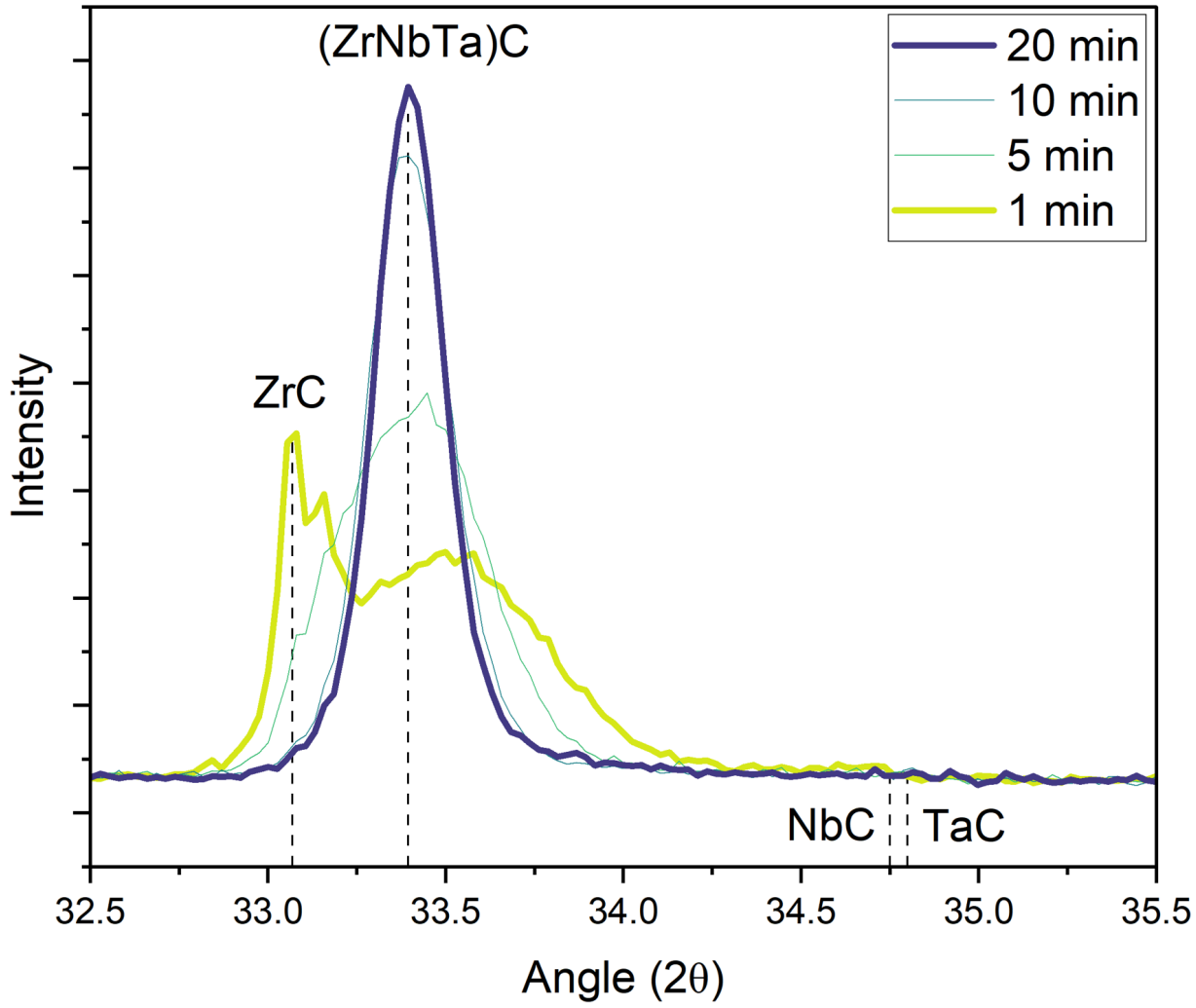


Figure 4.15: A comparison of XRD spectra of ($Zr_{0.8}$, $Nb_{0.1}$, $Ta_{0.1}$)C consolidated in the SPS with an applied load of 30 MPa at 2000 °C at various hold times showing the formation of a single phase solid solution.

Table 4.6: Phase 3 Results

Sintering Atmosphere	**Die Type**	**Pressure (MPa)**	**Relative Density (%)**	**Grain Size (μm)**	**Vickers Hardness (GPa)**	**(ZrNbTa)C Lat. Param. (Å)**
Vacuum	Standard	10	91.9 ± 0.9	2.1 ± 0.1	13.8 ± 0.3	4.646
Vacuum	Standard	30	96.2 ± 0.5	1.9 ± 0.1	16.9 ± 0.5	4.653
Vacuum	High Press.	60	97.6 ± 0.0	4.9 ± 0.3	18.0 ± 0.5	4.644
Argon	High Press.	15	97.5 ± 0.0	3.5 ± 0.2	16.2 ± 0.5	4.644
Argon	High Press.	30	94.9 ± 0.0	2.3 ± 0.2	13.6 ± 0.3	4.645
Argon	High Press.	60	98.7 ± 0.3	2.2 ± 0.2	18.0 ± 0.4	4.645
Argon	High Press.	90	98.9 ± 0.2	1.6 ± 0.1	18.6 ± 0.3	4.642

Table 4.6. **Figure 4.16** shows secondary electron micrographs illustrating the grain growth and microstructural evolution of the ($Zr_{0.8}$, $Nb_{0.1}$, $Ta_{0.1}$)C samples that were sintered in a vacuum. **Figure 4.17** shows secondary electron micrographs illustrating the grain growth and microstructural evolution of the ($Zr_{0.8}$, $Nb_{0.1}$, $Ta_{0.1}$)C samples that were sintered in an argon purged environment. A comparison of secondary electron micrographs of ($Zr_{0.8}$, $Nb_{0.1}$, $Ta_{0.1}$)C samples sintered at 2000 °C for 5 minutes at 30 MPa or 60 MPa in a vacuum versus an argon purged environment is shown in **Figure 4.18**.

The relationships between relative density, grain growth, and Vickers hardness compared to pressure for samples sintered in a vacuum versus an argon purged environment are shown in **Figures 4.19 and 4.20**, respectively. For the samples sintered in a vacuum, the grain size stayed relatively constant, around 2 μm, when sintered at 10 MPa and 30 MPa. At 60 MPa, the grain size of the samples sintered in a vacuum increased to about 5 μm. For the samples sintered in an argon purged environment, the grain size decreased with increasing pressure and the relative density decreased from 15 MPa to 30 MPa and then increased with increasing pressure. For all samples, independent of the sintering atmosphere, the relative density surpassed 95% of the theoretical density at 30 MPa with minimal grain growth. As seen in the previous two phases, the increase in the Vickers hardness value was nearly identical to the densification for both vacuum and argon sintering environments with respect to pressure (**Figures 4.19 and 4.20**). **Figure 4.21** shows the Vickers hardness and grain size as a function of relative density.

The XRD spectra of ($Zr_{0.8}$, $Nb_{0.1}$, $Ta_{0.1}$)C consolidated in the SPS in a vacuum at a temperature of 2000 °C for a hold time of 5 minutes and at pressures ranging from 10 MPa to 60 MPa are shown in **Figure 4.22**. The same spectra are overlayed in **Figure 4.23**. For each sample sintered in a vacuum, a single peak occurred for each pressure, indicating a solid solution ($Zr_{0.8}$, $Nb_{0.1}$, $Ta_{0.1}$)C phase. The intensity of the peaks for the 10 MPa and 60 MPa samples were higher than the intensity of the peak for the 30 MPa sample. The XRD spectra of ($Zr_{0.8}$, $Nb_{0.1}$, $Ta_{0.1}$)C consolidated in the SPS in an argon purged environment at a temperature of 2000 °C for a hold time of 5 minutes and at pressures ranging from 30 MPa to 90 MPa are shown in **Figure 4.24**. The same spectra are overlayed in **Figure 4.25**. The intensity of the single peak for each sample increases as the applied pressure during sintering

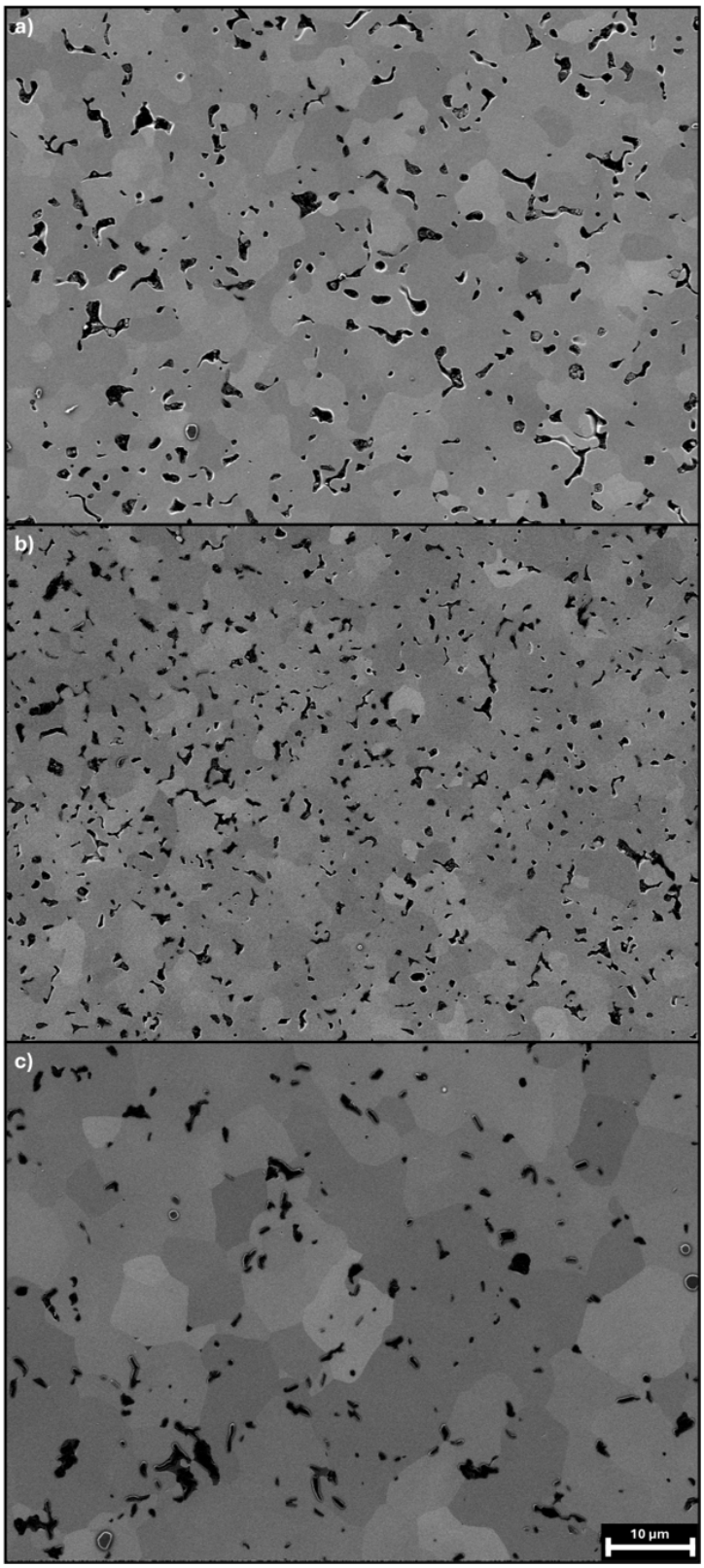


Figure 4.16: Secondary electron micrographs of ($Zr_{0.8}$, $Nb_{0.1}$, $Ta_{0.1}$)C consolidated in the SPS in a vacuum with a hold time of 5 minutes at 2000 °C with an applied pressure of a) 10 MPa, b) 30 MPa, and c) 60 MPa.

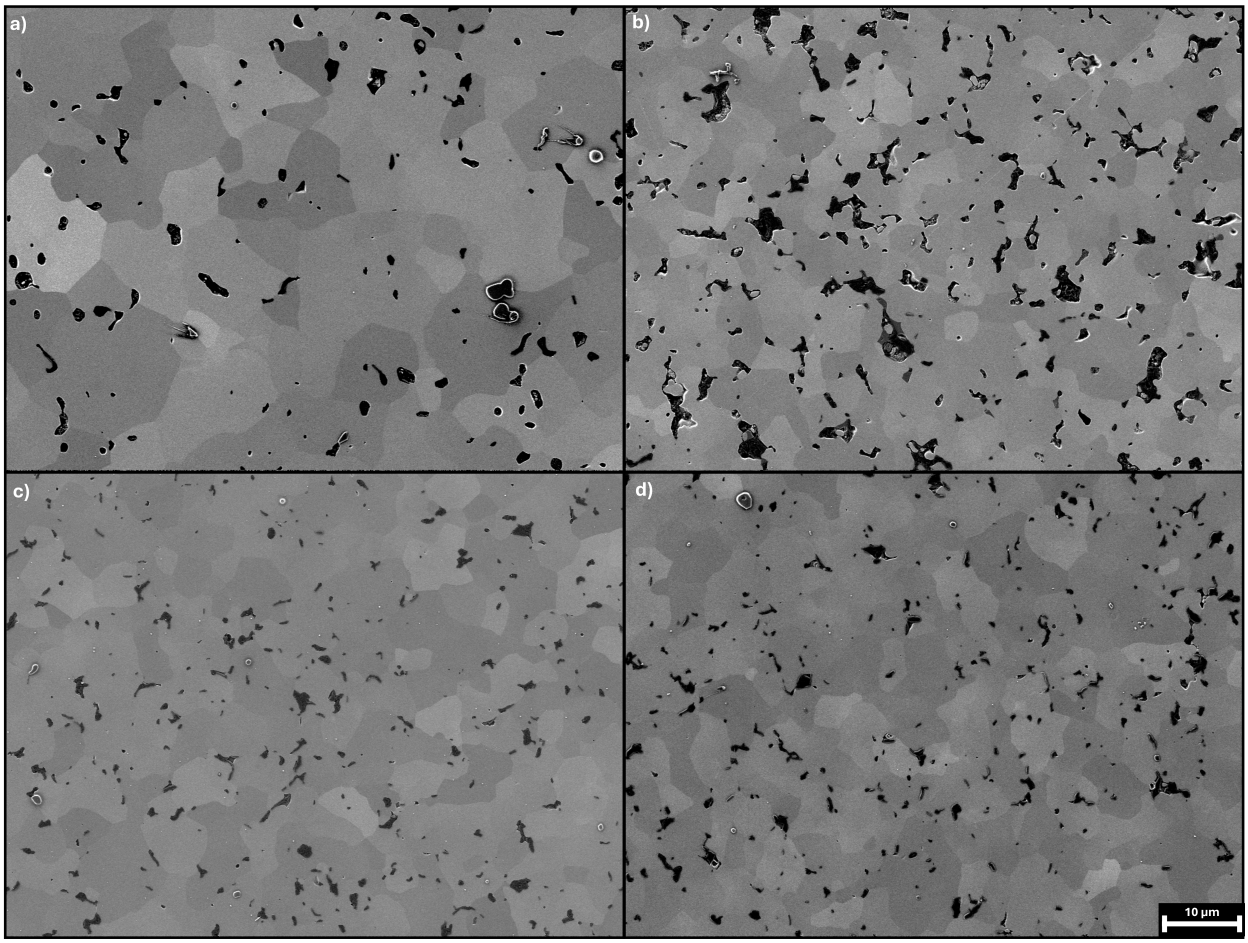


Figure 4.17: Secondary electron micrographs of ($Zr_{0.8}$, $Nb_{0.1}$, $Ta_{0.1}$)C consolidated in the SPS in an argon purged environment with a hold time of 5 minutes at 2000 °C with an applied pressure of a) 15 MPa, b) 30 MPa, c) 60 MPa, and d) 90 MPa.

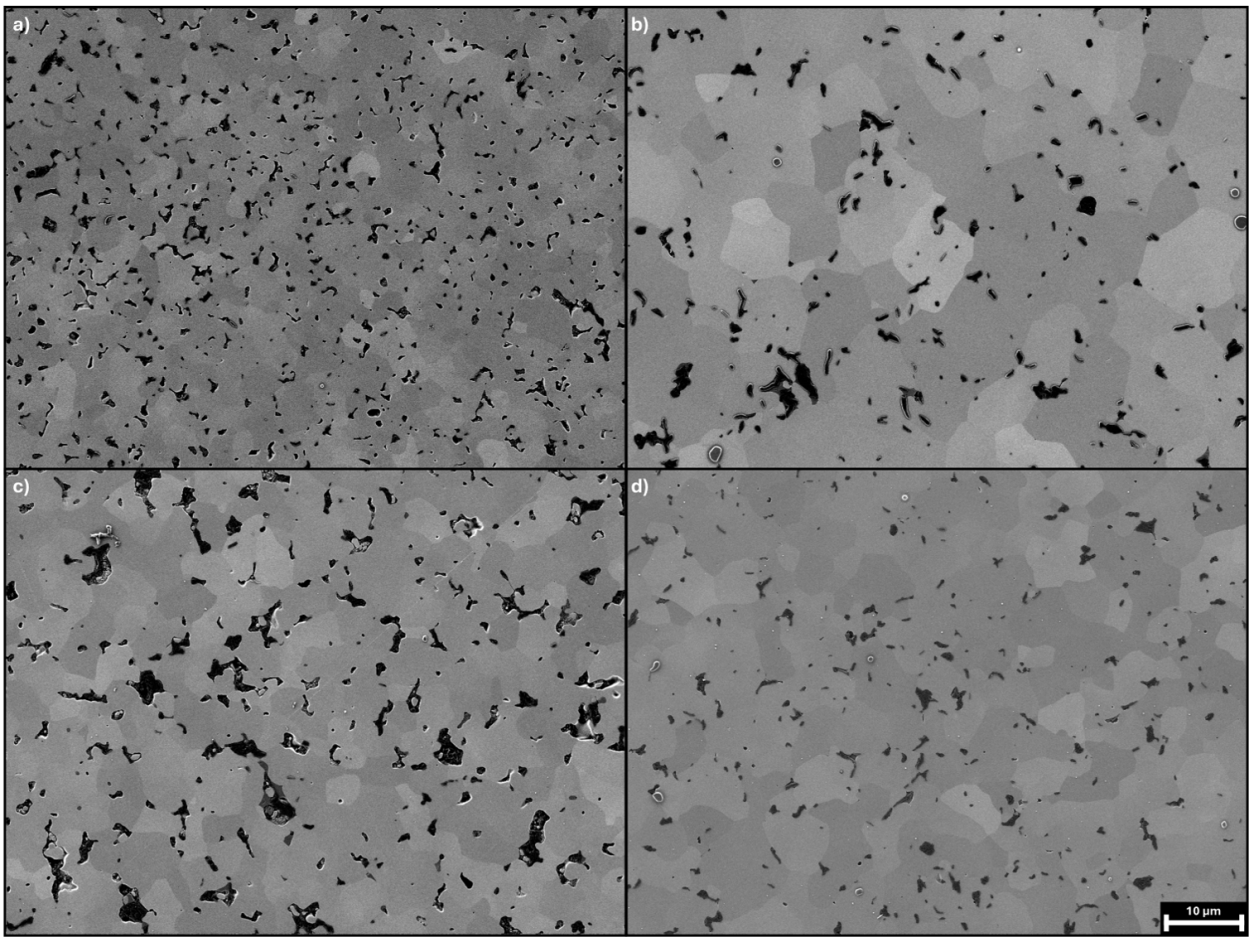


Figure 4.18: Secondary electron micrographs of ($Zr_{0.8}$, $Nb_{0.1}$, $Ta_{0.1}$)C consolidated in the SPS with a hold time of 5 minutes at 2000 °C in a vacuum with an applied pressure of a) 30 MPa and b) 60 MPa and in an argon purged environment with an applied pressure of c) 30 MPa and d) 60 MPa.

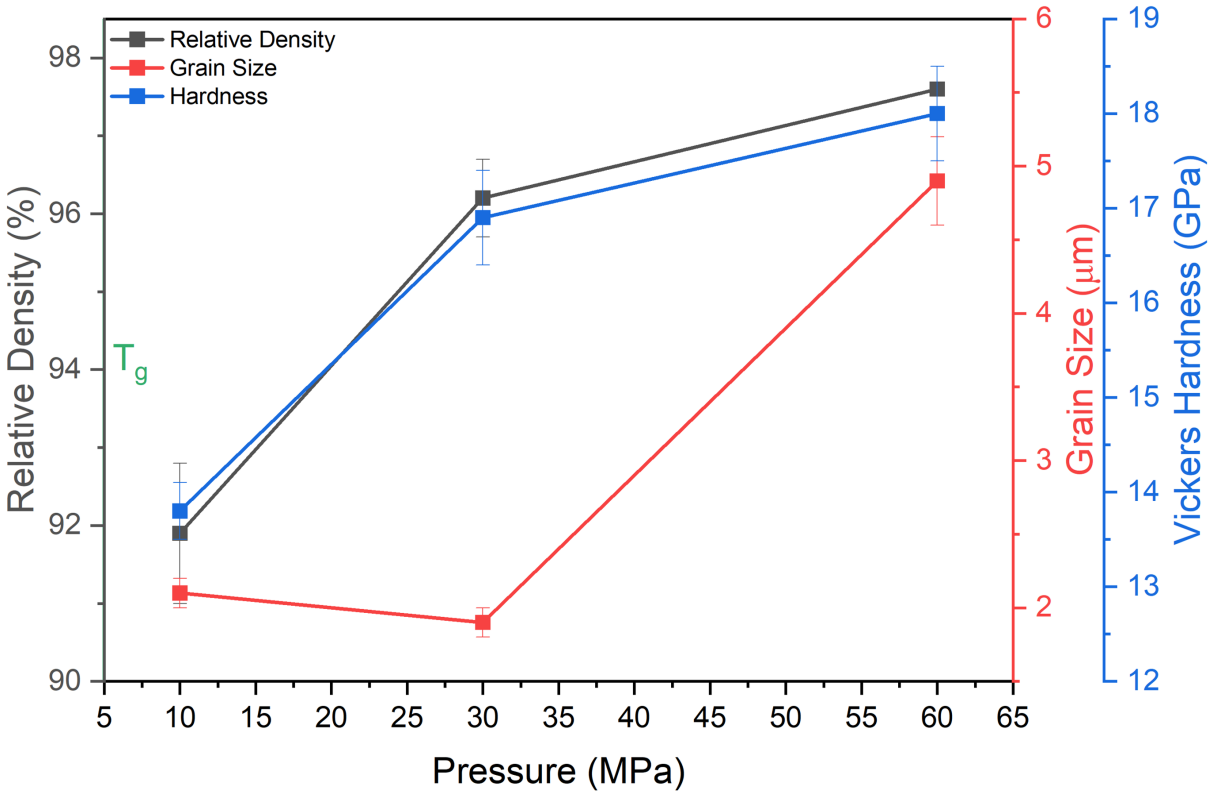


Figure 4.19: Relative density, grain size, and Vickers hardness as a function of applied pressure for ($Zr_{0.8}$, $Nb_{0.1}$, $Ta_{0.1}$)C consolidated in the SPS in a vacuum with a hold time of 5 minutes at 2000 °C.

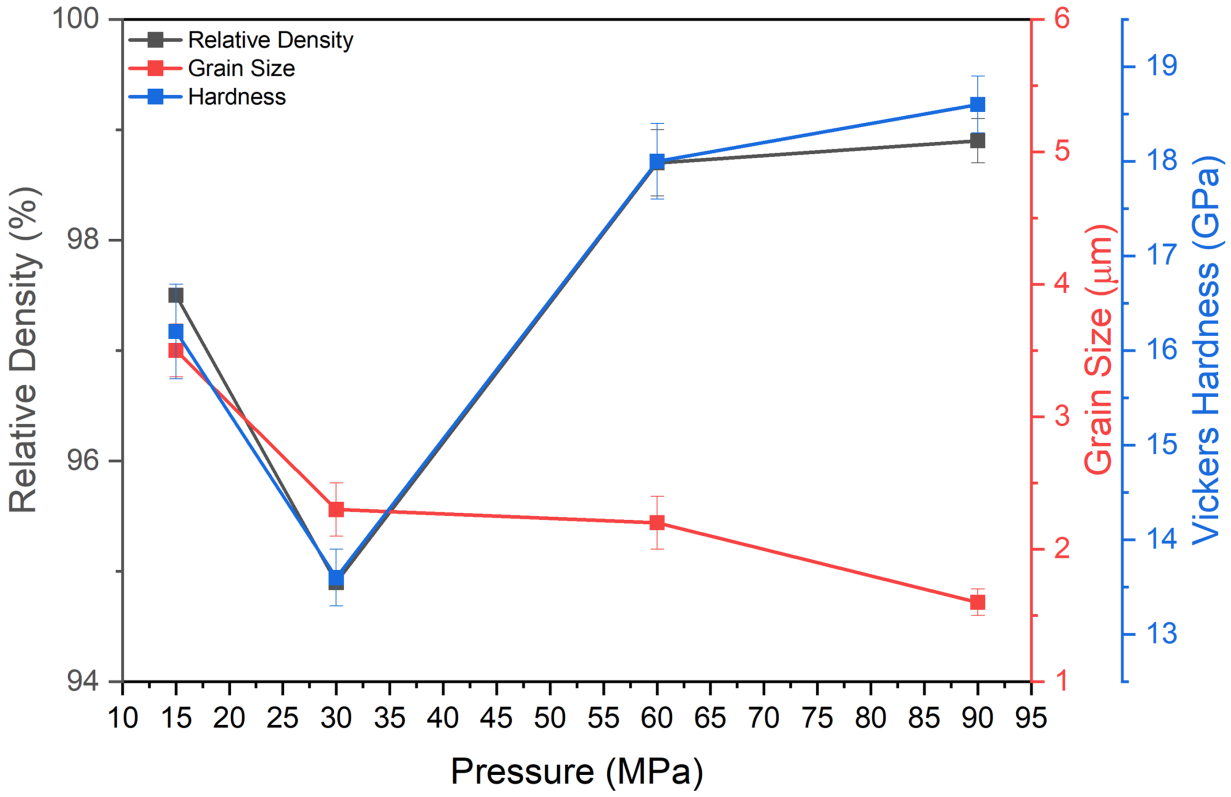


Figure 4.20: Relative density, grain size, and Vickers hardness as a function of applied pressure for ($Zr_{0.8}$, $Nb_{0.1}$, $Ta_{0.1}$)C consolidated in the SPS in an argon purged environment with a hold time of 5 minutes at 2000 °C.

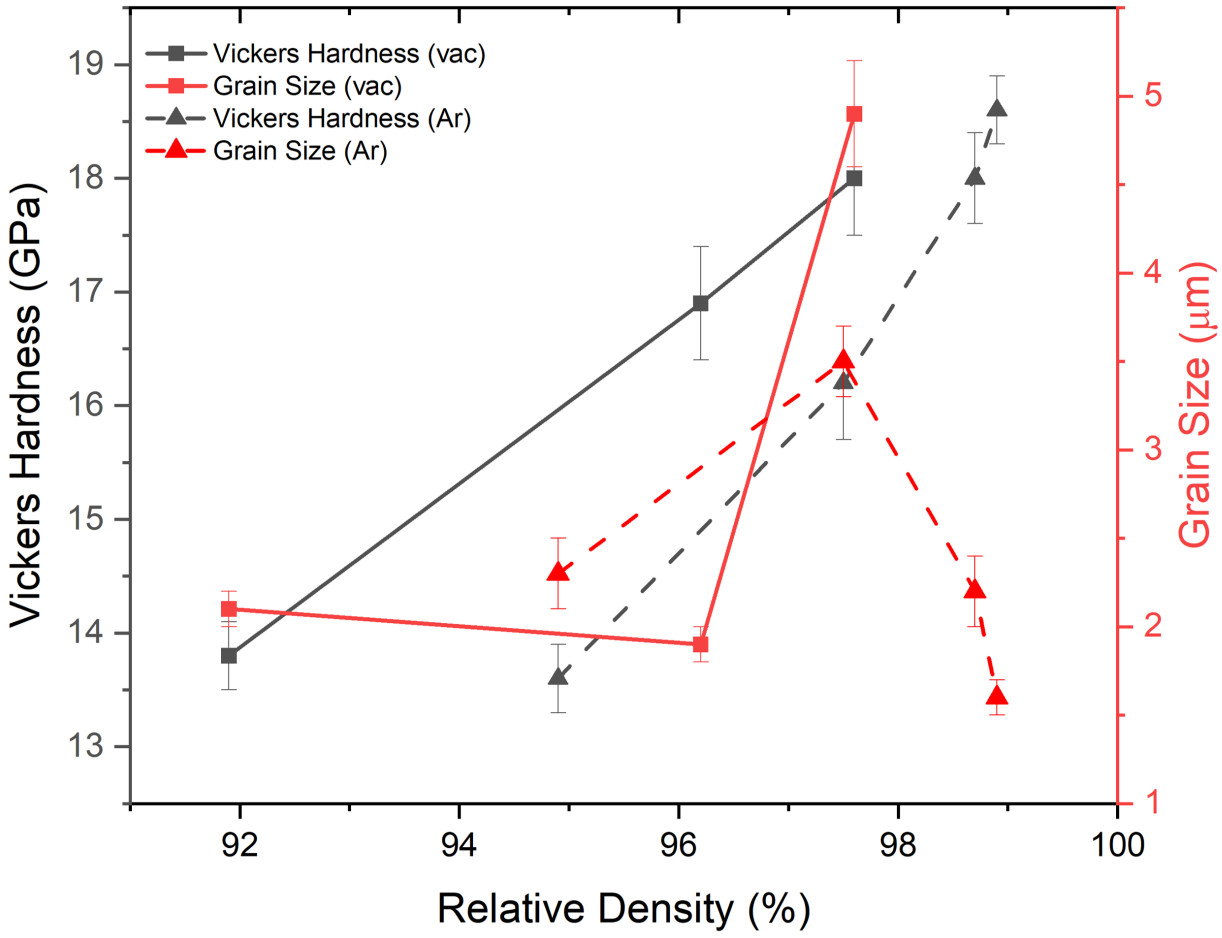


Figure 4.21: Vickers hardness and grain size as a function of relative density for ($Zr_{0.8}$, $Nb_{0.1}$, $Ta_{0.1}$)C consolidated in the SPS at various pressures with a hold time of 5 minutes at 2000 °C. Samples sintered in a vacuum are denoted with square markers and solid lines and samples sintered in an argon purged environment are denoted with triangle markers and dashed lines.

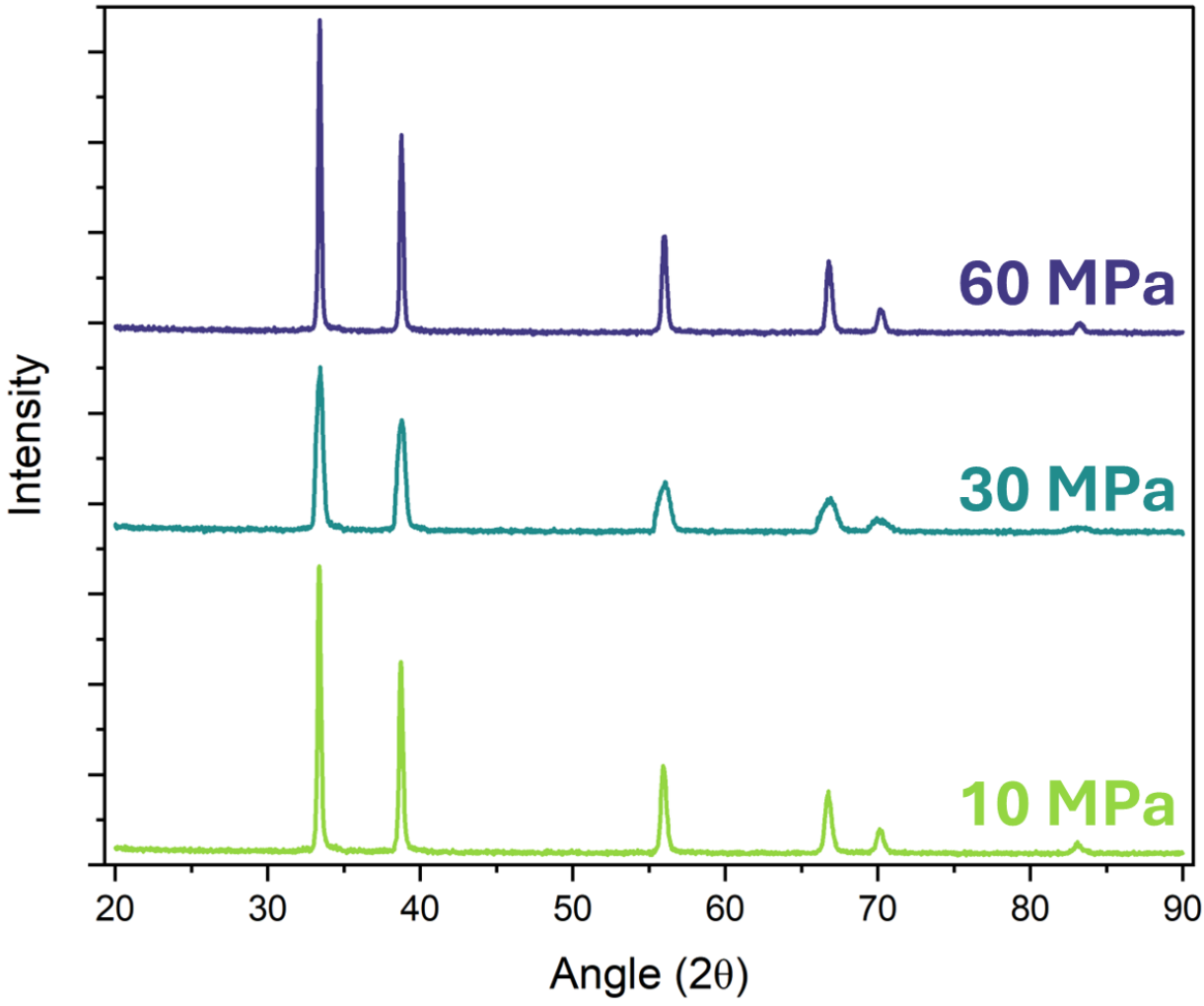


Figure 4.22: A comparison of XRD spectra of ($Zr_{0.8}$, $Nb_{0.1}$, $Ta_{0.1}$)C consolidated in the SPS in a vacuum with a hold time of 5 minutes at 2000 °C for applied pressures ranging from 10 to 60 MPa

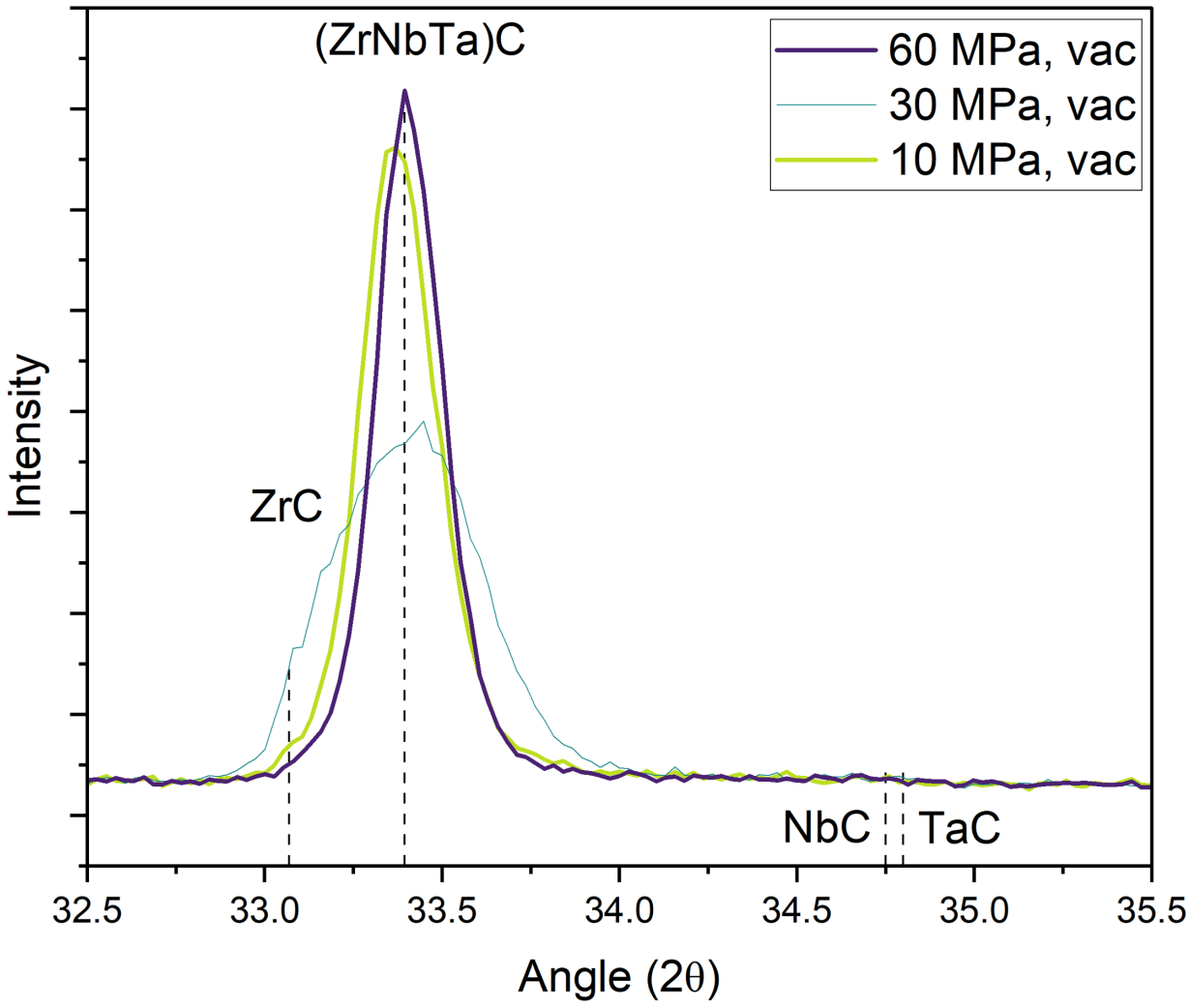


Figure 4.23: A comparison of XRD spectra of ($Zr_{0.8}$, $Nb_{0.1}$, $Ta_{0.1}$)C consolidated in the SPS in a vacuum with a hold time of 5 minutes at 2000 °C for various pressures.

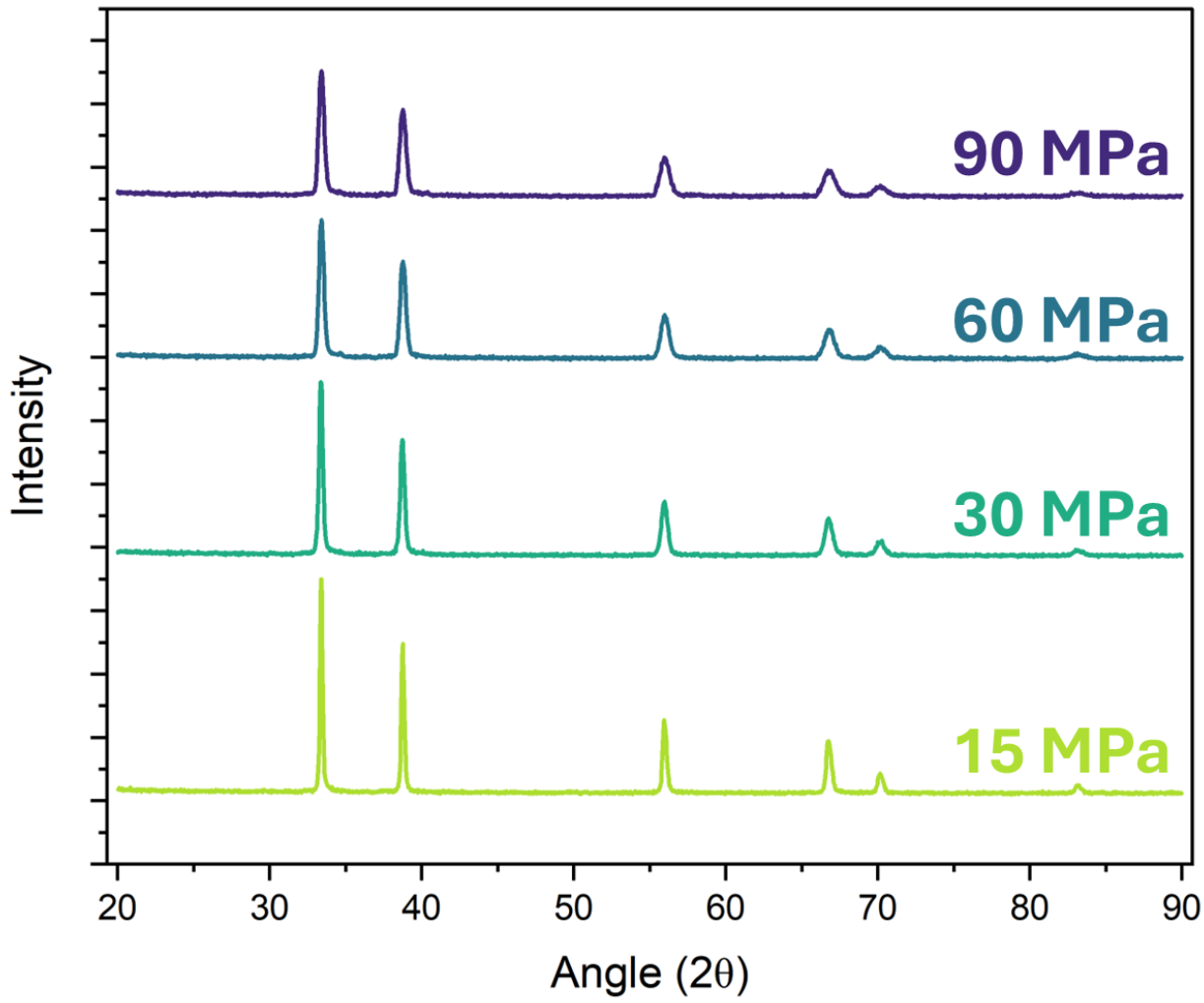


Figure 4.24: A comparison of XRD spectra of ($Zr_{0.8}$, $Nb_{0.1}$, $Ta_{0.1}$)C consolidated in the SPS in an argon purged environment with a hold time of 5 minutes at 2000 °C for applied pressures ranging from 15 to 90 MPa.

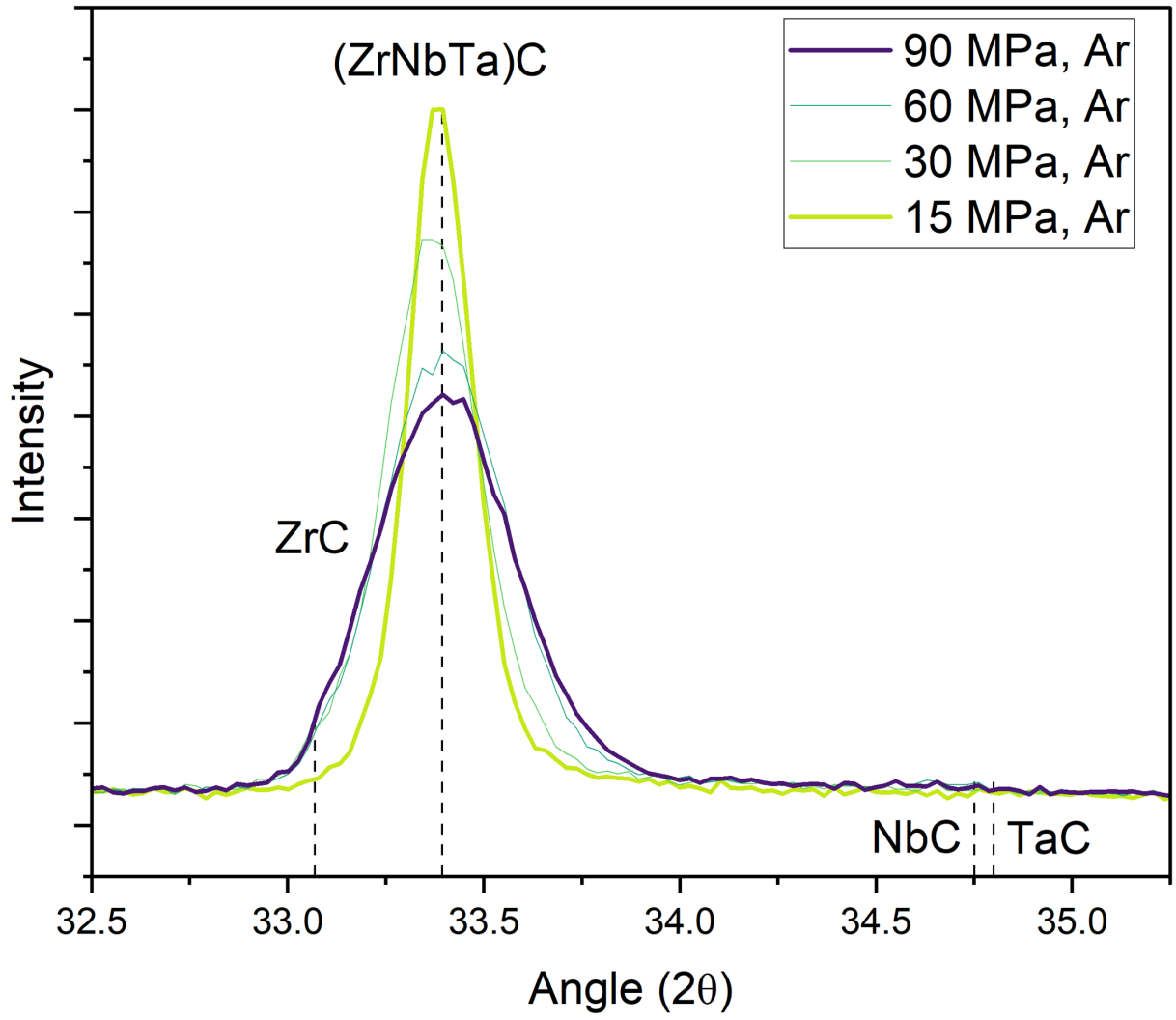


Figure 4.25: A comparison of XRD spectra of ($Zr_{0.8}$, $Nb_{0.1}$, $Ta_{0.1}$)C consolidated in the SPS in an argon purged environment with a hold time of 5 minutes at 2000 °C for various pressures.

decreases. The lattice parameters for the ($Zr_{0.8}$, $Nb_{0.1}$, $Ta_{0.1}$)C phase are recorded in **Table 4.6**.

Raman spectroscopy was performed on one sample that was sintered at 2000 °C for a 5 minute hold time with an applied pressure of 90 MPa. The Raman spectroscopy results are shown in **Figures 4.26a-g**. The grey matrix represents the bulk material, ($Zr_{0.8}$, $Nb_{0.1}$, $Ta_{0.1}$)C, with a distinct signal at 528 cm^{-1} (shown in **Figures 4.26d and e**). The two bright spots on the left side of the micrograph are TaC agglomerations, with a distinct signal at 164 cm^{-1} (shown in **Figures 4.26b and c**). The dark spots distributed throughout the micrograph are carbon pockets, with a signal at 1331 cm^{-1} (shown in **Figures 4.26f and g**).

The EDS results are shown in **Figure 4.27a-f**. The bulk matrix is a combination of Zr, Nb, Ta, and C with an even distribution of oxygen. The bright spot on the left side of the micrograph aligns with a Ta agglomeration, void of Nb and Zr, shown in **Figures 4.27d-f**. The dark spots in **Figure 4.27a** align with carbon concentrations (**Figure 4.27b**) and are void of Nb, Ta, and Zr (**Figures 4.27d-f**). Oxygen was distributed evenly throughout the sample, shown in **Figure 4.27c**.

4.5 Sintering Activation Energy Results

4.5.1 Bernard-Granger and Guizard Method Results

The sintering activation energy was calculated using the SPS displacement data from the consolidation of ($Zr_{0.8}$, $Nb_{0.1}$, $Ta_{0.1}$)C samples with an applied load of 30 MPa, a hold time of 5 minutes, and temperatures ranging from 1800 °C to 2000 °C. The final sintered height and the final density of each sample were used in conjunction with the displacement data output from the SPS, to calculate the instantaneous relative density with respect to the sintering temperature (**Equation 3.3**). The relationship of relative density and densification rate with sintering temperature of ($Zr_{0.8}$, $Nb_{0.1}$, $Ta_{0.1}$)C is shown in **Figures 4.28 and 4.29**, respectively. Relative density compared to time and soak time (at constant temperature)

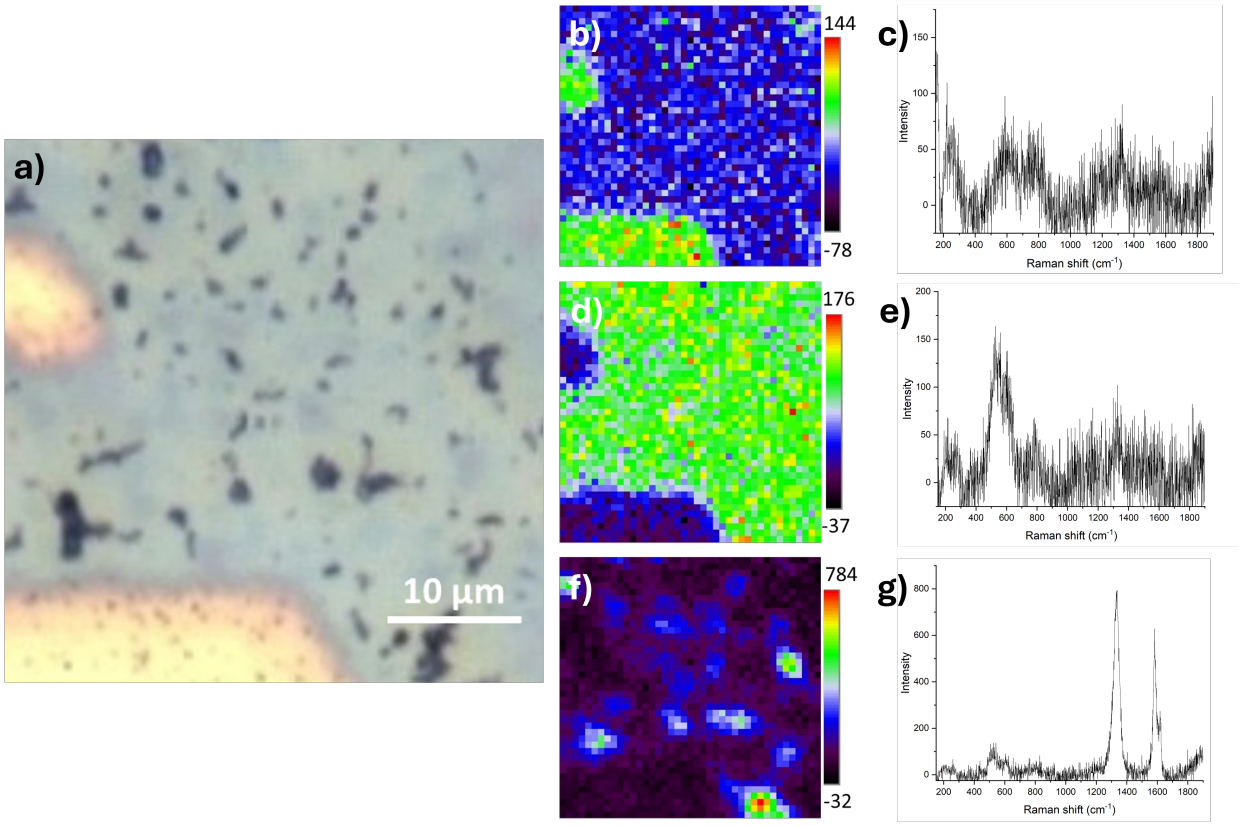


Figure 4.26: a) Micrograph of ($Zr_{0.8}$, $Nb_{0.1}$, $Ta_{0.1}$)C and the Raman maps and spectra of the b-c) bright spot in the micrograph, d-e) the bulk matrix, and f-g) the carbon pockets, respectively.

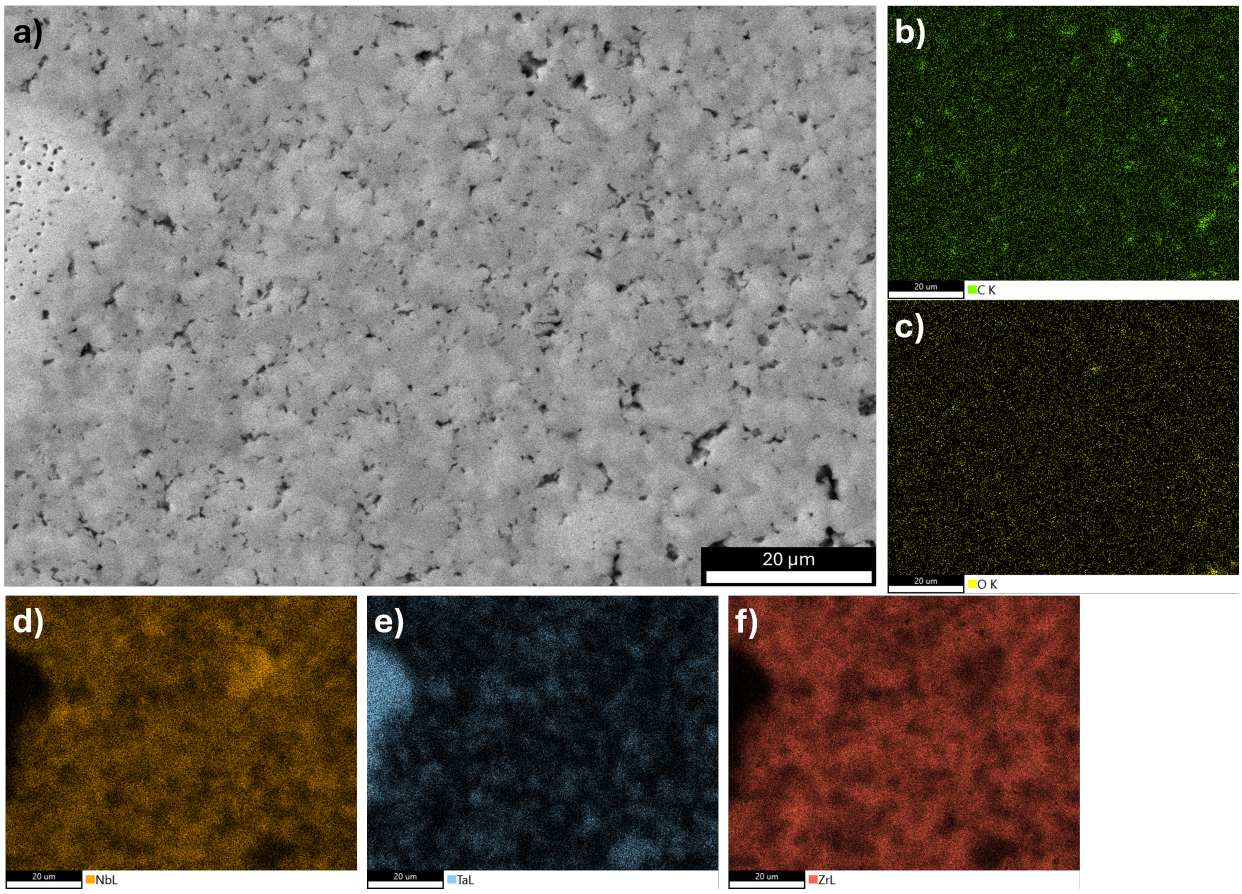


Figure 4.27: a) Secondary electron micrograph of ($Zr_{0.8}$, $Nb_{0.1}$, $Ta_{0.1}$)C and EDS maps of b) carbon, c) oxygen, d) niobium, e) tantalum, and f) zirconium.

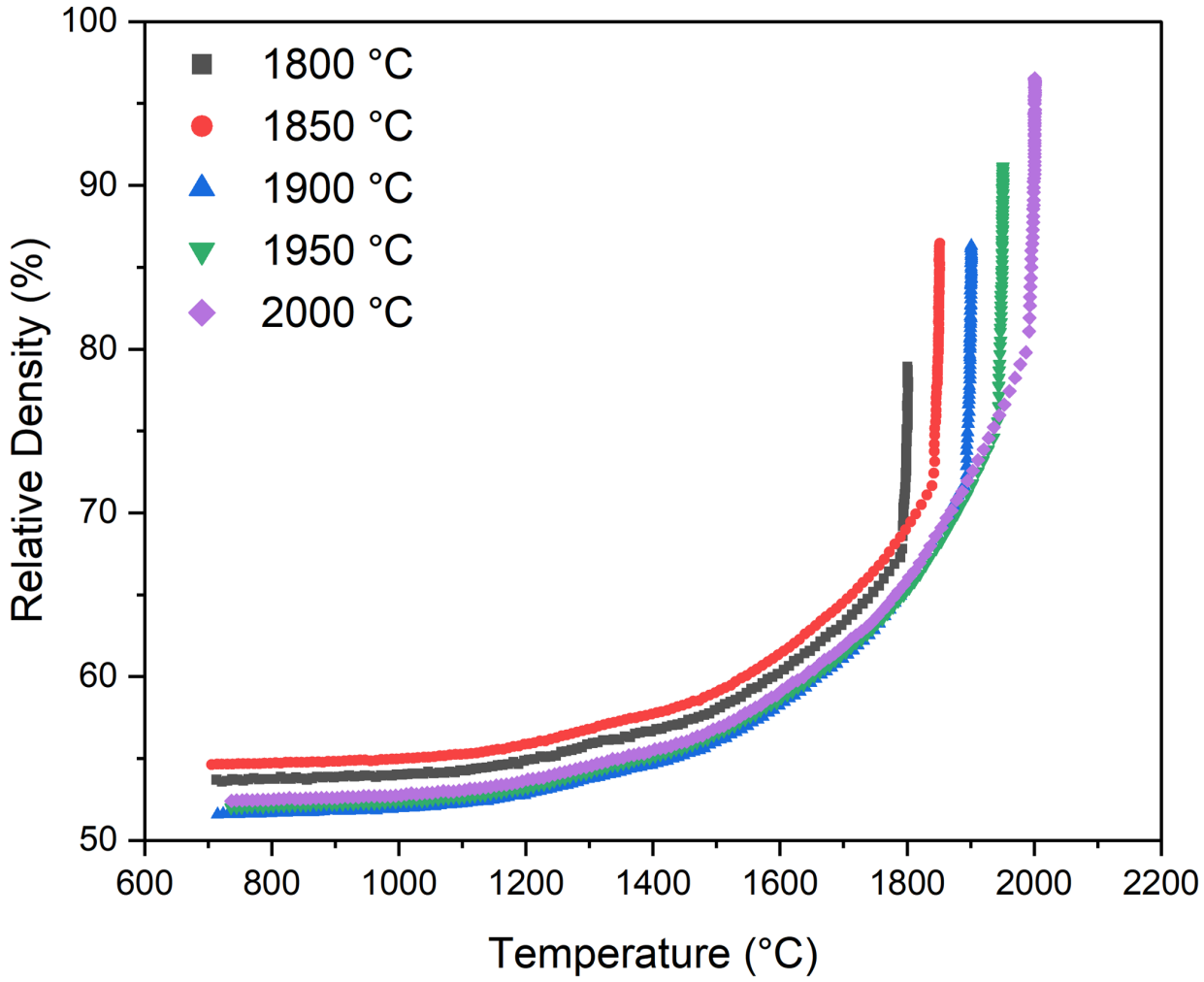


Figure 4.28: Relative density as a function of temperature for ($Zr_{0.8}$, $Nb_{0.1}$, $Ta_{0.1}$)C.

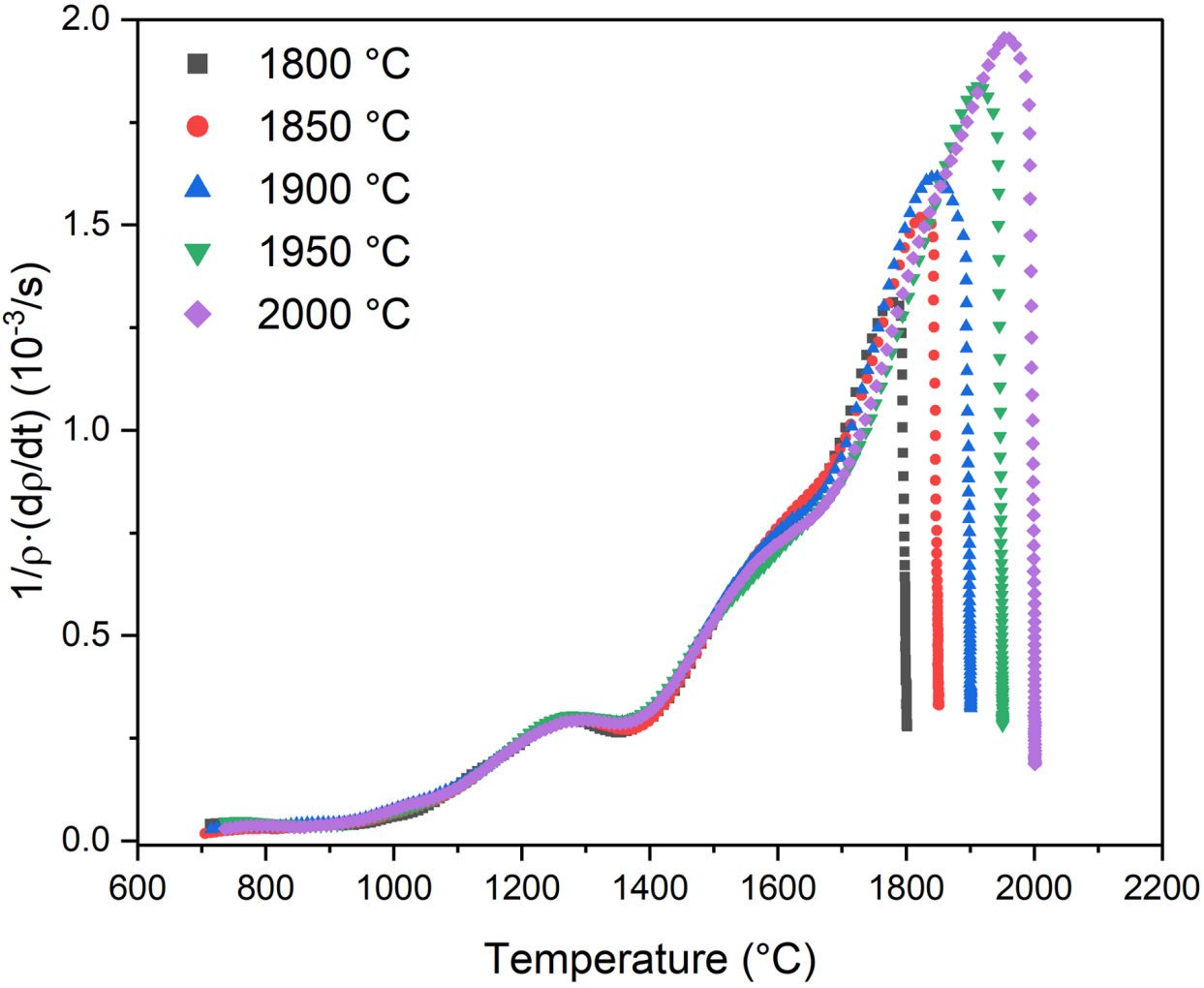


Figure 4.29: Densification rate as a function of temperature for ($Zr_{0.8}$, $Nb_{0.1}$, $Ta_{0.1}$)C.

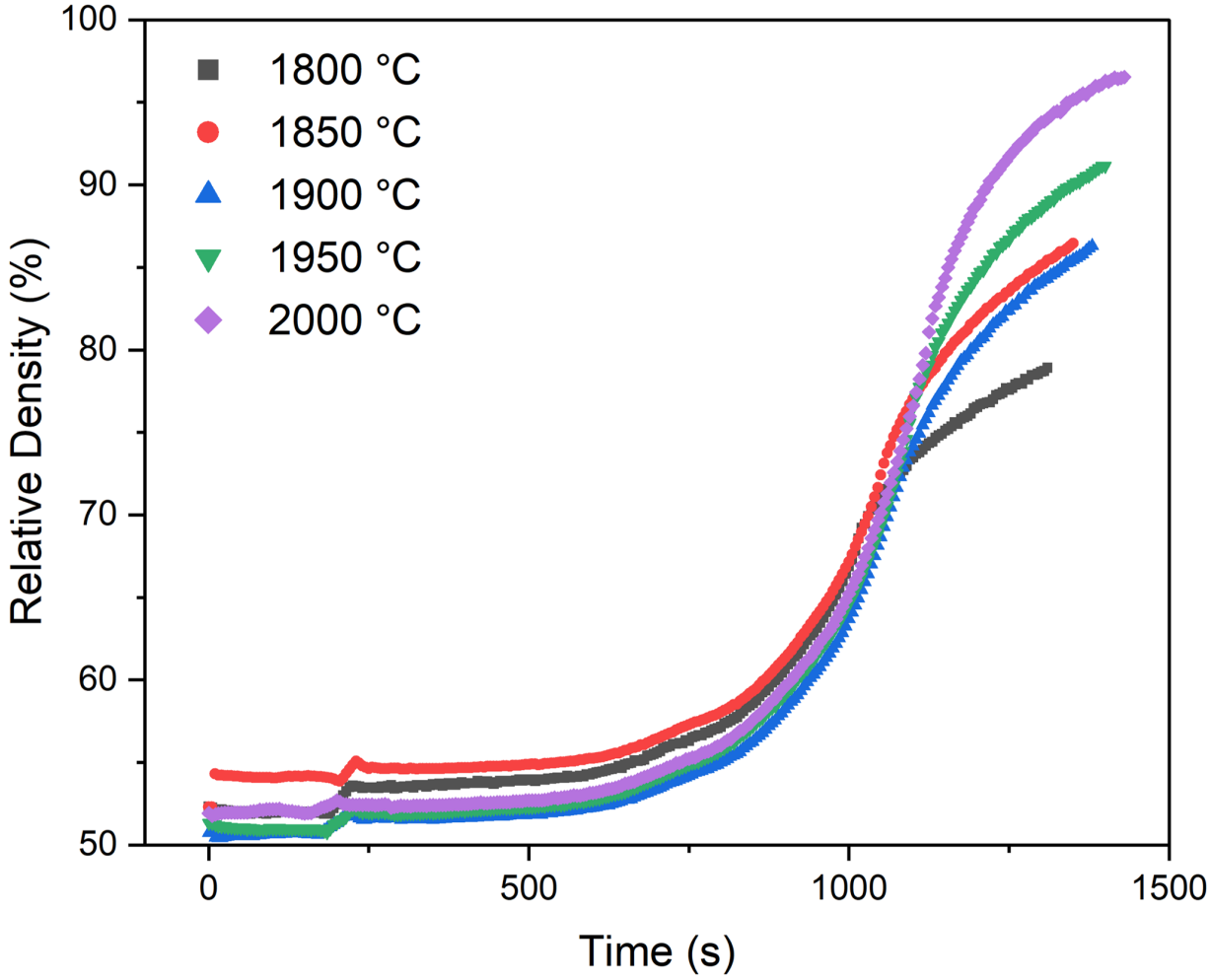


Figure 4.30: Relative density as a function of time for ($Zr_{0.8}$, $Nb_{0.1}$, $Ta_{0.1}$)C.

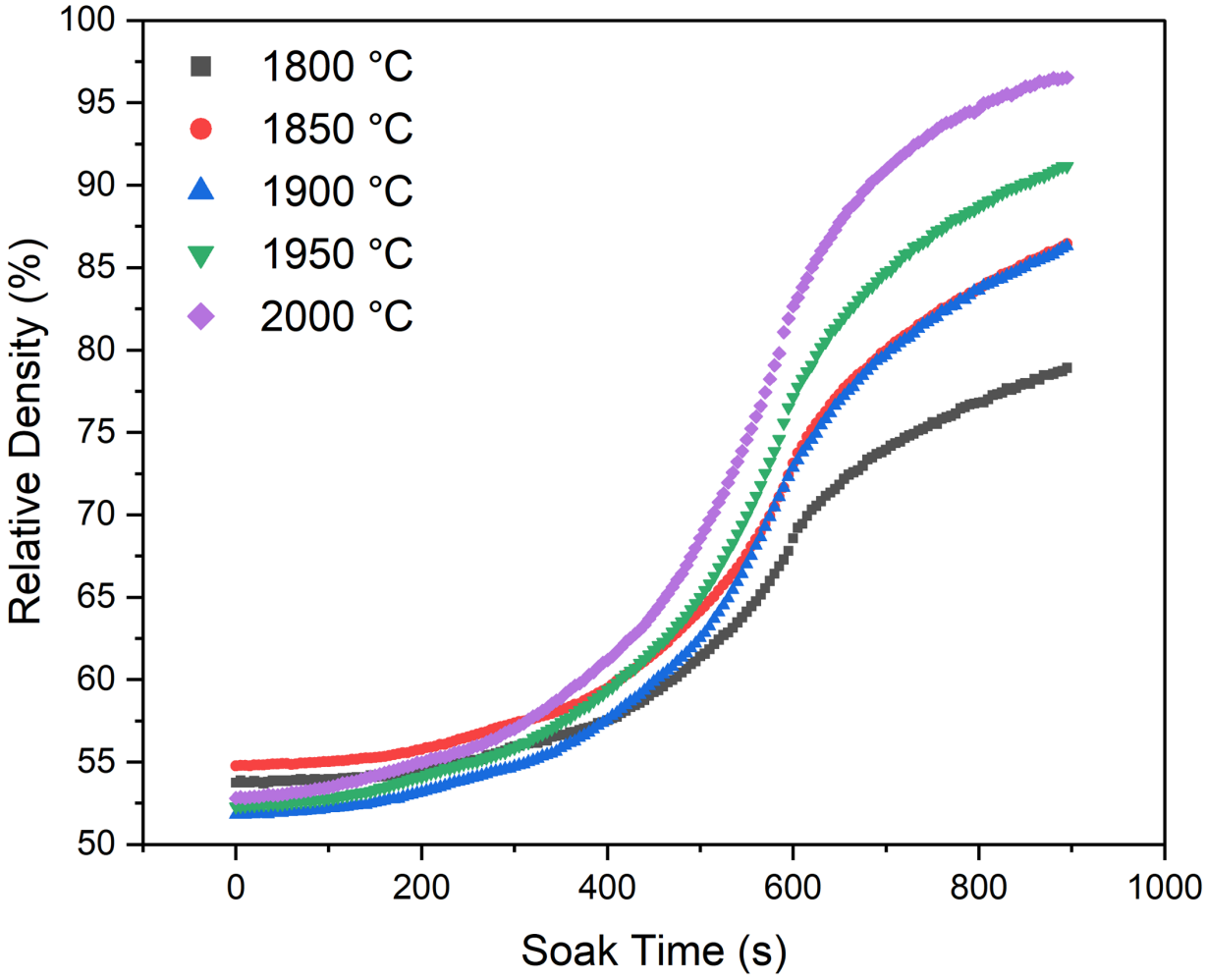


Figure 4.31: Relative density as a function of soak time for $(Zr_{0.8}, Nb_{0.1}, Ta_{0.1})C$.

is shown in **Figures 4.30 and 4.31**, respectively, with the latter figure being a truncated version of the former figure.

To calculate sintering activation energy, the Bernard-Granger model [68] was used (as discussed in **Section 3.2.1**). The temperature range of 1800 °C to 2000 °C was selected since the onset of grain growth occurs at approximately 2000 °C, shown in **Figure 4.7**, and the Bernard-Granger model assumes a constant grain size is maintained. Data from **Figures 4.28, 4.29, and 4.31** was used to determine the densification rate as a function of relative density, which is shown in **Figure 4.32**, and the stress exponent using **Equation 3.8** (shown in **Figure 4.33**). Since the Bernard-Granger model requires a constant temperature, the data shown in **Figure 4.31** was used for the calculations. Using **Equation 3.9**, the activation energy of sintering for ($Zr_{0.8}$, $Nb_{0.1}$, $Ta_{0.1}$)C was determined, with each point on **Figure 4.34** corresponding to an individual sample sintered at a temperature between 1800 °C and 2000 °C. A densification rate of 0.6 was used to calculate the activation energy, since that value fell right in the middle of the soak time for each sample, as seen in **Figure 4.32**. Note that using different values of the densification rate will only slightly change the calculated activation energy (around 1-2%). The stress exponent was determined to be approximately 1.75 and the sintering activation energy was calculated to be 502 kJ/mol.

4.5.2 Young-Cutler Method Results

The activation energy results calculated with **Equation 3.16** from the Young-Cutler method [74] are shown in **Figure 4.35**. Similar to the previous method used to calculate activation energy, this calculation used the SPS displacement data from the consolidation of ($Zr_{0.8}$, $Nb_{0.1}$, $Ta_{0.1}$)C samples with an applied load of 30 MPa, a hold time of 5 minutes, and temperatures ranging from 1800 °C to 2000 °C. An additional sample sintered at 2100 °C was also used in the activation energy calculation, since the Young-Cutler method does not assume a constant grain size during sintering. A clear change in the slope of the graph in **Figure 4.35** occurred around 1850 °C. The sintering activation energies for grain boundary diffusion were 701 kJ/mol and 276 kJ/mol for temperatures below 1850 °C and above 1850

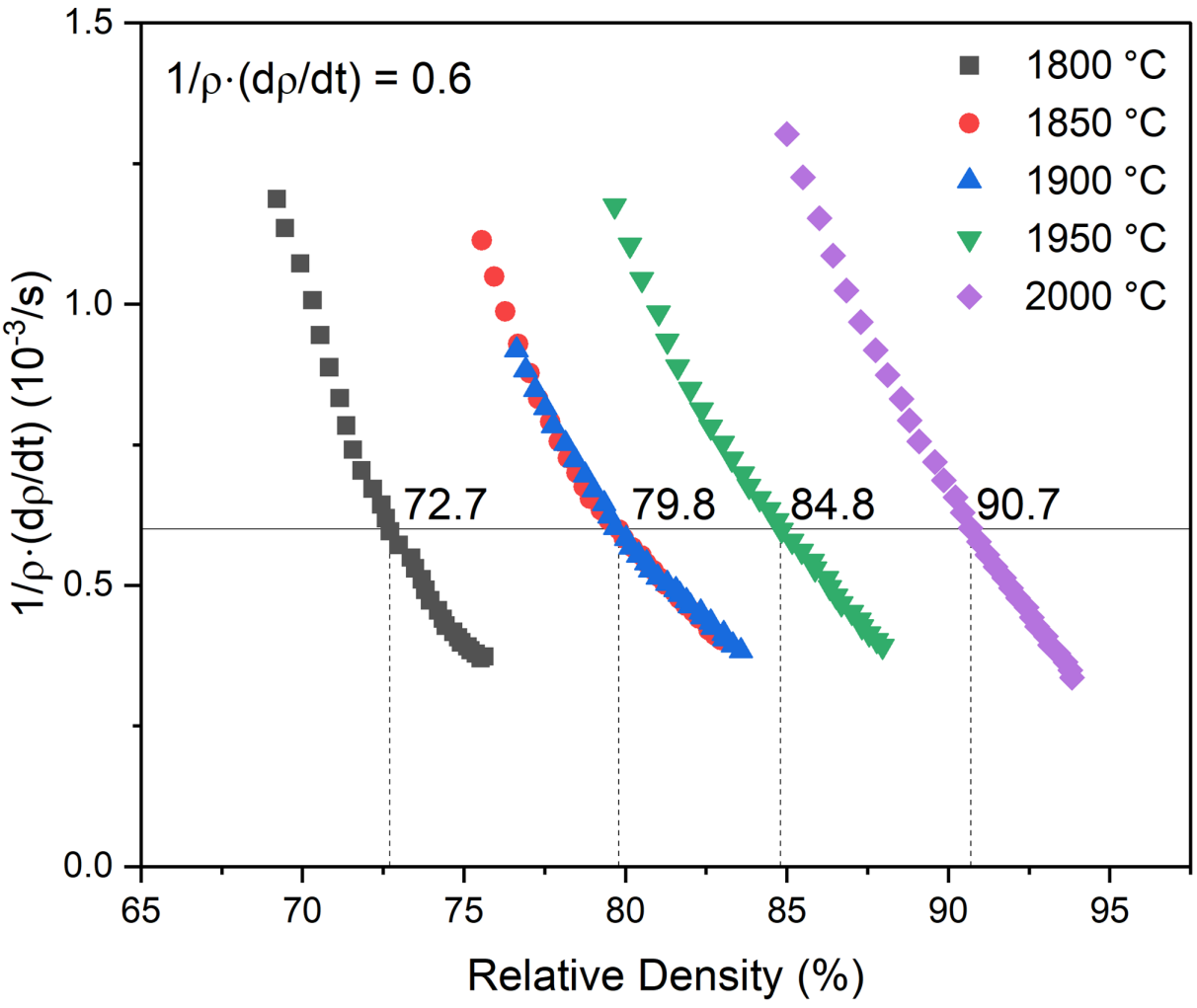


Figure 4.32: Densification rate as a function of relative density for ($Zr_{0.8}$, $Nb_{0.1}$, $Ta_{0.1}$)C.

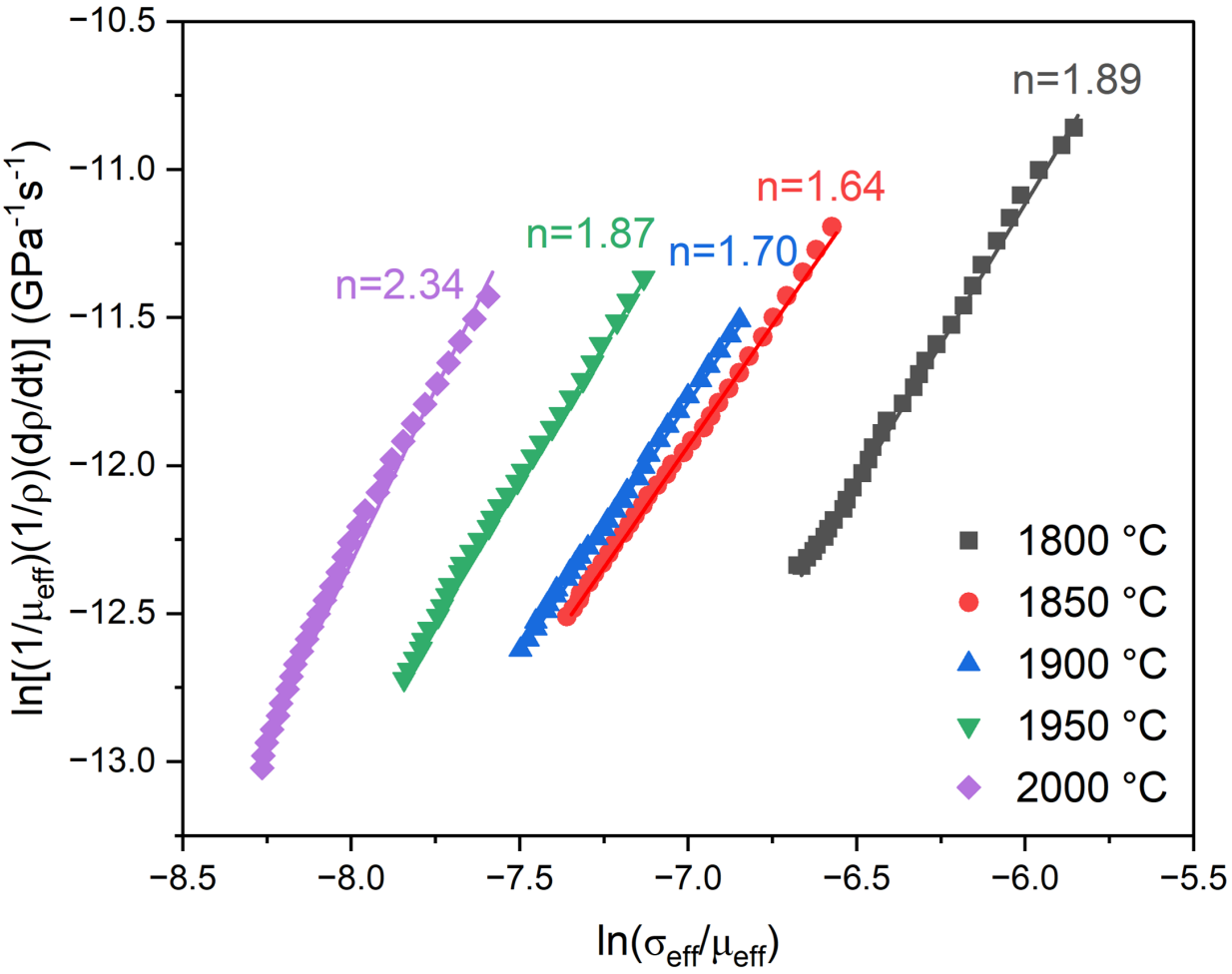


Figure 4.33: Determination of stress exponent n for $(Zr_{0.8}, Nb_{0.1}, Ta_{0.1})C$.

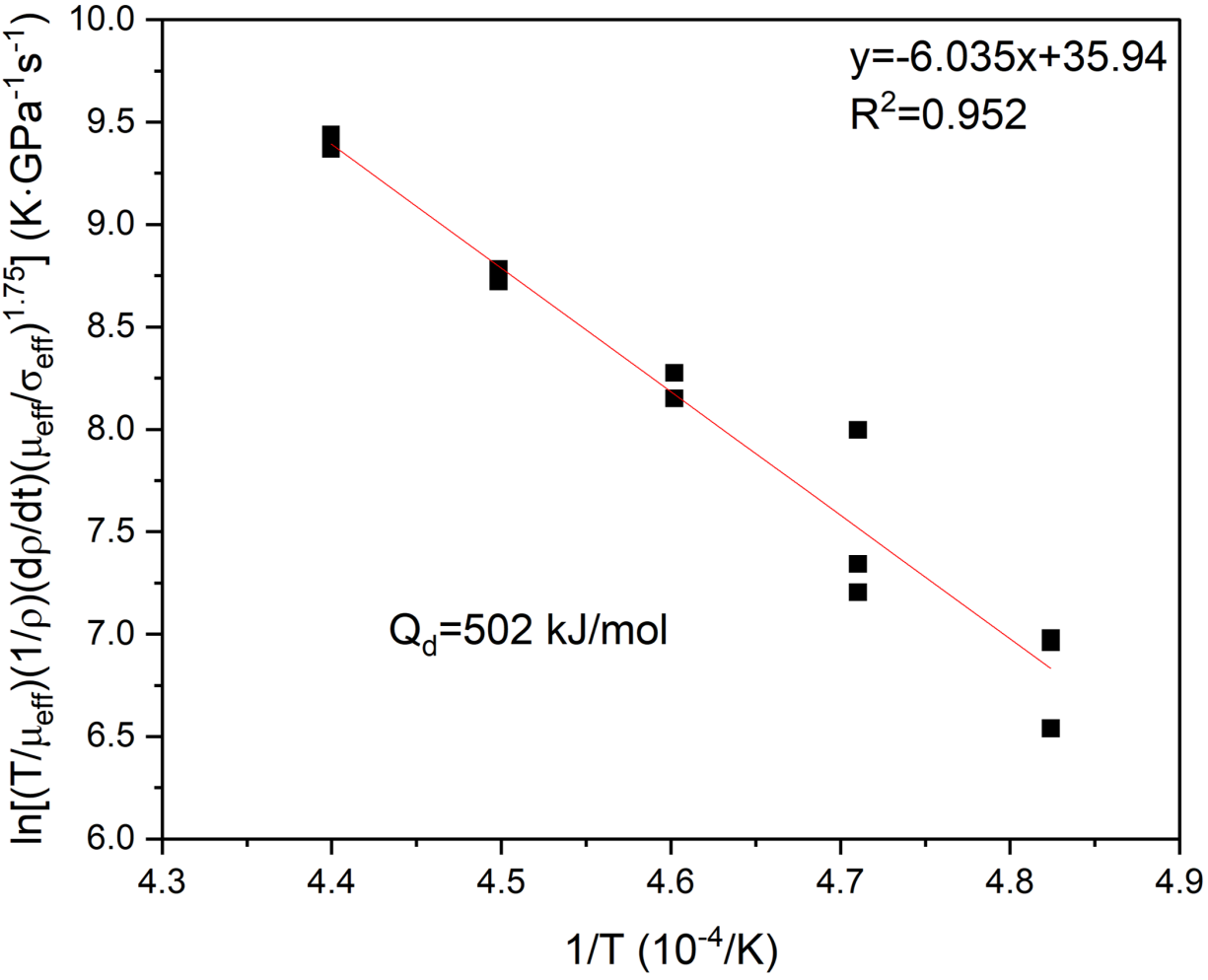


Figure 4.34: Activation energy for sintering of ($Zr_{0.8}$, $Nb_{0.1}$, $Ta_{0.1}$)C.

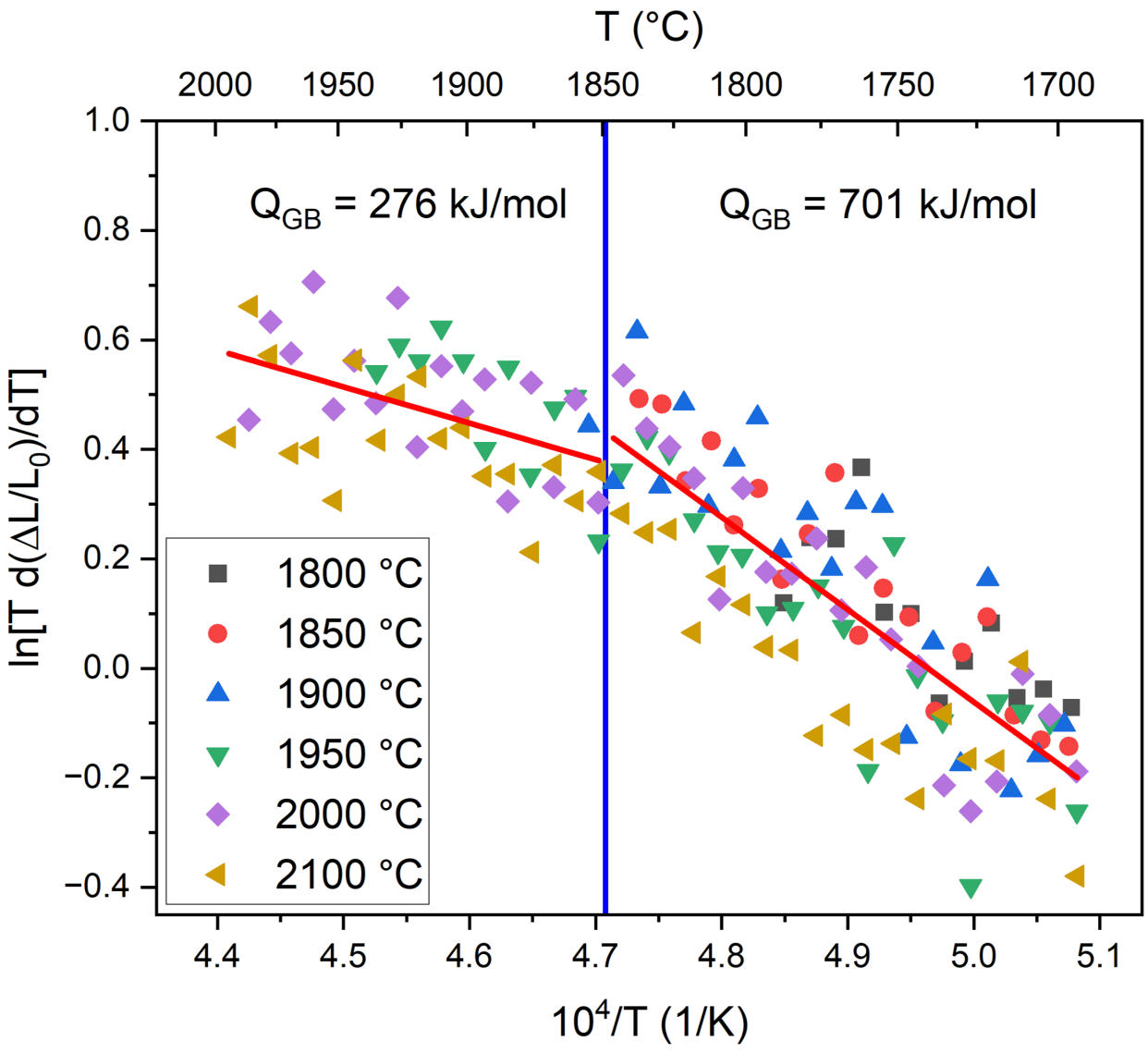


Figure 4.35: Activation energy for sintering of $(Zr_{0.8}, Nb_{0.1}, Ta_{0.1})C$ using the Young-Cutler method.

°C, respectively. The sintering activation energies for volume diffusion were 420 kJ/mol and 166 kJ/mol for temperatures below 1850 °C and above 1850 °C, respectively.

4.6 Grain Growth Activation Energy

Figure 4.36 shows the grain growth of ($Zr_{0.8}$, $Nb_{0.1}$, $Ta_{0.1}$)C samples consolidated in the SPS furnace at 2000 °C and 30 MPa for hold times of 5, 10, and 20 minutes. The hold times of 5, 10, and 20 minutes were selected since the onset of grain growth begins at around 5 minutes (shown in **Figure 4.12**). The coefficient of determination was calculated using grain growth exponents of 2, 3, and 4 (see **Equation 3.18**). The coefficient of determination is the highest at a value of m = 4, and slightly less for a value of m = 3.

Figure 4.37 shows the relationship between $ln(D_t^m - D_0^m)$ and $1/T$ from **Equation 3.19**, using grain growth exponent values of 3 and 4 for samples consolidated in the SPS furnace for 5 minutes with an applied pressure of 30 MPa at temperatures ranging from 1950 °C to 2100 °C. The grain growth activation energies for surface diffusion ($m = 4$) and volume diffusion ($m = 3$) were determined to be 2204 kJ/mol and 1842 kJ/mol, respectively.

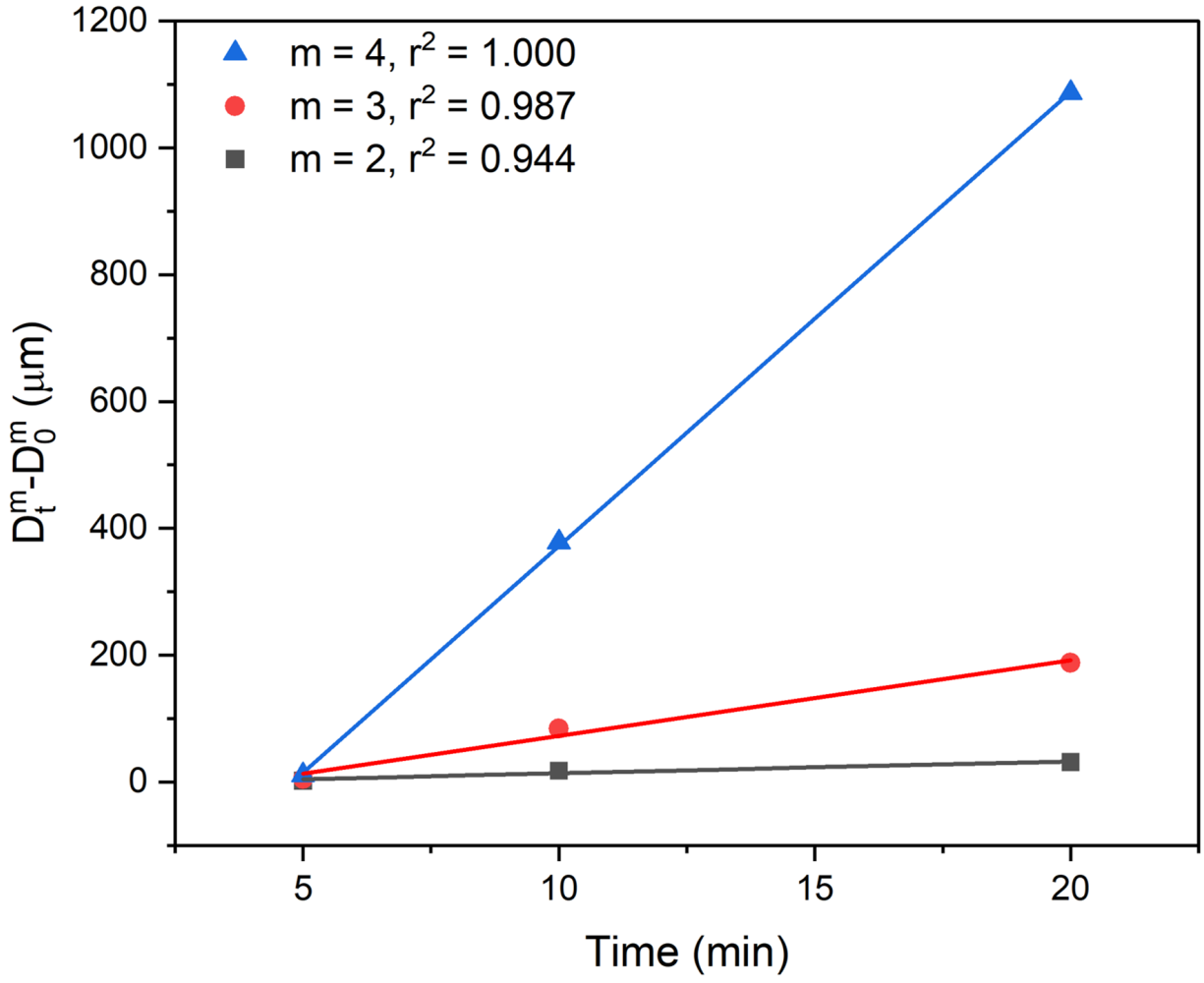


Figure 4.36: Grain growth exponent of ($Zr_{0.8}$, $Nb_{0.1}$, $Ta_{0.1}$)C.

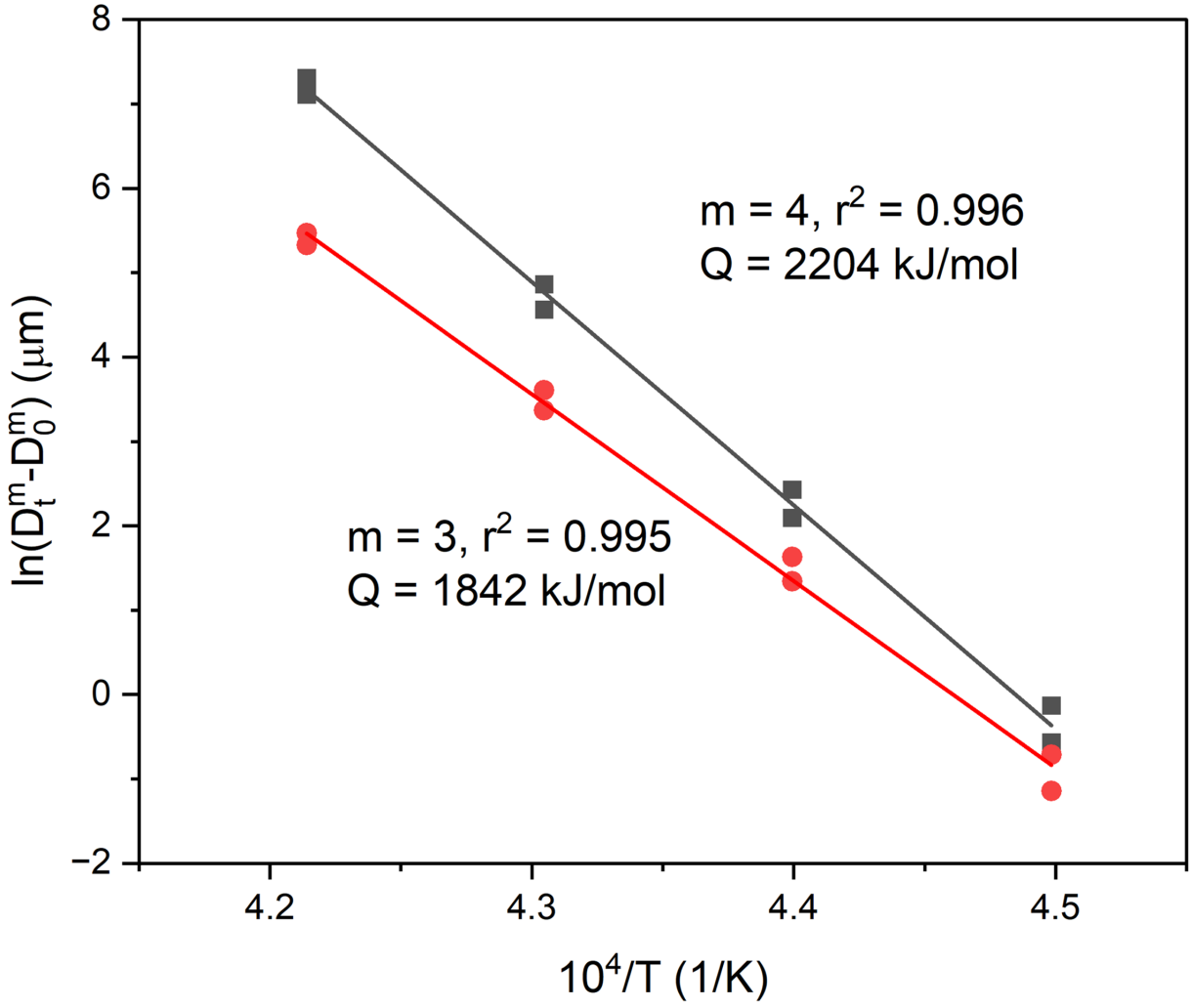


Figure 4.37: Activation energy for grain growth of $(Zr_{0.8}, Nb_{0.1}, Ta_{0.1})C$.

Chapter 5

Discussion

5.1 Powder Characterization

The NbC and TaC powders used for this study had large agglomerations of individual, micron sized particles, while the ZrC powder was free of any significant amount of agglomerations, as seen in **Figures 4.3 and 4.4**. The SEM micrographs of the powders showed that even the large clumps seen in the NbC and TaC powders were made up of smaller micron sized particles stuck together. The Raman spectra and EDS maps shown in **Figure 4.26** and **Figure 4.27** show the presence of a large (>20 μm in diameter) TaC agglomeration. More rigorous powder mixing methods (such as ball milling or planetary mixing) may be required in order to more effectively break up the larger powder agglomerations when mixing the powders together to create a tri-carbide powder.

The anion to cation ratio for each mono-carbide was calculated using published equations derived empirically from experimental results [78, 79, 80] using lattice parameters determined from XRD spectra, as well as from the elemental and phase concentrations found from LECO, XRF, and XRD results. **Figure 5.1** illustrates the steps for determining the stoichiometry of the ZrC (actually ZrC_xO_{1-x}) powder. First, the LECO combustion concentrations of C, O, and N content were subtracted out, leaving the composition of heavy elements remaining. Then, that number was multiplied by the concentration of the predominant metal (e.g. Zr in ZrC) from the XRF results (e.g. 99.9 wt%). Next, the atoms attributed to impurity phases (e.g. ZrO_2 and NbO_2) were subtracted out. The O/M (e.g. O/Zr) ratio was determined,

which was then used to determine the C/M ratio (e.g. C/Zr), representing the carbon contained in the NaCl-structured lattice. The remaining carbon was assumed to be excess, potentially forming graphite inclusions in the microstructure.

The evenly distributed oxygen seen in the EDS maps in **Figure 4.27** indicates that the oxygen was located in the NaCl-structured lattice of the sintered ($Zr_{0.8}$, $Nb_{0.1}$, $Ta_{0.1}$)C samples. In contrast, the carbon distribution in the Raman spectra and EDS maps, shown in **Figure 4.26** and **Figure 4.27**, respectively, indicate that in addition to carbon in the rock salt structured lattice, there are also clusters of free carbon in the microstructure. These carbon clusters also appear as dark spots in the micrographs of the high density samples, found at the grain boundaries. The presence of dispursed oxygen and pockets of carbon may have an effect on the sintering behavior of the ($Zr_{0.8}$, $Nb_{0.1}$, $Ta_{0.1}$)C samples.

The results of the anion to cation ratio approximation are shown in **Table 5.1**. The niobium and zirconium powders appear to be the oxycarbides $NbC_{0.91}O_{0.09}$ and $ZrC_{0.89}O_{0.11}$, instead of NbC and ZrC. The tantalum based powder contains much less oxygen, which is seen in the calculation of anion to cation ratio, resulting in $TaC_{0.99}O_{0.01}$. Since the error of the purity calculations is most likely greater than 1%, the tantalum based powder can be assumed to be primarily TaC. The niobium and zirconium oxycarbide powders may have resulted from the reduction of temperature and heat treatment time, due to newer manufacturing methods used to make NbC and ZrC [81].

5.2 Relative Density, Hardness, and Grain Size

The relationships between Vickers hardness and grain size versus relative density for all samples in this study are shown in **Figure 5.2**. In general, independent of the sintering parameters, the hardness values increase approximately linearly with the relative density. Across all three phases of this study, the hardness of each sample follows a linear trend with the same slope with the exception of the samples sintered in an argon purged atmosphere. The slope of the linear relationship between Vickers hardness and relative density for the Phase 3 samples sintered in argon (the green fitted line in **Figure 5.2**) is almost double the slope for the rest of the samples sintered in a vacuum (the red fitted line in **Figure 5.2**). The

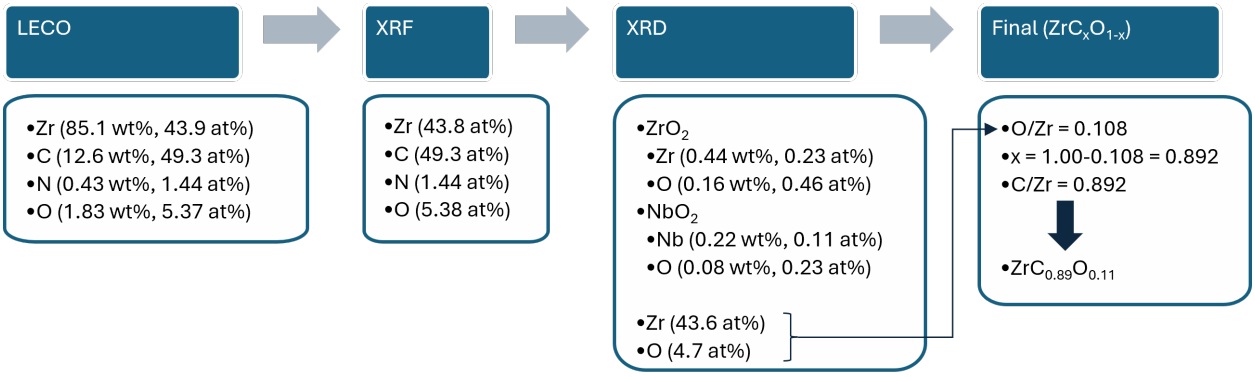


Figure 5.1: Flow chart for calculating C/M ratio of ZrC.

Table 5.1: Calculated anion to cation ratio (C/M).

Powder	**Lat. P. (Å)**	**C/M from Lat. P.**	**C/M from LECO, XRF, and XRD**	**Calc. Excess C (wt%)**
NbC (NbC_xO_{1-x})	4.465	0.905[a]	0.906	1.80
TaC (TaC_xO_{1-x})	4.451	0.960[b]	0.986	0.30
ZrC (ZrC_xO_{1-x})	4.687	0.862[c]	0.892	2.66

[a] *Calculated using equation from Storms and Krikorian [78]*
[b] *Calculated using equation from Bowman [79]*
[c] *Calculated using equation from Mitrokhin et al. [82], republished by Jackson and Lee [80]*

linear fit equations below (**Equations 5.1 and 5.2**) show the change in slope between the samples sintered in a vacuum versus the samples sintered in an argon purged environment, with slopes of 0.634 and 1.22, respectively.

$$H = -44.0 + 0.634RD \tag{5.1}$$

$$H = -102 + 1.22RD \tag{5.2}$$

Where H is the hardness of the sample in GPa and RD is the relative density.

The relationship between grain size and relative density, shown in **Figure 5.2**, is also similar across all samples in this study, with the exception of the samples sintered in an argon purged environment. For samples sintered in a vacuum, the grain size is generally constant until about 90% of the theoretical density of ($Zr_{0.8}$, $Nb_{0.1}$, $Ta_{0.1}$)C, where it begins to increase exponentially (the blue exponentially fitted curve in **Figure 5.2**). The equation for the exponentially fitted curve is shown below:

$$GS = \left(1.11 * 10^{-23}\right) \exp\left(\frac{RD}{1.82}\right) + 1.37 \tag{5.3}$$

Where GS is the grain size in μm and the y-intercept value, 1.37 (μm), represents the initial grain size. The approximate average particle size of the tri-carbide powder mixture can be approximated by calculating a weighted average (using the atomic ratios of 0.1 for NbC, 0.1 for TaC, and 0.8 for ZrC) of the mono-carbide starting powder particle sizes, which are 1.45 μm, 1.60 μm, and 1.35 μm for NbC, TaC, and ZrC respectively (from **Figure 4.2**). The calculated average particle size of the ($Zr_{0.8}$, $Nb_{0.1}$, $Ta_{0.1}$)C powder mixture is 1.39 μm which aligns with the y-intercept of the exponential fit function for the grain size, which is 1.37 μm.

Additionally, seen in **Figure 5.2**, rapid grain growth begins at about 96% of the theoretical density. For samples sintered in an argon purged environment, the grain size appears to decrease at higher relative densities. This decrease may be slightly misleading, because, at higher pressures, the densification mechanism generally changes [64, 65, 66].

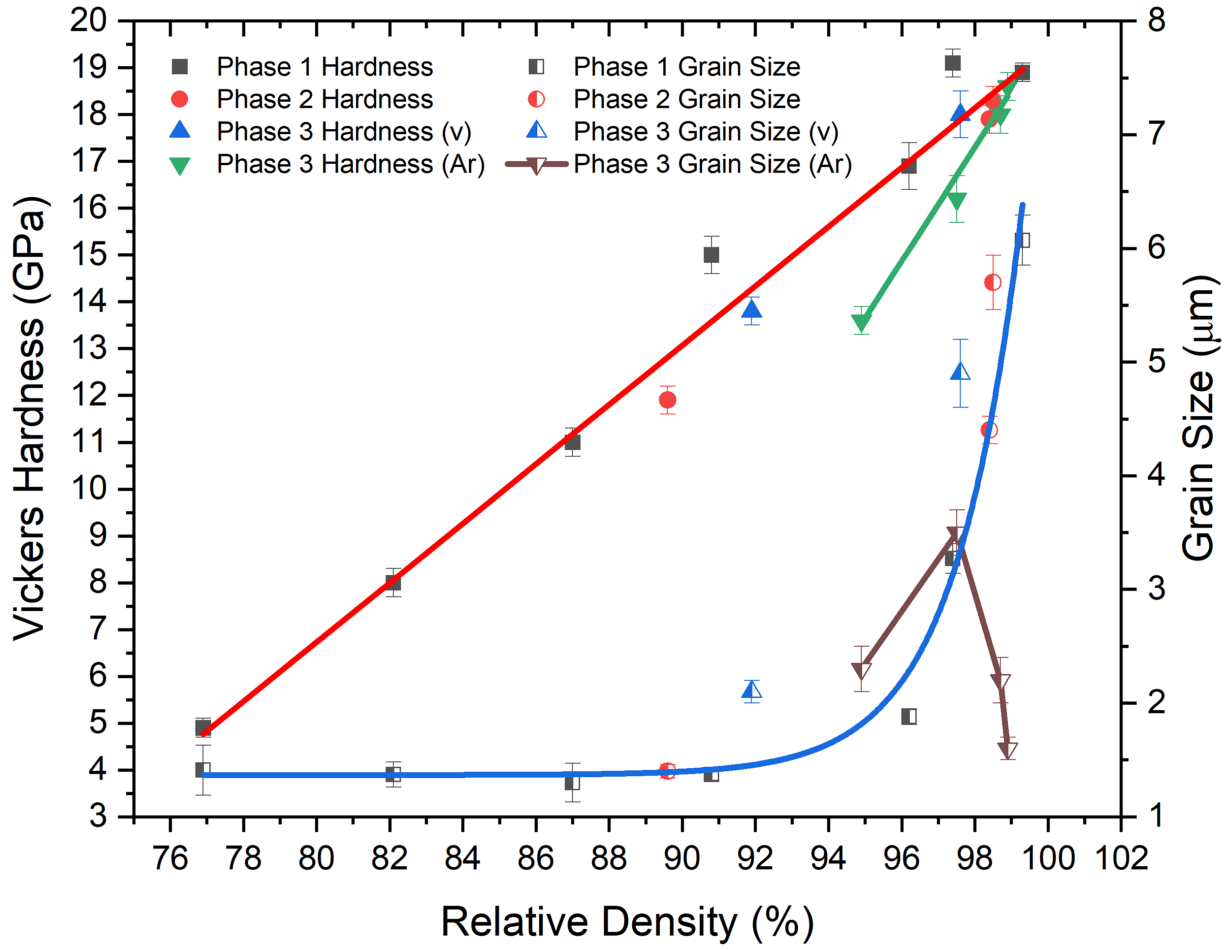


Figure 5.2: Vickers hardness and grain size as a function of relative density for all ($Zr_{0.8}$, $Nb_{0.1}$, $Ta_{0.1}$)C samples consolidated in the SPS.

The onset of rapid grain growth, T_g, was determined to be approximately 2000 °C for a 5 minute hold time and an applied pressure of 30 MPa. Longer hold times at T_g led to an increase in grain growth. Sintering temperatures less than or equal to T_g for a hold time of 5 minutes ultimately led to little to no grain growth. While sintering at 2000 °C with a 5 minute hold time, increasing pressure led to an increase in densification. In order to reach full densification, it is necessary to avoid trapped pores [64, 65, 66]. The formation of trapped pores normally occurs when the migration of grain boundaries is faster than the pores, leading to pore-boundary separation[64]. The pore-boundary separation causes the formation of intragranluar pores, or trapped pores, which generally prevents full densification. At temperatures lower than T_g, the grain boundaries do not move, or only move very slowly, which allows for full densification given a high enough applied pressure [64, 65]. Temperatures higher than T_g should be avoided to minimize the number of trapped pores. Additionally, elevated pressures generally cause plastic deformation. The combination of high pressure and low temperature (at or below T_g) mitigates the formation of trapped pores, which allows for densification via plastic deformation. The densification of a sample with little to no grain growth is an indication of plastic deformation being the dominant densification mechanism [64, 65]. Higher pressure during sintering leads to a higher contact force between particles. This higher contact force promotes plastic yielding, which leads to an increase in the contact area between particles, causing densification. With a high enough pressure, the dominant densification mechanism is plastic deformation [65].

Table 5.2 shows the impact of relative density on the hardness and grain size of samples sintered in a vacuum. The top half of the table lists samples with a relative density of about 90% and the bottom half of the table shows nearly fully dense samples. Regardless of the time, temperature, and pressures during sintering, the grain size and hardness values are nearly identical for the samples with similar relative densities. **Figure 5.3** shows the secondary electron micrographs of the samples listed in **Table 5.2**. In general, the microstructures of the samples with lower relative densities (**Figures 5.3 a, c and e**) are similar to one another and the samples with higher relative densities (**Figures 5.3 b, d, and f**) are similar as well.

Table 5.2: Impact of temperature, hold time, and applied pressure on RD, grain size, and Vickers hardness

	Phase	Temp. (°C)	Time (min.)	Press. (MPa)	RD (%)	Grain Size (μm)	Vickers H. (GPa)
Low	1	1900	5	30	87.0	1.3	11.0
RD	2	2000	1	30	89.6	1.4	11.9
∼90%	3	2000	5	10	91.9	2.1	13.8
High	1	2100	5	30	99.3	6.1	18.9
RD	2	2000	20	30	98.5	5.7	18.3
∼99%	3	2000	5	60	97.6	4.9	18.0

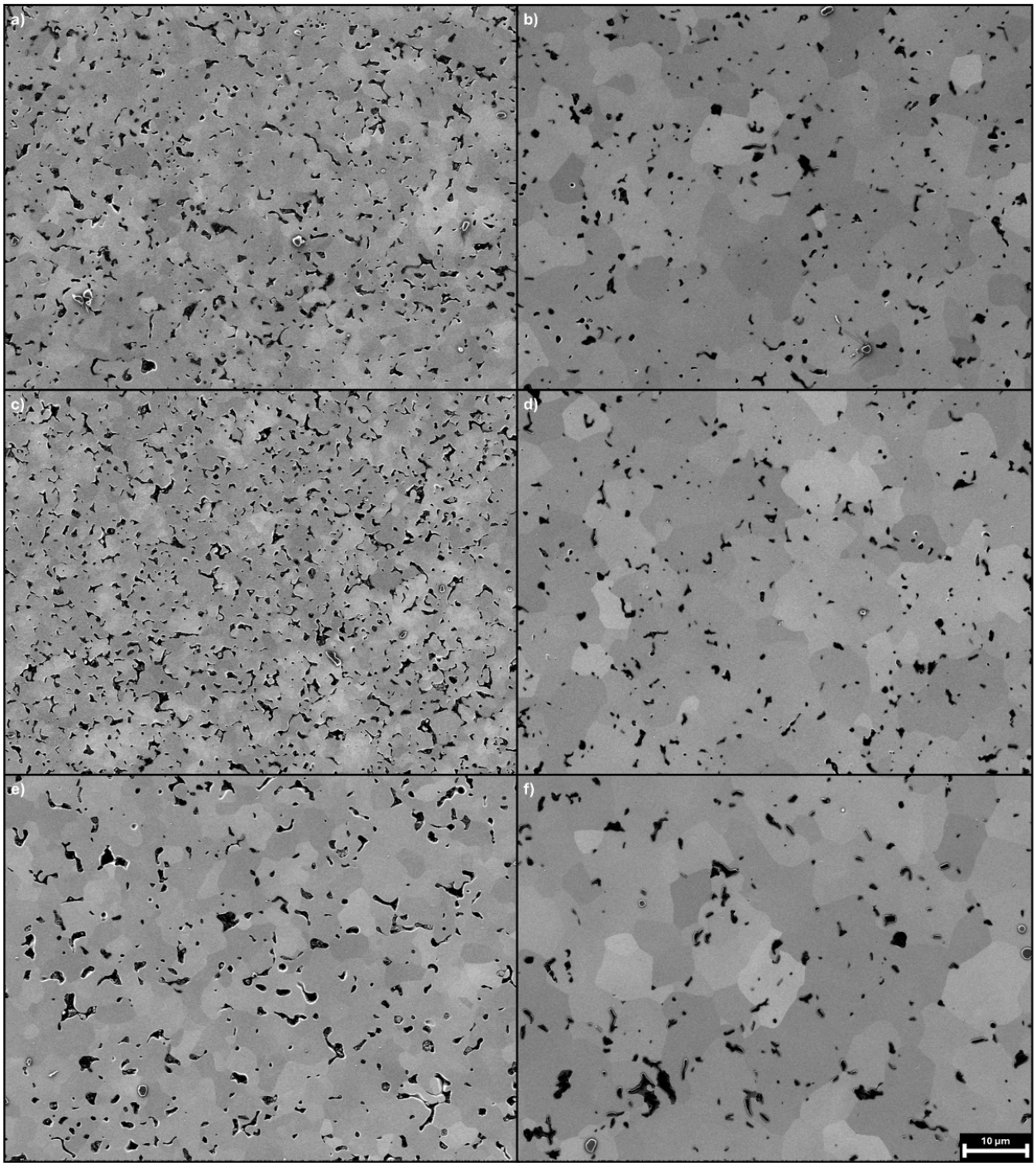


Figure 5.3: Microstructural comparison of ($Zr_{0.8}$, $Nb_{0.1}$, $Ta_{0.1}$)C samples sintered: with an applied pressure of 30 MPa for a hold time of 5 minutes at a) 1900 °C and b) 2100 °C; with an applied pressure of 30 MPa at 2000 °C with a hold time of c) 1 minute and d) 20 minutes; and at 2000 °C with a hold time of 5 minutes and an applied pressure of e) 10 MPa and f) 60 MPa.

Figure 5.4 is a graph of relative density versus lattice parameter for all samples in this study. There is a slightly sublinear relationship between relative density and lattice parameter, following Vegard's law, which predicts an approximately linear relationship between the lattice parameter and relative density. Using the lattice parameters from the starting powders, from **Table 5.1**, Vegard's law can be used to calculate the expected lattice parameter of the ($Zr_{0.8}$, $Nb_{0.1}$, $Ta_{0.1}$)C samples. The calculated lattice parameter for ($Zr_{0.8}$, $Nb_{0.1}$, $Ta_{0.1}$)C, using values of 4.465 Å, 4.451 Å, and 4.687 Å (from **Table 5.1**) for NbC, TaC, and ZrC, respectively, is 4.641 Å. The lattice parameters from the most dense sintered ($Zr_{0.8}$, $Nb_{0.1}$, $Ta_{0.1}$)C samples are approximately 4.644 Å, which approximately aligns with the calculated value using Vegard's law. The slight difference between the calculated and observed lattice parameters may be due to the fitting errors from the automated Rietveld refinement used to determine the phases and lattice parameters. It has also been shown that a higher oxygen content in oxycarbides will lead to a reduction in lattice parameter [81], which may be happening in this material. Additionally, any variations in stoichiometry due to errors in the atomic ratios of the powders while creating the mixture, may influence this result.

5.3 High Pressure Runs and Sintering Atmosphere

The sintering atmosphere plays an important role during densification. The vacuum environment led to destructive chemical erosion of the die and punches during the first higher pressure sintering run at 60 MPa. The chemical erosion reduced the diameter of the punches after a single sintering run. As a result, all subsequent SPS operations at 60 and 90 MPa were conducted in an argon purged environment, where minimal chemical erosion of the graphite tooling was observed throughout the duration of the study.

Also during the higher pressure runs, grade G540 graphite tooling was used, which is rated for higher pressures. However, as seen in **Table 3.1**, the electrical resistance and thermal conductivity of the high pressure die (grade G540) are different than those of the standard die (grade ET-10). The higher electrical resistance in the die leads to a slightly different path of the DC pulsed current passing through the graphite die and specimen powder. The alternate

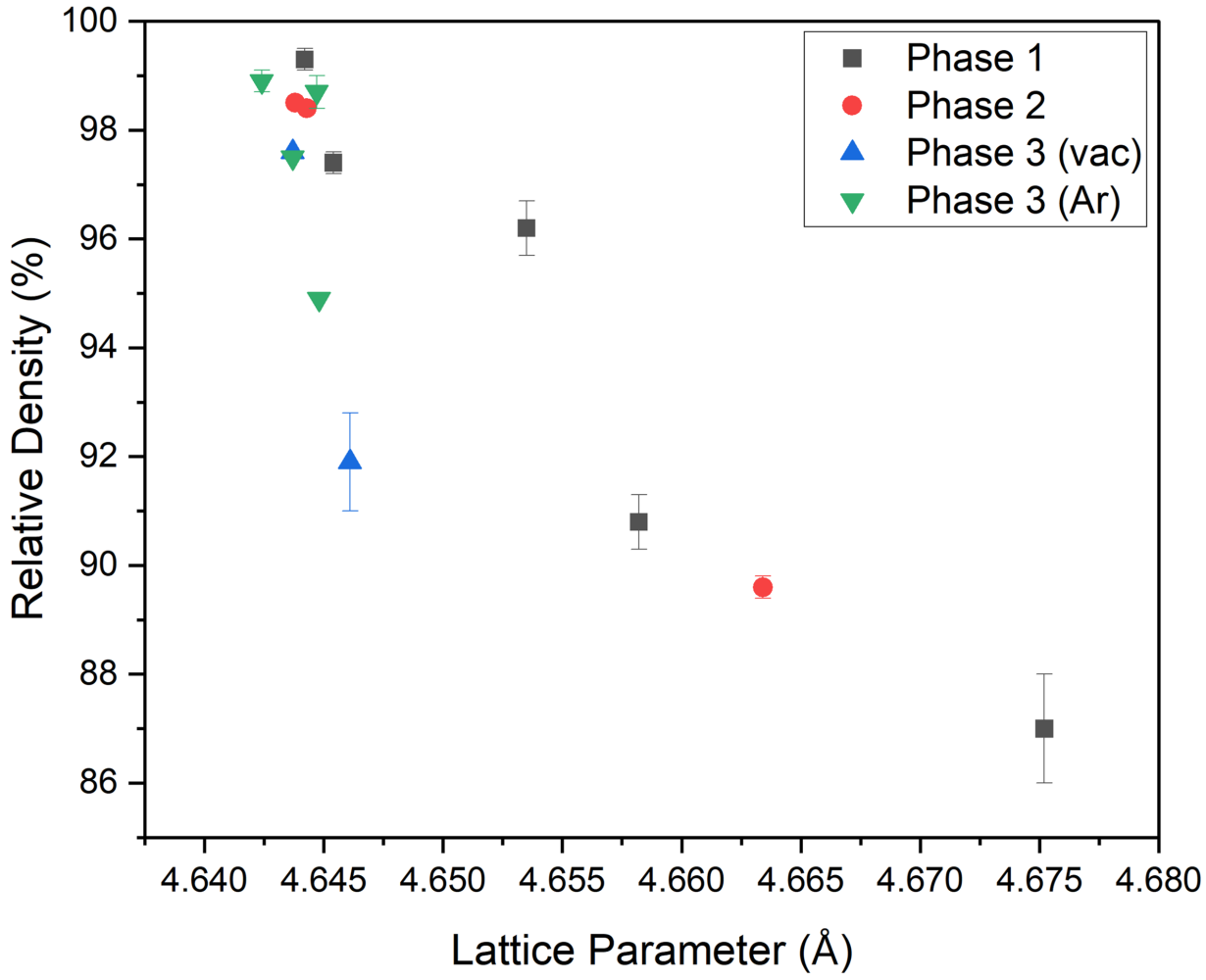


Figure 5.4: Comparison of relative density versus lattice parameter for all ($Zr_{0.8}$, $Nb_{0.1}$, $Ta_{0.1}$)C samples.

path of the current may lead to a difference in densification or temperature gradient radially throughout the sample. The lower thermal conductivity of the graphite also leads to a higher temperature gradient across the wall of the die. Since the SPS furnace is controlled based on the temperature input from the die wall, a higher temperature difference between the outer and inner wall of the die would lead to the center of the sintered sample being a higher temperature (for a die with lower thermal conductivity). Moreover, the current from the SPS furnace required to reach a set temperature would be higher if the temperature gradient across the wall of the graphite die was higher, since the actual centerline temperature of the die would be higher. Therefore, as seen in this study, the higher grade graphite of the high pressure die leads to significant differences in sample sintering behaviors.

Unlike the results seen while sintering in a vacuum (**Figures 4.7, 4.12, and 4.19**), sintering in an argon purged environment led to different relationships between relative density, grain size, and hardness with respect to pressure. **Figure 4.20** shows an initial decrease in density and hardness from 15 MPa to 30 MPa. From 30 MPa to 90 MPa, the relative density and hardness increased with increasing pressure. During the 15 MPa and 90 MPa sintering runs using the high pressure die, the SPS voltage approached the upper setpoint and the voltage had to be controlled manually. This manual control caused the hold temperature to be slightly lower than the target hold temperature (within 50 °C) for the first minute or two of the sintering run. A 10 MPa sintering run using the high pressure die was attempted, but even with manual control of the voltage, a high voltage error occurred, prematurely ending the sintering evolution. Taking manual control of the voltage could have impacted the relative density, hardness, and grain size of the samples and may explain the discontinuity in the results, shown in **Figure 4.20**, **Figure 4.21**, and **Figure 5.2**. The manual control operation could account for the slight difference in the density, a 2% difference, between the 15 MPa and 30 MPa sintering runs.

Another explanation could be that a threshold pressure has been observed at the point where the applied pressure begins to exceed the pressure driven by the intrinsic curvature of the particles [83]. When this threshold is overcome, the effect of the applied pressure becomes more influential. Pressure not only promotes densification by raising the driving force of sintering, encouraging the rearrangement of particles, and enhancing creep, it also reduces

diffusivity, leading to less grain growth and therefore inhibiting grain boundary mobility [83]. It is possible that this pressure threshold is modified by the sintering atmosphere, leading to the different densification of samples in argon versus a vacuum.

5.4 Sintering Activation Energy

Two separate methods were used to calculate the apparent sintering activation energy; one method was proposed by Bernard-Granger and Guizard [68], and the other was proposed by Young and Cutler [74]. The method proposed by Bernard-Granger and Guizard is outlined in **Section 3.2.1** and is based on the steady state creep model. During SPS, the linear strain rate is equivalent to the densification rate, which is analogous to high temperature creep [68, 70]. The critical assumptions for this densification method are that the activation energy is calculated based on sintering data during an isothermal period with a constant grain size. By maintaining a constant grain size under isothermal conditions, the underlying densification mechanism can be more easily identified [70]. Furthermore, the SPS compaction pressure and the Young's modulus of the sintered material are accounted for with the instantaneous effective stress and instantaneous effective shear terms, defined in **Equations 3.4 and 3.5**. Using this method, the apparent densification method, and its associated activation energy, were determined. Since constant grain size is one of the base assumptions for this method, only samples sintered between 1800 °C and 2000 °C, which had approximately the same grain size, were used in this calculation of densification activation energy. The values obtained for the stress exponents, which can used to determine the densification mechanism, were $\sim$1.75 for samples sintered between 1800 °C and 1950 °C, and $\sim$2.3 for samples sintered at 2000 °C. The grain size of samples sintered at 2000 °C, shown in **Table 4.4** and **Figure 4.7**, is slightly higher than those sintered at lower temperatures. This slight increase in grain size, due to the higher sintering temperature, may explain the difference in the value for the stress exponent for the sample sintered at 2000 °C. Also, it has been shown that higher temperatures and pressures lead to higher stress exponent values [68, 70]. In general, stress exponent values that are $\leq$2 represent a grain boundary sliding densification mechanism, while stress exponent values that are $\geq$3 represent a dislocation climb controlled densification mechanism [68, 70].

Therefore, the apparent densification mechanism for ($Zr_{0.8}$, $Nb_{0.1}$, $Ta_{0.1}$)C is grain boundary sliding.

The Young-Cutler method of determining sintering activation energy is more prevalent in literature. However, when compared to the method outlined by Bernard-Granger and Guizard, there are several shortcomings. The Young-Cutler method does not account for the changes in densification rate that occur due to the impact of density and grain size [84]. Unlike the previous method of calculating activation energy, the Young-Cutler method analyzes the densification data during a constant rate of heating period during sintering as opposed to isothermal conditions. They claim that isothermal conditions can lead to complications such as the inability to study the initial stage of sintering, densification occurring during fluctuations in temperature that happen while thermal equilibrium is being established, and the presence of additional stresses caused from rapid heat up rates that are commonly used for isothermal sintering studies [74]. Also, the Young-Cutler method is separated into grain boundary and volume diffusion components; the predominant densification mechanism between the two cannot be determined using this method. A single slope should be fitted to the plotted data points if a densification mechanism or combination of densification mechanisms with the same activation energy is present over the entire studied temperature range [74]. However, as shown in **Figure 4.35**, there are two distinct slopes for the plotted data; the steeper slope occurs at temperatures below 1850 °C. At temperatures greater than 1850 °C, the change in slope could be caused by a change in particle size distribution, a change in the mechanism of mass transport, or a change in the predominant densification mechanism [74].

Table 5.3 compares the densification activation energy results from the different methods used. The Bernard-Granger and Guizard method suggests that grain boundary sliding is the densification method and has an activation energy of 502 kJ/mol. The activation energies calculated from the Young-Cutler method for sintering temperatures below 1850 °C are 701 kJ/mol and 420 kJ/mol for grain boundary and volume diffusion mechanisms, respectively. The activation energy for grain boundary diffusion at temperatures below 1850 °C (701 kJ/mol) aligns closely with the weighted average (707.5 kJ/mol), relative to the cation stoichiometry of the powder mixture (i.e. 80% Zr, 10% Nb, 10% Ta), of the activation

energies of diffusion of Zr, Nb, and Ta in their respective mono-carbides, shown in **Table 5.4**. The activation energy for volume diffusion at temperatures below 1850 °C (420 kJ/mol) is close to the activation energies for the diffusion of C in NbC, TaC, and ZrC (370 kJ/mol [85, 86, 73], 440 kJ/mol [85, 87, 86, 73], and 440 kJ/mol [85, 88, 86, 73], respectively), shown in **Table 5.4**, and the weighted average of the carbon diffusion activation energies with respect to the powder stoichiometery was calculated to be 433 kJ/mol. Therefore, the grain boundary diffusion appears to be controlled by the diffusion of the metal cation in ($Zr_{0.8}$, $Nb_{0.1}$, $Ta_{0.1}$)C and the volume diffusion appears to be controlled by the diffusion of carbon in ($Zr_{0.8}$, $Nb_{0.1}$, $Ta_{0.1}$)C.

The activation energies from the Young-Cutler method were calculated using data from lower temperature ranges than from the Bernard-Granger and Guizard method. At lower temperatures, the densification is controlled by volume and grain boundary diffusion. At higher temperatures, the dominant densification mechanism is grain boundary sliding. Grain boundary sliding and diffusion based creep mechanisms tend to operate sequentially, with the overall densification rate being controlled by the slower of the two acting mechanisms [89, 57]. Taking that into account, the apparent densification mechanism for ($Zr_{0.8}$, $Nb_{0.1}$, $Ta_{0.1}$)C is therefore grain boundary diffusion with an activation energy of 701 kJ/mol since the activation energy for grain boundary diffusion is higher than for grain boundary sliding (502 kJ/mol). Note that this is only for temperatures up to 1850 °C. At temperatures higher than 1850 °C, the apparent densification mechanism for ($Zr_{0.8}$, $Nb_{0.1}$, $Ta_{0.1}$)C is grain boundary sliding, since the activation energy for grain boundary diffusion reduces to 276 kJ/mol at higher temperature.

These activation energy values are similar to the values from literature, seen in **Table 5.5**. In general, the ZrC densification activation energies from literature are higher than the values for NbC and TaC. The value for the densification activation energy of ZrC (technically ZrC_xO_{1-x}, similar to the material used in this study) sintered at temperatures ranging from 2006-2128 °C with an applied pressure of 25 MPa was 771 kJ/mol [90], which is close to the value calculated in this study using the Young-Cutler method for grain boundary diffusion (701 kJ/mol). However, the values of the activation energies from literature span over a wide range and should be used with caution; reported values of activation energy for ZrC range

Table 5.3: Densification Activation Energy Comparison

Method	**Densification Mechanism**	**Temperature Range (°C)**	**Activation Energy (kJ/mol)**
Bernard-Granger & Guizard	Grain Boundary Sliding	1800-2000 °C	502
Young-Cutler	Grain Boundary Diffusion	1700-1850 °C	701
Young-Cutler	Volume Diffusion	1700-1850 °C	420

Table 5.4: Mono-Carbide Diffusion Values From Literature

Mono -Carbide	**Diffusing Element**	**Approximate Act. E. (kJ/mol)**	**References**
NbC	C	370	[85, 86, 73]
NbC	Nb	525	[85, 86, 73]
TaC	C	440	[85, 87, 86, 73]
TaC	Ta	630	[87, 73]
ZrC	C	440	[85, 88, 86, 73]
ZrC	Zr	740	[85, 88, 73]

from 133.9 kJ/mol to 815 kJ/mol, depending on the experimental conditions and variables. The accuracy of these activation energies may be called into question since, particularly in the beginning stages of sintering, it is common to have simultaneous mechanisms at work [83], resulting in a combined effective activation energy. Generally, the value of the densification activation energy for ZrC is around 550-750 kJ/mol, which loosely agrees with the values from this study of 502 kJ/mol and 701 kJ/mol for grain boundary sliding and grain boundary diffusion mechanisms, respectively. Since ($Zr_{0.8}$, $Nb_{0.1}$, $Ta_{0.1}$)C is mostly ZrC with a small quantity of NbC and TaC, it is expected that the densification activation energy should be slightly less than ZrC due to the significantly lower values for the activation energies of NbC and TaC from literature.

5.5 Grain Growth Activation Energy

For ($Zr_{0.8}$, $Nb_{0.1}$, $Ta_{0.1}$)C, the primary grain growth mechanisms were determined to be surface diffusion ($m = 4$) and volume diffusion ($m = 3$) [57] with activation energies of 2204 kJ/mol and 1842 kJ/mol, respectively. In comparison, a similar results for the grain growth activation energy of ZrC was reported by Núñez-González et al. [91], who reported a value of 2380 kJ/mol. However, the calculated activation energies from this study were much higher than expected. As discussed previously, the diffusion activation energies shown in **Table 5.4** are all around 300-800 kJ/mol, but the calculated grain growth activation energies are around 2000 kJ/mol. Since the samples were still densifying during the onset of grain growth (see **Figure 4.7**), the activation energy for grain growth might be confounding with the activation energy for densification. Excess carbon accumulating between the grain boundaries, as seen in **Figure 4.26** and **Figure 4.27**, could also lead to an increased activation energy for grain growth, since it has been shown that dispersed solids inhibit grain growth [57]. Also, because the experiments performed for this study only covered the onset of grain growth (the grain sizes only varies from $\sim$1.3 μm to $\sim$6.1 μm), it is possible that additional data points from sintering at higher temperatures might lead to a different value for the grain growth activation energy.

Table 5.5: Sintering Activation Energies from Literature for NbC, TaC, and ZrC

Material	C/M	Temp. (°C)	Stress (MPa)	Stress Exp. (m)	Act. E. (kJ/mol)
NbC	∼1	1727-2527	2.9	–	217.6[a]
	0.98	1700-2200	60-100	3.7	240[b]
	0.99	2300	15.7	–	368.2[t]
	0.90-0.94	2430-2930	25	1.66	390[d]
TaC	∼1.0	1650-1750	80	1.2	252.94[e]
	0.95	1460-1810	–	4.5	400[f]
	1.0	2700	15.7	–	405.8[g]
	0.99	2000-2400	60-100	3.5	485[h]
	0.99-1.0	2350-2700	8-70	1	610-630[i]
ZrC	0.7-1.0	2300	15.7	–	133.9−192.5[j]
	0.79	1500-1600	140	3.3	480[k]
	∼1.0	1600	55	–	576[l]
	0.97	2200-2600	6.5-55	1	690[m]
	0.94	1942-2127	25	2	712[n]
	0.79	1500-1600	100	1	740[o]
	0.94	2006-2128	25	∼1.2	771[p]
	∼1.0	2000-2400	20-70	1.4-1.9	795-815[q]

[a] *Sintered, porosity ∼30% [92]*

[b] *Sintered, porosity - 2%, mean grain size - 20 μm, contents: non-combined C - 0.08%, O - 0.05%, N - 0.01%, W - 0.55% [73]*

[c] *Hot-pressed, porosity - 11% [93]*

[d] *Sintered in vacuum, porosity - 7-15%, mean grain size 7-12 μm [73]*

[e] *Spark plasma sintered, porosity ∼10-20%, mean grain size ∼0.7 μm [67]*

[f] *Hot-pressed in vacuum and annealed, porosity - 7%, mean grain size - 13 μm [73]*

[g] *Hot-pressed, porosity - 9.5% [93]*

[h] *Sintered, porosity - 3%, mean grain size - 5 μm, contents: non-combined C - 0.20%, O - 0.18%, N - 0.01%, W - 0.10% [73]*

[i] *Sintered materials, for $TaC_{0.99}$ (porosity - 2-5%, mean grain size - 4-16 μm) Q = 632 kJ/mol, for TaC∼1.0 (mean grain size - 10 μm) Q = 607 kJ/mol and for TaC∼1.0 (mean grain size - 16 μm) Q = 615 kJ/mol [73]*

[j] *Hot-pressed, porosity – 2.5-9% [93]*

[k] *$ZrC_{0.79}O_{0.13}$, Spark plasma sintered, fully dense, mean grain size - 5 μm [73]*

[l] *Spark plasma sintered, porosity – 5% [60]*

[m] *Sintered, porosity - 0.3-5.0%, mean grain size - 5-7 μm, contents: O+N - 0.15% [73]*

[n] *$ZrC_{0.94}O_{0.05}$, Spark plasma sintered, porosity – 23%, mean grain size - <1 μm [70]*

[o] *$ZrC_{0.79}O_{0.13}$, Spark plasma sintered, fully dense, mean grain size - 5 μm [73]*

[p] *$ZrC_{0.94}O_{0.05}$, Spark plasma sintered, porosity – 10%, mean grain size - 1 μm [90]*

[q] *Sintered, mean grain size - from 14 to 1000 μm, contents: non-combined C - 0.07%, O – 0.06%, N - 0.03% [73]*

Chapter 6

Conclusions

In this study, the fabrication and characterization of ($Zr_{0.8}$, $Nb_{0.1}$, $Ta_{0.1}$)C as a surrogate fuel for nuclear thermal propulsion (NTP) applications was studied. The findings provide valuable insights into the sintering behavior of the material, including the relationships between the hardness, grain size, and density of the samples consolidated at various sintering conditions and the activation energies for sintering and grain growth. Thorough characterization of the initial powders is essential; instead of starting with NbC, TaC, and ZrC powders, the powders were determined to be $NbC_{0.91}O_{0.09}$, TaC, and $ZrC_{0.89}O_{0.11}$, each were also found to contain oxide impurity phases identified using XRD.

The relationship between Vickers hardness and relative density was approximately linear, having an equal slope that was independent of the initial sintering conditions (temperature, pressure, and hold time) yet dependent on the sintering atmosphere. The relationship between grain size and relative density of samples sintered in a vacuum was exponential, with the initial grain size of the exponential fit, which was 1.37 μm, agreeing with the weighted average of the particle sizes of the mono-carbide powders used to make the ($Zr_{0.8}$, $Nb_{0.1}$, $Ta_{0.1}$)C powder, which was 1.39 μm. In general, the grain size and hardness of the samples depended on relative density rather than the sintering temperature or hold time. Nearly fully dense samples were achieved with minimal grain growth when sintering samples in a vacuum at 2000 °C for a 5 minute hold time and with an applied pressure of 30 MPa. The highest Vickers hardness values were around 18.5 GPa to 19 GPa and occurred at relative densities of around 98.0% to 98.5%; however, the highest recorded hardness values occurred

at relative densities where rapid grain growth had already begun. There appears to be a trade-off between achieving the highest hardness value while minimizing the grain size.

For samples sintered in an argon purged environment, the slope of the linear relationship between Vickers harness and relative density was approximately double the slope for the samples sintered in a vacuum. Also, the relationship between grain growth and relative density was not exponential, unlike samples sintered in a vacuum; this non-exponential relationship may also be a result of sintering at higher pressures. Additionally, the grade of graphite used for the SPS tooling led to a different SPS response, leading to differences in sample sintering behaviors, such as grain growth. The grade of graphite used in the tooling for an SPS study should always be recorded.

The sintering activation energy of ($Zr_{0.8}$, $Nb_{0.1}$, $Ta_{0.1}$)C was calculated using two methods. The first method, proposed by Bernard-Granger and Guizard [68], determined that the predominant densification mechanism is grain boundary sliding with an activation energy of 502 kJ/mol for samples sintered between 1800 °C and 1950 °C. The second method, the Young-Cutler method [74], indicated that the densification mechanism was grain boundary diffusion with an activation energy of 701 kJ/mol at temperatures below 1850 °C, which is seemingly driven by the diffusion of Zr throughout the lattice. Due to the sequential dependence of these two mechanisms, the densification mechanism was determined to be grain boundary diffusion up to 1850 °C (with an activation energy of 701 kJ/mol) after which it transitions to grain boundary sliding (with an activation energy of 502 kJ/mol.

The grain growth activation energy was calculated to be 2204 kJ/mol and 1842 kJ/mol, depending on the underlying grain growth mechanisms of surface diffusion and volume diffusion, respectively. These values were higher than expected, which may have been impacted by the simultaneous densification occurring during the initial stages of grain growth or due to the distributed carbon inclusions found in the samples.

Overall, ($Zr_{0.8}$, $Nb_{0.1}$, $Ta_{0.1}$)C demonstrates promising characteristics as a surrogate fuel for NTP. Its favorable sintering behavior, high density, optimal activation energy, and controlled grain growth position it as a suitable candidate for further exploration and potential application in advanced nuclear thermal propulsion systems. Future work should focus on UC based tri-carbides and replicate this study, comparing sintering behavior,

densification activation energy, and grain growth results. Additionally, mechanical and thermophysical work should be performed on not only the ($Zr_{0.8}$, $Nb_{0.1}$, $Ta_{0.1}$)C surrogate material, but also UC based tri-carbides. Homogenization studies should be performed to quantify the time and temperature needed to achieve chemical homogeneity. A deeper dive into the powder processing techniques should be studied to minimize the size and number of powder agglomerations. More investigation into the higher than expected grain growth activation energy is warranted. Higher sintering temperatures and longer hold times may be needed to allow for a more in-depth grain growth study. Hot, flowing hydrogen testing studies should be performed on any potential fuel candidate materials to fully understand their degradation in an NTP environment.

References

[1] W. G. Fahrenholtz, E. J. Wuchina, W. E. Lee, Y. Zhou, and G. Geiger, *Ultra-High Temperature Ceramics: Materials for Extreme Environment Applications.* Hoboken, UNITED STATES: John Wiley & Sons, Incorporated, 2021. 1, 3

[2] D. Ni, Y. Cheng, J. Zhang, J.-X. Liu, J. Zou, B. Chen, H. Wu, H. Li, S. Dong, J. Han, X. Zhang, Q. Fu, and G.-J. Zhang, "Advances in ultra-high temperature ceramics, composites, and coatings," *Journal of Advanced Ceramics*, vol. 11, pp. 1–56, Jan. 2022. 1

[3] E. Wuchina, E. Opila, M. Opeka, B. Fahrenholtz, and I. Talmy, "UHTCs: Ultra-High Temperature Ceramic Materials for Extreme Environment Applications," *The Electrochemical Society Interface*, vol. 16, p. 30, Dec. 2007. Publisher: IOP Publishing. 1

[4] W. G. Fahrenholtz and G. E. Hilmas, "Ultra-high temperature ceramics: Materials for extreme environments," *Scripta Materialia*, vol. 129, pp. 94–99, Mar. 2017. 1

[5] J. Binner, M. Porter, B. Baker, J. Zou, V. Venkatachalam, V. R. Diaz, A. D'Angio, P. Ramanujam, T. Zhang, and T. S. R. C. Murthy, "Selection, processing, properties and applications of ultra-high temperature ceramic matrix composites, UHTCMCs – a review," *International Materials Reviews*, vol. 65, pp. 389–444, Oct. 2020. Publisher: SAGE Publications. 1

[6] J. Justin and A. Jankowiak, "Ultra High Temperature Ceramics : Densification, Properties and Thermal Stability.," *Aerospace Lab*, pp. p. 1–11, Nov. 2011. Publisher: Alain Appriou. 1

[7] B. C. Wyatt, S. K. Nemani, G. E. Hilmas, E. J. Opila, and B. Anasori, "Ultra-high temperature ceramics for extreme environments," *Nature Reviews Materials*, pp. 1–17, Dec. 2023. Publisher: Nature Publishing Group. 1

[8] S. Zinkle, R. Nygren, and Y. Katoh, "Elements of a US R&D Plan to Develop Fusion Nuclear Materials," 1

[9] Y. Katoh, C. Parish, L. Tan, P. Edmondson, T. Koyanagi, L. Garrison, C. Ang, L. Snead, C. Henager, and S. Zinkle, "Emerging High Temperature Materials for Potential Application to Fusion," 2017. 1

[10] Space Nuclear Propulsion Technologies Committee, Aeronautics and Space Engineering Board, Division on Engineering and Physical Sciences, and National Academies of Sciences, Engineering, and Medicine, *Space Nuclear Propulsion for Human Mars Exploration*. Washington, D.C.: National Academies Press, July 2021. Pages: 25977. 3, 4

[11] D. Burns and S. Johnson, "Nuclear Thermal Propulsion Reactor Materials," Mar. 2020. 3, 6, 43

[12] S. K. Borowski, D. McCurdy, and T. Packard, "Nuclear Thermal Propulsion (NTP): A Proven, Growth Technology for 'Fast Transit' Human Missions to Mars," in *AIAA SPACE 2013 Conference and Exposition*, (San Diego, CA), American Institute of Aeronautics and Astronautics, Sept. 2013. 3

[13] A. Qualls and E. Hancock, "Recapturing NERVA-Derived Fuels for Nuclear Thermal Propulsion," in *47th AIAA/ASME/SAE/ASEE Joint Propulsion Conference & Exhibit*, (San Diego, California), American Institute of Aeronautics and Astronautics, July 2011. 3

[14] S. K. Borowski, D. R. McCurdy, and T. W. Packard, ""7-Launch" NTR Space Transportation System for NASA's Mars Design Reference Architecture (DRA) 5.0," *th Joint Propulsion Conference*, 2009. 3

[15] W. J. Emrich, *Principles of Nuclear Rocket Propulsion*. Elsevier, 2016. 3

[16] "Infographic: How Does Nuclear Thermal Propulsion Work?," Jan. 2020. 5

[17] D. Pelaccio and M. El-Genk, "A review of nuclear thermal propulsion carbide fuel corrosion and key issues," Dec. 1994. 9

[18] D. G. Pelaccio, M. S. El-Genk, and D. P. Butt, "Hydrogen corrosion considerations of carbide fuels for nuclear thermal propulsion applications," *Journal of Propulsion and Power*, vol. 11, pp. 1338–1348, Nov. 1995. 9, 38, 40, 41

[19] M. Stewart and B. G. Schnitzler, "A Comparison of Materials Issues for Cermet and Graphite-Based NTP Fuels," in *49th AIAA/ASME/SAE/ASEE Joint Propulsion Conference*, (San Jose, CA), American Institute of Aeronautics and Astronautics, July 2013. 9

[20] C. W. Watson, "Nuclear rockets: High-performance propulsion for Mars," Tech. Rep. LA-12784-MS, Los Alamos National Lab. (LANL), Los Alamos, NM (United States), May 1994. 7

[21] S. K. Borowski, D. R. McCurdy, and T. W. Packard, "Nuclear Thermal Propulsion (NTP): A proven growth technology for human NEO/Mars exploration missions," in *2012 IEEE Aerospace Conference*, (Big Sky, MT), pp. 1–20, IEEE, Mar. 2012. 8

[22] S. K. Bhattacharyya, "An assessment of fuels for nuclear thermal propulsion.," Tech. Rep. ANL/TD/TM01-22, Argonne National Lab., IL (US), Sept. 2002. 9, 18, 19, 23, 26, 27, 28, 29, 34, 35, 48, 57

[23] R. Matthews, R. E. Baars, T. Blair, D. P. Butt, R. E. Mason, W. A. Stark, E. K. Storms, and T. C. Wallace, "Fuels for space nuclear power and propulsion: 1983-1993," in *A Critical Review of Space Nuclear Power and Propulsion 1984-1993*, pp. 179–220, Los Alamos, NM: Los Alamos National Laboratory, 1994. 9, 36, 37

[24] T. Knight and S. Anghaie, "Advanced carbide fuels for space nuclear thermal propulsion," in *37th Joint Propulsion Conference and Exhibit*, (Salt Lake City,UT,U.S.A.), American Institute of Aeronautics and Astronautics, July 2001. 9

[25] G. L. Bennett, H. Finger, T. Miller, W. Robbins, and M. Klein, "Prelude to the future: A brief history of nuclear thermal propulsion in the United States," in *A critical review of space nuclear power and propulsion 1984–1993*, pp. 221–267, 1994. 10

[26] J. A. Dewar, *Project Rover: A Study of the Nuclear Rocket Development Program, 1953 - 1963*. Ph.D., Kansas State University, United States – Kansas, 1974. ISBN: 9798659257432. 10, 11, 13

[27] G. Hula, "Atomic Power in Space II: A history of space nuclear power and propulsion in the United States," Tech. Rep. INL/EXT-15-34409-Rev000, 1893110, Jan. 2015. 11

[28] R. E. Malenfant, F. P. Durham, and M. Klein, "Nuclear Thermal Rocket Reactors and Engine Systems: A Retrospective," Oct. 2021. 12

[29] J. L. Finseth, "Rover nuclear rocket engine program: Overview of rover engine tests," Tech. Rep. NASA-CR-184270, Feb. 1991. NTRS Author Affiliations: Sverdrup Technology, Inc. NTRS Document ID: 19920005899 NTRS Research Center: Legacy CDMS (CDMS). 13, 15, 16, 19

[30] D. R. Koenig, "Experience Gained from the Space Nuclear Rocket Program (Rover)," *Los Alamos National Laboratory*, 1986. 14, 17, 19, 20, 21

[31] W. H. Robbins and H. B. Finger, "An Historical Perspective of the NERVA Nuclear Rocket Engine Technology Program," Tech. Rep. E-6312, July 1991. NTRS Author Affiliations: Analytical Engineering Corp., Sverdrup Technology, Inc., Brook Park NTRS Meeting Information: Conference on Advanced Space Exploration Initiative Technologies; 1991-09-04 to 1991-09-06; undefined NTRS Document ID: 19910017902 NTRS Research Center: Legacy CDMS (CDMS). 16

[32] V. Zakirov and V. Pavshook, "Russian nuclear rocket engine design for mars exploration," *Tsinghua Science and Technology*, vol. 12, pp. 256–260, June 2007. 23, 24

[33] A. G. Lanin and I. I. Fedik, "Selecting and using materials for a nuclear rocket engine reactor," *Physics-Uspekhi*, vol. 54, p. 305, Mar. 2011. Publisher: IOP Publishing. 22, 39

[34] K. Palomares, P. Venneri, and M. Eades, *Survey of Fuel System Options for Low Enriched Uranium (LEU) Nuclear Thermal Propulsion*. Feb. 2017. 23, 42, 55

[35] "710 High-Temperature Gas Reactor Program Summary Report. Volume III. Fuel Element Development.," Tech. Rep. GEMP600V3, General Electric CO., Cincinnati, Ohio (Usa). Nuclear Materials and Propulsion Operation., 1967. Num Pages: 154. 23

[36] J. Walton, "An overview of tested and analyzed NTP concepts," in *Conference on Advanced SEI Technologies*, (Cleveland,OH,U.S.A.), American Institute of Aeronautics and Astronautics, Sept. 1991. 23

[37] G. Kruger, "A cermet fuel reactor for nuclear thermal propulsion," Jan. 1991. NTRS Author Affiliations: General Electric Co. NTRS Document ID: 19920001878 NTRS Research Center: Legacy CDMS (CDMS). 23

[38] K. Benensky, "Summary of Historical Solid Core Nuclear Thermal Propulsion Fuels," 2013. 23

[39] R. A. Haslett, "SPACE NUCLEAR THERMAL PROPULSION PROGRAM FINAL REPORT," 1995. 26

[40] "710 high-temperature gas reactor program summary report. Volume I. Summary," Tech. Rep. GEMP-600(Vol.1), General Electric Co., Cincinnati, Ohio (USA). Nuclear Materials and Propulsion Operation, Jan. 1967. 25

[41] S. A. Wright, "An in-pile testing program to study the performance characteristics of coated particle fuels," in *AIP Conference Proceedings*, vol. 271, (Albuquerque, New Mexico, (USA)), pp. 1173–1180, AIP, 1993. ISSN: 0094243X. 26

[42] S. Anghaie, T. W. Knight, J. Plancher, and R. Gouw, "Development of a Robust Tri-Carbide Fueled Reactor for Multimegawatt Space Power and Propulsion Applications," Tech. Rep. DOE/ID/14116, University of Florida (US), Aug. 2004. 26, 29, 30, 32, 33

[43] T. W. Knight and S. Anghaie, "Processing and fabrication of mixed uranium/refractory metal carbide fuels with liquid-phase sintering," *Journal of Nuclear Materials*, vol. 306, pp. 54–60, Nov. 2002. 31, 48

[44] W. D. Callister and D. G. Rethwisch, "Materials Science and Engineering," 2018. 43

[45] A. I. Gusev and S. V. Rempel', "Phase Diagram for the Zr–Nb–C System," *Doklady Physical Chemistry*, vol. 375, pp. 249–253, Dec. 2000. 43, 44, 45, 46

[46] J. P. Tosdale, "Refractory metal-carbide systems," Tech. Rep. IS-T-219, Ames Lab., Ames, IA (United States), May 1967. 43, 47, 48

[47] D. P. Butt and T. C. Wallace Sr., "The UZrC Ternary Phase Diagram above 2473 K," *Journal of the American Ceramic Society*, vol. 76, no. 6, pp. 1409–1419, 1993. _eprint: https://ceramics.onlinelibrary.wiley.com/doi/pdf/10.1111/j.1151-2916.1993.tb03919.x. 48, 49, 50, 51, 52

[48] A. Makhijani, L. Chalmers, and B. Smith, "Facts to Fuel an Informed Debate on Nuclear Proliferation and Nuclear Power," vol. 13, no. 1, 2005. 53

[49] F. S. Patton, *Enriched Uranium Processing*. Pergamon Press, 1963. Google-Books-ID: ABBAAAAAIAAJ. 53, 55

[50] P. F. Venneri and Y. Kim, "A feasibility study on low-enriched uranium fuel for nuclear thermal rockets – I: Reactivity potential," *Progress in Nuclear Energy*, vol. 83, pp. 406–418, Aug. 2015. 55

[51] S. B. Rawlins and L. D. Thomas, "Feasibility of Low-Enriched Uranium Fueled Nuclear Thermal Propulsion in the Low-Thrust Region Below 16klbf," *Annals of Nuclear Energy*, vol. 179, p. 109368, Dec. 2022. 55

[52] "High-Assay Low-Enriched Uranium," 2024. 54

[53] P. F. Venneri and Y. Kim, "A feasibility study on low enriched uranium fuel for nuclear thermal rockets – II: Rocket and reactor performance," *Progress in Nuclear Energy*, vol. 87, pp. 156–167, Mar. 2016. 55

[54] V. Patel, M. Eades, P. Venneri, and C. R. Joyner II, "Comparing Low Enriched Fuel to Highly Enriched Fuel for use in Nuclear Thermal Propulsion Systems," Tech. Rep. INL/CON-16-37619, Idaho National Lab. (INL), Idaho Falls, ID (United States), July 2016. 55

[55] C. R. Joyner, D. J. Levack, T. Jennings, M. Eades, and V. Patel, "Engine Design Attributes Relative to HEU and LEU Core Approaches for a Small Thrust NTP," in *52nd AIAA/SAE/ASEE Joint Propulsion Conference*, AIAA Propulsion and Energy Forum, American Institute of Aeronautics and Astronautics, July 2016. 55

[56] B. Schnitzler and S. Borowski, "Small Fast Spectrum Reactor Designs Suitable for Direct Nuclear Thermal Propulsion," in *48th AIAA/ASME/SAE/ASEE Joint Propulsion Conference & Exhibit*, (Atlanta, Georgia), American Institute of Aeronautics and Astronautics, July 2012. 56, 61

[57] M. N. Rahaman, *Ceramic Processing and Sintering*. CRC Press, second ed., July 2003. 57, 100, 171, 174

[58] M. Tokita, "Progress of Spark Plasma Sintering (SPS) Method, Systems, Ceramics Applications and Industrialization," *Ceramics*, vol. 4, pp. 160–198, June 2021. Number: 2 Publisher: Multidisciplinary Digital Publishing Institute. 58, 59, 60, 62, 63, 65

[59] O. Guillon, J. Gonzalez-Julian, B. Dargatz, T. Kessel, G. Schierning, J. Räthel, and M. Herrmann, "Field-Assisted Sintering Technology/Spark Plasma Sintering: Mechanisms, Materials, and Technology Developments," *Advanced Engineering Materials*, vol. 16, no. 7, pp. 830–849, 2014. _eprint: https://onlinelibrary.wiley.com/doi/pdf/10.1002/adem.201300409. 60, 64

[60] X. Wei, C. Back, O. Izhvanov, C. D. Haines, and E. A. Olevsky, "Zirconium Carbide Produced by Spark Plasma Sintering and Hot Pressing: Densification Kinetics, Grain Growth, and Thermal Properties," *Materials*, vol. 9, p. 577, July 2016. Number: 7 Publisher: Multidisciplinary Digital Publishing Institute. 60, 66, 71, 72, 73, 74, 175

[61] J. P. Kelly and O. A. Graeve, "Mechanisms of pore formation in high-temperature carbides: Case study of TaC prepared by spark plasma sintering," *Acta Materialia*, vol. 84, pp. 472–483, Feb. 2015. 60, 68, 69

[62] Z. A. Munir, D. V. Quach, and M. Ohyanagi, "Electric Current Activation of Sintering: A Review of the Pulsed Electric Current Sintering Process," *Journal*

of the American Ceramic Society, vol. 94, no. 1, pp. 1–19, 2011. _eprint: https://onlinelibrary.wiley.com/doi/pdf/10.1111/j.1551-2916.2010.04210.x. 67, 70

[63] M. Abedi, S. Sovizi, A. Azarniya, D. Giuntini, M. E. Seraji, H. R. M. Hosseini, C. Amutha, S. Ramakrishna, and A. Mukasyan, "An analytical review on Spark Plasma Sintering of metals and alloys: from processing window, phase transformation, and property perspective," *Critical Reviews in Solid State and Materials Sciences*, vol. 48, no. 2, pp. 169–214, 2023. ISSN: 1040-8436. 67

[64] J. Gu, J. Zou, J. Liu, H. Wang, J. Zhang, W. Wang, and Z. Fu, "Sintering highly dense ultra-high temperature ceramics with suppressed grain growth," *Journal of the European Ceramic Society*, vol. 40, pp. 1086–1092, Apr. 2020. 75, 76, 77, 78, 79, 161, 163

[65] W. Ji, S. S. Rehman, W. Wang, H. Wang, Y. Wang, J. Zhang, F. Zhang, and Z. Fu, "Sintering boron carbide ceramics without grain growth by plastic deformation as the dominant densification mechanism," *Scientific Reports*, vol. 5, p. 15827, Oct. 2015. Number: 1 Publisher: Nature Publishing Group. 81, 82, 161, 163

[66] Y. Zheng, J. Zou, W. Liu, W. Wang, W. Ji, and Z. Fu, "High pressure sintering of fully dense tantalum carbide ceramics with limited grain growth," *Journal of the European Ceramic Society*, vol. 43, pp. 5117–5124, Sept. 2023. 83, 84, 161, 163

[67] C. Liu, A. Wang, T. Tian, L. Hu, W. Guo, Q. He, J. Xie, W. Wang, H. Wang, and Z. Fu, "Sintering and densification mechanisms of tantalum carbide ceramics," *Journal of the European Ceramic Society*, vol. 41, pp. 7469–7477, Dec. 2021. 86, 87, 88, 89, 90, 91, 93, 100, 175

[68] G. Bernard-Granger and C. Guizard, "Spark plasma sintering of a commercially available granulated zirconia powder: I. Sintering path and hypotheses about the mechanism(s) controlling densification," *Acta Materialia*, vol. 55, pp. 3493–3504, June 2007. 100, 101, 103, 149, 169, 177

[69] M. Zhang, R. Li, T. Yuan, X. Feng, and S. Xie, "Effect of low-melting-point sintering aid on densification mechanisms of boron carbide during spark plasma sintering," *Scripta Materialia*, vol. 163, pp. 34–39, Apr. 2019. 100

[70] M. Gendre, A. Maître, and G. Trolliard, "A study of the densification mechanisms during spark plasma sintering of zirconium (oxy-)carbide powders," *Acta Materialia*, vol. 58, pp. 2598–2609, Apr. 2010. 100, 169, 175

[71] H. L. Brown, P. E. Armstrong, and C. P. Kempter, "Elastic Properties of Some Polycrystalline Transition-Metal Monocarbides," *The Journal of Chemical Physics*, vol. 45, pp. 547–549, July 1966. 101, 102

[72] N. Korklan, G. Hilmas, and W. Fahrenholtz, "Processing and Room Temperature Mechanical Properties of a Zirconium Carbide Ceramic," *Journal of the American Ceramic Society*, vol. 104, pp. 413–418, Jan. 2021. 101, 102

[73] I. L. Shabalin, *Ultra-High Temperature Materials II: Refractory Carbides I (Ta, Hf, Nb and Zr Carbides)*. Springer, 2019. 102, 171, 173, 175

[74] W. S. Young and I. B. Cutler, "Initial Sintering with Constant Rates of Heating," *Journal of the American Ceramic Society*, vol. 53, no. 12, pp. 659–663, 1970. _eprint: https://onlinelibrary.wiley.com/doi/pdf/10.1111/j.1151-2916.1970.tb12036.x. 103, 104, 149, 169, 170, 177

[75] J. Frenkel, "Viscous Flow of Crystalline Bodies under the Action of Surface Tension," *J. Phys. (U. S. S. R)*, vol. 9, no. 5, p. 385, 1945. 103

[76] D. L. Johnson, "New Method of Obtaining Volume, Grain-Boundary, and Surface Diffusion Coefficients from Sintering Data," *Journal of Applied Physics*, vol. 40, pp. 192–200, Jan. 1969. 103

[77] O. I. Lee, "The Mineralogy of Hafnium.," *Chemical Reviews*, vol. 5, pp. 17–37, Apr. 1928. 106

[78] E. K. Storms and N. H. Krikorian, "The Variation of Lattice Parameter with Carbon Content of Niobium Carbide," *The Journal of Physical Chemistry*, vol. 63, pp. 1747–1749, Oct. 1959. Publisher: American Chemical Society. 157, 160

[79] A. L. Bowman, "THE VARIATION OF LATTICE PARAMETER WITH CARBON CONTENT OF TANTALUM CARBIDE [1]," *The Journal of Physical Chemistry*, vol. 65, pp. 1596–1598, Sept. 1961. 157, 160

[80] H. F. Jackson and W. E. Lee, "2.13 - Properties and Characteristics of ZrC," in *Comprehensive Nuclear Materials* (R. J. M. Konings, ed.), pp. 339–372, Oxford: Elsevier, Jan. 2012. 157, 160

[81] C. Gasparrini, D.-s. Rana, N. Le Brun, D. Horlait, C. N. Markides, I. Farnan, and W. E. Lee, "On the stoichiometry of zirconium carbide," *Scientific Reports*, vol. 10, p. 6347, Apr. 2020. Publisher: Nature Publishing Group. 158, 166

[82] V. A. Mitrokhin, R. A. Lyutikov, and R. S. Yurkova, "Change in the Lattice Constant of Zirconium Carbide in the Region of Homogeneity," *Inorganic Materials*, vol. 11, pp. 978–980, Jan. 1975. 160

[83] Z. Z. Fang and H. Wang, "Densification and grain growth during sintering of nanosized particles," *International Materials Reviews*, vol. 53, pp. 326–352, Nov. 2008. Publisher: SAGE Publications. 168, 169, 174

[84] J. Wang and R. Raj, "Estimate of the Activation Energies for Boundary Diffusion from Rate-Controlled Sintering of Pure Alumina, and Alumina Doped with Zirconia or Titania," *Journal of the American Ceramic Society*, vol. 73, no. 5, pp. 1172–1175, 1990. _eprint: https://onlinelibrary.wiley.com/doi/pdf/10.1111/j.1151-2916.1990.tb05175.x. 170

[85] R. Salehin, X. Tang, G. B. Thompson, and C. R. Weinberger, "Vacancy-cluster and off-lattice metal-atom diffusion mechanisms in transition metal carbides," *Computational Materials Science*, vol. 199, p. 110713, Nov. 2021. 171, 173

[86] G. L. DePoorter and T. Wallace, "Diffusion in Binary Carbides," in *Advances in High Temperature Chemistry*, vol. 4, pp. 107–135, Elsevier, 1971. 171, 173

[87] X. Tang, R. Salehin, G. B. Thompson, and C. R. Weinberger, "Statistical study of vacancy diffusion in TiC and TaC," *Physical Review Materials*, vol. 4, p. 093602, Sept. 2020. Publisher: American Physical Society. 171, 173

[88] P. Barnier, C. Brodhag, and F. Thevenot, "Hot-pressing kinetics of zirconium carbide," *Journal of Materials Science*, vol. 21, pp. 2547–2552, July 1986. 171, 173

[89] M. Harmer, "Hot Pressing: Technology and Theory," pp. 222–225, Dec. 1991. 171

[90] G. Antou, N. Pradeilles, M. Gendre, and A. Maître, "New approach of the evolution of densification mechanisms during Spark Plasma Sintering: Application to zirconium (oxy-)carbide ceramics," *Scripta Materialia*, vol. 101, pp. 103–106, May 2015. 171, 175

[91] B. Núñez-González, A. L. Ortiz, F. Guiberteau, and M. Nygren, "Improvement of the Spark-Plasma-Sintering Kinetics of ZrC by High-Energy Ball-Milling," *Journal of the American Ceramic Society*, vol. 95, no. 2, pp. 453–456, 2012. _eprint: https://onlinelibrary.wiley.com/doi/pdf/10.1111/j.1551-2916.2011.05007.x. 174

[92] A. D. Panasyuk and P. S. Kislyi, "Some features of the sintering of niobium carbide," *Soviet Powder Metallurgy and Metal Ceramics*, vol. 4, pp. 275–280, Apr. 1965. 175

[93] G. V. Samsonov, M. S. Koval'chenko, R. Y. Petrykina, and V. Y. Naumenko, "Hot pressing of the transition metals and their carbides in their homogeneity regions," *Soviet Powder Metallurgy and Metal Ceramics*, vol. 9, pp. 713–716, Sept. 1970. 175

Vita

Jonas Kessing was born in Raleigh, North Carolina. In May 2014, he earned a Bachelor of Science degree in Mechanical Engineering from North Carolina State University. After graduation, while awaiting his security clearance, he worked as a mechanical design engineer for ASML. Once his clearance was granted, he joined the Naval Nuclear Laboratory (NNL) as a Reactor Operations Engineer in Charleston, SC.

During his tenure at NNL, he attended Nuclear Power School and completed several qualifications, including Engineering Officer of the Watch, Auxiliary Control Room Supervisor, and Engineering Duty Officer, on a training nuclear submarine. He also trained Navy personnel on the submarine subsystems including reactor operations, engine room procedures, and emergency core cooling systems. Additionally, he used the interactive display equipment (IDE) simulator, led classroom training, mentored Navy personnel, and conducted training and operational audits. Later, as the environmental safety engineer for the training submarine, he provided subject matter expertise in areas such as environmental safety, health, radiological controls, quality assurance, waste management, emergency planning, and fire protection to ensure safe and compliant work execution.

In June 2019, he began working as a Fuel Process Engineer for Nuclear Fuel Services, a subsidiary of BWXT, which manufactures nuclear fuel for naval submarines and aircraft carriers. His responsibilities included process engineering, project management, and mechanical design engineering for the Category 1 Fuel Fabrication Facility. As a project manager, he oversaw the completion of over two dozen projects focused on improving reliability, redundancy, and reducing operational costs. As the primary mechanical design engineer for the Fuel Process Engineering group, he developed 3D CAD models of existing and new equipment and designed testing equipment for various fuel manufacturing processes.

While working at BWXT, he earned a Master of Engineering Management degree from Old Dominion University.

In August 2022, he began pursuing a doctorate in Nuclear Engineering at the University of Tennessee. He concurrently obtained a Master of Science degree in Materials Science and Engineering in May 2024, presenting a capstone project on spark plasma sintering of solid solution carbide fuels for nuclear thermal propulsion. His research has focused on fabricating solid solution carbide surrogate fuels via spark plasma sintering for nuclear thermal propulsion applications.